AN INTEGRATED GEOCHEMICAL, PETROLOGIC, GEOCHRONOLOGICAL, AND METALLOGENIC STUDY OF THE POWDER HORN INTRUSIVE SUITE AND THE ASSOCIATED LODESTAR PROSPECT-A MAGMATIC-HYDROTHERMAL AURIFEROUS BRECCIA ZONE THAT LINKS EPITHERMAL AND PORPHYRY SYSTEMS, NORTHERN BURIN PENINSULA, NEWFOUNDLAND

JOHN GLENN HINCHEY

An integrated geochemical, petrologic, geochronological, and metallogenic study of the Powder Horn Intrusive Suite and the associated Lodestar Prospect-a magmatic-hydrothermal auriferous breccia zone that links epithermal and porphyry systems, Northern Burin Peninsula, Newfoundland.

By

© John Glenn Hinchey, B.Sc. (Hons.)

A Thesis Submitted to the School of Graduate Studies
in Partial Fulfilment of the Requirements for the Degree
of Master of Science.

Department of Earth Sciences,
Memorial University of Newfoundland

St.John's Newfoundland

Abstract

The Lodestar Prospect is associated with the Powder Horn Intrusive Suite and comprises auriferous sulphide-oxide mineralized polylithic breccias which have a magmatic-hydrothermal or phreatomagmatic origin. The best grades obtained by exploration companies from chip-channel sampling of the breccia were 4.98 g/t Au and 14.8 g/t Ag over 15.9 m, along with one area that returned an assay of approximately 2.0 % Zn. Earlier assays derived values of 6.13 g/t Au over 4.7 m and 4.91 g/t Au over 3 m. More recent channel samples 5.6 g/t Au over 8.5 m including 12.6 g/t Au over 1m.

The Powder Horn Intrusive Suite is a multi-phase intrusive suite, with both pre- and post-brecciation (mineralization) phases. Pre-mineralization rocks consist of (1) the late Neoproterozoic Musgravetown Group sedimentary rocks, which are hornfelsed close to the intrusion, (2) medium grained gabbro/diorite, and (3) minor felsic material; the gabbro phase has been U-Pb zircon dated at 603+/- 2 Ma . Post-mineralization phases include (1) fine grained gabbro/diorite, (2) felsic phases, and (3) diabase dykes; a felsic dyke has been U-Pb zircon dated at 605 +/- 5 Ma.

The main mineralized breccia, which occurs at the contact between sedimentary rocks and the pre-breccia gabbro/diorite, is exposed over approximately 25 meters and contains Au associated with Cu, As, and Zn. Arsenopyrite geothermometry suggests a crystallization temperature of approximately 425 +/- 50 ^{0} C for the sulphides. The mineralization occurs dominantly as the matrix to the breccia, whereas unmineralized sections of the breccia contain actinolite/chlorite as the matrix. The breccia clasts consist of host sedimentary material, pre-breccia gabbro/diorite, quartz-feldspar porphyry (QFP), diabase, and minor fine-grained granite. The sedimentary and gabbro/diorite clasts were locally derived from the wall-rock, however, the QFP clasts have not been observed as outcrop in the area of the showing and have REE patterns unlike felsic intrusive rocks in the vicinity of the prospect. Thus the QFP are assumed to be derived from depth. In places, these QFP clasts contain pre-breccia sulphide mineralization. They also appear to be finely comminuted, producing a rock-flour matrix in portions of the breccia which probably indicates transportation from depth. Many characteristics of the Lodestar Prospect suggest a magmatic-hydrothermal origin for the breccia produced by fluid exsolution from an auriferous intrusive system. Furthermore, the presence of exotic mineralized QFP clasts within the breccia suggests that the mineralization may be related to a deep Cu-Au porphyry system. If so, the prospect may have formed in a transitional environment between a deeper porphyry system and a shallow epithermal system. The Lodestar Prospect is, therefore, very significant because it indicates the possibility for porphyry-style mineralization within the Powder Horn Intrusive Suite, as well as elsewhere on the Burin Peninsula.

Acknowledgements

Numerous individuals require acknowledgement for their contributions during the production and completion of this thesis. First and foremost to my supervisor, Derek Wilton, I extend great thanks for suggesting and supervising the project. Derek provided constant support, both academic and financial, throughout the coarse of this study. His guidance and willingness to discuss problems at any time kept things constantly moving at a steady and encouraging pace, and his "open-door", yet hands off, approach to his supervisory role lead to a great learning experience: I thank you. P.S. Thanks for not using that final draft for kindling!

I wish to also thank Cyril O'Driscoll, Department of Mines and Energy (NDME), for his supervisory role and support during the field work associated with this thesis. Cyril introduced me to Avalon Geology. His field mapping experience and knowledge, as well as his vast understanding of the deposit types and potential of the Avalon Zone were invaluable during field component of this thesis. Cyril also gave constant support, and was willing to discuss any problems, throughout the writing and interpreting phases of this thesis. His presence, as well as field assistants Barry Sparkes and Greg Cochrane, made the summer on the Powder Horn a very enjoyable stay. Sean O'Brien, NDME, is also thanked for many detailed discussions and direction with respect to the project. Prospector Leroy Smith is thanked for his support of the project and his permission to use unpublished property information.

Funding for this project was provided from support from the NDME, and from a NSERC operating grant to Derek Wilton. The awarding of a Special Scholarship for Studies in the Sciences related to Resource Development and the Buchans' Scholarship Fund of ASARCO Incorporated is also acknowledged.

Technical staff, both at the Department of Earth Science and the NDME Laboratories, are acknowledged. The assistance of Pam King (XRF), Mike Tubrett (ICP-MS/LAM), Rick Soper (Laporatory services), as well as Alison Pye (mass spec. sulphur analysis), of the Department of Earth Sciences is greatly appreciated, as is that of Chris Finch of the NDME laboratories. Numerous professors at the Department of Earth Science, especially Mark Wilson and George Jenner, are thanked for their willingness to discuss any problems that I endured.

Fellow students, especially Darrell Hyde, Danny Mulrooney, Rod Smith, Richard Cox, Jason Krauss, Trevor MacHattie, as well as many others, thanks for the advice and good times over the last few years.

I extend a special thanks to my parents for their constant support and assistance throughout the course of the project and my university career. Finally, to my fiancee Alana Rawlings, I would like to sincerely thank you for your emotional support and your companionship and guidance throughout this project. You always made the dark days brighter and happier and gave constant inspiration to find the light at the end of the tunnel.

Table of Contents

Chapter Four: Major, Trace, and Rare-Earth Element Geochemistry of the PHIS and associated Lodestar Prospect, Isotope Geochemistry and Geothermometry of the Lodestar Mineralization, and the Nature of Invisible Gold.

Chapter 5: Discussions and Conclusions

List of Tables

List of Figures

List of Plates

Chapter 1: Introduction

1.1 Introduction

Gold mineralization has been known to occur within rocks of the Avalon Belt (O'Brien *et al.*, 1998), in the southern Appalachians, for at least 200 years and this area was the site of North America's first gold rush (Carpenter, 1972). Within this belt of Avalonian rocks, gold is associated with hydrothermal systems in a variety of magmatic and structural settings related to epithermal, transitional, and/or porphyry systems (O'Brien *et al.* 1998). In the Avalon Zone of the Newfoundland Appalachians, widespread auriferous mineralization has only been documented for about the past twenty years (Hussey, 1978; Taylor *et al.* 1979; McKenzie, 1983; 1986; O'Driscoll, 1984). Since then, numerous discoveries have been made, and large, auriferous, alteration belts have been delineated (*e.g.* Huard and O'Driscoll, 1984; 1986; McKenzie, 1986; Huard, 1990; Hayes and O'Driscoll, 1990; O'Brien *et al.* 1996; 1998; 1999; Dubé *et al.* 1998).

In 1998, prospector Leroy Smith discovered significant gold mineralization within polylithic breccias associated with the Powder Horn Intrusive Suite in the Goobies area of the Avalon Peninsula. He staked the area, and optioned it to Noveder Inc. who re-optioned the property to NDT Ventures Ltd. NDT carried out an exploration program on the property during December, 1998 which comprised prospecting, gridding, soil geochemical sampling, ground geophysical surveying, backhoe trenching and rock sampling. The best results obtained by NDT from chip-channel sampling of mineralized

breccia in the main showing were 4.98 g/t Au and 14.8 g/t Au over a 15.9 m width. In addition, one area returned an assay of approximately 2.0% Zn. Channel samples collected earlier by Noveder Inc. returned values of 6.13 g/t Au over 4.7 m and 4.91 g/t Au over 3 m. Ownership of the property reverted back to Mr. Smith in 1999. He named the occurrence the "Lodestar Prospect" and completed additional trenching and sampling in December, 1999. This work extended the main zone and added previously unknown zones.

1.2 Location and Access

The Powder Horn Intrusive suite (PHIS) and associated Lodestar Prospect are located in the Goobies-Come by Chance area within the Sound Island and Sunnyside NTS map sheets, 1M16 and 1N13 respectively (figure 1.1). The PHIS straddles these map sheets and is bounded by approximate latitudes 47° 53' N and 47° 58' N and longitudes 54° 03' E and 53° 56' E. This suite is exposed as an elliptical body located at the intersection between the isthmus of the Avalon Peninsula and the northern part of the Burin Peninsula. The Lodestar prospect is approximately 2 km west of the Trans Canada Highway and approximately 130 road km from St. John's. Access to the prospect is along the paved Burin Peninsula Highway (210) from which a gravel woods road turns east approximately 3.5 km south of the Trans Canada Highway intersection. The Lodestar prospect is located 1.4 km in along this woods road (figure 1.2).

1.3 Physiography and Vegetation

The topography of the intrusive suite varies from fairly steep and rough in the eastern half to more gentle topography in the western half. The eastern half consists of numerous hills with elevations ranging from 105 meters above sea level in the valleys up to approximately 305 meters above sea level on the hills. The valleys are dominated by bogs with black spruce growing up the sides of the hills. Outcrop is patchy in the valleys and the slopes with substantial outcrop on the tops of the hills. (Plate 1.1). The western half is dominated by gentle slopes covered with numerous small ponds, streams, bogs and patches of black spruce (plate 1.2). Outcrop in these areas is poor. The Lodestar prospect (Plate 1.3) occurs in a valley in the eastern part of the intrusion where development of a logging road stripped the area of overburden thereby exposing the showing.

1.4 Previous Work

Although significant work has been conducted and documented on the geology and tectonics of the Avalon Zone of the Appalachians, including the Burin Peninsula area, little work has been completed on the PHIS and surrounding area. Relevant previous work in the project area includes regional mapping by Rose (1948), Anderson (1965), McCartney (1958, 1967), O'Driscoll (1977) and O'Driscoll and Hussey (1976/77). Aside from this regional mapping, no other mapping more detailed than 1:50,000 nor

exploration work has been conducted in the area. The general geology and tectonic setting will be covered in a future section.

1.5 Methods

The initial stages of this project involved three months of field mapping in the PHIS. This work was conducted out of the town of North Harbour, Placentia Bay. Mapping of the intrusion was carried out through the use of color aerial photographs at a scale of 1:12,500. Most of the mapping was conducted by ground traverses from the many roads and trails in the project area. Two fly-camps were necessary to cover interior regions of the intrusive suite and one day of helicopter-hopping was necessary towards the end of the season in order to fill in details on hard-to-access areas.

The Lodestar prospect was studied in detail such that all clast types, matrix, and mineralization were closely examined. During mapping of the intrusion hand samples were taken at most stops and geochemistry samples were collected whereever possible. Three geochronology samples, of which two are presently dated, were collected from the area of the showing in order to bracket the age of mineralization and brecciation.

At the end of the summer all samples were transported to the Department of Mines and Energy in St.John's where they were catalogued and selected for assay, geochemistry, and/or petrographic analysis. Sample selection included a representative suite of samples from each phase of the intrusive suite, as well as from the mineralized breccia. These were analyzed for geochemistry/petrography, and in addition a

representative suite of mineralized samples were assayed.

Major and trace elements were analyzed by different methods on samples from various phases of the intrusion as well as on mineralized samples. Methods used for geochemical major and trace element analysis included ICP-EOS, XRF, ICP-MS, and INAA. REE data were derived for a smaller set of samples (27 samples) using ICP-MS. Major and trace element analyses were conducted on 53 and 63 samples respectively, by ICP-EOS at the Newfoundland Department of Mines and Energy (NDME) laboratories in St.John's (see Appendix A for analytic techniques and Appendix B for chemical analysis). Au assays, including a complimentary suite of elements, were conducted on 62 samples by INAA (Activation Laboratories for the NDME). Major and trace element analyses were conducted on 61 samples by X-Ray Fluorescence (XRF) at Memorial University, whereas trace and rare earth element analysis were carried out on 27 samples using Inductively Coupled Plasma - Mass Spectrometry (ICP-MS) also at Memorial.

Polished thin sections from all phases of the intrusive suite, as well as large polished thin sections of the mineralized breccia were examined in detail in order to describe the intrusive phases and breccia.

Due to the "invisible" nature of the gold within the breccia (to be discussed in a later section), the Scanning Electon Microscope was used for microscopic examination of sulphide textures, followed by analysis of sulphide phases by the Laser Ablation Micro-probe Inductively Coupled Plasma Mass Spectrometer (LAM-ICP-MS). The electron micro-probe was used to analyze arsenopyrite crystals for use in geo-thermometer studies.

Stable isotope studies were carried out using arsenopyrite, pyrite and chalcopyrite separates from the showing in order to aid in the characterization of the mineralization. These analysis were carried out using the Finnegan MAT252 isotope ratio mass spectrometer at Memorial University of Newfoundland.

1.6 Purpose and Scope

The purpose and scope of this study is to complete a detailed examination of the geology, geochemistry, geochronology, petrography, and metallogeny of the Powder Horn Intrusive Suite (PHIS). Prior to this project little work had been conducted on the PHIS. Interest in this area was sparked in 1998 by the discovery of significant gold-mineralization in polylithic breccias associated with the PHIS. As such, the main goals and basis of this project involved: 1) detailed work in mapping and describing the various phases of the PHIS, 2) geochronological work on the PHIS and associated mineralization, 3) detailed metallogenic studies on the Lodestar breccia hosted gold showing, 4) detailed description of the relationships between the various phases of the PHIS and the mineralized breccia, and 5) development of a genetic model for the brecciation-mineralization event.

This work is useful for interpretation of the regional significance of the Lodestar prospect with respect to the western Avalon Zone of the Newfoundland Appalachians. The interpretation of the showing as being a magmatic-hydrothermal breccia system related to a possible porphyry system at depth is the first documentation of this style of

mineralization in this area and should provide insight for future exploration in the area.

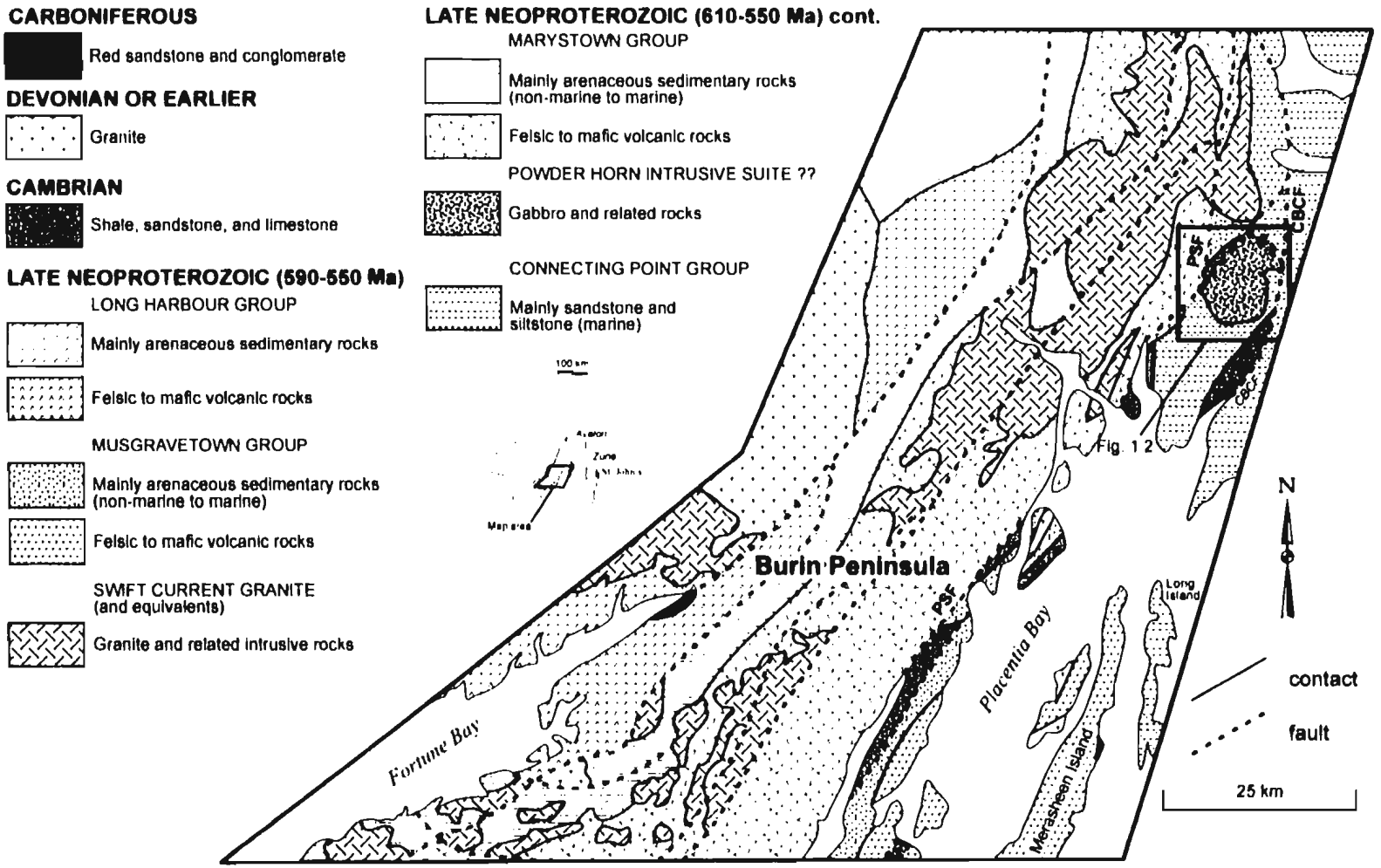

Figure 1.1: Generalized Geological map of the northern Burin Peninsula; PSF- Paradise Sound Fault, CBCF- Come By Chance Fault.Black box indicates map area for figure 1.2. (From Newfoundland Department of Mines and Energy).

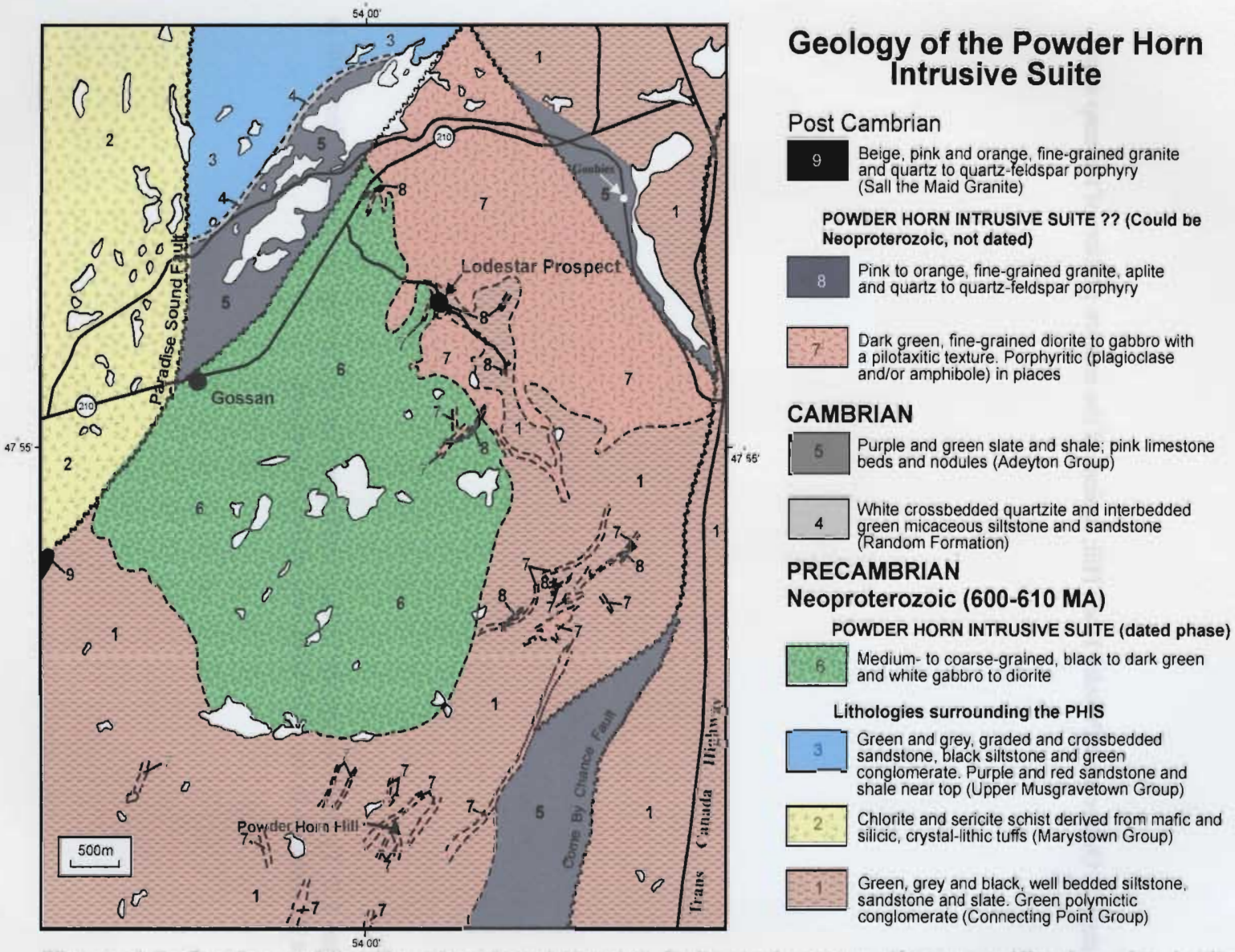

Figure 1.2: Geology of the Powder Horn Intrusive Suite and surrounding area.(Geology by J. Hinchey, 1999)

Plate 1.1: Outcrop on Powder Horn Hill; typical of the eastern portion of the map area.

Plate 1.2: Typical topography of the western portion of the map area. Power Horn Hill in the far distance in the right hand side of the photograph.

Chapter 2: Geological Setting

2.1 Regional Tectonic Setting

The Canadian Appalachian Orogen is exposed in Newfoundland, Nova Scotia, New Brunswick, and the southern part of Quebec. In Newfoundland, the Appalachian Orogen comprises four northeast-trending late Precambrian to lower Paleozoic tectonostratigraphic zones (Williams, 1978) which from west to east are termed the Humber, Dunnage, Gander, and the Avalon Zones (Figure 2.1). Portions of these zones were deformed by various structural events, including the Early and Middle Ordovician Taconic orogeny, the Devonian Acadian orogeny, the Silurian Salinic orogeny, and finally the Carboniferous-Permian Alleghanian Orogeny which dominantly affected the Humber-Dunnage Zones in Newfoundland (Williams, 1995).

Each of the tectonic zones has a separate and discrete history; individually recording aspects of the closing of the Iapetus ocean whereby the ancient margins of Laurentian and Gondwanan terranes collided. The Humber Zone represents the ancient passive continental margin of eastern North America (Laurentia); parts of the Dunnage Zone represent vestiges of the Iapetus Ocean; the Gander Zone represents the eastern margin of the ancient Iapetus Ocean; and finally the Avalon Zone represents the ancient Gondwanan margin (Williams, 1999).

All zonal boundaries, with the exception of the Avalon-Gander boundary, are marked by melanges and ophiolite complexes. The western boundary of the Humber Zone represents the Appalachian structural front, separating deformed orogenic rocks from the

undeformed rocks of the St. Lawrence Platform (Figure 2.1)(Williams, 1995). The boundary between the Humber and Dunnage Zones is demarked by the Baie-Verte-Brompton Line (Williams and St.Julien, 1982), a steep structure with discontinuous ophiolite slivers of the Advocate complex (Hibbard, 1983). The boundary between the Dunnage and Gander Zones is difficult to discern due to intermingling of the two zones in central Newfoundland. In northeast Newfoundland, the boundary is defined as the eastern margin of the Gander River Ultrabasic Belt Line (Blackwood, 1978, 1982), also termed the Gander River Ultrabasic Belt by Jenness (1958), and the Gander River Complex by O'Neill and Blackwood, (1989).The boundary between the Avalon and Gander Zones is a sharp tectonic line separating Upper Precambrian volcanic and granitic rocks of the Avalon Zone from Paleozoic gneissic and granitic rocks of the Gander Zone (Williams, 1995). This boundary is recognized as the Dover fault (Blackwood and Kennedy, 1975) in the north and the Hermitage Bay fault (Blackwood and O'Driscoll, 1976) in the south.

Hall et al., (1998) conducted geophysical studies on the structure of the Appalachian orogen from which they produced seismic profiles through the Atlantic region. They imaged the major structural boundaries; from which they determined that the belt was allochthonous. Their study indicated that the central mobile belt of the orogen has a thinner crust than its margins and that high-velocity lower crust, attributed to underplating, is found below the former Laurentian continental margin in Newfoundland. Due to observations that seismic fabrics have multiple intersection relationships indicating repeated activity on oppositely dipping shear zones, these workers concluded

that the final position of crustal material related to the orogen is probable more complex than a single process, doubly vergent collisional orogen as proposed by Quinlan et al., (1993).

2.2 Avalon Zone

2.2.1 Geological Origins of the Avalon Zone

Early stratigraphic interpretations of the Avalon Zone suggested that the late Neoproterozoic sequences defined an essentially uninterrupted deposition of volcanic, marine, and terrestrial siliciclastic rocks (Hughes and Bruckner, 1971; King et al., 1974; Williams, 1979). Based upon the regional homogeneity, Williams (1979) suggested that the lithological successions of the Avalon had accumulated over a 50-100 Ma period towards the end of the Proterozoic.

With the accumulation of geological and geochronological data, new models and insights have been derived for the stratigraphic and tectonic history of the Avalon. It is now envisioned that the Neoproterozoic evolution of the Avalon Zone or Avalonian system is much more complex than originally interpreted and involved the amalgamation and dispersal of a number of individual tectonic entities coupled to complex orogenic events ranging over a 200 My period (O'Brien et al., 1996). These orogenic events are referred to as the Avalonian cycle, involving four major tectonomagmatic events: ca 760 Ma, ca. 680 to ca. 670 Ma, from ca. 640 to ca. 600 Ma, and from ca. 595 to ca. 560 Ma.

2.2.2 Stratigraphy and General Geology

The Avalon Zone is unique compared to the other zones in the Newfoundland Appalachians and can be defined by its well preserved upper Precambrian volcanic and sedimentary sequences and overlying Cambrian-Ordovician shales and sandstones. Some of the major outstanding distinctions of the Avalon Zone are: 1) the Precambrian rocks largely predate the opening of Iapetus. 2) it has different trilobite fauna within the Cambrian compared to the Humber Zone. and 3) it contains unique mineral deposits such as pyrophyllite in upper Precambrian volcanics and manganese in Cambrian shales (Williams. 1995). The type area for the Avalon Zone is the Avalon Peninsula of Newfoundland. however. the zone extends west of the peninsula to the boundary with the Gander Zone (Figure 2.2). and offshore. out under the Grand Banks.

The following tectono-stratigraphic outline is summarized from Williams. 1995. O'Brien et al..1996. and O'Brien et al., 1983. Williams (1995) divided the Avalon stratigraphy by separating the upper Precambrian rocks that underlie most of the zone into three lithological units: a basal volcanic unit dominantly consisting of ignimbrites and volcanic breccias: a middle marine sedimentary unit consisting of grey-green siltstones. sandstones. and siliceous argillites. both of which are overlain by shales and sandstones; and an upper unit consisting of terrestrial sedimentary and volcanic rocks. dominated by red/green sandstones and conglomerates. Williams (opcit) has listed the rocks of each division as follows:

Lithological Unit	*Type Area of the Avalon Peninsula*	*West of the Avalon Peninsula*
Basal Volcanic Unit	Harbour Main Group	Love Cove (Jenness, 1963) and Marystown (Strong et al., 1978) Groups
Middle Marine Sedimentary Unit	Conception and St.John's Groups	Connecting Point Group (Hayes, 1948; Jenness, 1963)
Upper Unit of Terrestrial Sedimentary and Volcanic Rocks	Signal Hill and Musgravetown Groups	Musgravetown (Hayes 1948), Long Harbour (Williams,1971), and Connaigre Bay (Widmer, 1950, O'Driscoll and Strong, 1978)

O'Brien et al., (1996, 1983) have further divided the Avalon Zone into four distinct groupings of late Neoproterozoic tectonomagmatic and depositional events at 760 Ma, 685-590 Ma, 635-590 Ma, and 590-545 Ma. These four suites of Neoproterozoic rocks were amalgamated prior to subsequent deposition of latest Neoproterozoic cover successions and plutonic intrusions, which in turn occurred prior to the deposition of a 540-495 Ma (ie. Paleozoic) platformal cover sequence to Avalonian cycle rocks (O'Brien et al., 1996).

Before dealing with the proposed divisions of the Avalon Zone (east of the Dover and Hermitage Bay Faults), it should be noted that relics of late Neoproterozoic-early Paleozoic basement material (affiliated peri-Gondwanan rocks, Avalon Zone Material) occur to the west of the Avalon Zone in the Hermitage Bay Fault area in a package known as the Hermitage Flexure, and also as inliers farther northwest in the Dunnage Zone

(Figure 2.1)(O'Brien et al., 1996). For the purposes of this summary, however, only those units east of the Avalon-Gander boundary will be described and these "outlying" areas will not be described.

2.2.2.1 Oldest Precambrian Rocks

The oldest Precambrian rocks exposed in the Avalon Zone of Newfoundland are the Burin Group on the southeast Burin Peninsula (figure 2.2). These rocks represent a period of Upper Proterozoic, ca. 760 Ma, oceanic volcanism exposed in an approximately 50 X 5 km fault-bounded belt. Lithologies are dominated by pillow lavas, gabbros, volcanic breccias, hyaloclastite, and epiclastic/pyroclastic volcanic rocks (Taylor,1976). Recent work by the Newfoundland Department of Mines and Energy has also identified narrow thrust belts of ultramafic material (locally serpentinized) within the group (O'Driscoll et al., 2001). Towards the base of the group are stromatolite-bearing carbonate olistostromes which Strong et al., (1978) assumed to have formed from the collapse of a shelf carbonate-siliclastic sequence.

The Burin group was thrust over late Proterozoic sediments, and the group itself was overthrust by late Proterozoic subaerial volcanics represented by the Marystown Group. Strong et al., (1978) suggested that the tectonic boundaries of the Burin Group were post-Cambrian in age. The Wandsworth Gabbro, represented by a gabbro sill, is interpreted to have been co-magmatic with the mafic volcanic and associated sedimentary rocks of the group, and was dated at 763 +/- 3 Ma (U-Pb zircon, Krogh et al., 1988), thereby separating the Burin Group as a whole from other Precambrian rocks from the

Avalon. Similar ages, compositions, and regional settings have lead many workers to draw a link between the Burin Group and the ca.760 Ma suite of Pan-African (Gondwana) ophiolite belts (Bou Azzer Ophiolite), thus linking the Pan-African and Avalonian Belts (Leblanc, 1981; Strong 1979; O'Brien et al., 1983).

2.2.2.2 685-670 Ma Arc Related Felsic Volcanics and associated Plutonics

This subdivision (of the Avalon Zone) is identified by Neoproterozoic activity which produced arc-related felsic volcanics with associated arc plutonics (O'Brien et al., 1996). This part of the Avalonian cycle is interpreted to consist dominantly of contractional tectonics. This suite, restricted to the Connaigre Peninsula of southern Newfoundland (Figure 2.2), consists of low-grade volcanic units associated with bimodal plutonic rocks. This suite forms the basement to younger Neoproterozoic rocks. The two major units associated with this event are the Tickle Point Formation (O'Brien et al., 1992) and the Furby's Cove Intrusive Suite (O'Brien et al., 1992).

The Tickle Point Formation consists dominantly of calc-alkaline and pyroclastic rocks, and is locally associated with basalt, andesite, and siliciclastic, mafic volcaniclastic, and carbonate sedimentary rocks. This unit is intruded by the Furby's Cove Intrusive Suite which consists of mixed granitic and gabbroic, presumably comagmatic, phases. Dates derived from these two units are 682+/- 3 Ma for Tickle Point Formation rhyolites, and 673 +/- 3 Ma for Furby's Cove Intrusive Suite granite (O'Brien et al., 1994).

2.2.2.3 635-590 Ma Arc Related Plutonism, Volcanism, and Sedimentation

This suite is dominated by plutonism, coeval volcanism, and sedimentation within an arc environment (King, 1990; Sears,1990; O'Brien et al.,1990, 1994). The products of this event were partially deposited upon and emplaced within the previously described 685-670 Ma suite of volcanic and plutonic rocks.

The dominantly subaerial volcanic successions which dominate the 635-590 Ma suite are complex and represent a continuum from basalt and andesite through dacite and rhyodacite, to rhyolite (O'Brien et al., 1996, 1998 and references therein). The major volcanic sequences erupted during this tectonic period consist of the Love Cove (Jenness, 1963), part of the Marystown (Strong et al.,1978), Connaigre Bay (Widmer, 1950), Long Harbour (Williams, 1971), and the Harbour Main (Rose 1952) groups (Figures 2.2, 2.3, 2.4).

The Love Cove (590 +/- 30 Ma, Dallmeyer et al.,1981) and lower Marystown (608 +20/-7 Ma, Krogh et al., 1988) groups of the western portion (ie. Burin Peninsula) of the Avalon Zone can be correlated with the Harbour Main Group (three distinct fault blocks dated at 589.5 +/- 3 Ma, 631 +/- 2 Ma, and 606 +3.7/-2.9 Ma, Krogh et al., 1988) volcanic rocks from the eastern portion (ie. Central Avalon Peninsula) of the Avalon Zone (figures 2.2, 2.3,and 2.4). Together they are inferred to represent a broad anticlinorium that extends from the southern tip of the Burin Peninsula to the northeast coast of Newfoundland (Williams, 1995). Both groups of rocks are lithologically diverse. The rocks in the west are dominated by felsic to mafic, subaqueous to subaerial volcanics.

They form suites of flows and volcaniclastics with lower portions comprising a continuum of compositions from basalt to andesite to rhyolites; the middle parts consisting of clastic and epiclastic continental deposits, and the upper sections consisting of bimodal suites of continental basalts and rhyolites (Williams, 1995; O'Brien et al.,1990). The Harbour Main Group in the east consists of at least 1800 m of felsic to mafic, submarine to subaerial volcanic rocks. Lithologies in the type area for the group consist of subaerial ash flows, terrestrial sediments, and basalt (O'Brien et al., 1990).The Connaigre Bay Group (626 +/- 3 Ma, Tucker unpublished data , O'Brien et al., 1996) and its presumed equivalent, the Long Harbour Group, are both characterized by subaerial, bimodal volcanic rocks separated by a thin shallow marine sedimentary unit (O'Brien et al., 1990) (figure 2.2).

Associated with these volcanic rocks are thick successions of marine silicicalstic rocks including the Conception Group of the Avalon Peninsula and the Connecting Point Group from the central portion of the Avalon Zone, directly east of the Paradise Sound Fault. The Conception Group represents a continuous stratigraphic succession of marine clastic rocks dominated by green/grey siliceous fine grained sedimentary rocks, but also includes conglomerate, tuff, agglomerate, pillow lava, and mafic dykes (Williams et al., 1995). It should be noted that a tuff near the top of this group has been isotopically dated by U-Pb at 565 +/- 3 Ma (Benus, in King 1988), thereby implying a depositional span of approximately 50 Ma years. The Connecting Point Group (Hayes, 1948; and Jenness, 1963) comprises a 4-5 km thick section of clastic rocks that occupy a major basin in the

central part of the Avalon Zone. These rocks conformably overlie the Love Cove Group. Knight and O'Brien, (1988) describe the group as being characterized by two sequences of turbidites deposited in basinal and slope settings.

Both the volcanic and sedimentary groups associated with the 635-590 Ma event were intruded by plutonic rocks. Shortly after the eruption of the volcanic sequences a number of calc-alkaline plutonic complexes: eg. Holyrood Intrusive Suite (Krogh et al., 1988; King 1990); and the Simmons Brook Intrusive Suite (Williams, 1971; S.J. O'Brien et al., 1992) were intruded. In the Goobies area, the sedimentary units were also intruded and hornfelsed by the Powder Horn Intrusive Suite; (Hinchey et al., 2000, O'Brien et al., 2000).

2.2.2.4 590-545 Ma Plutonic, Volcanic and Structural event

The final episode in the four fold tectono-stratigraphic framework as outlined by O'Brien et al, (1996) consists of a complex volcanic, plutonic, structural event, associated with widespread deep marine to deltaic and fluviatile sedimentation (King, 1990). This event is described as being dominantly extensional with minor contractional episodes and it encompasses the Ediacaran-bearing and younger sedimentary lithologies (O'Brien et al., 1996).

In the southwestern portion of the Avalon Zone, this event was marked by post 590 Ma intrusive suites (gabbro, diorite, quartz diorite, granodiorites, and alaskitic granites) emplaced into basement material on the Connaigre Peninsula (figure 2.2). The Long Harbour Group, a stratified volcanic/sediment succession consisting of subaerial

volcanic rocks at the base, overlain by marine siliciclastic sediments, followed by rhyolites and basalts capped by red beds, was also intruded by high-level alkaline to peralkaline felsic plutons (O'Brien et al., 1996)(figure 2.2). On the Burin Peninsula, the volcanic-sedimentary units comprising this event are dominated by the Marystown Group.

In the type area of the Avalon Zone, on the Avalon Peninsula, this event is recorded by the upper portions of the Conception Group and the overlying St.John's and Signal Hill Groups (King, 1990) (figure 2.3). Hayes and O'Driscoll, (1994) suggest that this stratigraphic package may represent a late Neoproterozoic cover sequence deposited above the 630-600 Ma basement material. The Conception Group is initially dominated by basinal deep water turbidite successions followed by glaciogenic debris flows and tillites (Gardner and Hiscott, 1988), and secondary turbidite sequences. With continued sedimentation, the St.John's Group (deltaic sandstones and shales) and the Signal Hill Group (fluvial and alluvial sediments) were deposited (King, 1988a, 1990).

Subaerial sedimentary and volcanic rocks, represented by the Musgravetown Group dominated this event in the northwestern portion of the Avalon Zone (figure 2.2, 2.4). This material forms a cover sequence to the 620-610 basement material. The lithologies range from early alluvial conglomerates and sandstones to later subaerial bimodal volcanics.

2.2.2.5 Early-Middle (540-495 Ma)Paleozoic Record

The Cambrian-Ordovician in the Avalon Zone records a widespread 540-495 Ma platformal sedimentation event. The sediments were dominated by shale successions with internal variations representing variations in Paleozoic basin depths (deeper in the west). The early (lower) Cambrian lithologies were dominated by shale, fine-grained siliciclastics, and limestone deposition, followed by green/grey/black shales of the middle Cambrian, and finally by black micaceous shale and siltstone in the Late Cambrian.

Silurian closure of the Iapetus ocean resulted in the collision of the Avalonian (Gondwanan) and the Laurentian margin, producing new basins along the edge of the Avalonian (Gondwanan) basement. Silurian metamorphic and structural characteristics in this area are related to metamorphism and plutonism farther west, all of which are presumably related to the amalgamation of the Avalon and Gander Zones. Brittle deformation in the Devonian period led to granitic plutonism in the Avalon which crosscut Silurian structures.

2.3 Geological Framework of the Burin Peninsula

The Burin Peninsula is located on the western limit of the Avalon Zone, the eastern margin of the Newfoundland Appalachian orogen (Figure 2.1, 2.2). As described earlier, the Neoproterozoic geology of the Burin peninsula records generation of subaerial volcanic and plutonic successions and associated marine/terrestrial sedimentation of the 760-540 Ma Avalonian cycle of peri-Gondwanan affinity (O'Brien et al., 1999). These

successions are in turn covered by Cambrian sequences consisting of quartz-arenite-shale units. These sequences were deformed by Silurian-Devonian tectono-thermal events, and were overlain by terrestrial volcanic and siliciclastic rocks, coeval with granitic plutons.

Neoproterozoic volcanic activity in the Burin Peninsula occurred mainly in the period between 590-565 Ma. As described above, this time period in the Avalon Zone represented large scale development of magmatic arcs within arc, arc-adjacent, and continental extensional settings. These were associated with the deposition of sedimentary sequences in marine, deltaic, and terrestrial siliciclastic basins (O'Brien et al., 1999).

The lithologies on the Burin Peninsula define a regionally flexured anticlinorium containing sub-aerial volcanic and coeval plutonic rocks in the core. The core is comprised of the Marystown Group and associated intrusives. The eastern side of the northern and central part of the peninsula are bound by the marine to terrestrial volcanic and sedimentary succession of the Neoproterozoic Musgravetown Group and underlying Connecting Point Group (marine turbidites), whereas the eastern side in the southern part of the peninsula is bounded by the Burin Group. The Long Harbour Group overlies the northwestern portion of the peninsula. These successions pass into shallow marine, sub-aerial volcanics and terrestrial clastics, and finally into Cambrian strata.

2.4 Gold Mineralization and other prospects in the Newfoundland Avalon Zone

2.4.1 Introduction

The 640-600 Ma and 600-560 Ma volcanic, plutonic, and volcanogenic sedimentary rocks, and their regionally analogous units, of the Avalonian Belt host a number of hydrothermal alteration "belts" and associated gold-bearing systems. Within the Appalachian Avalonian system as a whole, there are five major gold-bearing systems that have been brought to production. These are: 1) the Hope Brook Au-Cu mine in the Hermitage Flexure area of the Newfoundland Avalon Zone, and 2) the Brewer (Au-Cu), 3) Haile, 4) Ridgeway, and 5) Barite Hill gold mines in northern South Carolina (Figure 2.5). These auriferous hydrothermal systems occur in various magmatic and structural settings and display signatures related to epithermal, transitional hypabyssal, and porphyry environments (O'Brien et al., 1998).

Within the Newfoundland Avalon Zone of the Appalachian orogen, there are two major auriferous hydrothermal alteration systems associated with the 640-600 Ma and 600-560 Ma volcanic/plutonic/volcaniclastic sedimentary rocks. There are also a number of smaller scale, yet important prospects associated with these major systems. The Hope Brook Mine, situated in the Hermitage Flexure area, is the only gold deposit to reach production in the Avalon Zone in Newfoundland, however, for this study only systems within the Avalon Zone (sensu stricto) will be dealt with, thereby omitting a discussion of the Hope Brook Mine.

As with the stratigraphic and tectonic analysis of the Newfoundland Avalon Zone,

the following discussion on gold-bearing hydrothermal systems within the zone is compiled from a significant amount of literature. The summary will focus on the two hydrothermal alteration systems with associated gold mineralization at 640-600 Ma, and 600-560 Ma. The report by O'Brien et al. 1998 and references therein are the main source of information for this summary.

2.4.2 640-600 Ma Hydrothermal Alteration and Gold Mineralization

The earliest group of hydrothermally altered rocks and associated gold mineralization includes 640-600 Ma rocks. As described in a previous section, three groups of volcanic rocks are associated with this event, consisting of the Harbour Main Group on the Avalon Peninsula (King, 1988, 1990; Krogh et al., 1988; O'Brien and O'Driscoll 1996; O'Brien et al., 1997); the Connaigre Bay Group on the western Connaigre Peninsula (O'Driscoll and Strong, 1979; O'Brien et al., 1995); and parts of the Love Cove Group and overlying Connecting Point Group in the western part of Bonavista Bay (O'Brien and Knight, 1988; Knight and O'Brien, 1988; Dec et al., 1992).

2.4.2.1 Eastern Avalon High-Alumina Belt

The main mineralized hydrothermal system in the 640-600 Ma event is the Eastern High Alumina Belt (Hayes and O'Driscoll, 1990) (figure 2.3). This system has been reported on by several authors including: Saunders, 1986, 1991; Hayes and O'Driscoll, 1990; Hayes, 1997; O'Brien and O'Driscoll, 1996 a,b; O'Brien et al., 1997, 1998, 1999; Mills et al., 1999. This belt represents a large continuous zone of hydrothermal alteration situated primarily within the pre 620 Ma rocks of the Harbour

Main Group, and to a lesser degree within parts of the eastern margin of the Holyrood Intrusive Suite. The area has been referred to as the Holyrood Horst and consists of the periclinal dome of Late Proterozoic subaerial volcanics and plutonic rocks which makes up the core of the Avalon Peninsula (figure 2.3). These rocks are typically of low metamorphic grade with some areas of the older successions hydrothermally altered by 620 Ma granitic intrusions. The belt has a strike length of approximately 15 km, and consists of a zone with advanced argillic and silicic alteration of the rock units. The extensive alteration associated with this belt was initially known for its pyrophyllite, including the former Armstrong World Industries Canada Ltd. Oval Pit Mine at Manuels. Recent work (O'Brien et al., 1996 a,b, 1997, 1998, 1999; Mills et al., 1999; and others) has led to the discovery of high and low-sulphidation epithermal gold systems associated with the high alumina, advanced argillic alteration in the zone. These systems may be related to porphyry systems at depth, thus making this area attractive in terms of economic potential. The hydrothermal alteration of the subaerial successions in the Harbour Main Group resulted in large areas of argillic, advanced argillic and silicic alteration with associated hydrothermal brecciation. Figure 2.3 illustrates a simplified geology map showing major pyrophyllite and gold prospects. The main characteristics of these prospects, as outlined by O'Brien et al., 1998, are summarized in table 1 following.

Table 1a: 640-600 Ma Pyrophyllite Deposits

Deposit Name	Host Rock	Alteration	Alteration Products	Production History
Oval Pit Mine	Harbour Main Group: subaerial ash-flow tuffs, rhyolite flows, volcanic breccia.	Argillic, Advanced Argillic, Silicic	Pyrophyllite, silica, sericite, diaspore, minor barite and rutile.	In Production Continuously from 1956-1996
Mine Hill Quarry	Tuffaceous material from the Harbour Main Group	Advanced Argillic and silicic	Pyrophyllite, sericite, quartz, silica	Pre-1950's attempts at commercial production
Trout Pond Prospect	Lithophysae bearing rhyloites	Advanced Argillic	Pyrophyllite, sericite, silica	Mid 1930's and 1940's
Dog Pond Prospect	Flow Banded Rhyolite and Lithophysae bearing rhyloites	Advanced Argillic	Pyrophyllite, silica, pyrite	Mid 1930's and 1940's

Table 1b: 640-600 Ma Auriferous Hydrothermal Prospects

Prospect Name	Style of Mineralization	Alteration	Assay Results
Mine By-pass Prospect	Hydrothermal Breccia	sericite, silica, hydrothermal breccia, pyrite	Up to 1.8 g t Au, 6 g t Ag
Roadcut Prospect	Hydrothermal Breccia	advanced argillic, silicic, sericite, pyrite, chlorite, pyrophyllite, k-feldspar	Avg 3 g t Au 10m, Up to 11.2 g t Au in silica-rich breccia, 210 g/t Ag
Steep Nap Prospect	Low-Sulphidation style, veins	chlorite, hematite, sericite, silica, adularia	veins contain up to 2.2 g/t Au
Hydrothermally Altered Intrusions	Altered Intrusions	sericite, hematite, pyrite, silica, pyrite	Butler's Pond: 6 % Cu, 12.6 g/t Au

2.4.3 600-560 Ma Hydrothermal Alteration and Gold Mineralization

The other major mineralized hydrothermal alteration system within the Newfoundland Avalon Zone occurs within 600-560 Ma volcanic, plutonic, and sedimentary rocks. Most of the alteration and mineralization associated with this suite occurs in the Avalonian system to the west of the Avalon Peninsula, in Bonavista and Fortune Bays, the Burin Peninsula, and the Hermitage Flexure area (Hope Brook Gold Mine). Within the Avalon Zone (sensu stricto), the best known and documented example of hydrothermal alteration and gold mineralization is the Hickey's Pond and related gold occurrences on the Burin Peninsula (figure 2.6) which are summarized below.

2.4.3.1 Hydrothermal Alteration and Gold Mineralization on the Burin Peninsula

The Burin Peninsula consists of subaerial calc-alkaline volcanic rocks with associated co-magmatic composite intrusions, locally overlain by volcanoclastic arenaceous sediments. The volcanic rocks making up the core of the peninsula belong to the Marystown Group. Within the north-central portions of the peninsula, these lithologies host belts of advanced argillic alteration with mineral assemblages including pyrophyllite, alunite, quartz, sericite, pyrite, specular hematite, rutile, barite, chloritoid and lazulite (Huard and O'Driscoll, 1986; O'Driscoll et al., 1988; Huard 1990)(figure 2.6). Within these belts gold, copper, and arsenic mineralization is associated with silicic alteration and hydrothermal breccias.

As indicated in figure 2.6, the prospects on the peninsula form two separate belts, located on opposite sides of the Swift Current Granite. The best known mineralized

prospect on the peninsula is the Hickey's Pond showing. The specular hematite showing at Hickey's Pond was initially documented by Dahl, (1934) as a potential source of iron.

Gold values of up to 12.4 g/t over 1.2 m were reported by Corona Corporation from the Hickey's Pond showing (Dimmell and MacGillivray, 1989). Lithologies at the showing consist of advanced argillic alteration zones with highly strained quartz, alunite, specular hematite bearing, altered felsic pyroclastic rocks, intermixed with areas of silicic alteration. O'Brien et al., (1998) suggest that the presence of 1.86 % As and 3.41% Cu within a silicic-altered zone at the showing indicates a high-sulphidation, epithermal gold mineralization signature. The other showings located on figure 2.6 also represent auriferous showings, thereby indicating a fairly continuous, extensive zone of mineralization associated with hydrothermal alteration.

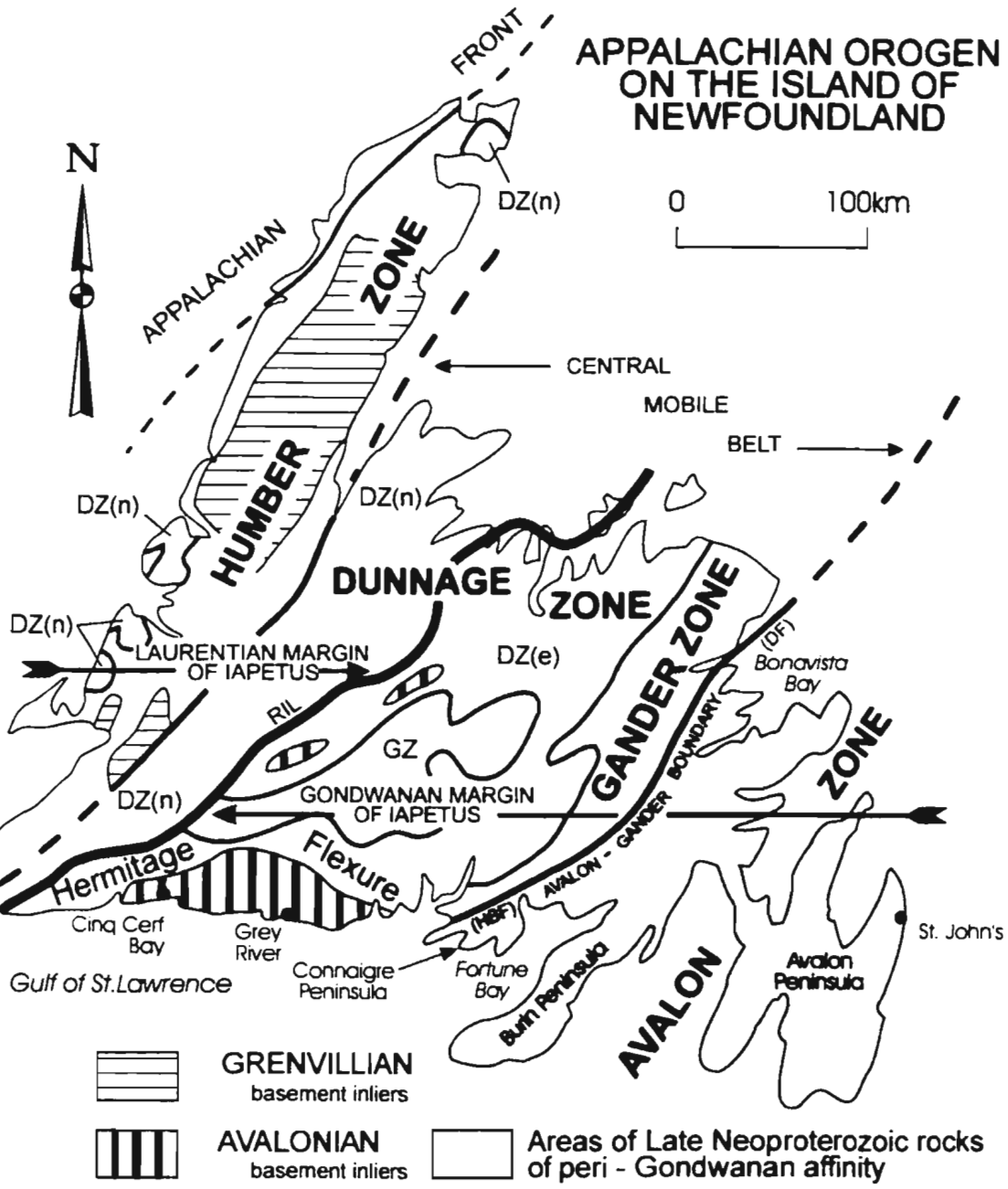

Figure 2.1. Tectonostratigraphic subdivision of the Newfoundland Appalachians, showing distribution of Avalonian rocks. DZ(e)= Dunnage Zone: Exploits subzone; DZ(n)= Dunnage Zone: Notre Dame subzone; GZ= Gander Zone; HBF= Hermitage Bay Fault; DF= Dover Fault; RIL= Red Indian line (from O'Brien et. al. 1996)

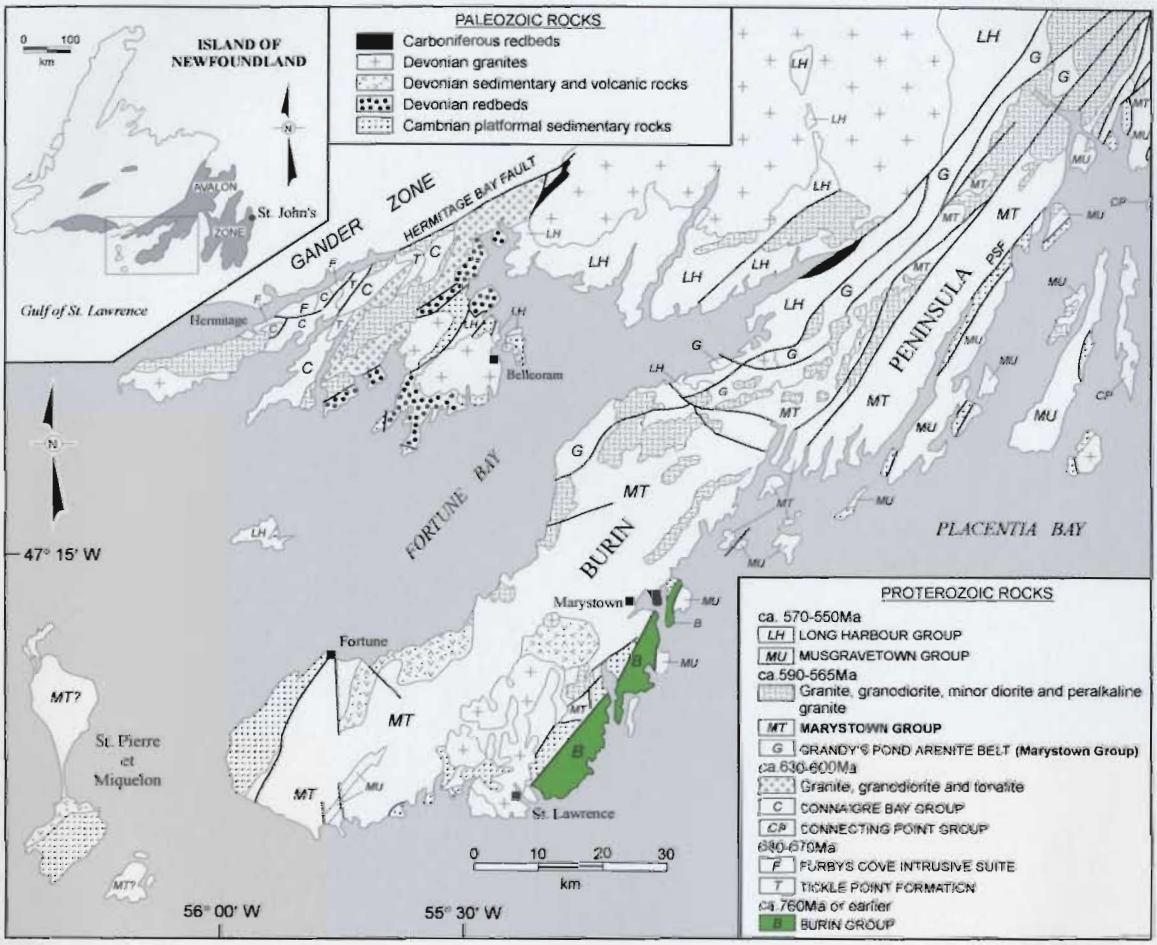

Figure 2.2: Geological map of the southeastern Avalon Zone with the Burin Group highlighted (after O'Brien et al., 1986 and Dunning et al., 1995)

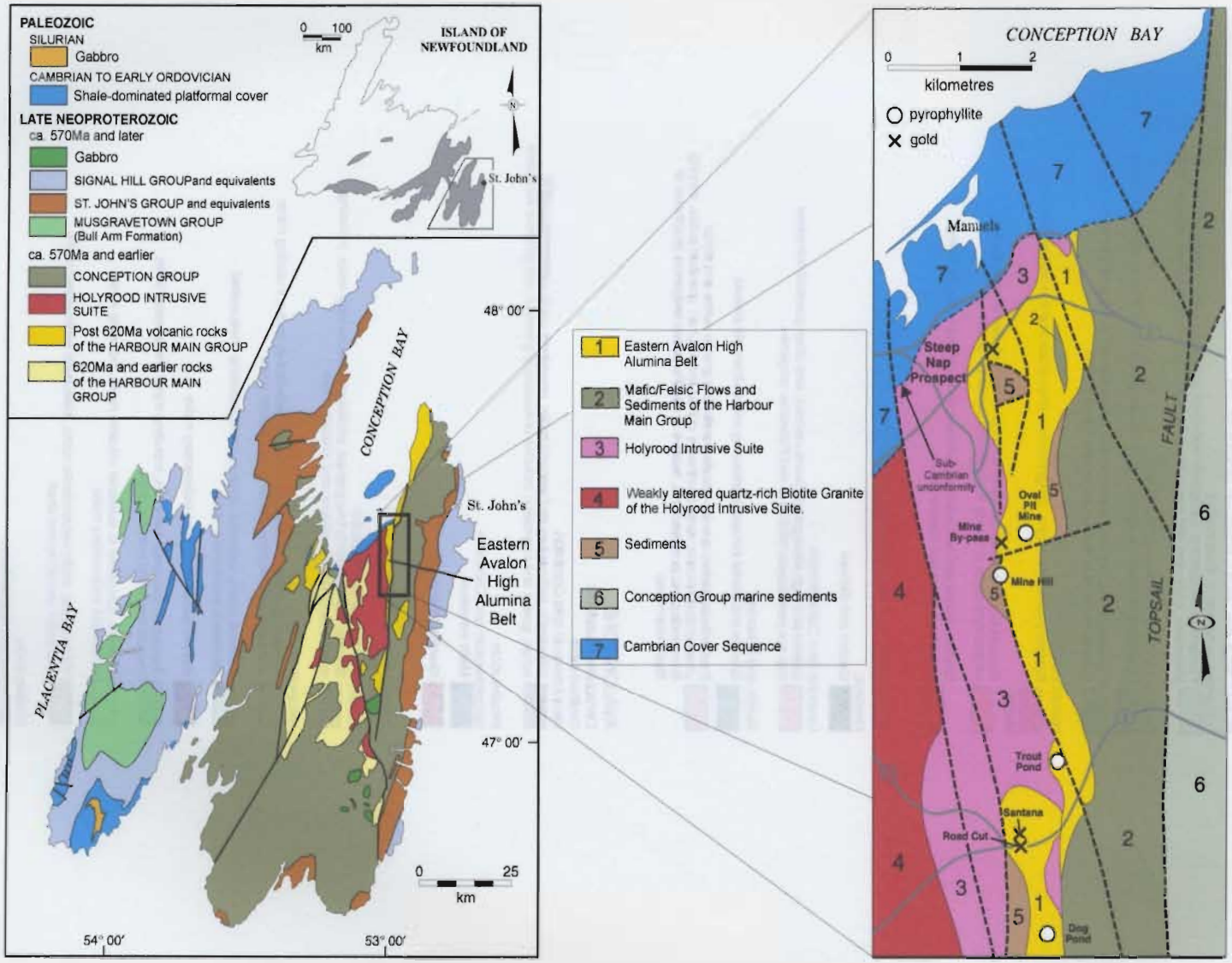

Figure 2.3: Geological Map of the Avalon Peninsula with a blowup of the Eastern Avalon High Alumina Belt and surrounding area. (Modified from King 1988, Hayes and O'Driscoll, 1990; and O'Brien et al., 1998)

Legend of figure 2.4

POST-ORDOVICIAN OVERLAP SEQUENCES

Carboniferous (Visean to Westphalian)

Fluviatile and lacustrine, siliciclastic and minor carbonate rocks; intercalated marine, siliciclastic, carbonate and evaporitic rocks; minor coal beds and mafic volcanic flows

Devonian and Carboniferous (Tournaisian)

Fluviatile and lacustrine sandstone, shale, conglomerate and minor carbonate rocks

Fluviatile and lacustrine, siliciclastic and carbonate rocks; subaerial, bimodal volcanic rocks; may include some Late Silurian rocks

Silurian and Devonian

Shallow marine sandstone, conglomerate, limey shale and thin-bedded limestone

Silurian

Bimodal to mainly felsic subaerial volcanic rocks; includes unseparated sedimentary rocks of mainly fluviatile and lacustrine facies

Shallow marine and non-marine siliciclastic sedimentary rocks, including sandstone, shale and conglomerate

POST-ORDOVICIAN INTRUSIVE ROCKS

Mesozoic

Gabbro and diabase

Devonian and Carboniferous

Granite and high silica granite (sensu stricto), and other granitoid intrusions that are posttectonic relative to mid-Paleozoic orogenies

Silurian and Devonian

Gabbro and diorite intrusions, including minor ultramafic phases

Posttectonic gabbro-syenite-granite-peralkaline granite suites and minor unseparated volcanic rocks (northwest of Red Indian Line); granitoid suites, varying from pretectonic to syntectonic, relative to mid-Paleozoic orogenies (southeast of Red Indian Line)

AVALON ZONE

Central Newfoundland

Stratified rocks

Neoproterozoic and Cambrian

Siliciclastic sedimentary and volcanic rocks; amphibolitic and quartzofeldspathic schist, gneiss and migmatite; includes unseparated granitoid and gabbroic intrusions

Intrusive rocks

Neoproterozoic and Cambrian

Mafic intrusions

Granitoid intrusions

Eastern Newfoundland

Stratified rocks

Neoproterozoic to Early Ordovician

Shallow marine, mainly fine grained, siliciclastic sedimentary rocks, including minor unseparated limestone and volcanic rocks

Neoproterozoic

Fluviatile and shallow marine siliciclastic sedimentary rocks, including minor unseparated limestone and bimodal volcanic rocks

Bimodal, mainly subaerial volcanic rocks, including unseparated siliciclastic sedimentary rocks

Marine deltaic siliciclastic sedimentary rocks

Sandstone and shale turbidites, including minor unseparated tillite, olistostromes and volcanic rocks

Bimodal, submarine to subaerial volcanic rocks, including minor siliciclastic sedimentary rocks

Pillow basalt, mafic volcaniclastic rocks, siliciclastic sedimentary rocks, and minor limestone and chert

Intrusive rocks

Neoproterozoic to Cambrian

Mafic intrusions

Granitoid intrusions, including unseparated mafic phases

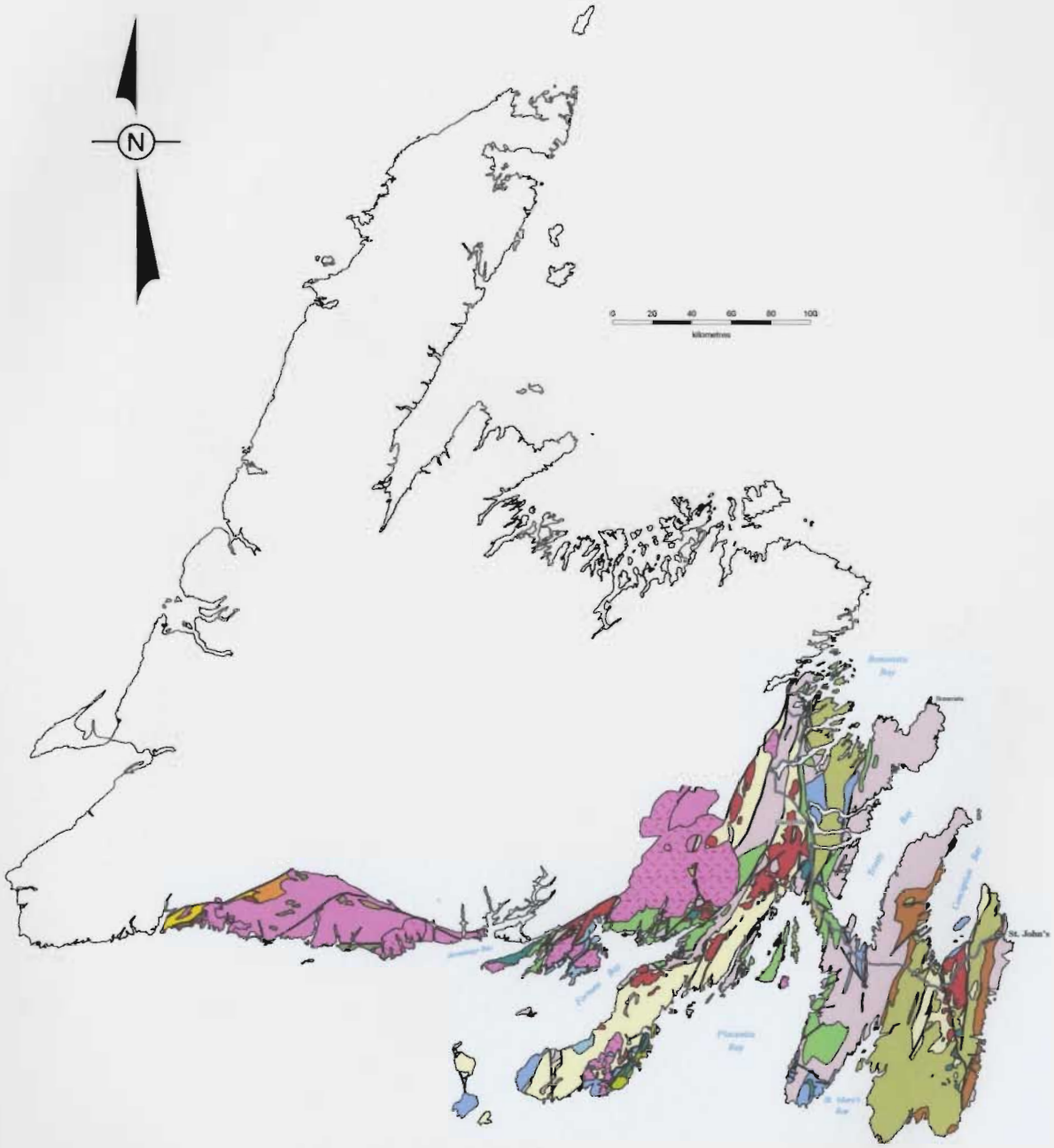

Figure 2.4: Geological Map of Avalon Zone. (modified from Colman-Sadd et al., 1990) Legend located on opposing page.

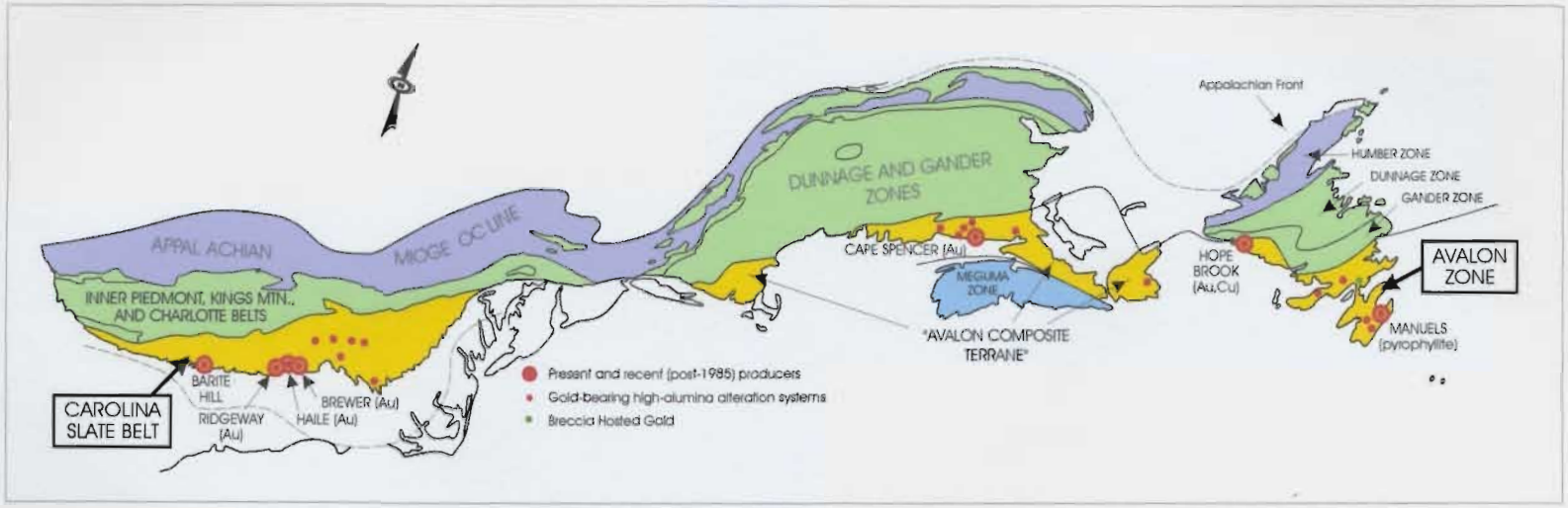

Figure 2.5: Gold-Bearing systems within the Applachian Avalonian Belt. (Modified from O'Brien et al., 1998 and Williams and Hatcher, 1983.)

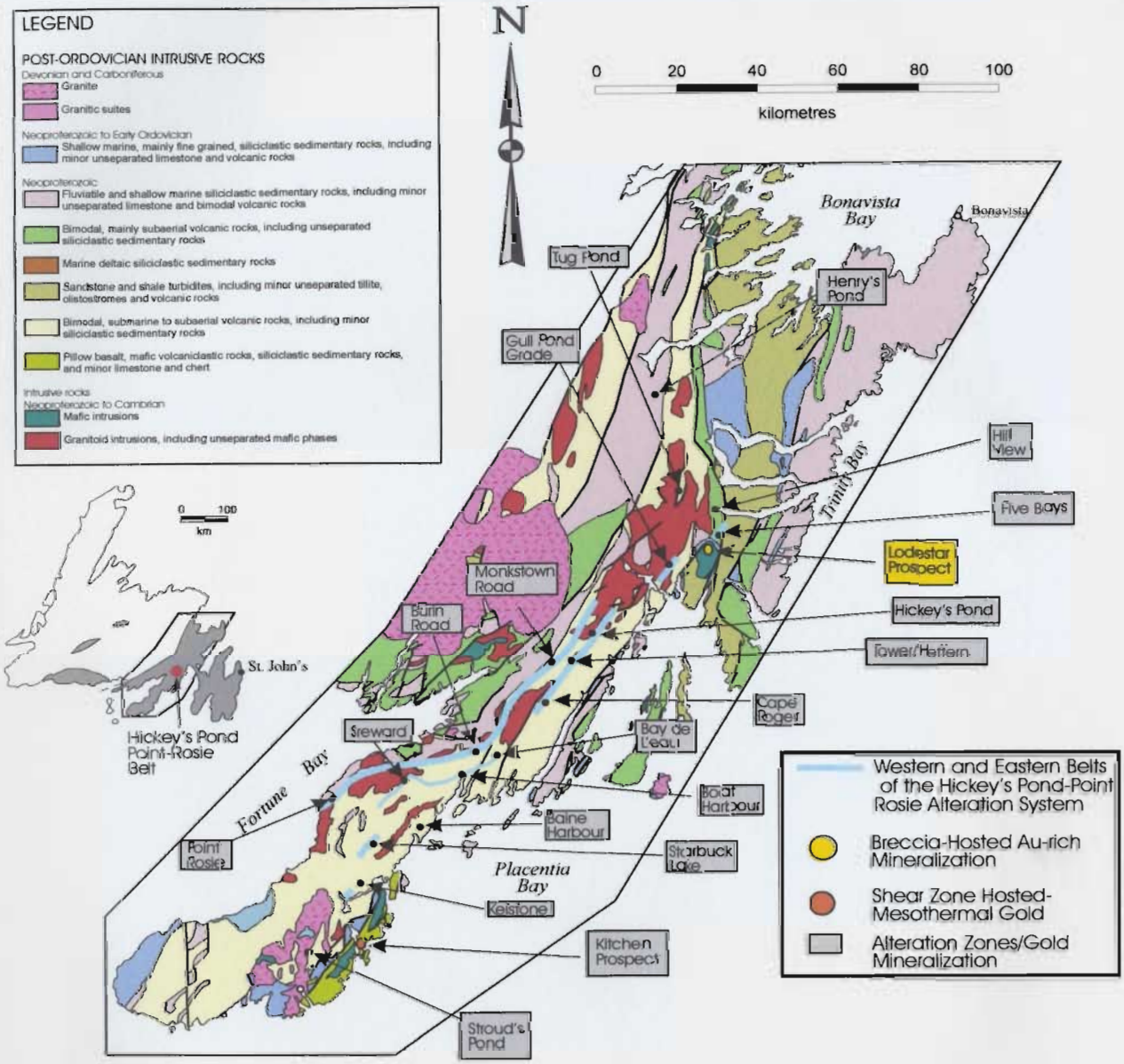

Figure 2.6: Alteration Zones and Gold Occurrences on the Burin Peninsula. (Modified from O'Brien et al, 1998, Colmann Sadd, 1990)

Chapter 3: General Geology and Petrography of the Powder Horn Intrusive Suite, the Lodestar Magmatic-Hydrothermal Auriferous Breccia and surrounding area.

3.1 Introduction

Prior to the mapping undertaken for this study, no other work more detailed than 1:50,000 scale had been conducted on the Powder Horn Intrusive Suite (PHIS) or the surrounding area. For the purposes of this project, the PHIS along with the immediate host rocks, as well as the mineralized breccia (Lodestar Prospect) were mapped in detail. All phases of the PHIS were mapped and classified with respect to the mineralized magmatic-hydrothermal breccia (Lodestar Prospect).

Phases were subdivided into those that were pre-, post-, and/or syn-breccia (mineralization), based on field relationships. The pre-mineralization rocks consist of late Neoproterozoic Connecting Point Group sedimentary units, hornfelsed in areas close to pre- and post-breccia intrusive phases. Pre-breccia intrusive phases consist of medium-grained gabbro/diorite, and minor felsic intrusive material. Post-mineralization phases include fine-grained gabbro/diorite, felsic phases, and diabase dykes. In the area of the breccia, some felsic intrusive units are actually syn-brecciation.

The mineralized breccia, which occurs at the contact between the host sedimentary rocks and pre-breccia gabbro/diorite, is exposed over approximately 25 meters and contains auriferous sulphide mineralization with associated copper, arsenic, and zinc. The sulphide mineralization dominantly forms the matrix to the breccia,

whereas in unmineralized sections of the breccia, the matrix contains actinolite/tremolite, chlorite, epidote, and/or rock flour. Breccia clasts consist of the host sedimentary material, pre-breccia gabbro/diorite, quartz-feldspar porphyry, diabase, and minor fine-grained granite. The sedimentary and gabbro/diorite clasts were locally derived from the wall-rock lithologies, however, the quartz-feldspar porphyry (QFP) clasts have not been observed in outcrop near the showing and are therefore assumed to have been derived from depth. In places, the QFP clasts contain pre-breccia mineralization in the form of arsenopyrite, and they are also locally finely comminuted, producing a rock-flour matrix in portions of the prospect, likewise suggesting transport from depth.

3.2 Regional Geology

The Goobies-Come By Chance area (figures 1.1, 1.2) is divided into two structurally contrasting geological terrains by a system of faults that are an extension of the Paradise Sound fault (PSF) and the Come By Chance fault (CBCF). Southeast of the faults, the area is underlain by a thick succession of late Neoproterozoic sedimentary rocks (Connecting Point Group) that are locally overlain or faulted against mixed volcanic and sedimentary assemblages of the Musgravetown Group. These, in turn, are overlain or faulted against Lower Cambrian shales. Rocks of the belt have been openly to tightly folded about northeast-trending axes and do not display schistosity. Northwest of the PSF is a belt of chlorite-sericite schists derived from volcanic, sedimentary, and intrusive rocks considered to be part of the Marystown Group. Intrusive rocks (figure 1.2)

are granite, quartz-feldspar porphyry, and diorite of the Sall the Maid Intrusive Suite, bordering the western side of the map area, and diorite, gabbro, and felsic dykes of the Powder Horn Intrusive Suite.

Rocks belonging to the Connecting Point Group (Hayes, 1948) are located in the south-central portions and on the eastern side of the map area (figure 1.2). They include green, grey, and brown, regularly bedded with locally cross-bedded and laminated sandstone, siltstone and shale. In places, thick, massive (sometimes pebbly) sandstone beds occur within the thinly bedded sequences. A medium- to coarse-grained green conglomerate unit occurs towards the top of the sequence. In places, detrital magnetite is common as thin lenses and wisps within the beds. These rocks have been altered to a dense black hornfels close to the Powder Horn Intrusive Suite, although sedimentary features can generally still be recognized within the sedimentary unit.

The Connecting Point Group is sometimes difficult to distinguish from the overlying Musgravetown Group (Hayes, 1948) exposed in the northern part of the map area. This latter unit consists of green to grey, graded and cross bedded sandstone, pebbly sandstone, conglomerate and grey to black thinly bedded sandstone and shale. This similarity led to errors in previous mapping by McCartney, (1967), and the author during this project, but U-Pb dating aided in distinguishing the two units (described later in this report).

Marystown Group (Strong et al., 1978) rocks are exposed in the northwestern part of the map area (figure 1.2) where they are composed of mafic to silicic volcanic flows

and pyroclastic rocks, including crystal, lithic, and crystal-lithic tuffs and agglomerates. These rocks have been isoclinally folded and are overprinted by a strong penetrative north-to northeast trending, steeply dipping foliation and have been regionally metamorphosed to chlorite and sericite schists. These rocks were originally included in the Love Cove Group because of similarities in composition and deformation. O'Brien and Knight, (1988) demonstrated in the Bonavista Bay area that the Love Cove Group conformably underlies the Connecting Point Group and has an age of 620 +/- 2 Ma (O'Brien et al., 1989). A recent age for what had been mapped as Love Cove units on the Burin Peninsula indicated that they are ca. 572 Ma (O'Brien et al., 1999) and thus are younger than the Love Cove Group. These rocks are therefore equivalent in age to rocks of the Musgravetown Group (O'Brien, 1987; O'Brien et al., 1989; O'Brien and Knight, 1988), which unconformably overlies the Connecting Point Group.

The Random Formation (Walcott, 1900) overlies the Musgravetown Group in the north-central part of the map area and consists of white to brown orthoquartzite, quartz sandstone, and inter-bedded dark grey to green micaceous siltstone and sandstone (figure 1.2). Rocks of the Adeyton Group (Jenness, 1963) in turn overlie the Random Formation and are characterized by red, purple, and green shale and slate containing nodules and nodular beds of pink and grey algal limestone. The limestones contain fossils consisting mainly of the shelly fauna hyolithids. Rocks of the Adeyton Group are also exposed as faulted blocks along the Come By Chance Fault, splays of this fault, and the Paradise Sound Fault. Minor outcrops of black shale are exposed in the town of Goobies and may

be Middle Cambrian remnants (McCartney, 1958). A fault block containing possible Cambrian shales also occurs within the Connecting Point Group in the map area. These are red and green shales with layers rich in limestone nodules. Field relationships suggest that this Cambrian unit was intruded and hornfelsed by a fine grained gabbro or diabase intrusive. No geochronology, however, has been conducted on these intrusive phases.

The Sall the Maid Granite outcrops on the western edge of the map area where it extends southwestward along the trace of the Paradise Sound Fault to the North Harbour area as discontinuous intrusive bodies (figure 1.2). It is composed of beige to pink and orange, fine-grained granite, quartz +/- feldspar porphyry, and green to grey diorite. It intrudes the late Neoproterozoic and Lower Cambrian rocks in the North Harbour area and is presumed to be Devonian in age.

3.3 Powder Horn Intrusive Suite

The Powder Horn Intrusive Suite is a multi-phase intrusion, dominated by diorite/gabbro and lesser amounts of felsic and diabasic material (figure 1.2). The intrusion is exposed as an elliptical body at the intersection of the Isthmus of Avalon and the northern part of the Burin Peninsula, near the town of Goobies (figure 1.1). This study was initiated to investigate the origin of auriferous sulphide mineralization associated with polylithic breccias at the Lodestar prospect.

Contact relationships between the phases of the intrusion and country rock are well enough exposed to allow the determination of the relationship between the phases

and the mineralization. Due to the lack of subsurface data it is difficult to interpret the nature and extent of the mineralized breccia at depth. Preliminary interpretation suggests that the mineralized breccias have a phreatomagmatic or magmatic–hydrothermal origin, to be discussed in further detail in a later section.

Work carried out during the 1999 field season identified five significant rock units, each with internal variations; these phases were defined as either pre- or post-brecciation (mineralization). The existence of pre- and post-breccia phases within the intrusion is important in terms of the timing and mode of emplacement of the mineralization (see below).

The pre-mineralization rocks consist of (1) a sedimentary unit, which is assumed to host the intrusion and which has been intensely hornfelsed, (2) a medium- to coarse-grained, equigranular, black and white gabbro/diorite, and (3) small felsic dykes, presumed to be pre-mineralization due to the occurrence of a dyke which is brecciated in part of the showing where the breccia is un-mineralized (figure 1.2). This felsic dyke likely represents a syn-brecciation phase. The post-mineralization rocks consist of (1) fine-grained, dark-green, equigranular diorite to gabbro with pilotaxitic texture, (2) pink to orange quartz–feldspar porphyry dykes and fine-grained granite dykes, and (3) diabase dykes (figure 1.2).

3.3.1 Pre-Breccia Units

3.3.1.1 Host Sedimentary Units: Connecting Point Group (~610 Ma)

As previously described, sedimentary rocks (Connecting Point Group; unit 1, figure 1.2) in the vicinity of the intrusion have been intensely hornfelsed. In places, however, the hornfelsed sedimentary rocks still exhibit narrow laminations and bands of dark and light material, presumably remnants of primary depositional layering (plate 3.1). This remnant layering can be compared to the layering within the group in the area surrounding the intrusive body (plate 3.2). These rocks commonly contain dark magnetic bands, indicating the presence of either detrital magnetite or the introduction of magnetite into the sediments by the intrusive rocks (plate 3.1). In areas close to the intrusion, the sedimentary rocks are completely hornfelsed to a very fine-grained black rock (plate 3.3), that defines a thermal aureole to the intrusion. This hornfelsed sedimentary material is locally magnetic. Due to the grain size and the extent of the hornfelsing, identification of metamorphic minerals in hand sample is difficult. Away from the intrusive phases, the sedimentary rocks consist of thinly bedded to massive, black, grey and green sandstones, pebbly sandstones, siltstones and shales (plate 3.2), commonly displaying preserved structures, ie. cross bedding (plate 3.4).

The Connecting Point Group sedimentary rocks are both overlain by, and fault-bounded against, a sequence of quartzites, sandstones, and red and green shales with beds and nodules of pink and grey limestone that correspond to the Cambrian Random Formation and Adeyton Group (units 4 and 5, figure 1.2), (plate 3.5).

Field relations imply that the host sedimentary rocks were consolidated at the time of gabbro intrusion and were subsequently partially melted or migmatizied. This resulted in a partial "mixing" of the sediments and gabbro, producing schlieren textures (plate 3.6). Due to the lack of hydrous minerals (ie. amphiboles), and the "competent" sedimentary outcrops at contact localities, it was concluded that the sedimentary rocks must have been solid at the time of intrusion. The fact that the sedimentary rocks were hornfelsed, and that gabbroic sills locally crosscut sedimentary outcrops, corroborate this idea.

Petrographically the host sedimentary units are fairly homogeneous comprising quartzarenite, arenite, and lithic arkose. In general all of the sedimentary rocks were hornfelsed and altered. The petrographic sections, however, still display some primary textures and characteristics of the original clastic protolithologies. All samples are dominated by fine-grained, equigranular quartz (up to ~ 65-70 %) that was both primary and re-crystallized (plate 3.7, 3.8). Alteration minerals comprise chlorite, hornblende, epidote, actinolite/tremolite, and biotite, thus defining the alteration as middle-upper greenschist facies. Except for relict primary layering preserved in some sections, there is no obvious foliation. The layering appears as alternating layers of quartz rich, biotite, and oxide (magnetite) material in thin section (plate 3.7).

3.3.1.2 Pre-Breccia Medium-Grained Gabbro/Gabbrodiorite (~ 603 Ma)

The other major pre-mineralization unit is medium to coarse-grained, equigranular, black and white gabbro/diorite of the Powder Horn Intrusive Suite (unit 6,

figure 1.2)(plate 3.9). This unit occupies the central portion of the map area (figure 1.2) where it intrudes the host sedimentary rocks and is itself intruded by fine-grained gabbro, felsic and diabase dykes, and the breccia. These rocks are slightly magnetic in places due to accessory magnetite. There is some compositional variation within this intrusive rock that gives rise to two main subdivisions (not separated on figure 1.2). The first group contains plagioclase, pyroxene, amphibole, biotite and rare quartz, whereas the second group consists of only plagioclase, pyroxene, and biotite. A gradational transition between the two subdivisions whereby one phase locally (over 10's of meters) grades into the other phase is locally observed; no sharp contacts were encountered. For the purposes of description both of the varieties will be dealt with in unison and treated as a single plutonic body.

The degree of alteration varies throughout this pre-breccia gabbro/diorite phase from very altered to samples with only minor alteration, and is related to cross-cutting faults and associated fluid flow. In outcrop, mafic minerals in altered samples have a noticeable green colour indicating the presence of variable proportions of chlorite, hornblende, actinolite, and tremolite. Grain sizes vary within the unit from dominantly medium grained (1-3 mm crystals with some larger ophitic pyroxene crystals) (plate 3.9, 3.10); ranging up to coarse-grained varieties with crystals ranging up to 2 cm; to outcrops with grain size variations resulting in coarse grained "pods" within medium grained rocks. Areas where felsic dykes intrude the coarse-grained material are commonly marked by accumulations of mafic material (plate 3.11).

Petrographically the pre-breccia gabbro/diorite varies from gabbro to diorite, with quartz percentages ranging from 0-15 % (plate 3.12, 3.13). Petrographic determination of the An contents in some plagioclase suggests An contents of less than 50. However, since the rocks are locally altered and hydrated, the measured An contents may not be of primary origin and therefore can not be used to define rock type. For the purposes of this project, no detailed microprobe analysis were conducted on plagioclase crystals, hence the samples will be referred to as gabbro-diorite.

Alteration intensity varies throughout the intrusion, and is most intense in areas around faults, felsic intrusions, and in the area of the breccia showing. This unit is typically un-foliated, but locally exhibits a weak foliation of the mafic minerals in areas of alteration. This variability in degree of alteration influences mass gain and loss effects, to be discussed in a future section.

The fresh, relatively unaltered version of the pre-breccia gabbro/diorite typically consists of approximately 40-50 % plagioclase, 25-30 % clinopyroxene, 5-10 % orthopyroxene, minor primary biotite, minor (5-10 %) secondary hornblende, biotite, minor actinolite/tremolite, and variable amounts of magnetite (plate 3.13). Accessary minerals include apatite, sphene, rutile, and zircon. The altered samples of this unit contain variable amounts of secondary sericite, hornblende, biotite, actinolite, tremolite, chlorite, epidote, and minor carbonate (plate 3.14). The magnetite in the samples is interpreted to be both primary and secondary in nature based upon textural evidence to be discussed in following descriptions. Both fresh and altered varieties contain minor

amounts of pyrite and chalcopyrite disseminated throughout, typical of most gabbros (cf. Foster, 1991).

Typical grain sizes in the pre-breccia gabbro/diorite range from ~ 1 to ~ 4 mm for plagioclase and pyroxene crystals with the majority of crystals ~ 2.5-3 mm, whereas quartz crystals are typically smaller with average sizes of ~ 0.5-1 mm. As mentioned above the unit is locally coarse-grained with crystals up to 2 cm.

The pyroxene crystals in the gabbro/diorite occur in two different forms consisting of large subhedral-euhedral solitary crystals commonly displaying carlsbad twinning (plate 3.13) and groups of smaller anhedral-subhedral crystals (plate 3.15). Where preserved, the main texture within the lithology is a sub-ophitic to ophitic texture with plagioclase crystals partially enclosed in pyroxene oikocrysts (plate 3.16). Unaltered plagioclase in this unit dominantly consists of subhedral to euhedral granular crystals, however most samples display variable amounts of sericitization. Plagioclase crystals typically display albite twinning. Where present, quartz crystals are anhedral and are dispersed throughout the thin sections (plate 3.12).

Pyroxene (dominantly cpx) undergoes uralitization whereby it is altered to hornblende, biotite, actinolite/tremolite, chlorite, +/- epidote (plate 3.17). This reaction implies that the gabbro/diorite underwent upper-greenschist-lower-amphibolite facies conditions. The most common reaction observed in thin section consists of clinopyroxene with a reaction corona of hornblende, which in turn is surrounded by biotite (plate 3.17). Chlorite locally occurs as a further alteration product from the amphiboles (hornblende,

actinolite/tremolite), and secondary quartz along with re-crystallized quartz are also common phases. Thin sections indicate that the rocks have undergone selective hydrothermal alteration, thereby indicating that some fluids, probably associated with faulting or other intrusive phases, were the driving force behind the alteration. Some of the most altered samples occur near the western side of the intrusive suite near the Paradise Sound Fault and near the intrusive breccia of the Lodestar Prospect (figure 1.2).

Medium-grained gabbro from the Lodestar Prospect consists totally of alteration products. These samples comprise approximately 25-30 % chlorite and 65 % sericite (plate 3.18). The remainder of the rock consists of actinolite/tremolite, epidote and some primary? and secondary anhedral quartz crystals. Petrographic relationships observed within these samples indicate that the primary pyroxene goes through an alteration sequence whereby it initially alters to hornblende/biotite and actinolite/tremolite, which in turn alters to chlorite. Pseudomorphs of plagioclase are present consisting of sericite and minor epidote, representing sericization and saussuritization respectively.

As mentioned, magnetite in the gabbro/diorite has two different forms. In the dominant form, magnetite occurs as anhedral crystals overprinting alteration products (plate 3.17). Magnetite is also interstitial or present as phases with a symplectitic texture whereby the magnetite is inter-grown in a vermicular fashion with other phases (dominantly within alteration assemblages).

3.3.1.3 Pre-Breccia Felsic Dykes

The final unit classified as pre-breccia is a single small felsic dyke which is brecciated (plate 3.19 a-b). This dyke is a very fine-grained granitic/aplitic intrusion. It appears to initially intrude the breccia, but is then brecciated itself, thereby indicating the possibility that it is of syn- to pre-breccia origin (plate 3.19 a-b). Although a number of other felsic dykes intrude the pre-breccia medium-grained gabbro/diorite, the dyke at the showing is the only one that can be unambiguously classified as pre-breccia. The fact that there is at least one pre-breccia dyke is important for understanding the mechanism of brecciation and will also be dealt with in a further section. Many more felsic dykes are observed to intrude the post-breccia fine-grained gabbro and these will also be described in a later section.

3.3.2 Post-Breccia Units

3.3.2.1 Post-Breccia Fine-Grained Gabbro-Diorite

Post-mineralization, fine-grained, dark green, diorite to gabbro (unit 7, figure 1.2) is the predominant post-breccia phase and varies throughout (plate 3.20). This unit occupies the north central part of the map area and it also occurs in the form of a number of variably sized dykes throughout the map area (figure 1.2). In places, this unit is simply equigranular with a pilotaxitic texture and no phenocrysts (plate 3.20, 3.21a), whereas in other areas it contains phenocrysts of plagioclase and/or amphibole (plate 3.21b) with some plagioclase phenocrysts ranging up to 1 to 10 cm in length. This phase of the intrusion is also slightly magnetic in places (i.e., contains some accessory magnetite).

Primary sulphides (dominantly pyrite) are also disseminated throughout this phase (plate 3.21).

Petrographically this post-breccia unit varies in composition from gabbro-diorite to leuco-norite to gabbronorite with percentages of quartz ranging from 5-10 %. As with the pre-breccia gabbro/diorite, this unit displays variable alteration throughout, ranging from relatively fresh to totally altered, thereby making original textures and compositions difficult to determine. As with the pre-breccia gabbro, this variability in degree of alteration affects mass gain and loss ratios.

The dominant phase consists of quartz leuco-gabbro-norite, whereas gabbro-diorite and leuco-norite are less common. Mineralogically the dominant phase consists approximately of 45-65 % plagioclase, 20-30 % pyroxene (of which typically ~ 80 % is clinopyroxene), up to ~ 10 % quartz, ~5 % primary biotite, with the remainder consisting of the alteration products of hornblende, sericite, actinolite/tremolite, chlorite, epidote, re-crystallized quartz, and secondary biotite (plate 3.22). Magnetite, apatite, zircon, and rutile are present both as minor primary phases and presumably as alteration products associated with the intrusion (plate 3.23). The gabbro-diorite variety of this phase has a similar mineralogy with an increased proportion of quartz (10-15%), whereas the leuco-norite variety has increased proportions of orthopyroxene (~ 15 %) relative to clinopyroxene (~5%). The more altered samples of this phase consist of the same primary mineral components, with increases in the proportions of secondary hornblende, sericite, actinolite/tremolite, chlorite, epidote, secondary quartz, and secondary biotite.

Typical grain sizes of the post-breccia gabbro/diorite observed in thin section range from ~ 0.5-1 mm for pyroxene with plagioclase typically ranging from 0.2-0.5 mm (plate 3.22). However, in some cases this unit has coarser mineralogy with plagioclase laths and pyroxene oikocrysts ranging up to 2 mm in length and width respectively. Locally this unit contains large plagioclase and/or amphibole phenocrysts, with some plagioclase phenocrysts ranging up to 10 cm in length. Magnetite is typically present as small (< .1 mm) anhedral blebs, whereas accessary minerals such as apatite occur as very fine crystals (plate 3.22, 3.23, 3.24).

Within the post-breccia gabbro/diorite unit, the main textures consist of an interstitial pilotaxitic texture (variety of trachytic texture) whereby there is an arrangement of sub-parallel crystalline ground-mass plagioclase laths around pyroxene crystals (plate 3.24). In some cases the plagioclase crystals appear to be randomly arranged, thereby defining the texture simply as interstitial, inter-granular texture. A sub-ophitic to ophitic texture is also observed in which the plagioclase laths form chadacryts within pyroxene (dominantly cpx) oikocrysts. Therefore, a full textural definition of this unit includes pilotaxitic, interstitial, inter-granular, and sub-ophitic to ophitic textures. In fresher examples of this unit, sub-hedral to euhedral plagioclase crystals exhibit albite twinning, whereas the pyroxene crystals are typically anhedral masses with local granular textures in very-fine-grained varieties. Oxides (magnetite) and sulphides (dominantly pyrite) are disseminated throughout.

Within the altered samples, as with the other gabbro phase, pyroxene and

plagioclase are variably altered and replaced. Pyroxenes are uralitized as alteration occurs in the form of hornblende, biotite, actinolite/tremolite, chlorite, +/- epidote; plagioclase is altered to sericite.

3.3.2.2 Post-Breccia Felsic Dykes

The felsic dykes (unit 8, figure 1.2) associated with the PHIS range from very fine- grained aplite, through fine-grained granite, feldspar porphyry, to quartz–feldspar porphyry (plate 3.25). These felsic phases are assumed to represent high-level intrusions and dominantly occur as post-breccia phases. However, as described above, minor pre- and syn-breccia phases also occur. The dykes are typically narrow (cm up to ~ 1 m), and in the case of the post-breccia varieties, intrude all other phases of the intrusion including the two gabbro phases.

The same variations in mineralogy as described above for field samples were observed through petrographic examination. For the purposes of petrographic examination, thin sections of the fine-grained aplite, the feldspar porphyry, and the quartz-feldspar porphyry were examined.

The fine-grained aplite variety consists of ~ 40-50 % quartz with the remainder dominated by alkali-feldspar (~40 %) and plagioclase feldspar. There are minor amounts of biotite and magnetite, along with minor epidote (alteration product) (plate 3.26). The rock typically occurs as a very-fine grained, equigranular unit with a granophyric (type of micrographic) texture defining crudely radiate inter-growths of the quartz and alkali-feldspar (plate 3.26).

The feldspar-porphyry and the quartz-feldspar porphyry contain feldspar (locally zoned) and quartz/feldspar phenocrysts, as well as local euhedral phenocrysts of hornblende, in a fine-grained matrix consisting of quartz, alkali-and plagioclase feldspar (plate 3.27). The phenocrysts range from <1 mm up to ~ 1 cm in size and are set in a quartz dominated matrix with crystals approximately 0.01-0.03 mm in size (plate 3.27). Local biotite and magnetite are also common. These sections also exhibit granophyric textures associated with quartz-alkali-feldspar intergrowths. Aggregates of recrystallized quartz are common, as are minor alteration phases of epidote, chlorite, biotite, and actinolite/tremolite.

A potential temporal relationship exists between textural varieties within the "Post-Breccia" phase. It appears that the porphyritic variety is definitely post-breccia (ie. intrude the post-brecia fine-grained gabbro); whereas those which are potentially pre-breccia (ie. only observed to intrude the pre-breccia gabbro) are typically fine-grained with granophyric textures.

3.3.2.3 Diabase and other minor phases.

Diabase dykes intrude all phases of the Powder Horn Intrusive Suite and they locally crosscut each other (plate 3.28). In the field these dykes appear as very fine-grained dark units. Petrographically the dykes are very-fine grained lithologies dominantly consisting of plagioclase and minor pyroxene with secondary actinolite, tremolite, chlorite, and epidote. Pyrite and magnetite are locally observed.

3.4 CONTACT RELATIONSHIPS OF THE INTRUSIVE PHASES

All phases of the Powder Horn Intrusive Suite intrude, and thermally metamorphose the surrounding sedimentary rocks, which are dominated by the late Neoproterozoic Connecting Point Group. This relationship is evident in areas where relict primary layering or banding in the sediments is crosscut or cut-off by different phases of the suite (plate 3.29).

In some areas, small inclusions or xenoliths of sedimentary rocks, commonly magnetic, are present within the intrusive phases, thereby indicating intrusive contact relationships. These sedimentary xenoliths are especially common in the pre-mineralization (early) gabbro/diorite. Schlieren textures are common at the contact between the sediments and the early gabbro/diorite indicating possible partial assimilation of the sedimentary rocks (plate 3.6).

Intrusive contacts between the post-breccia (late) gabbro and the pre-breccia (early) gabbro/diorite are generally sharp and marked by chilled margins, such a relationship is also preserved where the post-mineralization felsic dykes are in contact with early and late gabbro/diorite. However, in some localities the contact between the pre- and post-breccia gabbro/diorite phases appears to be inconspicious to gradational. All phases appear to have been intruded by diabase dykes.

In the southeastern part of the map area (figure 1.2), a dyke presumed to be of the post-breccia diorite/gabbro, intrudes and thermally metamorphoses Cambrian shales, resulting in the shales being hornfelsed. The contact is rather poorly exposed along a

brook that flows from the Powder Horn Hill area to the Come By Chance river. This indicates that at least this phase of the intrusion, depending on proper classification of the intruding dyke, is potentially post-Cambrian.

3.5 MINERALIZATION

Contact relationships observed at the Lodestar prospect (figure 1.2, 3.1)(plate 1.3) indicate that the breccia was emplaced in the contact region between the early gabbro/diorite and the host sedimentary rocks. Both of these units were at least locally sampled by the breccia as indicated by their presence as clasts within the breccia (plate 3.30). The mineralized breccia has been intruded by the fine-grained diorite (plate 3.31), quartz–feldspar porphyries (plate 3.19a-b), aplite dykes, and diabase dykes (plate 3.28).

Another breccia was discovered in the area of Powder Horn Hill. This breccia resembled the mineralized breccia at the Lodestar showing due to the presence of gabbroic clasts, as well as large alkali-feldspar clasts. Petrographically, however, this breccia differs in that it has a crystalline matrix consisting of plagioclase feldspar, alkali-feldspar, and actinolite/tremolite/chlorite, presumably representing alteration products from original pyroxene. Therefore this breccia was classed as being intrusive rather than hydrothermally derived.

3.5.1 CHARACTERISTICS OF THE MINERALIZED BRECCIAS

3.5.1.1 Field Descriptions

The mineralized breccia (plate 1.3) is exposed over approximately 20 m (figure 3.1) and contains gold in association with copper, arsenic and zinc sulphides. The sulphide mineralization occurs as the matrix in parts of the breccia (plate 3.30, 3.32 a-d), whereas, un-mineralized parts of the breccia have a rock-flour or actinolite/chlorite matrix (plate 3.33 a-c). The breccias at the main showing, as well as proximal breccias, contain hydrothermal (secondary) magnetite in the matrix (plate 3.34 a,b). The breccia contains rounded to angular clasts of the host sedimentary rocks, the early diorite/gabbro, quartz porphyry, quartz–feldspar porphyry, diabase and minor fine-grained granite (plate 3.30, 3.35 a-c). Clast size varies from <1 cm up to ~ 50 cm, but the clasts are typically <10 cm. The sedimentary and gabbro/diorite clasts were derived from the wall rocks which the breccia transects, and therefore are presumed to be locally derived. This is supported by the fact that some clasts are brecciated in such a way that adjacent clasts have matching margins and can thus be reassembled like jigsaw puzzle pieces (plate 3.33 c, 3.36). In some cases, sulphide mineralization fills small cracks in the clasts produced by the brecciation (plate 3.36).

The quartz porphyry, quartz–feldspar porphyry, and fine-grained granite clasts (plate 3.35 a-c) have not been observed in outcrop in the area of the showing and therefore are presumed to represent exotic clasts derived from a deeper unexposed high-level epizonal quartz-feldspar porphyry intrusion. Various textural evidence supports this

idea. Some of the quartz and quartz–feldspar clasts appear to contain pre-breccia mineralization that consists of fine disseminations of sulphide mineralization within the clasts (plate 3.35 b,c). As well, localized rims (1-3mm) of mineralization (arsenopyrite) surround these clasts, thereby indicating a chemical affinity between the mineralization and these felsic clasts. Also, the rock-flour matrix appears to consist of finely comminuted pieces of these clasts; comminution presumably being due to the upward transport process. Within the rock flour matrix, small quartz clasts and pieces of broken up quartz-feldspar porphyry material are also surrounded by arsenopyrite mineralization (plate 3.33 c).

Another texture associated with the QFP clasts consists of crenulate or ptygmatically folded quartz layers (unidirectional solidification texture) (plate 3.37). This texture has been related to porphyry deposits (Kirkham and Sinclair, 1988), a subject to be dealt with in a later section. The idea of varying sources, or varying depths of clast acquisition is important in the classification of breccia type and the understanding of the brecciation processes, subjects also to be dealt with in a later section.

The breccia is dominantly clast-supported with varying amounts of matrix (~ 5 to 15%). The matrix consists of sulphides/oxides, chlorite/actinolite/tremolite, and rock flour, all of which vary in proportion throughout the breccia (plate 3.32 a-e, 3.33 a-c, 3.34 a-b). Where mineralized, the matrix consists of arsenopyrite, pyrite, chalcopyrite, and magnetite, with minor amounts of visible bornite and sphalerite (plate 3.32 a-e, 3.34 b, 3.35 b, c). The matrix mineralization overprints, and is preferentially affiliated with, some

of the breccia clasts and is therefore, assumed to be syn- to post-brecciation. The overprinting texture is predominantly associated with the quartz and quartz–feldspar porphyry clasts whereby mineralization, in the form of arsenopyrite and/or pyrite, rims and overprints the clasts (plate 3.35 b, c,); again indicating chemical affinity between the mineralization and the clasts.

Within the breccia, the different sulphide minerals appear to be segregated into arsenopyrite-rich, pyrite-rich zones, and sphalerite-rich zones; presumably linked to differences in fluid compositions and mineral crystallization sequences. The mineralized zones contain sulphides as veinlets and semi-massive pods within the matrix (plate 3.30, 3.32 a-d). This "segregation" of the various sulphide phases within veins and pods suggest a post-breccia mineralizing event.

Within the main breccia showing, mineralized zones or areas of brecciation are commonly directly juxtaposed against non-mineralized breccia zones. In many instances it appears as though these mineralized and non-mineralized zones actually consist of large (~1-2m) fault bounded blocks of brecciated material (ie. re-brecciation?) (plate 3.38).

Individual blocks of breccia juxtaposed against each other has also been observed where a section of breccia with rock-flour dominated matrix is juxtaposed against a section of breccia with no rock-flour matrix. However, due to the relatively small size of the breccia outcrop and the lack of sub-surface data, this observation could not be investigated further.

Minor alteration in the form of sericite/biotite is visible as concentric rings around

the sedimentary clasts (plate 3.30, 3.39), and some chlorite and epidote alteration is also observed in the area of the breccia, although this alteration is not very substantial. The gabbroic clasts within the breccia also display severe alteration as mentioned above.

3.5.1.2 Petrographic analysis of the mineralized breccia

3.5.1.2.1 Introduction

Petrographic examination of the Lodestar Breccia included detailed descriptions of the clast types and associated alteration, descriptions of the matrix component of the breccia (mineralized and non-mineralized components), as well as detailed examination of the mineralization and associated alteration. Samples for petrographic analysis were collected such that each of these breccia characteristics could be fully investigated. As mentioned above, mineralized and un-mineralized sections of the breccia are commonly juxtaposed and potentially fault bounded against each other. Therefore sample selection was based on clast type, matrix characteristics, and mineralization characteristics rather than on specific location within the breccia outcrop. The following descriptions attempt to subdivide the breccia into various components in order to gain a more comprehensive understanding of the nature of brecciation and mineralization.

3.5.1.2.2 Clasts within the breccia and associated alteration

Breccia clasts have been exposed to the fluids associated with the brecciation event as well as the mineralizing fluids, and therefore display pervasive alteration of their original mineralogy. The medium-grained, pre-breccia gabbro/diorite clasts display intense alteration whereby the original pyroxene (dominantly cpx) has been totally

altered to chlorite, actinolite/tremolite, and biotite, and the original plagioclase have been totally altered to sericite (plate 3.18). In addition to remnant original quartz crystals preserved within the clasts (plate 3.18), secondary quartz veins are also observed to locally transect thin sections indicating silica alteration (plate 3.40). Oxides and sulphides in the form of magnetite and arsenopyrite/pyrite, respectively, overprint these clasts, indicating secondary mineralization.

Original compositions of the host sedimentary unit are still identifiable as fine-grained quartz, however, alteration rims representing increased proportions of the alteration phases sericite and biotite, overprint the outer portions of the clasts. This is to be expected as the outer portions of the clasts would be the most affected by the brecciating and mineralizing fluids.

The other major type of clast observed in the breccia consists of quartz- and quartz-feldspar porphyritic phases. These clasts consist of euhedral porphyritic quartz crystals (ranging up to 3mm) set in a very fine grained rock consisting almost entirely of quartz and re-crystallized quartz (plates 3.41). These clasts are typically surrounded by an approximately 1-3 mm rim of arsenopyrite mineralization and they are also overprinted by a fine dissemination of arsenopyrite and pyrite, potentially of primary origin (plate 3.42).

3.5.1.2.3 Matrix: Mineralization and Non-mineralized Matrix

The most common non-mineralized matrix consists of fibrous actinolite/tremolite with varying amounts of chlorite and epidote (plate 3.43). Some quartz veining and re-

crystallized quartz are also locally observed. This matrix material typically makes up approximately 15 % of the breccia lithology. The actinolite/tremolite matrix occurs as long fibrous crystals (ranging from <1 mm to ~3 mm long), whereas chlorite and epidote typically occur as fine-grained masses filling spaces around and between clasts. Some areas of the breccia matrix are dominated by almost 100 % chlorite (plate 3.33 b). A relationship exists between the matrix and alteration within the clasts whereby there is a zonation or typical distribution of matrix type to alteration phases moving from the matrix to the clasts. This zonation is described in the following section dealing with the mineralization.

The other major type of "non-mineralized" breccia comprises rock flour matrix which consists of fine-grained, comminuted clasts, dominated by quartz- and quartz-feldspar porphyries (plate 3.43 c, 3.44). Petrographically this matrix appears as crystals of quartz (derived from QFP clasts) associated with some broken up pieces of QFP clasts with re-crystallized quartz, and the remainder of the matrix dominated by chlorite. Some of the relict QFP clasts associated with this rock flour matrix have overprinting mineralization in the form of arsenopyrite. This type of matrix is important in the model description, and will be dealt with further in a later section on breccia formation.

Auriferous mineralization makes up a substantial portion of the matrix of the breccia and it is this mineralization which makes the showing economically interesting. The mineralized matrix typically consists of a mixture of the above described non-mineralized matrix and variable amounts of arsenopyrite, pyrite, chalcopyrite, sphalerite,

and magnetite. Minor bornite and covellite are observed in some altered sections. Textures of the sulphide minerals range from sub- to euhedral crystals to anhedral disseminations or masses, to rims of mineralization as mentioned above. Some vein-like mineralization is also present along with minor veinlets of mineralization cutting through clasts (plate 3.36). Textures of individual sulphides, along with textures between sulphides are variable throughout the mineralized breccia. Arsenopyrite, which occurs as the dominant sulphide within the matrix, varies in texture from large (5-6 mm) sub- to euhedral crystals, to smaller (less than 1mm) euhedral crystals, to anhedral masses of crystals forming massive sulphide, to fine grained disseminations within the matrix and within some clasts (plate 3.45). Pyrite ranges from anhedral to subhedral crystals of varying sizes, to masses of anhedral crystals again making up a semi-massive to massive sulphide portion of the matrix (plate 3.45 c, g, 3.46 a, b). Sphalerite and chalcopyrite typically occur as anhedral masses or disseminations of variable sizes filling in or overprinting sections of matrix or other sulphide phases (plate 3.47 a-b). Sphalerite typically has exsolutions of chalcopyrite, commonly referred to as chalcopyrite disease (plate 3.47 b). Covellite is associated with one section of sphalerite (plate 3.48), representative of secondary oxidation.

Textures between sulphide phases are variable, thereby making it difficult to determine an accurate paragenetic sequence. Some samples indicate that the arsenopyrite, at least locally, formed prior to pyrite, chalcopyrite, and sphalerite. This relationship is observed in a number of sections whereby veins containing pyrite, chalcopyrite, and

sphalerite locally crosscut massive arsenopyrite (plate 3.46 b). In other areas, veins of chalcopyrite fill in cracks within arsenopyrite (plate 3.45), and sphalerite and chalcopyrite are exsolved from arsenopyrite (plate 3.49). However, contradictory textural observation suggests that arsenopyrite also occurs as a later crystallizing phase, whereby, bladed actinolite crystals forming the matrix clearly crosscut pyrite (thereby making the actinolite a later phase than the pyrite), but is itself overprinted by arsenopyrite, thereby making arsenopyrite a later phase than the actinolite and therefore later than the pyrite (plate 3.45 c). Another local textural observation illustrating arsenopyrite as a later crystallizing phase is observed where arsenopyrite occurs as an exsolution phase from chalcopyrite (plate 3.50). Contact relationships are also observed between pyrite and chalcopyrite whereby chalcopyrite is observed to "eat" away and intrude pyrite (plate 3.46 a). Along with these textural contact relationships between the sulphides, other areas of mineralization indicate a syn-formation or crystallization sequence for the sulphides. These areas illustrate all the major sulphides occurring in contact with each other without any obvious texturally defined temporal discrepancies (plate 3.51). The areas where pyrite and chalcopyrite crystallized at approximately the same time will be used in a future section dealing with geothermometry using sulphur isotopes.

As mentioned above a relationship exists between the matrix and alteration within the clasts whereby there is a zonation, or typical distribution, of alteration phases passing from the matrix to the clasts. This zonation is commonly observed and can be fully described with the use of thin sections containing both mineralized and non-mineralized

matrix components in contact with brecciated clasts. Within these samples, mineralized matrix components (consisting of semi-massive to vein-like mineralization) make up the "central" portion of the matrix. Moving towards the clasts, the mineralization is followed by actinolite/tremolite, chlorite +/- epidote, sericite/biotite, and finally the clast itself. This zonation is outlined in plate 3.52 a-b. The zonation is presumably related to the composition and temperature of the matrix forming fluids.

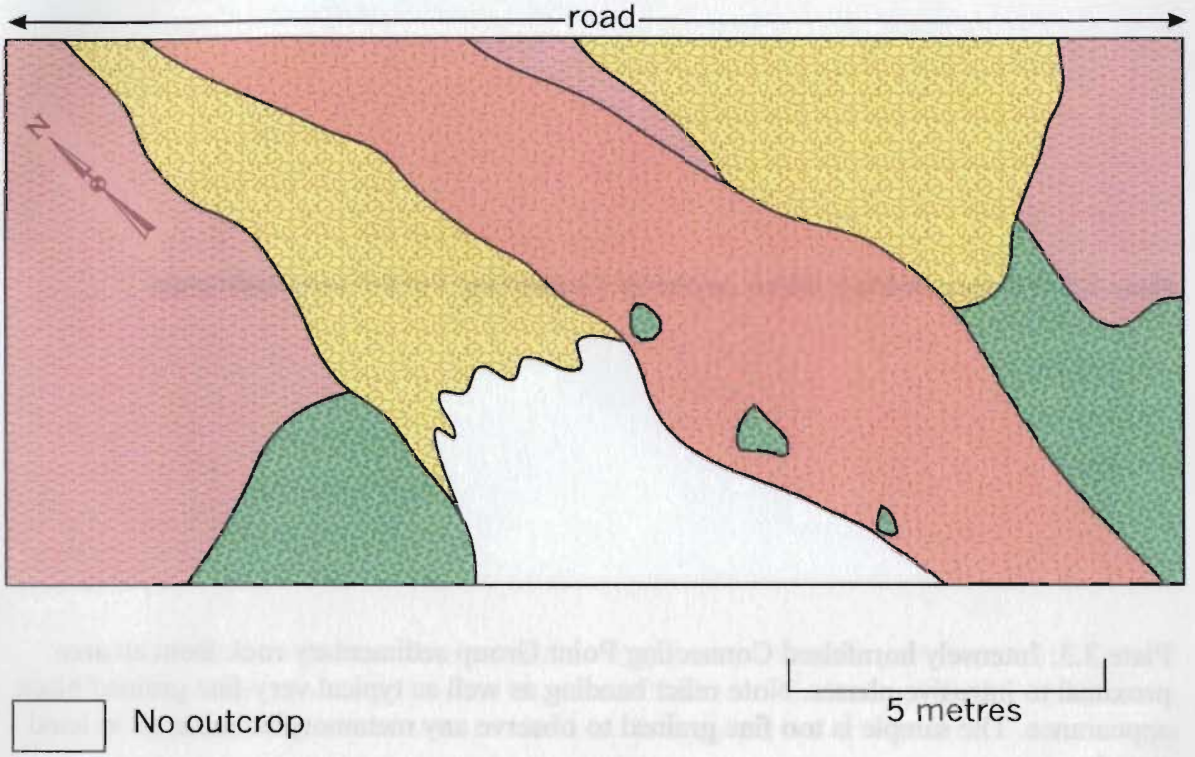

Figure 3.1: Plan view of the main mineralized zone of the Lodestar Breccia.

Plate 3.1: Presumed relict primary bedding within hornfelsed Connecting Point Group sedimentary rocks; note dark vs light layering, the dark layers are magnetic (ie. magnetite bearing).

Plate 3.2: Primary bedding within unaltered Connecting Point Group sediments.

Plate 3.3: Intensely hornfelsed Connecting Point Group sedimentary rock from an area proximal to intrusive phases. Note relict banding as well as typical very-fine grained black appearance. The sample is too fine grained to observe any metamorphic minerals in hand sample.

Plate 3.4: Cross-bedding structures preserved in Connecting Point Group rocks from an area distal to the intrusive phases. Cross-bedding structures are associated with turbidites within the unit. White lines added for demonstration of cross-bedding.


3.1


3.2

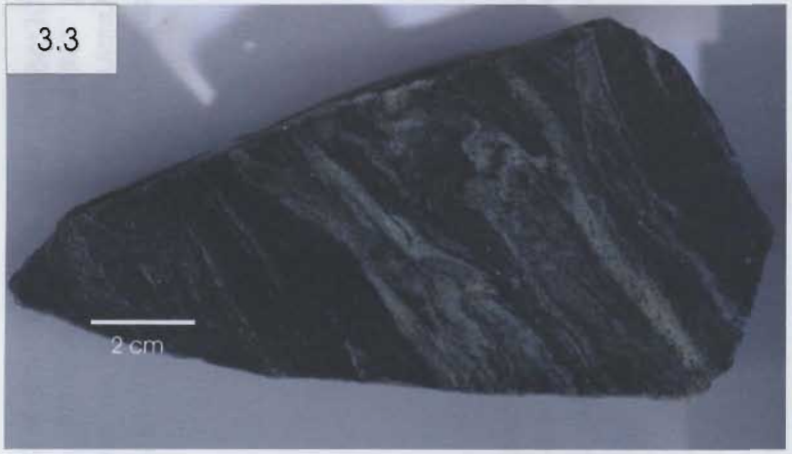
3.3
2 cm


3.4

Plate 3.5: Beds and nodules of pink-grey limestone within the Adeyton Group. Note the red shales between the limestone nodules, delineated by the white lines.

Plate 3.6: Schlieren texture developed where the host Connecting Point Group sedimentary rocks have been intruded by gabbroic phases. The sediments are interpreted to have been solid at the time of intrusion and were partially melted or migmatized by the intrusive. The schlieren textures are observed at the interface between the gabbro and the sedimentary rock whereby the two units appear to mix together.

Plate 3.7: Typical fine-grained, hornfelsed Connecting Point Group. Note the alternating layers of quartz-rich material and more biotite/oxide-rich layers, presumably representing preserved primary layering. F.O.V.= 5mm. (JH-99-88b)

Plate 3.8: Recrystallized quartz within Connecting Point Group hornfelsed sedimentary rocks. Note the large, bright remnant primary quartz crystals versus the amalgamations of "spotted" fine-grained recrystallized quartz. Minor epiodote (high-birefringence) also present in veinlets. F.O.V.= 5mm. (JH-99-30a)


3.5

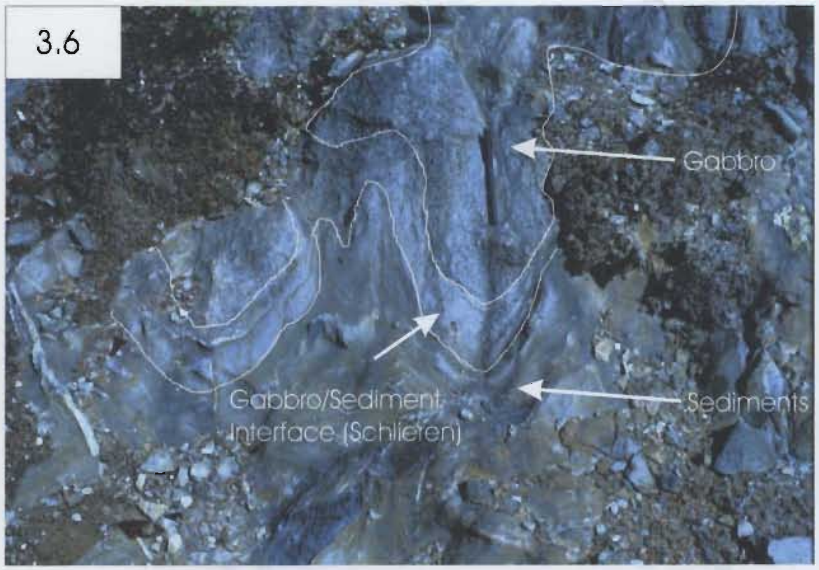
3.6
Gabbro
Gabbro/Sediment
Interface (Schlieren)
Sediments


3.7

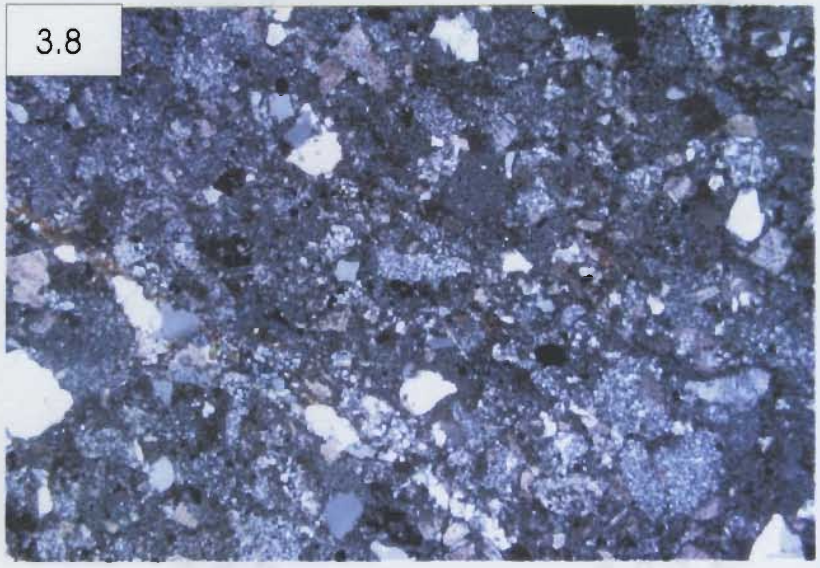
3.8

Plate 3.9: Outcrop photograph of typical massive, homogeneous, medium-grained, pre-breccia gabbro/gabbrodiorite; note stubby green pyroxenes. This intrusive phase dominantly consists of pyroxene, plagioclase, and biotite, however, some varieties contain variable amounts of quartz and amphibole.

Plate 3.10: Polished slab of the pre-breccia, medium-grained gabbro/gabbrodiorite. Note green tint in plagioclase due to sericitization; and the small veinlet of epidote/chlorite in the bottom left corner of the photograph.

Plate 3.11: Contact relationship between small felsic intrusive dyke emplaced in the pre-breccia gabbro/gabbrodiorite and surrounded by mafic rich material (pyroxenes) accumulations at the intrusive contacts. Similar mafic-rich wisps or pods are observed within "massive" pre-breccia gabbro/gabbrodiorite, presumably related to crystal density contrasts and crystal settling.

Plate 3.12: Thin section of diorite end-member, pre-breccia gabbroic intrusion. Note fairly high proportions of quartz and hornblende (green); quartz crystals are an- to sub-hedral and are dispersed throughout the section; feldspars are cloudy due to sericite alteration. F.O.V. = 5mm. (JH-99-40).

3.9

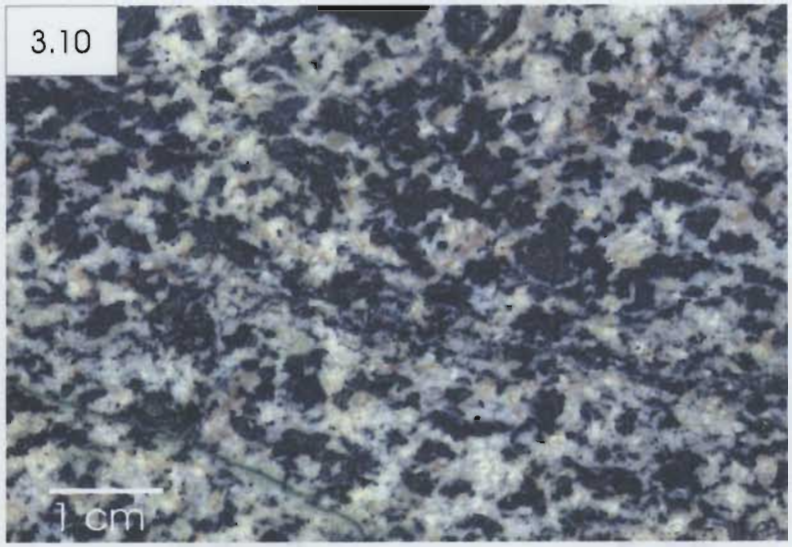

3.10

3.11

3.12

Plate 3.13: Photomicrograph of fresh, unaltered pre-breccia gabbro. The sample consists of approximately 40-50 % plagioclase, 25-30 % clinopyroxene, and minor biotite, hornblende, actinolite/tremolite, and magnetite. F.O.V.= 5mm. (JH-99-41).

Plate 3.14: Sample of intensely altered pre-breccia gabbro/gabbrodiorite. Note that practically all the plagioclase has been altered to sericite and practically all the pyroxene has been altered to chlorite/actinolite/tremolite, unaltered primary quartz crystals (white/grey clear crystals) and primary? interstitial magnetite (opaque). F.O.V.= 5mm. (JH-99-2a).

Plate 3.15: Fresh, unaltered variety of the pre-breccia gabbro/gabbrodiorite intrusive phase with pyroxene present as groups of anhedral-subhedral small crystals. These groups of small crystals display interstitial textures whereby they fill in zones between plagioclase and larger pyroxene crystals. F.O.V.= 5mm. (JH-99-34).

Plate 3.16: Photomicrograph illustrating the dominant texture of the pre-breccia gabbro/gabbrodiorite. The main texture, as observed, is a sub-ophitic to ophitic texture whereby plagioclase crystals are partially enclosed within pyroxene oikocrysts. F.O.V = 5mm. (JH-99-175).


3.13

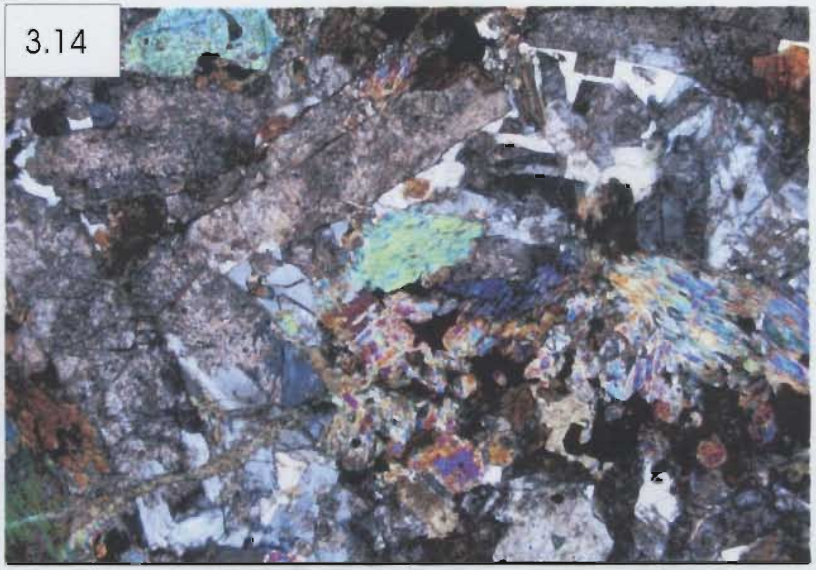
3.14


3.15


3.16

Plate 3.17: Photomicrograph of alteration within pre-brecia gabbro/gabbrodiorite. Note significant alteration of the original plagioclase to sericite (sericitization) and epidote (saussuritization), and alteration of the original pyroxene to hornblende, biotite, actinolite/tremolite, and minor chlorite/epidote. Note also the reaction corona whereby original pyroxene is surrounded by a reaction rim of hornblende and biotite. F.O.V. = 5mm. (JH-99-49b).

Plate 3.18: Photomicrograph of pre-breccia gabbro/gabbrodiorite clast separated from the breccia outcrop (Lodestar prospect). Plate illustrates a gabbroic clast in which all the pyroxenes have been altered to chlorite and the plagioclase has been totally altered to sericite. Other sections of the same clast illustrate pyroxene being altered to actinolite/tremolite/biotite. Note the anhedral, primary un-altered quartz (white/grey). Magnetite is also associated with the alteration products. F.O.V.= 5 mm. (JH-99-141e).

3.17

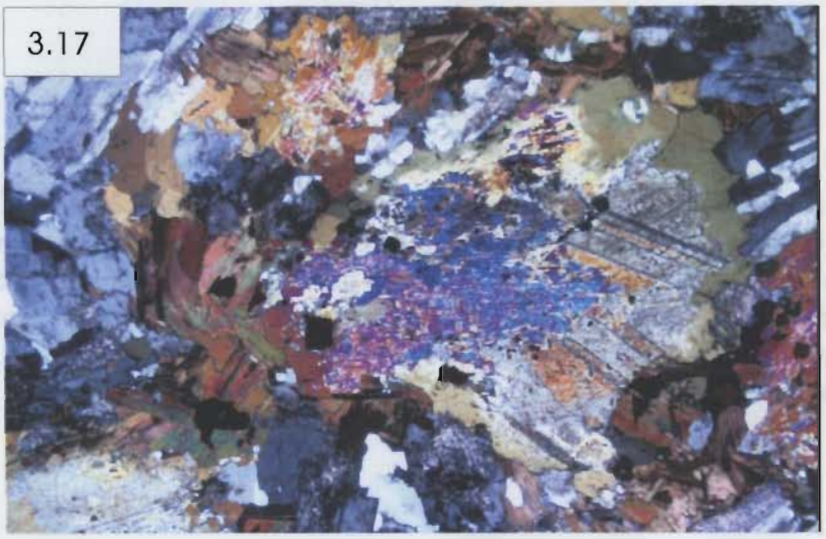

3.18

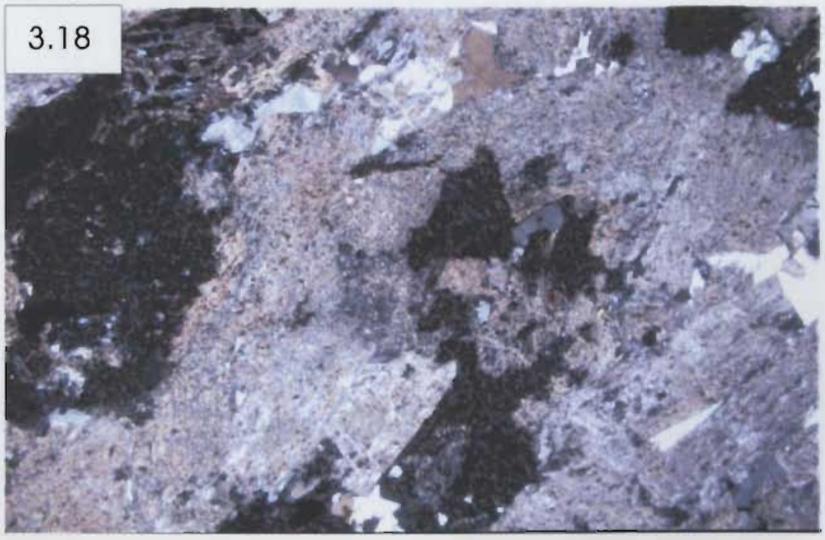

Plate 3.19 a, b: Small pre-breccia felsic dyke (white). Note in figure 3.19 a, that in the bottom portion of the plate the dyke appears to be bimodal (felsic with a more mafic component). In this area the dyke actually seems to intrude the breccia. However, in the blow-up portion of the figure, plate 3.19 b, the felsic portion of the dyke is definitely brecciated. These relationships indicate the potential of syn-breccia felsic dykes. Note the chip channel used for assay.

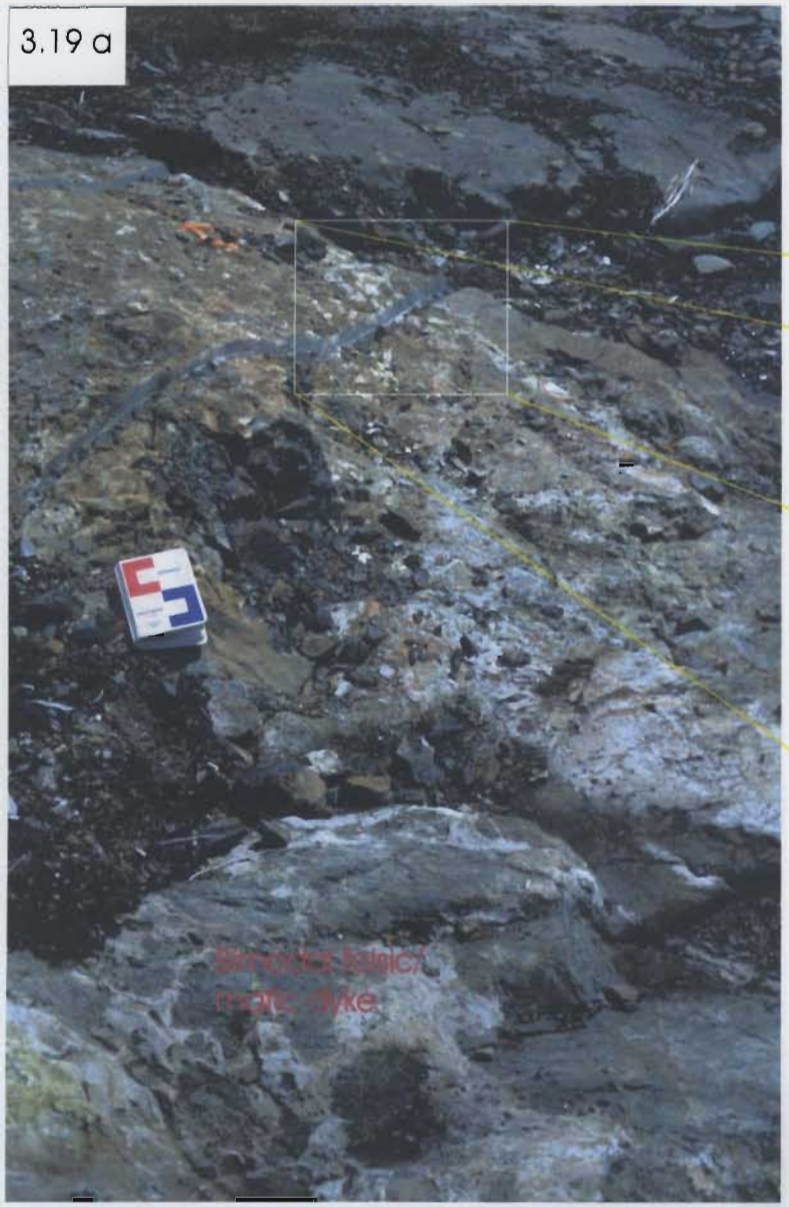
3.19 a
Brecciated felsic-mafic dyke


3.19 b
Brecciated felsic dyke
Sediments
Competent felsic dyke

Plate 3.20: Typical, homogeneous, equigranular variety of the post-breccia fine-grained gabbro-diorite. This variety of this phase of the intrusion lacks any phenocrysts and displays a pilotaxitic texture.

Plate 3.21 a: Polished slab of the massive, homogeneous post-breccia gabbro-diorite illustrating the presence of minor sulphides, dominantly pyrite (highlighted).

Plate 3.21 b: Polished slab of the plagioclase "megacryst"-bearing phase of the post-breccia fine-grained gabbro-diorite. As with all other samples of the gabbroic intrusive, this slab contains minor amounts of pyrite and magnetite.

Plate 3.22: Gabbronoritic variety of the post-breccia gabbroic intrusion. Note pilotaxitic texture and sericite alteration of plagioclase. Opaques are dominated by magnetite and pyrite. F.O.V.= 5mm. (JH-99-153)


3.20

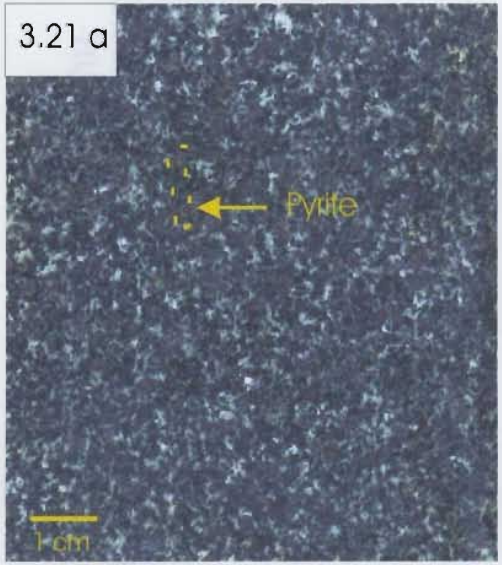
3.21 a
Pyrite
1 cm

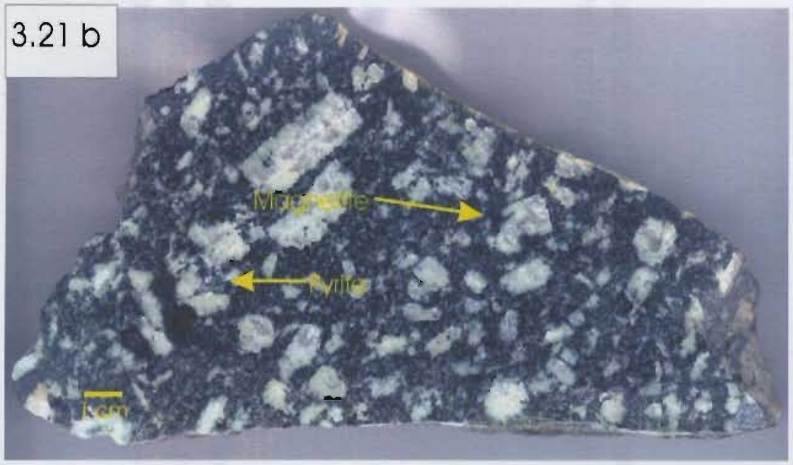
3.21 b
Magnetite
Pyrite
1cm


3.22

Plate 3.23: Accessory apatite (clear, high relief) in the post-breccia gabbro-diorite. Apatite is a common accessory phase in both the pre- and post-breccia gabbros. F.O.V.= 1.3 mm. (JH-99-146).

Plate 3.24: Pilotaxitic or trachytic texture within the post-breccia gabbro-diorite. Texture is defined by elongated, sub-parallel crystalline plagioclase crystals. F.O.V.=5 mm. (JH-99-19c).

Plate 3.25 a: Fine-grained, biotite-granite phase of the post-breccia felsic intrusive. Note the epidote (green) veinlets cutting through the sample.

Plate 3.25 b: Feldspar-quartz porphyritic phase of the post-breccia felsic intrusive. Note the biotite (black), and the greenish tint associated with some of the plagioclase and potassium feldspar due to sericite alteration.


3.23


3.24

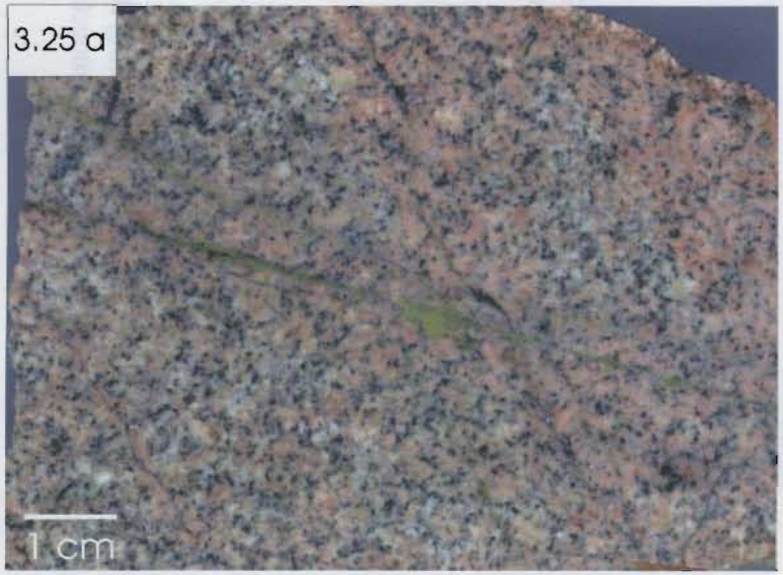
3.25 a
1 cm

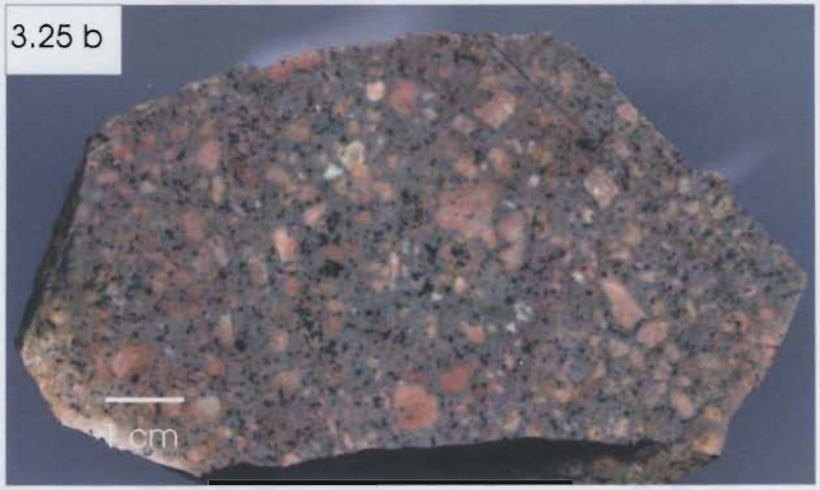
3.25 b
1 cm

Plate 3.26: Photomicrograph of granophyric texture within a very fine-grained variety of the post-breccia felsic intrusive phase. Texture is defined by crudely radiating inter-growths of quartz and alkali-feldspar. F.O.V.= 1.3 mm. (JH-99-126a).

Plate 3.27: Quartz-feldspar-hornblende porphyritic phase of the post-breccia felsic intrusive. Note euhedral hornblende in top right of photomicrograph, as well as the euhedral quartz crystal at left, and minor epidote speckled throughout. F.O.V = 5 mm. (JH-99-100).

Plate 3.28: Two post-breccia diabase dykes crosscutting each other, the mineralized breccia (above and left of field book), and the host sedimentary unit (right of the field book).

Plate 3.29: Contact relationship illustrating the post-breccia fine-grained gabbro intruding, and crosscutting the bedding within Connecting Point Group.

3.26

3.27

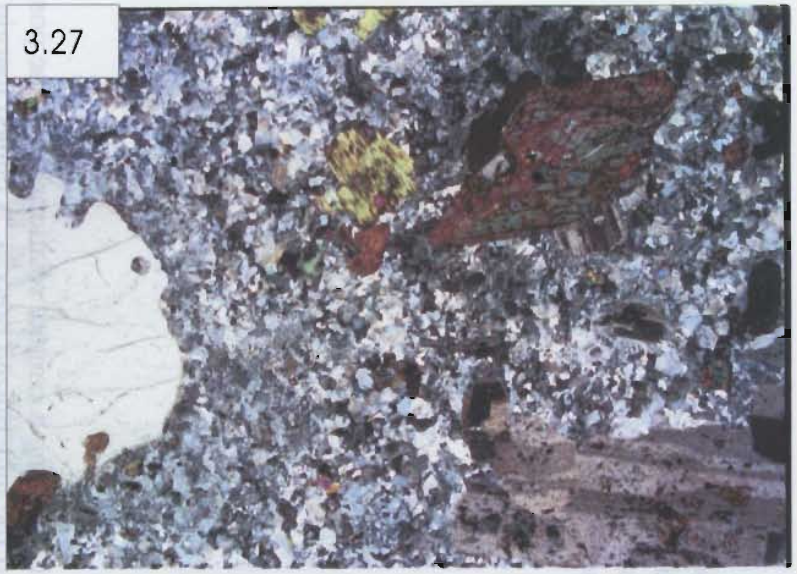

3.28

3.29

Plate 3.30: Photograph of the Lodestar breccia where the mineralization (dark brown/black) appears to be post-breccia forming a vein-like structure within the breccia. Note other patches of mineralization (brown areas) within the breccia. Fragments dominantly consist of sedimentary clasts (some with concentric banding) and gabbroic clasts.

Plate 3.31: Outcrop at the Lodestar prospect illustrating a contact relationship of the post-breccia gabbro-diorite intruding and cutting off the mineralized breccia. A chilled margin occurs within the fine-grained gabbro towards the contact with the breccia.

Plate 3.32 a: Photograph of sulphide mineralization (dominantly pyrite with some arsenopyrite) composing the matrix to the breccia.


3.30

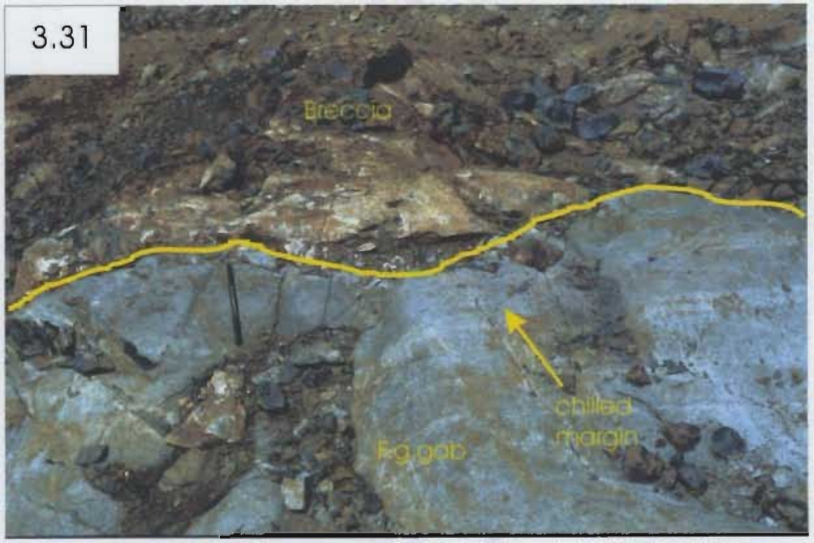
3.31
Breccia
chilled
margin
fg gab


3.32 a

Plate 3.32 b: Polished slab of Lodestar breccia. Note that the sulphide mineralization is in the form of pyrite (py) and arsenopyrite (asp) locally forming the matrix to the breccia. Dominant clasts are of the pre-breccia gabbro/gabbrodiorite (Gab. clast), host sedimentary material (Sed. clast), and one small quartz-feldspar porphyry (QFP) clast (upper right hand side of slab) rimmed by arsenopyrite.

Plate 3.32 c: Polished slab of Lodestar breccia. Matrix consists of a mixture of actinolite/tremolite/chlorite, and arsenopyrite. Dominant clast type is of the host sedimentary unit with minor gabbroic and granitic clasts.

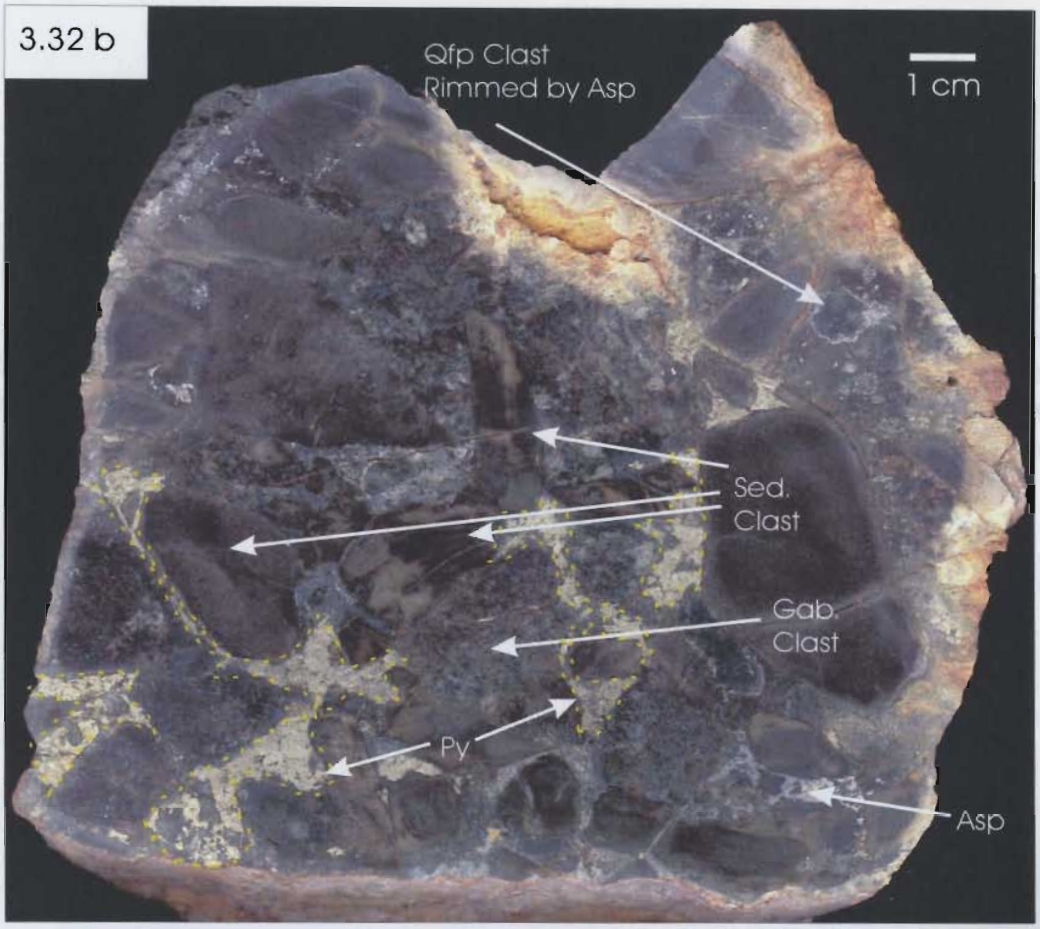
3.32 b
Qfp Clast
Rimmed by Asp
1 cm
Sed.
Clast
Gab.
Clast
Py
Asp

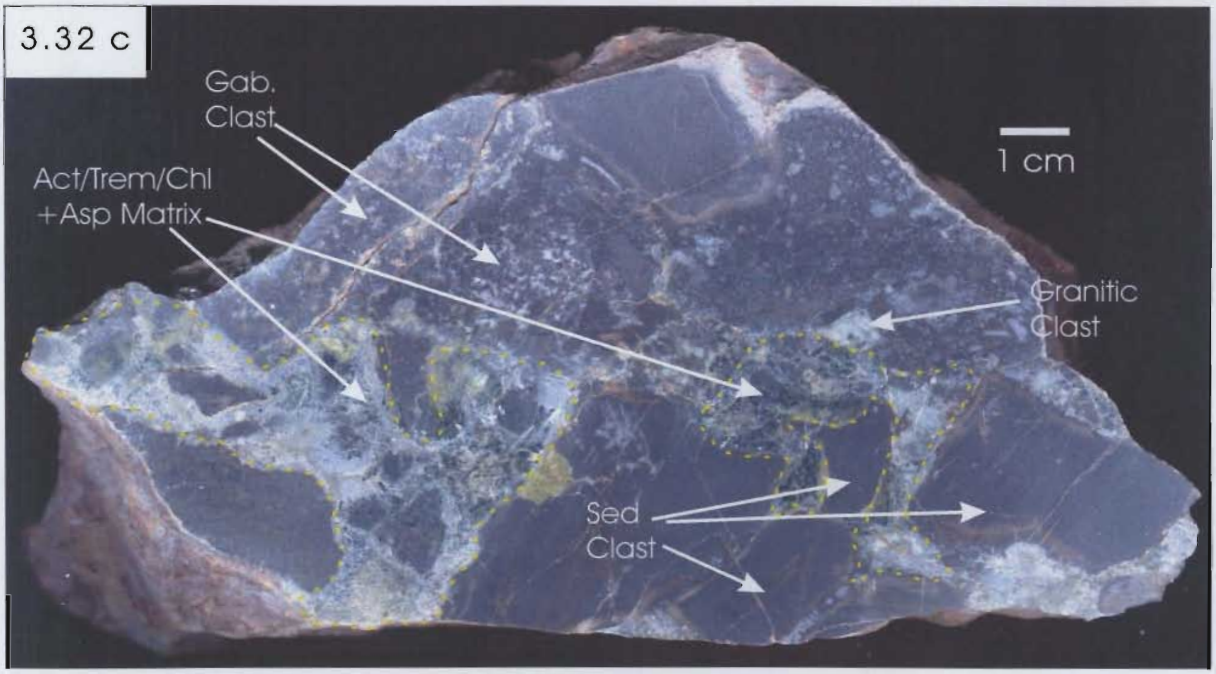
3.32 c
Gab.
Clast
Act/Trem/Chl
+Asp Matrix
1 cm
Granitic
Clast
Sed
Clast

Plate 3.32 d: Polished slab of Lodestar breccia illustrating semi-massive to massive sulphide mineralization in the form of arsenopyrite (asp) with minor pyrite (py) and chalcopyrite (cpy). Clasts consist of pre-breccia gabbro, host sedimentary clasts, and quartz-feldspar clasts. It should be noted that a portion of this sample returned assay results of 58.5 g/t Au and 25 % As.

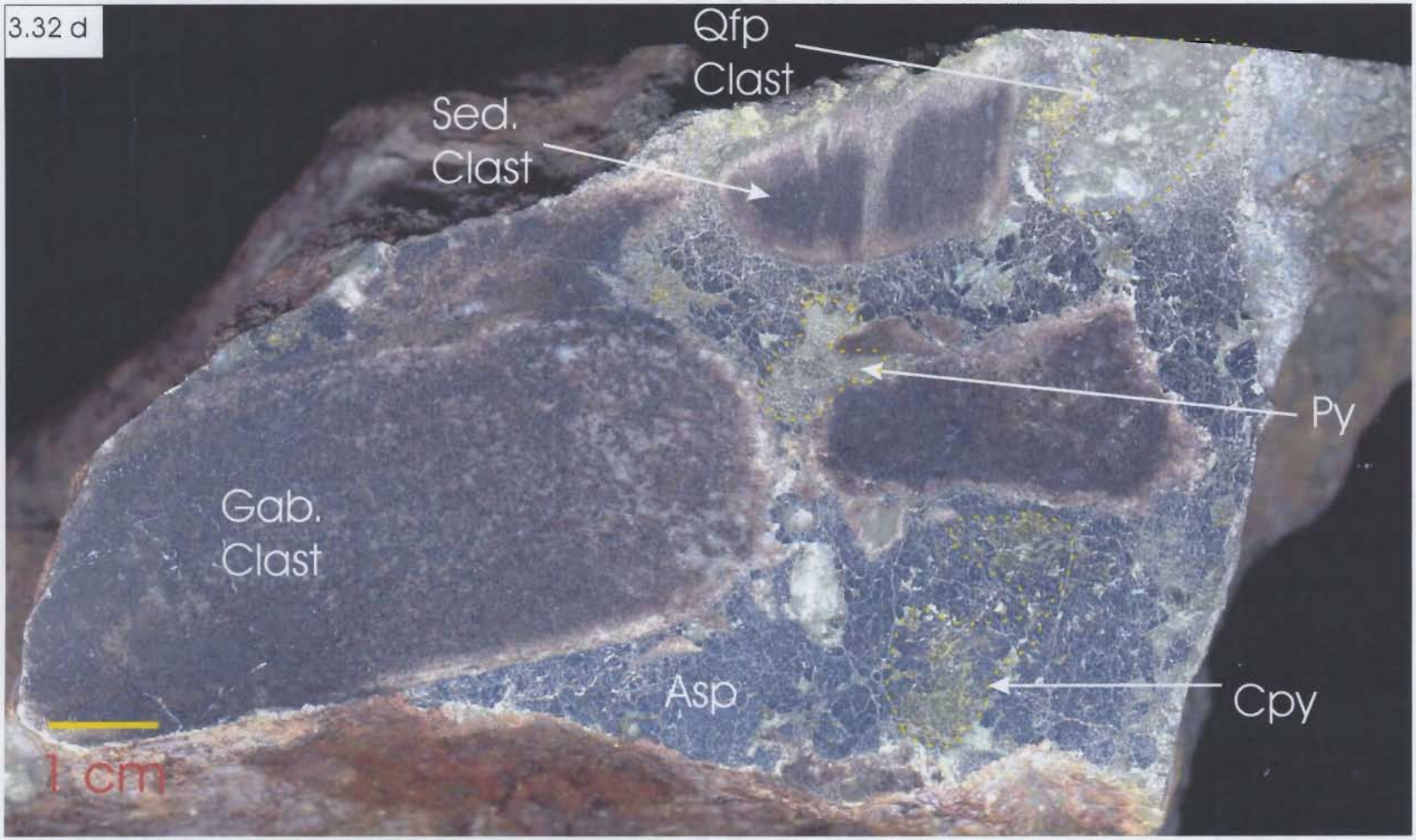
3.32 d
Qfp
Clast
Sed.
Clast
Py
Gab.
Clast
Asp
Cpy
1 cm

Plate 3.33 a: Picture of the Lodestar breccia illustrating an area with rock-flour matrix. This matrix consists of finely comminuted quartz-feldspar porphyritic (QFP) material, presumably sampled from depth and "milled" during rapid upward transport. Note the relict QFP clasts that are resistant to weathering.

Plate 3.33 b: Picture of the Lodestar breccia illustrating an area where the matrix of the breccia is dominated by chlorite. Note the cross-cutting contact relationship of the breccia with the host sedimentary unit.

Plate 3.33 c: Polished slab from a portion of the Lodestar breccia illustrating the rock flour matrix (RFM). Note all of the very finely comminuted and broken up parts of QFP clasts (light coloured crystals and fragments) that are preferentially rimmed by arsenopyrite (very-fine grained grey material associated with QFP fragments). Some of the locally derived sedimentary clasts display a "jigsaw" texture whereby individual clasts can visibly be reassembled.

3.33 a

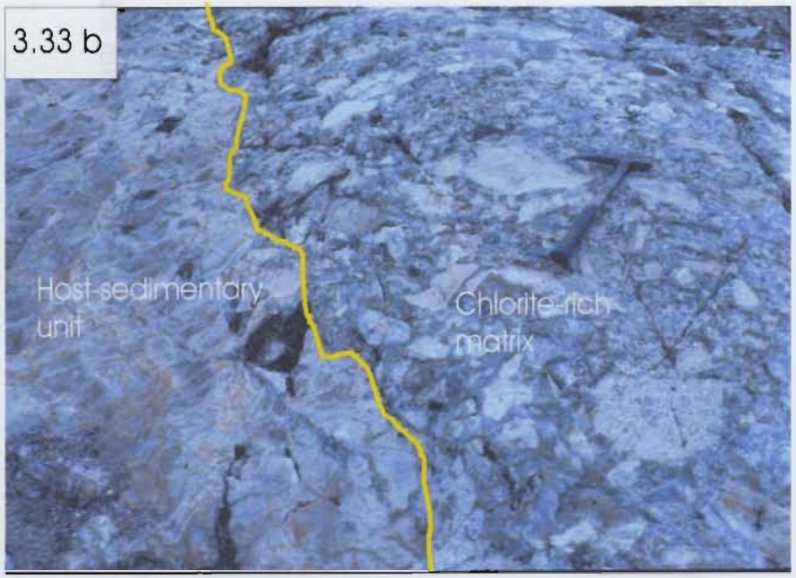

3.33 b

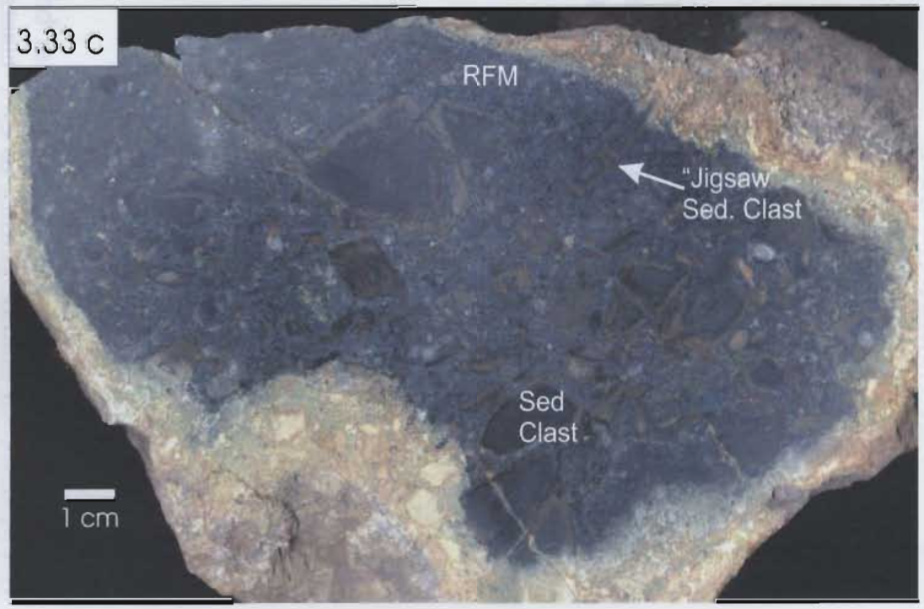

3.33 c

Plate 3.34 a-b: Examples of hydrothermal (secondary) magnetite (circled) as an interstitial phase of the matrix of the Lodestar breccia.

Plate 3.35 a: Close-up picture of the Lodestar breccia illustrating QFP clasts presumably sampled from depth. Note also the prominent pre-breccia gabbroic clast in the bottom left hand corner.

Plate 3.35 b: Polished slab of the Lodestar breccia. Clast type varies from gabbroic, to sedimentary, to granitic (Grn.), to QFP clasts (locally rimmed by arsenopyite); whereas the matrix consists of sulphide mineralization (pyrite and arsenopyrite) and actinolite/tremolite/chlorite.


3.34 a

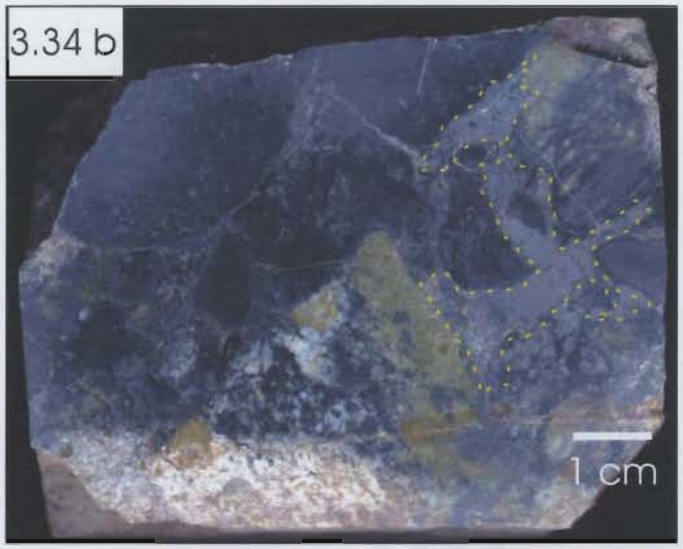
3.34 b
1 cm


3.35 a

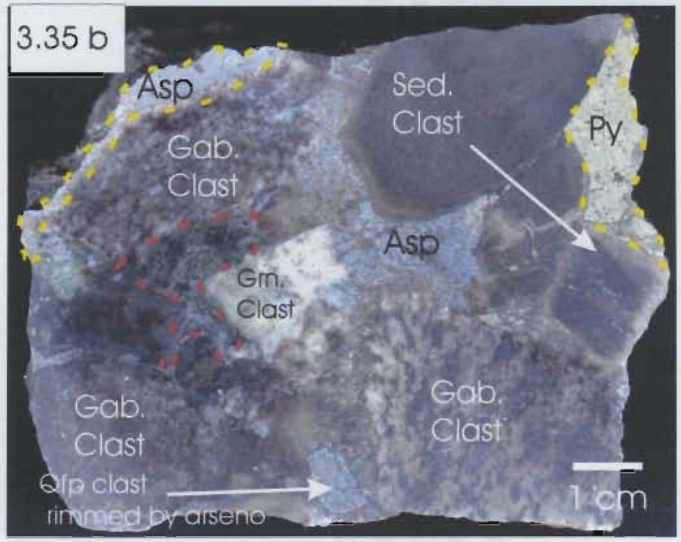
3.35 b
Asp
Gab.
Clast
Sed.
Clast
Py
Asp
Gm.
Clast
Gab.
Clast
Gab.
Clast
Qfp clast
rimmed by arseno
1 cm

Plate 3.35 c: Large polished slab of the Lodestar breccia. Clast types consist of pre-breccia gabbro, host sedimentary material, QFP clasts, and one small granitic clast (right center). Mineralization (arsenopyrite and pyrite) forms part of the matrix, and arsenopyrite is also intimately associated with (rimming and overprinting) the QFP clasts. Minor chalcopyrite is also present.


3.35 c
2 cm
Minor chalcopyrite
Granitic clast
Qfp. Clast rimmed/ overprinted by arsenopyrite
Gab. Clast
Sed. Clast
Qfp. Clast

Plate 3.36: Polished slab of the Lodestar breccia illustrating both "jigsaw" puzzle texture of some of the locally derived sedimentary clasts and mineralization filling small cracks or fractures within granitic clasts (Bottom right). It has been proposed that some of this mineralization filling in these fractures may be of pre-breccia origin.

Plate 3.37: Crenulate or ptygmatically folded quartz layers (unidirectional solidification texture) observed in some of the QFP clasts from the Lodestar breccia; commonly referred to as "brain-rock".

Plate 3.38: Photograph illustrating juxtaposed mineralized and essentially non-mineralized "blocks" of breccia within the Lodestar prospect. This relationship could infer re-brecciation of the original breccia or faulting within the breccia; or it could just be an artifact caused by localized inflow of mineralizing fluid pulses into the breccia.

Plate 3.39: Alteration texture observed within some sedimentary clasts whereby the clasts have alteration rims of sericite and biotite.

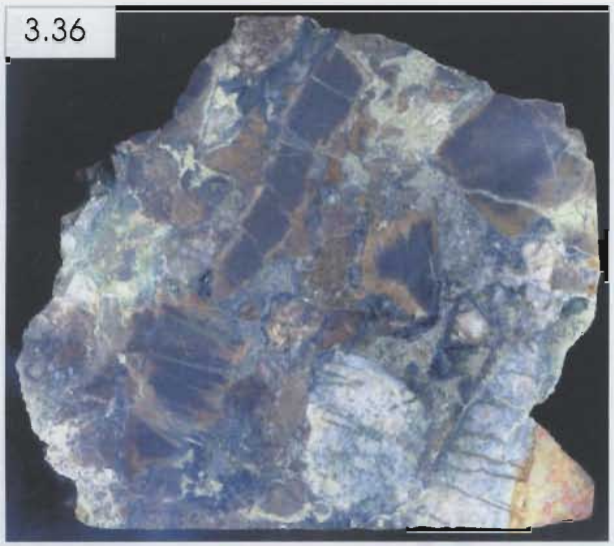
3.36


3.37


3.38


3.39

Plate 3.40: Recrystallized quartz veining observed throughout the breccia. These veins are locally associated with mineralization, thereby indicating that the quartz is secondary. Some secondary fluid inclusions are associated with these veins, however, they are uninformative. F.O.V. = 8.45 mm. (JH-99-min3).

Plate 3.41: Photomicrograph of a QFP clast from the Lodestar breccia. Note the euhedral porphyritic quartz crystals within the fine grained background dominated by quartz and recrystallized quartz, and the disseminations of arsenopyrite (opaque) within the clast. F.O.V. for all plates = 5mm. All photomicrographs from JH-99-141a.

Plate 3.42: Photomicrograph illustrating a common texture associated with QFP clasts whereby the clast is rimmed by a discontinuous 1-3 mm rim of arsenopyrite, and is also locally (bottom right of clast) overprinted by arsenopyrite. F.O.V = 5mm (JH-99-RFM).

Plate 3.43: Photomicrograph of typical actinolite/tremolite/mineralization matrix within the Lodestar breccia. F.O.V.= 8.45 mm. (JH-99-MAT).

3.40

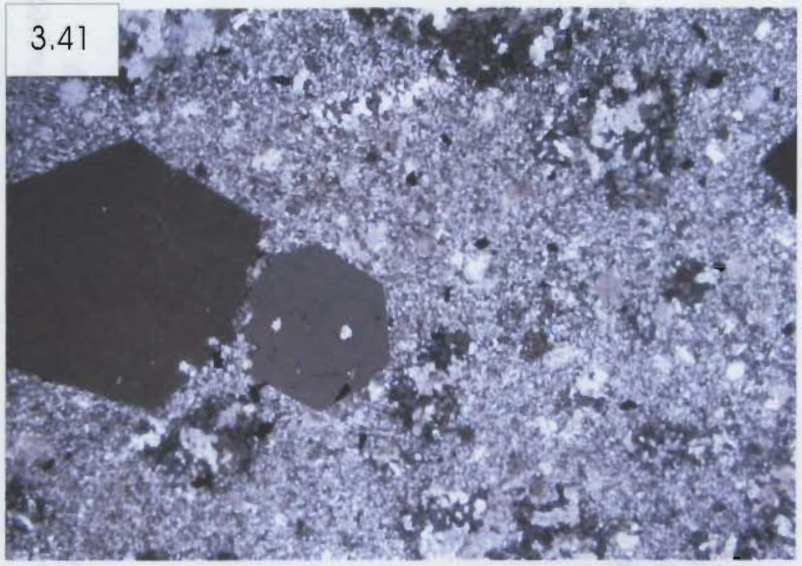

3.41

3.42

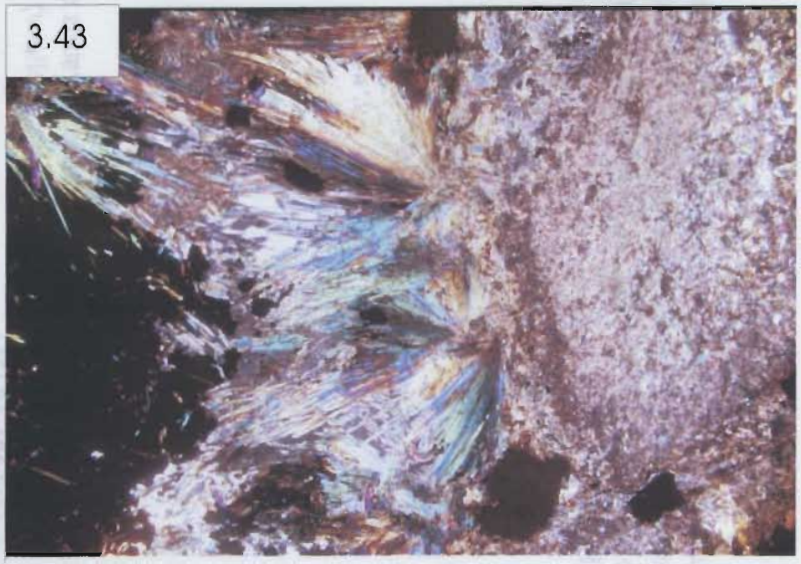

3.43

Plate 3.44: Photomicrograph of rock flour matrix, in contact with a sedimentary clast, associated with the Lodestar breccia. The rock flour matrix (RFM) consists of comminuted quartz crystals (white) within finely "milled" rock fragments. F.O.V.= 5mm. (JH-99 141 I).

Plate 3.45 a, b: Small, sub-euhedral crystals of arsenopyrite (white) intergrown with sphalerite (grey). Note chalcopyrite (yellow) "disease" within the sphalerite. F.O.V.=0.65 mm. (JH-99-141H).

Plate 3.45 c: Large euhedral crystal of arsenopyrite (right side of photo) crosscutting actinolite/tremolite matrix. Note that the same matrix is observed to crosscut pyrite (left side of photo). F.O.V.=5mm. (JH-99-MAT).

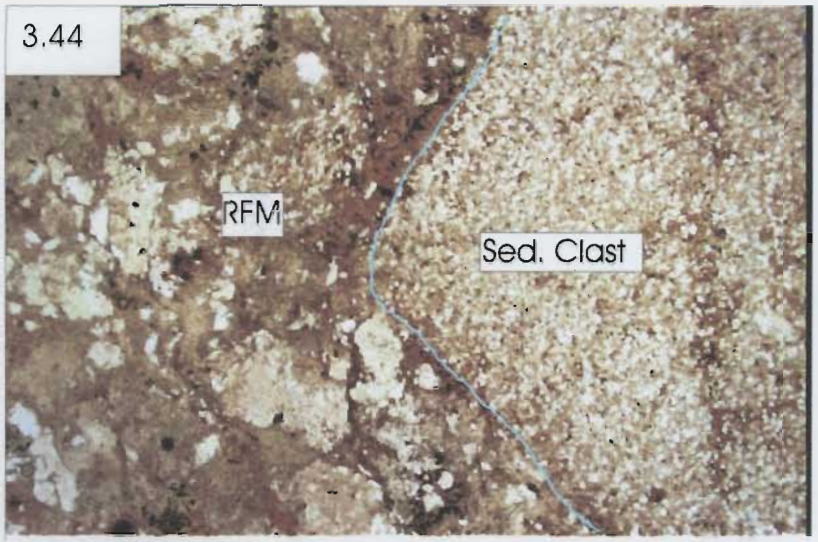
3.44
RFM
Sed. Clast

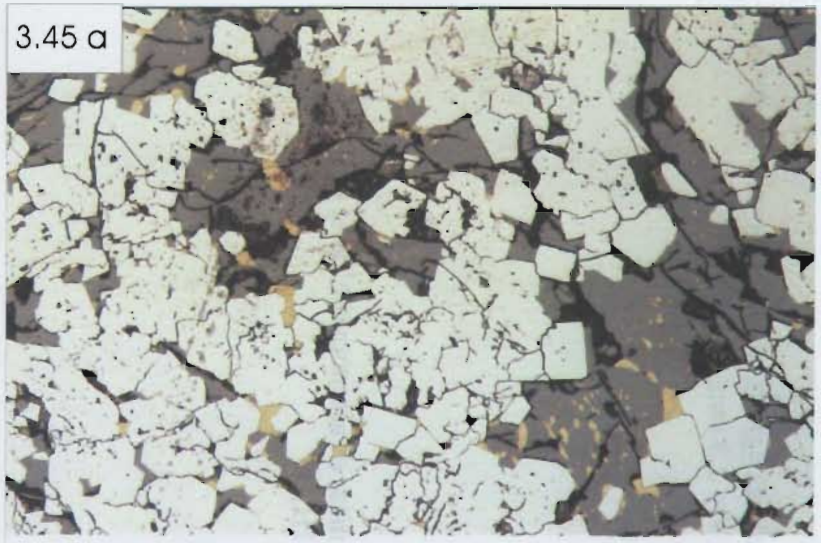
3.45 a


3.45 b


3.45 c

Plate 3.45 d: Coeval arsenopyrite (white), sphalerite (grey), and chalcopyrite (yellow) within the matrix of the Lodestar breccia. F.O.V.= 1.3 mm. (JH-99-MIN4).

Plate 3.45 e: Matrix consisting of an anhedral mass of arsenopyrite (left) and actinolite/tremolite. F.O.V.= 5mm. (JH-99-141H).

Plate 3.45 f: Textural relationship between massive arsenopyrite (white) and chalcopyrite (yellow) whereby chalcopyrite fills small fractures or cracks within the arsenopyrite. F.O.V.= 1.3 mm. (JH-99-MIN7).

Plate 3.45 g: Contact between pyrite (yellow-white) (right hand side of photo) and arsenopyrite (white) (left hand side of photo). Note interstitial chalcopyrite (bright yellow). F.O.V. = 1.3 mm. (JH-99-141H).

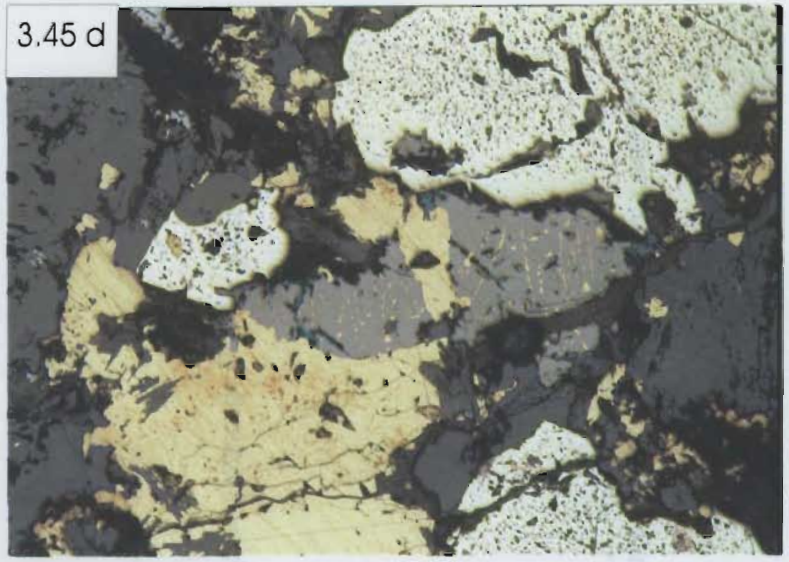
3.45 d

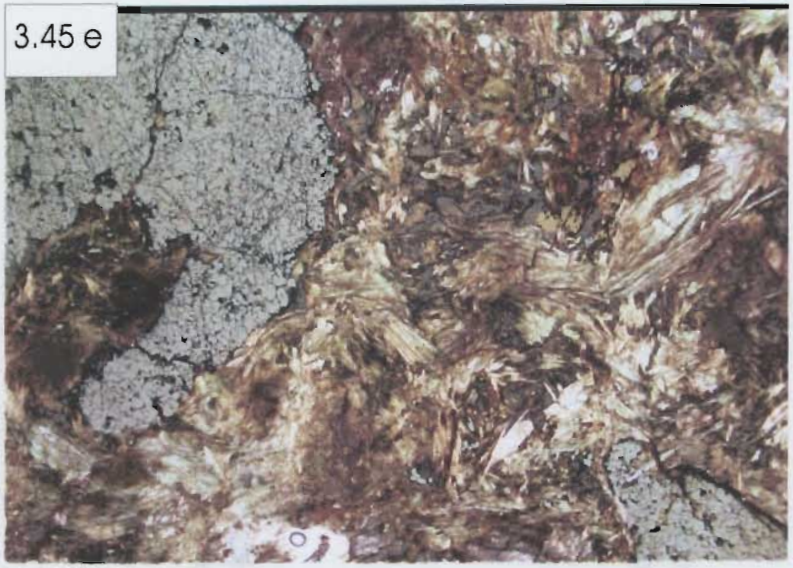
3.45 e

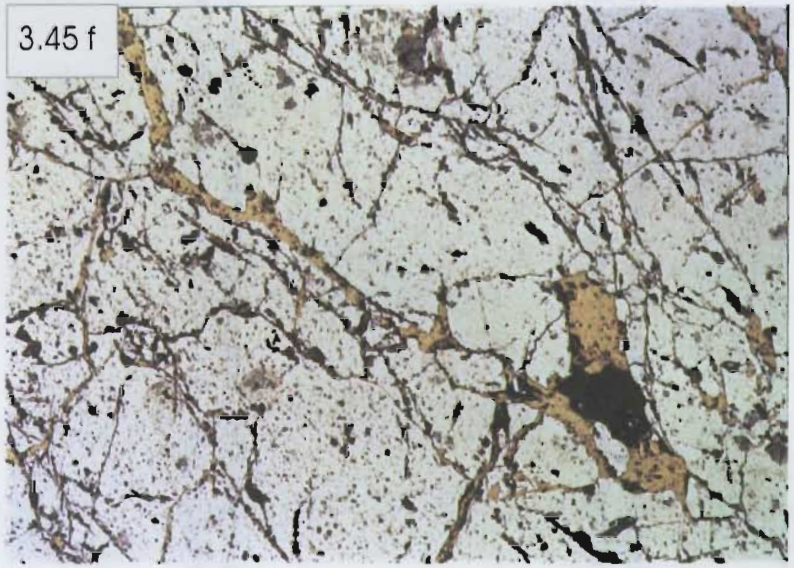
3.45 f

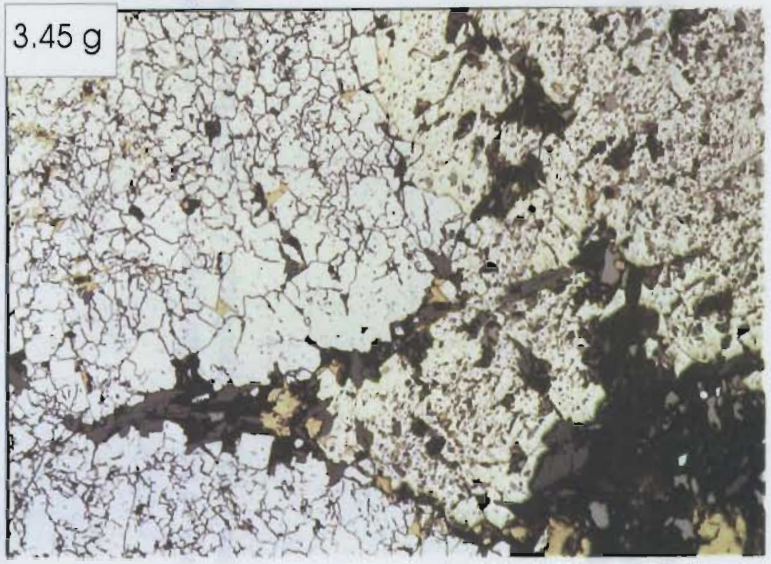
3.45 g

Plate 3.46 a: Contact relationship between pyrite (dark) and chalcopyrite (bright area) whereby chalcopyrite appears to "eat" away and intrude pyrite. F.O.V.= 1.3 mm. (JH-99-MIN8).

Plate 3.46 b: Chalcopyrite (yellow)- pyrite (yellow-white)- sphalerite (grey) vein cutting massive arsenopyrite (white). F.O.V.=0.65 mm. (JH-99-MIN7).

Plate 3.47 a: Contact relationship between sphalerite (grey), arsenopyrite (white), chalcopyrite (yellow) and gangue (dark). F.O.V. = 5mm. (JH-99-MIN1).

Plate 3.47 b: Chalcopyrite (yellow) disease within sphalerite (grey). Texture is a product of exsolution. F.O.V.= 1.3 mm. (JH-99-MIN1).

3.46 b
3.47 b
3.46 a
3.47 a

Plate 3.48: Covellite as a secondary oxidation product of sulphides (sphalerite and chalcopyrite). F.O.V.= 1.3 mm. (JH-99-BOR).

Plate 3.49: Textural relationship whereby chalcopyrite (yellow) appears to be exsolved from arsenopyrite (white) and sphalerite (grey) appears to cross-cut arsenopyrite, indicating that in this area arsenopyrite formed first followed by chalcopyrite and sphalerite. F.O.V.= 1.3 mm. (JH-99-MIN1).

Plate 3.50: Textural relationship whereby it appears as though arsenopyrite (white) has exsolved from, or is disseminated within, chalcopyrite (yellow). F.O.V.= 1.3 mm. (JH-99-MIN1).

Plate 3.51: Evidence of syn-formation of the major sulphide phases of arsenopyrite (white), chalcopyrite (yellow), and sphalerite (grey). F.O.V.= 1.3 mm. (JH-99-MIN 1).

3.49
3.51
3.48
3.50

Plate 3.52 a-b: Photomicrographs (ppl and xpl) illustrating a zonation or regular distribution of alteration phases moving from the matrix to the clasts. Mineralized matrix makes up the central portion of the matrix (top of plates). Moving down the page, towards the clast, the sulphide mineralization is followed by actinolite/tremolite +/- chlorite/epidote, increasing sericite/biotite, and finally the clast itself. F.O.V. from top to bottom of plates = 12 mm. (JH-99-141H).


3.52 a
Mineralization
Act/Trem
Act/Trem
+/- Chl/epidote
Increasing Sericite/
biotite
Sed clast

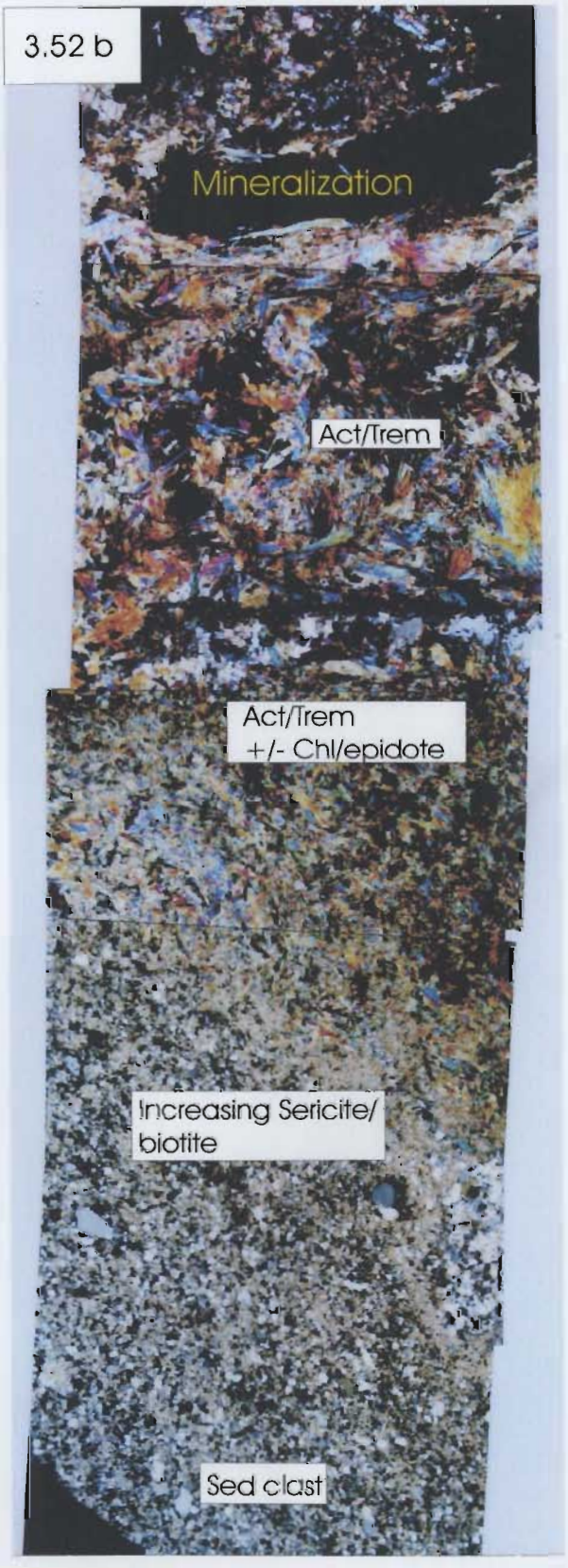
3.52 b
Mineralization
Act/Trem
Act/Trem
+/- Chl/epidote
Increasing Sericite/
biotite
Sed clast

Chapter 4: Major, Trace, and Rare-Earth Element Geochemistry of the PHIS and associated Lodestar Prospect, Isotope Geochemistry and Geothermometry of the Lodestar Mineralization, and the Nature of Invisible Gold.

4.1: Introduction

Derivation of major, trace, rare-earth element (REE), isotopic, and microanalytical geochemical data is very important for understanding the petrology and petrogenesis of different rock types within a given area. The initial focus of this chapter is to discuss the major, trace, and REE chemistry of the various phases of the PHIS and the mineralized breccia (Lodestar showing) associated with the intrusion. The three main phases of the intrusion will be examined in detail; they will be distinguished through the use of chemistry, and some explanation of mass gain/loss related to alteration will be given. In terms of the breccia showing, the main goals of the geochemical study are to link some of the clasts within the breccia to the surrounding host rocks and intrusive phases, and to study the chemical correlations or affinities of various elements (ie. Au-As) present within mineralization. Further work includes derivation of sulphur isotope ratios, geothermometry calculations (based upon sulphur isotope and arsenopyrite geothermometers), and laser-ablation-microprobe inductively coupled mass spectrometry (LAM-ICP-MS) studies on the nature of "invisible-gold" within the showing.

Throughout the course of this geochemical study, several sets of geochemical data were collected using a variety of analytical techniques. The first set of chemical data were

derived from Au + 33 instrumental neutron activation analysis (INAA)(conducted at Activation Laboratories in Ontario): the results of which are useful for precise gold determinations in mineralized samples. Major and trace element analysis were subsequently completed via inductively coupled plasma emission spectrometry (ICP-ES), at the Newfoundland Department of Mines and Energy (NDME) Laboratory in St. John's Newfoundland. Additional major and trace element analyses were completed on pressed-powder pellets in the X-ray Fluorescence (XRF) facilities at Memorial University of Newfoundland, following the methods outlined by Longerich (1995). The REE were analyzed by inductively-coupled plasma mass-spectrometry (ICP-MS) following the HF/HNO3 preparation method of Jenner et al. (1990). All analytical methods were compared and contrasted with respect to detection limits, accuracy, and precision to determine which analytical method was best for each element; after which best data were compiled into one geochemical data set. Sulphur isotope analysis was carried out using a Carlo Erba automatic gas chromatographic elemental analyzer coupled to an isotope ratio mass spectrometer, in this case a Finnigan MAT 252 Isotope Ratio Mass Spectrometer at the Department of Earth Sciences laboratory. Arsenopyrite geothermometry analysis was conducted using a 1991 Cameca SX-50 electron microprobe, also housed in a laboratory at the Department of Earth Sciences; and lastly, studies of the "invisible" nature of gold within the Lodestar prospect were conducted using an in-house built LAM-ICP-MS at the Department of Earth Sciences. Details regarding these analytical techniques and tables of results, including sampling protocol, elements analyzed, analytical methods, precision,

and accuracy of each method are outlined in appendix A and B.

Care must be taken, as always, when chemically analyzing plutonic rocks. Due to processes such as fractional crystallization and crystal accumulation, the rocks usually do not represent the original liquid composition, thereby introducing difficulties in data interpretation. This discussion, however, has attempted to overcome this difficulty by choosing appropriate geochemical plots which eliminate the effects of cumulate formation and fractionation.

For the purposes of the following geochemical investigations, it should be noted that a wide range of samples from each phase of the PHIS were analyzed; consisting of: nine pre-breccia medium-grained gabbro/diorite samples, fifteen post-breccia, fine-grained gabbro/diorite samples, twelve felsic material samples, three diabase dyke samples, two sedimentary material samples, three felsic clast samples separated from the breccia, three gabbro clast samples separated from the breccia, and ten mineralized breccia samples. Only the three major phases of the intrusion, the breccia clasts, and the mineralized samples will be dealt with in detail; and no detailed examination of diabase or the host sedimentary material was carried out. A summary of the geochemical data, including averages; standard deviations; maximum and minimum values of each element analyzed in each unit are given in table 4.1, with detailed results listed in appendix B.

4.2 Powder Horn Intrusive Suite Rocks

4.2.1 Discrimination Diagrams

As a first order evaluation of the Powder Horn Intrusive Suite, all samples were plotted on major and trace element discrimination diagrams in an attempt to determine geochemical affinities. It should immediately be noted that for both the major and trace element discrimination diagrams, and the following variation diagrams, samples of breccia clasts are plotted, however they will not be dealt with until a future section (section 4.3) on the breccia showing itself. Major element discrimination plots used were the AFM and total alkalis vs silica (TAS) diagrams of Irvine and Baragar (1971), and Jensens' (1976) cation plot. Plotted trace element discrimination plots were from Winchester and Floyd's (1977) Nb/Y vs Zr/TiO_2 and Zr/TiO_2 vs SiO_2 diagrams. These plots, although commonly used in the study of plutonic and cumulate lithologies, are actually intended for the classification of volcanic rocks which accurately and reliably represent liquid compositions. The plots are not meant to be used with plutonic rocks involving cumulate, or phenocrystic phases; therefore many of the trends observed simply indicate relative proportions of minerals such as plagioclase (rich in CaO, Na_2O and Al_2O_3) and pyroxene (rich in MgO and FeO). It should also be noted that the fields outlined in the diagrams have no meaning in the context of the plutonic rocks studied in this thesis. Using the plots with these limitations in mind, they provide very useful cursory information on the geochemical affinities and similarities in chemical compositions.

The three major element discrimination plots illustrate relatively close clustering within each of the three main plutonic phases consisting of the pre-breccia gabbro/gabbrodiorite, the post-breccia gabbrodiorite, and felsic intrusive units. On the AFM plot (figure 4.1) there is a clear division between the phases with the fine-grained, post-breccia gabbrodiorite plotting in the tholeiitic part of the diagram, thereby indicating that it constitutes a more mafic composition than the medium-grained gabbro/gabbrodiorite which plots slightly below the tholeiitic field, in the calc-alkaline field; as would be expected, the felsic unit plots down in the $Na_2O + K_2O$ corner of this diagram. Jensen's cation plot (figure 4.2) also separates the plutonic phases into individual clusters of data. Both plots illustrate similar data groupings whereby the clusters indicative of each rock type define a crude trend propagating from the $Na_2O + K_2O$ and Al_2O_3 apexes towards the FeO* (+TiO_2) sides of the diagrams. These trends simply reflect varying proportions of plagioclase to mafic minerals (ie. pyroxenes) within the various plutonic phases. The TAS plot (figure 4.3) illustrates similar divisions between the rock types whereby the fine-grained, post-breccia gabbro-diorite data is clustered in the alkaline field, with the pre-breccia gabbro/gabbrodiorite clustered below the dividing line in the subalkaline field, and finally the felsic material plotting in the SiO_2 rich portion of the subalkaline field. Based upon an earlier version of TAS devised for volcanic rocks by Cox et al. (1979), Wilson (1989) used the TAS diagram for preliminary classification of plutonic rocks. Using his classification, the intrusive phases

are defined as follows:1) the pre-breccia mafic unit is classified as gabbro/diorite, 2) the post-breccia mafic unit is classified as gabbro, 3) and the post-breccia felsic unit is classified as granite/granodiorite. Although most samples from the individual rock types plot in relatively confined clusters, there are some exceptions whereby some samples appear to be separated from the others (ie. a felsic sample plotting in the alkaline field on the TAS diagram), irregularities which will be dealt with in a later section.

The trace element discrimination plots of Winchester and Floyd (1977) are based on the incompatible/immobile trace elements of Zr, Nb, Y, as well as TiO_2 and SiO_2 (figures 4.4 a, b). Both of these plots illustrate distinct chemical differences between the three main rock types (eg. figure 4.4 a illustrates an important difference in that the post-breccia gabbroic phase is definitely more alkalic than the pre-breccia gabbroic phase). However, as with the major element discrimination plots, it should be noted that these diagrams are used only as a primary method of distinction and their labels and fields are not applicable.

4.2.2 Major element variation diagrams

Due to the variations observed both petrographically and in outcrop between the phases of the PHIS, it was difficult to choose a single index with which to measure fractionation trends and mineralogical trends within the intrusive suite. The major purpose of variation diagrams is to illustrate chemical variation between samples and to identify trends in the data; hence the "variation" element plotted on the x-axis should be selected to show maximum variability between samples and/or to show a particular trend

in the data. Normally this variation element would be the oxide which shows the greatest range in the data set, usually SiO_2. However, for the purposes of this investigation, two fractionation indices were used to completely decipher the data. These indices consist of SiO_2 and MgO. The Mg number ([Mg]) fractionation index was also investigated, however it was found to be non-diagnostic. By using the two indices, the chemical variations associated with the variable intrusive lithologies, ranging from strictly gabbro to aplite, is sufficiently covered and realized.

4.2.2.1.1 SiO_2 versus Major Element Plots (Harker Diagrams).

Harker diagrams represent one of the most common methods for the display of major element data. Most igneous rock suites, including the Power Horn Intrusive Suite, have variable SiO_2 contents since SiO_2 is typically the major constituent of the rock. Within this geochemical investigation, Harker diagrams proved to be very useful in providing information about variation in the different rock types, including fractionation and mineralogical trends. Under conditions of hydrothermal alteration and medium-high grades of metamorphism, SiO_2 is mobile, making it of little use in geochemical investigations; however, with the low grades of metamorphism and the lack of any widespread hydrothermal alteration associated with the PHIS, SiO_2 can be considered to be a reliable index of fractionation. The major oxides of Fe_2O_3, TiO_2, MgO, MnO, CaO, K_2O, Na_2O, and Al_2O_3, all of which are variably controlled by mineralogical compositions, were plotted against SiO_2. The three main phases of the PHIS have significantly different wt % of SiO_2 ranging as follows: 1) pre-breccia medium-grained

gabbro/diorite (SiO_2= 46.91-56.97 wt%, avg=51.2 wt %, std=2.7, n=9), 2) post-breccia gabbro/diorite (SiO_2 = 40.03-46.44 wt %, avg=43.62 wt %, std=1.74, n=15), and 3) post-breccia felsic material (SiO_2= 59.18-77.66 wt%, avg = 74.07 wt %, std=5.02, n=12), (Table 4.1).

The plots of SiO_2 versus Fe_2O_3, TiO_2, MgO, and MnO are controlled by the presence of mafic minerals, dominantly pyroxenes; and all four of these plots (figures 4.5 a-d) show well developed trends with negative slopes whereby the post-breccia fine-grained gabbro diorite plot high in the low-silica end of the diagrams and the felsic material plots low on the diagrams on the high-silica end. The plot of SiO_2 versus Fe_2O_3 (pre-breccia gabbro/diorite Fe_2O_3 = 8.77-12.94, post-breccia gabbro/diorite= 12.71-18.66, felsic material= 0.92-4.66) illustrates the most prominent, mafic mineral dependant trend (figure 4.5 a). The strong negative trend observed in this plot results from the separation of the relatively mafic, post-breccia gabbro/diorite, from the less mafic (more dioritic) pre-breccia gabbro diorite and the felsic material; thereby defining a continuum between the quartz rich felsic material, through to the "dioritic" pre-breccia mafic phase, and finally to the more mafic-rich post breccia gabbroic phase of the PHIS. The plots of SiO_2 versus MgO and MnO (values given in table 4.1) (figure 4.5 b,c) yield similar trends to that of SiO_2 versus Fe_2O_3, again explained by the proportion of mafic minerals (dominantly pyroxene) present in each phase. However, the plot of SiO_2 versus TiO_2 is slightly more random than the previous plots (figure 4.5 d). Within this plot there is significantly more variation of values within each rock type (pre-breccia medium-grained

gabbro/diorite TiO_2 = 0.724-1.472, avg=1.04, std=0.25; post-breccia fine-grained gabbro/diorite = 2.03-3.89, avg= 3.05, std=0.58; felsic material = 0.046-0.409, avg= 0.174, std= 0.138), however, a logarithmic shaped fractionation trend can still be identified. The variation in this diagram is attributed to the variation in the amount of Ti in minerals such as pyroxene, and the variable amount of oxides associated with the gabbroic phases of the PHIS.

The plots of SiO_2 versus CaO, K_2O, Na_2O, and Al_2O_3 (figures 4.5 e-h) are dominantly controlled by feldspars, both plagioclase and potassium feldspar. The plot of SiO_2 versus CaO (figure 4.5 e) (pre-breccia medium-grained gabbro/diorite CaO = 5.78-10.83, avg = 8.13, std = 1.51, post-breccia fine-grained gabbro/diorite= 5.17-9.13, avg = 7.63, std = 1.07, felsic material = 0.17-8.03, avg = 1.30, std = 2.06) shows a similar negative trend to the plots of SiO_2 versus Fe_2O_3, TiO_2, MgO, and MnO (figure 4.5 a-d), with the difference that this trend is controlled by the proportions of feldspar (plagioclase), and to a lesser extent the proportions of clinopyroxene present. (It should be noted that the relatively high standard deviation associated with the CaO values for the felsic material is linked to one felsic sample (JH-99-061) which has significant plagioclase feldspar associated with alkali-feldspar, minor quartz and significant epidote alteration. This sample raises the maximum values and standard deviations of the felsic material when dealing with such elements as CaO, Al_2O_3, Sr, and Ga. However, the trends associated with the felsic data are not significantly affected by this sample and are considered reliable). In this plot, the post-breccia gabbro/diorite plots relatively high

(avg=7.63 wt %) at the low SiO_2 end (avg = 43.62) of the plot, indicating relatively high proportions of Ca-rich feldspar (plagioclase), relative enrichment in clinopyroxene compared to orthopyroxene, and low proportions of quartz. The pre-breccia, medium-grained gabbro/diorite plots at approximately the same level with respect to CaO (avg = 8.13 wt %) again resulting from relatively high proportions of plagioclase and clinopyroxene, but it contains elevated levels of SiO_2 compared to the post-breccia mafic unit, thereby indicating increased proportions of quartz (more dioritic). As would be expected, the felsic material plots low with respect to CaO at the high SiO_2 end of the diagram, indicating that it contains the lowest amount of Ca-rich feldspar (plagioclase) and the highest proportions of quartz. It should be noted that although each phase of the intrusion has well defined clusters of data with respect to SiO_2, there is some variation in the sets of data with respect to CaO. This variation is explained by element mobility due to the breakdown of some Ca-rich feldspars and clinopyroxenes into alteration products such as sericite and amphibole/chlorite, thereby decreasing the proportion of Ca in altered samples.

Unlike the other Harker diagrams, the plots of SiO_2 versus K_2O and Na_2O (figures 4.5 f,g) have trends with variable positive slopes, whereas the plot versus Al_2O_3 (figure 4.5 h) has a scatter of data points. The plot versus K_2O illustrates the most pronounced positive slope trend whereby both the pre- and post-breccia gabbroic phases plot with relatively low proportions of K_2O (avg = 1.14 and 1.01 wt % respectively) at the low SiO_2 end of the diagram, whereas the felsic material plots with relatively high proportions

of K_2O (avg = 4.11 wt %) at the high SiO_2 end of the diagram. The trend in this plot is directly attributable to proportions of primary alkali-feldspar and biotite, as well as secondary sericite present in the intrusive phases. The plot versus Na_2O displays a slight positive (to flat) slope whereby the pre- and post-breccia gabbro/diorite phases have average Na_2O values of 3.06 and 3.30 respectively, whereas the felsic material has an average Na_2O of 4.39 wt %. The trend observed in this plot is related to proportions of Na-rich feldspar and alteration products, dominantly in the form of sericite.

The plot of SiO_2 versus Al_2O_3 (figure 4.5 h) does not illustrate any obvious trend in the data. Although there is still a relatively tight cluster of data associated with each intrusive phase, there is no overall trend. The gabbro/dioritic phases have higher proportions of Al_2O_3 than the felsic material, due to increased proportions of plagioclase, and therefore increased sericite (Al-rich) as an alteration product. The Al_2O_3 present in the felsic phases is related to the proportion of the alkali-feldspar present.

SiO_2 versus P_2O_5 illustrates that the post-breccia gabbro/diorite has substantially higher levels of P_2O_5 (avg = 0.40) than in the pre-breccia gabbro/diorite (avg = 0.210) or the felsic material (avg = 0.04); an expected observation due to the significantly higher amounts of apatite observed petrographically in this unit.

4.2.2.1.2 SiO_2 versus trace elements (Harker diagrams)

In order to conduct a check on the behavior of the major elements, and to carry out more detailed geochemical studies, trace elements were selected to plot against the SiO_2 index. Similar to the major element plots, these plots are used to illustrate

fractionation trends as well as effects of mineral phases and assemblages upon geochemical trends. For the purpose of this trace element investigation, SiO_2 was plotted against the trace elements of Sc, V, Y, Sr, Rb, Ga, Zr, Ta, and Nb (figures 4.6 a-i).

The plots of SiO_2 versus Sc, V, and Y are all controlled by the pyroxene content of the samples. The plot versus Sc (figure 4.6 a) has a significant negative slope with the post-breccia, fine-grained gabbro/diorite plotting relatively high (Sc= 26.8-38.0, avg= 33.67, std= 3.13) in the low SiO_2 end of the diagram, the pre-breccia medium-grained gabbro/diorite plotting with similar Sc values (Sc= 17.7-60.8, avg=33.84, std= 10.95) with slightly higher SiO_2 values and the felsic material plotting with relatively low Sc values (Sc= 0.9-5.5, avg= 2.45, std= 1.54) and higher SiO_2 values. This trend simply indicates that the two gabbro/dioritic phases have a higher content of pyroxene (especially orthopyroxene) and lower amounts of quartz than the felsic material. The higher SiO_2 wt % content for the pre-breccia gabbro simply indicates a higher proportion of quartz (locally qualifying it as more dioritic) within this unit. The plot of V (table 4.1) versus SiO_2 (figure 4.6 b) illustrates the same negatively sloped trend, directly attributable to the proportion of pyroxene (especially orthopyroxene), and to a lesser extent the proportion of quartz, within the intrusive phases. Both of these negatively sloped trends associated with the Sc and V indicate that the post-breccia, fine-grained gabbro/dioritic phase of the PHIS is relatively more mafic (ie. contains higher proportions of pyroxene (opx) and lesser proportions of quartz) than the pre-breccia medium-grained gabbro/diorite.

The other plot related to the pyroxene content of the intrusive phases is that of Y

(figure 4.6 c). This plot illustrates a slightly negatively sloped trend whereby the post-breccia gabbro/diorite has a relatively higher proportion of Y (22.84-60.82 ppm,avg=37.42 ppm, std=10.37) and lower SiO_2 than the pre-breccia gabbro/diorite (Y= 14.58-25.64, avg = 19.65 ppm, std = 3.46). However, this plot is different in that the felsic material is not as well confined and has relatively high Y (7.00-45.26 ppm, avg = 30.59, std = 12.82), representing alteration and/or fractionation.

The plots of SiO_2 versus Sr, Rb, and Ga (figure 4.6 d-f) are trace element checks for the major elements of CaO, K_2O, and Al_2O_3 respectively. These elements were chosen due to their chemical similarities to the major elements, especially the similarities in their oxidation states, thereby allowing substitution.

The plot of Sr displays a negatively sloped trend whereby the post-breccia, fine-grained gabbro/diorite plots with relatively high Sr and low SiO_2 (Sr range = 238.75-523.68, avg = 398.69, std = 66.25), the pre-breccia, medium-grained gabbro/diorite also plots with relatively high Sr and low SiO_2 (Sr range = 329.51-633.08, avg = 469.62, std = 84.76), and the felsic material plots with relatively low Sr and high SiO_2 (Sr range of 10.64-807.01, avg = 125.95, std = 210.52). Variation within this plot is the result of variable degrees of plagioclase alteration, and as with the plot versus CaO, Sr is strongly controlled by the proportion of plagioclase (and to some extent clinopyroxene) in the intrusive phases.

The plot of SiO_2 versus Rb (figure 4.6 e) mirrors that of SiO_2 versus K_2O, as would be expected since Rb substitutes for K. The plot has a positively sloped trend with

the post-breccia, fine-grained gabbro/diorite plotting with relatively low Rb and high SiO_2 (Rb values ranging from 11.84-33.89 ppm, avg = 21.83, std = 7.55); the pre-breccia, coarse-grained gabbro/diorite plotting with slightly elevated amounts of Rb and SiO_2 (Rb ranging from 11.44-41.52 ppm, avg = 29.17, std = 10.53); and the felsic material plotting with increased Rb and SiO_2 (Rb ranging from 19.9-141.29 ppm, avg = 99.71, std = 32.94). This trend results from the fact that the felsic material has relatively higher proportions of potassium feldspar (Rb substitutes for K) and quartz, than the two gabbro/dioritic phases of the intrusion which have relatively high proportions of pyroxene, with the only K being derived from secondary sericite.

Unlike the SiO_2 verus Al_2O_3 plot which does not illustrate any appreciable trends, the plot versus Ga (figure 4.6 f) displays a negatively sloped trend, assumed to be related to the fact that the gabbro/dioritic phases of the intrusion have much higher percentages of plagioclase feldspar relative to the felsic phases. Plagioclase, as well as its dominant alteration phase of sericite, contain abundant Al, and since the Ga can substitute for Al in the plagioclase (and therefore sericite), these phases would be expected to contain increased levels of Ga, thereby increasing Ga in the gabbro/diorite intrusive phases.

The last three trace elements plotted against SiO_2 consisted of the incompatible/immobile trace elements of Zr, Ta, Nb (figure 4.6 g-i). The purpose of these incompatible/immobile (trace element) versus mobile (SiO_2) plots was to separate each of the intrusive phases from each other and to cluster the data, not to illustrate any fractionation trends. All three of these plots (figures 4.6 g-i) prove useful in

distinguishing and clustering the various groups of rocks.

Upon close examination of some of the Harker diagrams it appears as though the trends observed argue against any possible fractionation trends, especially for the two gabbro/diorite units. Some of the more problematical diagrams include SiO_2 versus the incompatible elements of Y, Zr, and Nb. In typical fractionation trends it would be expected that with increasing SiO_2 there should be an increase in the incompatible elements. However, in the above mentioned plots the opposite trend is observed (figure 4.6). An explanation of these "reverse" trends lies in the fact that the intrusive system as a whole is an open system and therefore the various phases of the intrusion were produced under slightly different conditions leading to variable mineral phases present. As indicated in chapter three, the post-breccia gabbro/diorite was observed to contain significantly more accessory minerals (such as apatite, zircon, rutile, etc). Due to the nature and ability of these accessory minerals to contain elevated concentrations of incompatible elements the trends are explained and are interpreted to represent fractionation trends. Similar rational is used to explain some of the "reverse" trends observed when MgO was plotted against the same suite of elements, described in the proceeding sections.

4.2.2.2.1 MgO versus major element plots

The second fractionation index used was MgO. Although some of the MgO versus major elements were useful in differentiating the various suites of rocks (as in the harker diagrams), some of the plots were limited in the ability to distinguish between the two

gabbro phases. Similar to the Harker diagram plots, MgO was plotted against the major elements of Fe_2O_3, TiO_2, MnO, Al_2O_3, CaO, SiO_2, and K_2O. The plot versus Na_2O was of no use and was omitted. Due to the limitations associated with the ability of the MgO fractionation index to distinguish between the two gabbroic phases, these plots will not be dealt with in great detail.

The MgO wt % of the three main phases of the intrusive suite are as follows: the pre-breccia, medium-grained gabbro/diorite has MgO values ranging from 2.97-7.75 wt %, avg = 5.72 wt %, std = 1.37; the post-breccia, fine-grained gabbro/diorite values range from 4.21-8.47 with an average and standard deviation of 6.06 and 1.12 respectively; and the post-breccia felsic material ranges from 0.02-0.61 wt % with an average and standard deviation of 0.24 and 0.20 respectively.

The plots of MgO versus Fe_2O_3, TiO_2, and MnO are dominantly controlled by the proportions of pyroxene within each of the main intrusive phases, and all three of these plots define a positive slope. The plots versus Fe_2O_3 and TiO_2 (figures 4.7 a,b) are useful in distinguishing between all three of the intrusive phases whereas the plot versus MnO (figure 4.7 c) is limited to simply distinguishing between the mafic (pyroxene-rich) phases and the more felsic phases. Both plots versus Fe_2O_3 and TiO_2 indicate an apparently substantial chemical difference between the two gabbro/diorite phases. Fractionation trends on these plots are distorted due to the variable amounts of pyroxene, sulphide phases, and oxide phases in the two gabbro/diorite phases. Since the post-breccia gabbro/diorite contains significantly more sulphide (pyrite) and oxides than the pre-

breccia phase, it plots as expected with higher Fe_2O_3 and TiO_2. With this interpretation of these plots the two gabbro/diorite phases can be considered to be chemically related.

The plots versus Al_2O_3 and CaO (figure 4.7 d, e) also define positive slopes, however, unlike the previous plots they are controlled by proportions of plagioclase, clinopyroxene, and the alteration minerals of sericite, chlorite, and amphibole. These plots are limited in their discriminating ability in that they simply distinguish between the mafic and felsic intrusive end-members. The plot versus Al_2O_3 is dominantly controlled by the plagioclase (and its dominant alteration product of sericite) content of the intrusive phases, whereas the plot versus CaO, although also partially controlled by the proportion of plagioclase, depends on the proportion of pyroxene (especially clinopyroxene) within each phase.

The plots versus SiO_2 and K_2O (figure 4.7 f,g) both have negative slopes, related to the relative proportions of quartz, alkali-feldspar, and K-rich alteration products (sericite, biotite). In the case of the SiO_2 plot, the proportion of quartz is the major distinguishing factor between the intrusive rock types, whereas the K_2O plot is dominantly related to the proportions of alkali-feldspar and K-rich alteration products. The plot versus SiO_2 distinguishes between all three of the major intrusive rock types, whereas the plot versus K_2O simply distinguishes between the mafic and felsic end-members.

4.2.2.2.2 MgO versus trace elements

As with the corresponding Harker diagrams, MgO was plotted against the trace elements Sc, V, Y, Sr, Rb, Ga, Zr, Ta, and Nb (figures 4.8 a-i). These plots are useful both as checks on the major element plots and as a method of a more detailed geochemical investigation.

Plots of MgO versus Sc, V, and Y are all controlled by the proportion of pyroxene in the intrusive phases. The two plots versus Sc and V have well defined positively sloped trends (compared to their negatively sloped trends in the Harker diagrams) whereby the pre- and post- gabbro/dioritic phases plot relatively high at the high MgO end of the diagrams, and the felsic material plots close to the origin. As with the majority of the major element plots against MgO, these plots simply distinguish between the mafic and felsic end-members of the intrusion. The trends in these diagrams result from the relatively high proportion of pyroxene associated with the gabbroic units, compared to the pyroxene-poor, quartz-rich felsic unit.

The other plot related to the pyroxene content of the intrusive phases (MgO versus Y, figure 4.8 c) also shows a slightly positive trend whereby the post-breccia gabbro/diorite has a relatively higher proportion of Y than the pre-breccia gabbro/diorite. However, as with the Harker diagram of SiO_2 versus Y, this plot is different in that the felsic material has relatively high Y in contrast to the levels of Sc and V; presumably related to Y concentration in some mineral phase present in the felsic unit (ie. alkali-feldspar, quartz, plagioclase).

The plots of MgO versus Sr, Rb, and Ga (figures 4.8 d-f) are used as checks on the major element plots of CaO, K_2O, and Al_2O_3 respectively. All three of these plots illustrate the same trends as their associated major elements, as would be expected due to their chemical similarities and ability to exchange for each other.

The plots of MgO versus the incompatible/immobile trace elements of Zr, Ta, and Nb (figure 4.8 g-i) were used in an attempt to divide the various groups of rocks into relatively tight clusters of data. As indicated above some of the plots (MgO versus Y, Zr, Nb) illustrated "reverse" patterns than would be expected for "normal" fractionation; a phenomena explained above.

4.2.3 Trace element - Trace element plots

All geochemical plots discussed up to this point have involved major elements (mobile elements) plotted against other major elements (mobile) and a variety of trace elements (variable element mobility and compatibility). These plots, although useful as a first approximation and interpretation of the data, have inherent uncertainty due to variability in element mobility associated with processes such as hydrothermal alteration, fractional crystallization, etc.

Rollinson (1993) describes two methods of identifying igneous source characteristics. The first method utilized to determine any similarities or differences between the source rocks and the major intrusive phases of the PHIS involves using various pairs of incompatible/immobile trace element ratios with similar bulk partition coefficients. By choosing such elements to plot against each other, the effects of

fractional crystallization are eliminated; therefore the slope of a correlation line on such a bivariate plot gives the ratio of the elements in the source, allowing for the relationship of various phases of the intrusion to be determined. The other method of identifying igneous source characteristics (Rollinson (1993)) involves using incompatible trace element (with similar partition coefficients) ratio-ratio plots. Such plots reduce the effects of fractionation and allow for the characteristics of the mantle source for mafic magmas to be identified. The rational for this method is that different mantle sources should plot on different correlation lines, thereby allowing for comparison of mantle sources of different rock units, in the case of this study the source of each phase of the PHIS.

Before describing these plots, a significant inherent problem must be dealt with. Although the plots involving incompatible elements work well when dealing with the mafic (gabbroic) phases of the intrusive suite, the felsic (granitic and to some extent dioritic) phases pose a problem due to the fact that they commonly contain many minor accessory phases which can incorporate many of the trace elements traditionally regarded as 'incompatible'. The result is that when using these plots, the resultant ratios and correlation lines may not illustrate proper fractionation trends. Instead of the expected fractionation trend, ranging from the most mafic phase of the intrusion to the most felsic phase of the intrusion, the phases (especially the felsic phases) plot out of place. However, these plots are still deemed to be insightful and useful due to their consistent ratios and correlation lines.

The first method used to investigate the igneous source characteristics of the

phases of the PHIS was to plot the ratios of incompatible/immobile trace elements, consisting of: Zr versus Nb, Ta, and Hf; Nb versus Ta; and La versus Nb (figures 4.9 a-e). The concentrations of these elements in each intrusive phase is given in table 4.1 and appendix B. The first four plots involve extremely incompatible/immobile elements (Zr, Nb, Ta, and Hf) (figures 4.9 a-d), thereby making them the most important. All four indicate that all phases of the PHIS plot on a common correlation line with the same slope (same ratio), suggesting that all of the phases were derived from the same source (ie. all phases had the same ratio of concentrations of these elements in their source) and may be related through the process of fractional crystallization. In all of these plots of incompatible elements the post-breccia gabbro/diorite has significantly higher proportions of the incompatible elements, a relationship related to the presence of greater amounts of accessory minerals. The other plot consisting of La versus Nb (figure 4.9 e) illustrates a similar trend, however, it has larger spreads in the data (poorly defined correlation lines) due to the relatively higher compatibility and mobility of La. Other plots such as Y-Zr, Nb-Zr, and Y-Nb illustrate similar trends in the data and suggest similar conclusions regarding fractionation trends.

As discussed, the other method described by Rollinson (1993) works on the rationale that the ratios of incompatible trace elements effectively remove the effects of fractionation. For the purposes of the investigation the ratio-ratio plots used were Nb/Th versus Nb/Ce and Th/Tb versus Th/Ta (figures 4.10 a,b). Although the two plots (especially 4.10 b) illustrate rough correlations in the data whereby the gabbro phases plot

approximately on the same correlation line, their usefulness is limited due to the previously mentioned problem with "incompatible" elements when dealing with granitic and dioritic rocks. However, the plots are useful in defining constrained fields for the different intrusive phases.

4.2.4 Normalized Rare-Earth Element and Extended Multi-element plots.

Rare-Earth Element (REE) and trace element analysis were conducted on a sub-set of samples from the PHIS using the HF/HNO3 analytical ICP-MS package from the Department of Earth Sciences laboratory, Memorial University of Newfoundland. Details of the procedure are given in appendix A. A total of 27 samples were analyzed consisting of: 1) four samples of the pre-breccia, medium-grained gabbro/diorite; 2) five samples of the post-breccia, fine-grained gabbro/diorite; 3) six samples of the felsic material; 4) three samples of QFP clasts separated from the breccia; 5) three samples of medium-grained gabbro/dioritic clasts separated from the breccia; and 6) six samples of mineralization. REE plots are normalized to the primitive mantle values of Hofmann (1988); whereas the extended multi-element plots are normalized to primitive mantle values of Taylor and McLennan (1985). It should be noted that although most of the chemical data presented within these plots were obtained from this analytical method (ICP-MS), some element concentrations were derived by other procedures (ie. Zr) due to inherent dissolution problems. As with the previous bivariate plots, only the actual intrusive phases of the PHIS will be dealt with in this section; breccia clasts and mineralization will be dealt with in later sections.

The purpose of these plots is to investigate the geochemical variability within each individual intrusive phase of the PHIS and to assess the geochemical differences between each of the phases. In order to avoid confusion and cluttering of data, each intrusive phase is plotted separately on normalized REE and extended multi-element plots and comparisons are made between plots.

4.2.4.1 Pre-breccia gabbro/diorite normalized REE and Extended Multi-Element Plots.

As described, the pre-breccia, medium-grained gabbro/diorite intrusive phase is a relatively homogeneous unit with little chemical variation. The primitive mantle normalized REE plot indicates that all pre-breccia gabbro/diorite samples have very similar REE trends with overall decreases from the LREE to the HREE. The samples have variable concentrations of total REE, and display minor variation in Eu and Tm (figure 4.11 a). The degree of fractionation in LREE/HREE patterns associated with this intrusive unit, for all REE, is given by La_N/Yb_N which has an average ratio of 5.13 with a standard deviation of 0.88 for all samples; LREE fractionation (La_N/Sm_N) is indicated by an average value of 2.16 with a standard deviation of 0.38; and finally the HREE fractionation (Gd_N/Yb_N) defines an average ratio of 1.77 and a standard deviation of 0.10. As described in chapter 3, samples of the pre-breccia gabbro/diorite ranged from fresh, relatively un-altered samples to very altered samples, and from being strictly gabbroic to more dioritic samples. The samples selected for REE analysis covered all of these variations. The most obvious effect on the REE pattern was the relationship between the

degree of alteration within samples and the total amount of REE present (ie. the greater the alteration within a sample, the higher the total REE). The most altered sample analyzed (JH-99-002a) displays the highest total REE, whereas the freshest sample (JH-99-41) has the lowest total amount of REE. This correlation is interpreted to be related to mass gain/loss effects and is expected since the process of alteration strips out mobile/compatable elements (mass loss) leaving behind incompatible/immobile (alteration resistant) elements such as the REE; thereby relatively increasing their proportions in the altered samples.

Another correlation was observed in the Eu anomalies whereby all but the freshest sample had slight negative Eu anomalies (ie. the more alteration in a sample, the larger the negative Eu anomaly). This correlation is explained by the fact that Eu^{2+} can substitute for Ca^{2+} in plagioclase feldspar, and that Eu^{2+} is not strictly immobile with hydrothermal alteration. The relatively fresh samples should have the best plagioclase, hence they would be expected to contain the most Eu; likewise, in altered samples the plagioclase is altered to sericite, thereby removing Ca and inevitably Eu, essentially a mass gain/loss driven process. However, since Eu is compatible in plagioclase and is affected by processes such as crystal fractionation, this correlation could also be simply related to variations in original compositions.

The last correlation observed is that associated with the slightly different trend (steeper LREE fractionation) and increased Tm within one of the samples (JH-99-040). This variation is presumed to be related to slight chemical variation between original

compositions of gabbro and diorite as this sample is relatively more dioritic than the others.

The extended multi-element plot of the pre-breccia unit showed similar trends to the REE plots whereby the freshest, least-altered sample (JH-99-041) plotted with typically lower amounts of the REE and trace elements (figure 4.11 b). Basically, this plot defined overall decreases in elemental abundances from the left hand side (relatively less incompatible elements) to the right hand side (relatively more incompatible elements). Since all sample patterns have approximately the same slopes and trends, the variation in total elemental concentration is again related to the degree of alteration associated with the samples and mass gain/loss processes. The most obvious variability is associated with elements such as Sr, K, and Rb: Sr concentration (due to its ability to substitute for Ca in plagioclase) is greater within the fresh sample, whereas K and Rb are associated with alteration and are therefore more enriched in the altered samples. The major difference associated with the variability in rock composition from gabbroic to dioritic is that the dioritic sample (JH-99-040) has a positive Tl anomaly whereas the remainder of the samples (more gabbroic) have negative Tl anomalies.

4.2.4.2 Post-breccia gabbro/diorite normalized REE and Extended Multi-Element Plots.

As with the pre-breccia unit, the post-breccia fine-grained gabbro/dioritic unit has previously been illustrated to comprise a homogeneous unit with minor chemical variability. The primitive mantle REE-normalized plot indicates that all samples of this

unit have very similar REE trends with overall decreases from the LREE to the HREE. As with the pre-breccia gabbro/diorite, the samples have variable amounts of total REE (figure 4.12 a). Average La_N/Yb_N is 4.66 with a standard deviation of 0.55; average La_N/Sm_N is1.64 with a standard deviation of 0.029; and average Gd_N/Yb_N is 2.17 with a standard deviation of 0.22. As with the pre-breccia samples, the fine-grained gabbro/diorite samples ranged fresh, un-altered samples to very altered samples, and from gabbro (sensu-stricto) to more dioritic samples. Relationships between the degree of alteration and the total REE present suggest a correlation whereby the more alteration in a sample, the higher its total amount of REE; interpreted to be related to mass gain/loss effects.

The extended multi-element trace element plot for the post-breccia unit defines similar trends to the REE plots whereby the freshest, least-altered sample plots with typically lower amounts of the REE and trace elements (figure 4.12 b). This plot illustrates overall decreases in elemental abundances from the left hand side (relatively less incompatible elements) to the right hand side (relatively more incompatible elements) of the diagram. Since all sample patterns have approximately the same slopes and trends, the variation in total amounts of elements is directly related to the degree of alteration associated with the samples and mass gain/loss processes. One sample pattern, (JH-99-146), representing the most altered sample, does illustrate a significant variation whereby although it contains relatively higher overall elemental patterns, it contains significantly less Tl and Cs than the other samples. Apart from this difference, the most obvious

variability is associated with elements such as Sr, K, and Rb, with similar reasoning as the pre-breccia patterns.

In comparison to the pre-breccia unit, the post-breccia gabbro/diorite illustrated distinctively higher REE patterns. However, the general trend of both sets of patterns is very similar (indicating that they are related) and the relatively higher proportion of REE in the post-breccia phase is explained by the presence of significantly higher proportions of accessory minerals (ie. zircon, apatite, etc) which can contain high proportions of the REE's.

4.2.4.3 Felsic material normalized REE and Extended Multi-Element Plots.

The final major intrusive phase of the PHIS to be examined with REE and extended trace element multi-element plots constitutes the felsic intrusions. Despite the large lithological and petrological variation observed in this unit, the major and trace element chemistry imply that the unit is fairly homogeneous. The purpose of the normalized REE and extended trace element plots was to further examine this homogeneity and to investigate any internal chemical variation associated within this phase.

Both plots are based upon five samples of the felsic intrusive material, ranging from very fine grained aplitic, to medium-grained granitic to porphyritic material. As with some of the bivariate plots, the REE plots and the extended trace element plots are influenced by the fact that many of the "incompatible" elements are actually compatible in highly differentiated granitic phases; (ie. due to the large number of accessory phases

such as zircon, apatite, sphene, or hornblende which accept many REE and trace elements).

On the normalized REE plot of the felsic material (figure 4.13 a), all samples have a similar, yet somewhat variable trend across the diagram. All samples illustrate overall decreases from the LREE to the HREE, however the samples show variable amounts of total REE fractionation and variable Eu anomalies. The group of samples analyzed consisted of two quartz-feldspar (+/- hornblende) porphyritic rocks, two very-fine-grained granitic dykes, and one aplitic sample (figure 4.13 a). The quartz-feldspar (+/- hornblende) porphyritic samples have the highest total REE abundances as would be expected since the porpyhritic phases have the ability to incorporate REE; whereas the fine-grained granitic material and aplitic sample, both with very few accessory phases, have lower REE concentrations. The negative Eu anomalies result from plagioclase fractionation out of the crystallizing magma, and the aplitic sample illustrates the largest negative Eu anomaly due to the total absence of plagioclase (ie. it is the most fractionated sample).

The extended trace element plot of the felsic material illustrates a trend with a relative decrease from the less incompatible (left hand side elements) to the more incompatible elements (figure 4.13 b). The other four samples have very similar trends, whereas the aplitic sample is depleted in some of the large-ion lithophile (LIL) elements such as Ba, Sr, and Cs; thereby indicating that it could be a later phase.

4.3 Chemical analysis of gabbroic and QFP clasts separated from the Lodestar Breccia.

The second step in this geochemical investigation was to study the geochemistry associated with clasts separated from the auriferous Lodestar breccia showing in the PHIS to compare/contrast the chemical signatures of the clasts to those for the regional intrusive rock types in order to determine the relationship, if any, of the clasts to the "host" intrusive phases of the breccia.

As described in chapter 3, the main clasts types associated with the Lodestar breccia consist of sedimentary, medium-grained gabbroic/dioritic, and QFP/granitic clasts. The sedimentary clasts are presumed to be derived from the "host" sedimentary unit, the Connecting Point Group. However, without detailed geochemical studies, the origin of the gabbroic and QFP/granitic clasts is uncertain. Due to the close spatial relationship, and the crosscutting nature of the breccia with respect to the pre-defined pre-breccia gabbro/dioritic unit, it was assumed that the gabbroic clasts within the breccia were locally derived from the "host"wallrocks to the breccia. The relatively un-altered and un-comminuted state of these clasts supported this assumption.

The origins of the felsic QFP and granitic clasts within the breccia, however, was more difficult to determine from simple field and petrologic investigations. The variability in these clasts, in addition to their comminuted nature whereby they formed the rock flour matrix (suggesting transport from depth) and the presence of potential primary mineralization within these clasts, all pose difficulties in directly linking the felsic clasts

to the local felsic intrusive material. Also, the fact that the majority of the felsic intrusive material is observed to crosscut the post-breccia, fine-grained gabbro/diorite, suggests that the clasts are different, at least temporally, from the felsic intrusive material.

All of the previously described plots also included geochemical data from the breccia clasts. These data will be discussed first, followed by normalized REE and extended multi-element plots.

4.3.1 Gabbroic clasts from the Lodestar Breccia

On the AFM plot (figure 4.1), the gabbroic clasts plot with very similar geochemical characteristics to the pre-breccia gabbro/diorite unit. The clasts are slightly displaced towards the $Na_2O + K_2O$ apex due to minor potassic alteration and alteration reactions such as plagioclase alteration to sericite. A similar trend is observed on the Jensen cation plot (figure 4.2), whereby the clasts are slightly displaced towards the Al_2O_3 apex of the plot, due to alteration whereby plagioclase and pyroxene are broken down into relatively Al-richer phases such as sericite, biotite, amphiboles, and chlorite. Irvine and Baragar's (1971) TAS plot (figure 4.3) indicates a more substantial variation between the clasts and the host unit, whereby the host gabbro/dioritic unit plots within the subalkaline field and the clasts plot in the alkaline field. This variation can be best explained by the chemical mobility of the elements involved as related to potassic and sericitic alteration of the clasts. The two Winchester and Floyd (1977) discrimination plots do not distinguish element mobility and indicate that the clasts and host gabbro/dioritic material are chemically undistinguishable (figure 4.4 a,b).

As previously mentioned, variations within the intrusive phases of the PHIS required that two different indexes of fractionation, consisting of SiO_2 and MgO, be used in order to investigate the chemical signatures of the intrusive phases. In this comparison of the gabbro/dioritic clasts to the host gabbro/dioritic intrusive phase, both sets of plots give similar results and will therefore be dealt with together. Due to element mobility problems, and the enhanced degree of hydrothermal alteration associated with the breccia clasts compared to the intrusive gabbroic unit, these plots will not be discussed in great detail.

Generally speaking, in both sets of plots, relative to the pre-breccia gabbro/diorite, the gabbro/diorite clasts illustrate relative increases in the proportions of Al_2O_3, K_2O, Rb, and Ga and relative decreases in proportions of CaO and Sr; the relative increases and decreases being related to alteration of plagioclase and pyroxene to sericite, biotite, chlorite, and amphibole (Al and K rich phases) and the breakdown of plagioclase and pyroxene (clinopyroxene). The elements of SiO_2, TiO_2, Fe_2O_3, MnO, MgO, Na_2O, Sc, V, Y, Nb, Ta, and Zr have similar proportions in both the clasts and the pre-breccia gabbro/diorite material (figures 4.5 - 4.8). Of importance in this group of common elements are Nb, Ta, and Zr which are considered to be incompatible/immobile elements and therefore are not as subject to redistribution due to hydrothermal alteration. Since these elements have common proportions in both the clasts and the pre-breccia intrusive material, they indicate a probable common source or precursor for both units.

Due to potential major element mobility problems, a number of incompatible/immobile trace elements with similar partition coefficients were plotted against each other. For the purposes of comparing the clasts to the pre-breccia gabbroic unit, Zr, Nb, Ta, Hf, and La were chosen and plots of Zr versus Nb, Ta, and Hf and La versus Nb and Ta were constructed. As discussed previously, Zr, Nb, Ta, Hf, and to a lesser extent La are typically incompatible/immobile, and are especially useful for reducing the effects of fractionation within mafic magmas. However, upon investigation of the plots, it was discovered that the trace elements were actually slightly mobile (observed due to the degree of variation associated with the intrusive phase samples), due to the problems associated with dioritic and felsic lithologies. This problem was enhanced due to the small number of samples selected from each rock type to be analyzed for REE by the ICP-MS HF/HNO3 trace element package, coupled with the compositional variation within the samples. It was therefore concluded that these plots were unable to define fractionation and alteration processes, and they were therefore deemed incapable of determining the similarities/differences in the parental magma of the gabbro/dioritic clasts and the intrusive. However, even with these limitations, it should be noted that, as shown in figure 4.9, the gabbro/diorite clasts plot close to, or on, the correlation lines linking the phases of the PHIS; thereby implying that the clasts are related to the intrusive suite, and more particularly to the pre-breccia gabbro/diorite (due to the similar ratios observed for both).

The last geochemical test used to investigate correlations between the clasts and the pre-breccia gabbro/diorite involved plotting a normalized REE plot and an extended multi-element plot (figures 4.14 a,b). Within both of these plots the gabbroic clasts illustrate similar trends to the pre-breccia gabbro/diorite trends, thereby indicating a common precursor for both. Variation within Eu and Tm in the normalized REE plot (4.14 a) is explained in section 4.2.4.1. Minor variation is also observed in some of the more mobile, less incompatible elements in the extended plot; however this variation is related to alteration effects and is disregarded when comparing the two units.

4.3.2 Felsic clasts from the Lodestar Breccia

As with the gabbro/diorite clasts, the first series of geochemical plots used to compare/contrast the felsic clasts separated from the breccia to the surrounding felsic intrusive phases from the PHIS consisted of major and trace element discrimination plots. All five of these variation diagrams (figures 4.1 - 4.4 a,b) illustrate variability between the clasts and the felsic intrusive phases. However, due to chemical mobility associated with these plots and the inherent difficulties associated with incompatible elements when describing felsic lithologies, these differences cannot be substantiated and the plots will be disregarded for the purposes of this investigation.

Both series of fractionation index plots (figures 4.5-4.8) illustrate similar trends when comparing the felsic clasts to the felsic intrusive phases of the PHIS. The plots illustrate relative increases in the proportion of Fe_2O_3, MgO, Y, Nb, Ta, and Zr in the clasts compared to the intrusive phase, and relative decreases in proportions of Na_2O and

K_2O for the clasts relative to the intrusive suite (figure 4.5 - 4.8), with all other elements occurring in similar proportions for both units. The relative increases and decreases of Fe_2O_3/MgO and Na_2O/K_2O associated with the clasts is presumably related to minor amounts of mineralization on the surface of, and filling fractures within, the clasts. However, the substantial increase in the proportions of Y, Nb, Ta, and Zr (all relatively immobile and incompatible elements)(figures 4.6, 4.8) are regarded as a "real" difference between the two units, related to different parental sources.

As mentioned above, due to inherent problems, incompatible/immobile trace element ratio plots are problematical when attempting to decipher fractionation and alteration processes, and are therefore deemed unreliable in the determination of similarities/differences of parental magmas when dealing with felsic lithologies. However, even with this limitation, some important observations regarding the relationship of the felsic clasts from the Lodestar breccia to the felsic intrusive phase (and all other phases) can be acquired from the plots in figure 4.9. Within these plots, including Zr versus Nb, Ta, and Hf, and La versus Nb and Ta (figures 4.9 a-e), the felsic clasts always plot significantly higher than the general correlation lines linking the phases of the PHIS; thereby indicating different ratios of the elements in the source rocks of the felsic clasts, and thereby suggesting different sources for the clasts and the intrusive material.

In order to further evaluate this geochemical difference between the felsic clasts and the felsic intrusive phase of the PHIS, a normalized REE plot and an extended multi-

element plot were constructed. As illustrated on figure 4.15 a, the normalized REE plot displays two significantly different trends for the clasts and the intrusive phase whereby the clasts have a much lower degree of fractionation associated with their LREE than the intrusive phase, giving the clasts a much "flatter"overall REE trend. Significant differences are also illustrated within the extended multi-element plot (figure 4.15 b) whereby some key incompatible/immobile elements such as Nb, Zr, and U have substantially different proportions (ie. greater than could be explained by incompatible/immobile element mobility associated with felsic lithologies) in the clasts and the intrusive phase, thereby indicating differences in the two units.

Based upon these plots, it is concluded that the felsic clasts from the Lodestar breccia were derived from a different parental magma source than the felsic intrusive phase of the PHIS. This conclusion will be discussed further in a later chapter dealing with deposit modeling.

4.4 Mineralization associated with the Lodestar Breccia Showing

When analyzing the geochemical data from a mineralized breccia one must confront the limitations of such analysis. Due to the nature of a mineralized breccia, the extent of quantitative analysis possible is minor. Without knowing the exact percentages of clast types, matrix types, and types of mineralization, quantitative analysis is basically impossible. However, valuable information such as correlations between elements associated with the mineralization, variations in the grades of mineralization, isotopic

ratios, geothermometry results, as well as many other analytical results can be obtained, provided that the necessary conditions are met.

For this investigation of the mineralization associated with the Lodestar prospect assay results and correlations between elements will be evaluated. It will be followed by more detailed investigations of sulphur isotope data, geothermometry, and an investigation of the nature and distribution of the gold in the mineralization.

4.4.1.1 Assay results from the Lodestar prospect

As described in chapter three, the Lodestar Prospect consists of a sulphide-oxide mineralized breccia. The prospect contains significant gold, and copper, zinc and arsenic, within a polylithic breccia associated with the PHIS. The best grades obtained by exploration companies from chip-channel sampling of the mineralized breccia were 4.98 g/t Au and 14.8 g/t Ag over a 15.9 m assay length, with one assay of ~ 2.0 % Zn. Other assays returned values of 6.13 g/t Au and 4.91 g/t Au over 3m. The highest grade assays returned from the property (58.5 g/t Au with 260 g/t Ag) came from grab samples of massive arsenopyrite (carrying 25% As) (this study). All assay results obtained from grab samples of mineralized breccia are reported in appendix B.

4.4.1.2 Elemental correlations associated with the Lodestar Breccia mineralization.

Initial investigations of the Lodestar breccia mineralization focused on the determination of any correlation between the metals (Au, Cu, Pb, Zn, Ag, and As) associated with the sulphide minerals which form the matrix of the breccia. Field descriptions, in conjunction with petrographic work, indicate that the main sulphide

phases associated with the breccia consist of arsenopyrite, pyrite, chalcopyrite, sphalerite, and minor galena. The purpose of this investigation was to determine which sulphide phases took the gold mineralization, and to examine any other metal correlations that exist. As with the trace elements analyzed, there was overlap as some elements were analyzed by more than one analytical method; the limits of detection, accuracy, and precision were all evaluated so that the best set of analytical data was utilized. Au and As were best analyzed by INAA; Cu, Zn, and Ag were best analyzed by ICP-ES; and Pb was best analyzed by XRF (limited subset of samples analyzed by ICP-MS).

Since gold is economically the most important element in the Lodestar Breccia, it was plotted against all other elements in order to determine correlations (figures 4.16 a-e). Although the results indicate relative correlations between Au and all other elements, the best correlation is between Au and As (figure 4.16 a). Preliminary conclusions indicate that the majority of the gold is associated with arsenopyrite; a conclusion which was tested in a later section (section 4.4.4) dealing with laser-ablation-microprobe-inductively-coupled-mass-spectrometry (LAM-ICP-MS) analysis of the nature and location of the gold within sulphide phases.

In addition to the plots involving gold, several other bivariate plots of metals were produced (figure 4.17 a-c) including: a) Pb versus Zn, b) Zn vs Cu, and c) Cu vs Ag. All three of these plots, as well as others, illustrate positive correlations; as would be expected due to the occurrence of all major sulphide phases in the analyzed samples.

4.4.2 Sulphur Isotope Geochemistry

4.4.2.1 Introduction and theory

Sulphur isotope geochemistry has become an integral component of ore deposits research (eg. Ohmoto, 1972; Rye and Ohmoto, 1974; Ohmoto and Rye, 1979; Faure, 1986; Rollinson 1993). It has many uses in the study of hydrothermal ore deposits including determination of: 1) the origin of the sulphur, 2) the temperature of formation of the sulphides present, 3) the degree of equilibrium attained, and 4) the constraints on the mechanism of ore deposition (Rollinson, 1993). For the purposes of this study the origin of the sulphur and the temperature of formation will be studied. The origin of the sulphur will be dealt with in this section whereas geothermometry will be examined in the proceeding section (section 4.4.3).

Sulphur isotopes are widely distributed throughout the lithosphere, biosphere, hydrosphere, and atmosphere of the earth (Faure et al. 1986). Sulphur occurs in a number of forms including: 1) oxidized as sulphate in the oceans and in evaporites, 2)native sulphur as cap rocks to salt domes and in some volcanics, and 3) reduced as sulphides in metallic mineral deposits associated with igneous, sedimentary, and metamorphic rocks. Each of these environments has distinctive sulphur isotopic ratios; thus determination of the isotopic composition of sulphur is particularly useful in the study of sulphide ore deposits.

There are four naturally occurring stable isotopes of sulphur whose approximate abundances are: ^{32}S = 95.02%, ^{33}S = 0.75%, ^{34}S = 4.21%, and ^{36}S = 0.02% (Ohmoto and

Rye, 1979; Faure, 1986; Rollinson, 1993). The ratio between the two most abundant isotopes ($^{34}S/^{32}S$) is used in sulphur isotope geochemistry, with the ratio being expressed as parts per thousand relative to the Canon Diablo meterorite (CDT) triolite (FeS) reference standard (believed to be representative of the bulk undifferentiated earth (Ohmoto and Rye, 1979)) in the form of:

$$\delta^{34}S\ ‰ = [\ ^{34}S/^{32}S\ (sample) - \ ^{34}S/^{32}S\ (standard)\ /\ ^{34}S/^{32}S\ (standard)|\ *\ 1000$$

The standard (CDT) has a $^{34}S/^{32}S$ ratio of 0.04500045 (Ohmoto and Rye, 1979). Therefore, the measure of $\delta^{34}S$ ‰ of a given terrestrial S sample can be assumed to be a measure of the change that has taken place in the samples' isotopic composition since its initial formation and emplacement into the crust (Faure et al. 1986).

The variations observed in sulphur isotope compositions are caused by two main processes: 1) reduction of sulphate ions to hydrogen sulphide by anaerobic bacteria which results in the enrichment of ^{32}S in the sulphide, 2) and various isotopic exchange reactions between sulphur-bearing ions, molecules, and solids through which ^{34}S is generally concentrated in the compounds that have the highest oxidation state of S or the greatest bond strength (Faure et al. 1986).

Criteria have been developed which allow distinction between reservoirs with sulphur of igneous-hydrothermal origin from those with sulphur of sedimentary syn-genetic origin. The range of $\delta^{34}S$ ‰ values for these two sources are summarized in figure 4.18. Although this distinction between reservoirs is useful, it should be noted that results do not point to a single source of the sulphur due to extensive overlap of $\delta^{34}S$ ‰

ratios. Ohmoto and Rye (1979) indicate that primary sulphides in mantle-derived rocks can be assumed to inherit the $\delta^{34}S$ ‰ ratios of their parental magma melt and source region, which usually lie in the range of 0 +/- 3 ‰. It must be realized, however, that due to changes in the pH and fugacity of oxygen (Faure, 1986), as well as other controlling conditions such as mantle S-isotope heterogeneity and potential mantle metasomatism due to crustal fluids and other lithologies (eg. sedimentary units) (Kyser, 1990; Wilson et al., 1996), the $\delta^{34}S$ ‰ value of mantle derived (magmatic) sulphides can shift.

A total of 23 sulphide separates were analyzed for their sulphur isotope ratios. The sulphur isotope analytical technique is described in appendix A. The samples consisted of: chalcopyrite (seven samples), pyrite (nine samples), arsenopyrite (six samples), and one sample of bornite. Twenty-two of the sulphide separates were from the mineralized matrix of the breccia, with one sample of pyrite from the fine-grained gabbro/diorite.

4.4.2.2 Determination of the origin of the sulphur present

Sulphur isotope ratios derived from the sulphide separates are summarized in Table 4.2. The single pyrite separate from the post-breccia, fine-grained gabbro/diorite ($\delta^{34}S$ ‰ = 0.95) lies well within the normal accepted range of magmatic sulphur ($\delta^{34}S$ ‰ = +/- 3). This result is expected since the pyrite in the gabbroic phase appears to be directly related to primary igneous activity.

The remainder of the matrix sulphide mineral separates have fairly homogeneous $\delta^{34}S$ ‰ ratios ranging from 3.07 - 4.41. These values, however, lie above the normally accepted magmatic sulphide $\delta^{34}S$ ‰ range. Although the values obtained from the

mineralization are slightly above the "typical" range of magmatic sulphides, they are still interpreted as magmatic sulphide values. The most probable cause of the slight variation from the normal magmatic values was crustal contamination of the magma whereby the mineralizing fluids were contaminated by assimilation and partial migmatization of the host sedimentary rocks, thereby resulting in a slight positive shift in the $\delta^{34}S$ ‰. The presence of the rock flour matrix supports the contamination argument.

Outgassing of SO_2 might also be important as a variant in the range of $\delta^{34}S$ ‰ ratios due to the presence of hydrothermal magnetite, a phase which is indicative of elevated oxygen activities (Rollinson, 1993). Faure et al. (1984) and Faure (1986) proposed that this high activity of oxygen leads to the stabilization of SO_2 as the dominant sulphur species in gas, and depending on the $\delta^{34}S$ ‰ composition of this degassing SO_2, the remaining sulphur within the melt will be isotopically shifted. The sulphur remaining in the melt after SO_2 degassing will either be depleted or enriched in ^{34}S, depending on the partial pressure (fugacity) of oxygen: a relationship based upon the fact that the sulphate/sulphide ratio of the melt increases with increasing oxygen fugacity and that this ratio affects the $\delta^{34}S$ ‰ value of the escaping sulphur–bearing gases (Faure, 1986).

The presence of hydrothermal magnetite indicates high activities of oxygen, thus the sulphur isotopic ratios in the mineralization associated with the breccia may be isotopically enriched. Therefore outgassing of SO_2 under conditions of high oxygen fugacity can shift the $\delta^{34}S$ ‰ in the positive direction; as observed in the Lodestar

samples.

The influence of these two variables is believed to have slightly displaced the $\delta^{34}S$ ‰ values from the Lodestar mineralized samples slightly above their original magmatic sulphide range. Similar results were obtained and documented from the Kidston gold-bearing breccia pipe in Queensland, Australia; whereby sulphur isotope values from pyrite, pyrrhotite, and sphalerite separates ranged from 2.2 and 4.3 ‰; with the sulphides still interpreted to be magmatitically derived (Baker and Andrew, 1991).

4.4.3 Geothermometry (Sulphur isotope and arsenopyrite geothermometers)

4.4.3.1 Introduction

Determination of the formation temperature of the Lodestar mineralization was complicated since no primary fluid inclusions were observed. Secondary inclusions were discovered in patches of recrystallized quartz but were of no use. Since the method using fluid inclusions was unavailable, two other methods were used to determine the approximate temperatures of the mineralization: 1) sulphur isotope geothermometry, and 2) arsenopyrite geothermometry; each of which has its own limitation and uncertainty.

4.4.3.2 Sulphur isotope geothermometry

There is extensive literature on the use, both experimental and in nature, of sulphur isotope ratios as geothermometers (eg. Sakai, 1968; Friedman and O'Neil, (1977); Ohmoto and Rye, (1979); Neilsen, 1979). Both the theoretical and experimental results indicate that equilibrium exchange reactions between co-genetic sulphide minerals

and ore-forming fluids allow the temperature of equilibrium to be estimated from $\delta^{34}S$ ‰ values of co-existing sulphides (Faure et al. 1986). Table 4.3 indicates various calibrations for sulphur isotope thermometry using a variety of mineral pairs. This temperature determination is subject to a number of assumptions, the most important of which are:1) isotopic equilibrium was established between the two minerals; 2) the isotopic composition was not changed by post depositional processes; and 3) the mineral phases were cleanly separated from each other during the analysis preparation procedures.

Due to the nature of the mineralization within the matrix of the breccia at the Lodestar prospect it was difficult to obtain a sample in which all of the necessary conditions for dependable geothermometry studies were met. Sulphide separates were obtained from cut mineralized slabs of the breccia. The only sulphide mineral pair that met the conditions and could be cleanly separated from the slabs consisted of pyrite-chalcopyrite. For this study four pairs separates were used for sulphur-isotope thermometry; however, of these four pairs only one pair displayed direct equilibrium contact within a slab; therefore this mineral pair will be the main focus. As listed in table 4.3, the calibration equation derived for the pyrite-chalcopyrite sulphur isotope thermometer is:

$$T = ((0.67 +/- 0.04) * 10^3)/(\delta^{34} S_{pyrite} - \delta^{34} S_{chalcopyrite})$$

where the temperature is in Kelvin and the uncertainties are +/- 35 (uncertainty in the calculated temperature due to uncertainty in the equation) and +/- 40 (due to analytical uncertainty of +/- .2 per mil) (Ohmoto and Rye, 1979).

The $\delta^{34}S$ ‰ ratios obtained for the equilibrated pyrite-chalcopyrite separates were 4.01 and 3.09 respectively. Using the above equation and associated uncertainties these ratios determine a temperature ranging from 616.8 - 780.2 K (343.8 - 507.2 °C) with an average of 698.5 K (~ 425 °C). Other separates were deemed not to be in equilibrium based upon textural relationships: the $\delta^{34}S$ ‰ ratios obtained for the pyrite and chalcopyrite from these samples were as follows (stated as pyrite and chalcopyrite values): 3.96 and 4.58, 3.44 and 3.65, and 4.41 and 4.08.

4.4.3.3 Arsenopyrite geothermometry

The other system used to calculate the mineralization temperature was the arsenopyrite geothermometer developed by Kretschmar and Scott (1976). As with the sulphur isotope thermometer there have been numerous studies on arsenopyrite thermometry (Kretschmar and Scott, 1976; Scott, 1983; Sharp et al., 1985; Kerr et al., 1999).

Within the iron-arsenic-sulphur system, arsenopyrite is the only ternary phase (FeAsS) (Ohmoto et al., 1997). Arsenopyrite is one of the few sulphides that is relatively refractory, thus it can exhibit solid-solution temperature-pressure variations (Sharp et al., 1985) which allow it to be used as a geothermometer. Kretschmar and Scott (1976) determined the phase relationships in the Fe-As-S system between the temperature ranges of 363-688 ° C. In the higher temperature range of approximately 491-688 ° C, arsenopyrite coexists with pyrrhotite, loellingite, arsenic, or an As-S liquid within the assemblages 1-4 in figure 4.19; whereas at the lower temperature ranges of 363 - 491 ° C

it coexists with pyrite, pyrrhotite, loellingite, arsenic, or As-S liquid within assemblages 5-8 (figure 4.19). Since the composition of arsenopyrite is known to be sensitive to both temperature and equilibrium with coexisting phases, it is only useful in geothermometry studies when it is in one of the buffered assemblages (1-8) illustrated in figure 4.19. Although arsenopyrite is a common mineral present within ore deposits, potential buffering phases such as loellingite, arsenic, and As-S liquid typically are not, thereby limiting the application of the thermometer (Scott, 1983). Another serious limitation is the fact that it is essential for S activity be known in order to obtain reasonable results. It should be noted that in the process of developing the arsenopyrite geothermometer illustrated in figure 4.19, Kretschmar and Scott (1976) made use of Barton's (1969) work involving the measurement of the sulphur activity dependance on sulphidation reactions involving arsenopyrite within the Fe-As-F system, illustrated in figure 4.20.

Within the scope of this study, it appears that these major limiting conditions are overcome in that petrographic relationships indicate that arsenopyrite formed in association with, and potentially from reaction between, an arsenic-rich liquid and pyrite. This relationship and phase assembly correspond to the assemblage number 5 in Kretschmar and Scott's (1976) study, thereby fulfilling the sulphur activity condition, and allowing for a temperature to be directly obtained from figure 4.19. Without the presence of a Fe-S buffering phase it would be necessary to determine the sulphur activity by an alternative method.

It should be noted that a critical re-examination of the arsenopyrite geothermometer by Sharp et al., (1985) concluded that the thermometer is valid for deposits metamorphosed to greenschist and lower amphibolite facies (ie. like P-T at the Lodestar prospect) but gives temperatures that are too low for upper amphibolite and granulite facies metamorphosed deposits, and inconsistent temperatures for low-temperature deposits. Examinations by Scott (1983) indicate that in situations where no other Fe-As-S buffering phases are present, an appropriate sulphur activity sliding scale buffer is required which occurs commonly with arsenopyrite, does not form solid-solutions with it, and whose isopleths cut those of arsenopyrite at high angles (ie. sphalerite coexisting with pyrite and/or pyrrhotite). This method of using the Fe-Zn-As-S system (Scott, 1983) for geothermometry determinations was attempted using arsenopyrite atomic weight percent As and mole % FeS of sphalerite from mineralized samples. However, due to apparent non-equilibrium conditions between the two phases, the mole % FeS from the sphalerite was too low to be in the stability field of arsenopyrite, making this thermometer uninformative.

Three different mineralized thin sections were analyzed on an electron microprobe: an in house facility at the Department of Earth Science, Memorial University of Newfoundland, centered around a 1991 Cameca SX-50 instrument operated with Oxford (link) software. Analytical conditions used within this study are as follows: accelerating voltage = 20.00 kV; beam current = 40.20 nA; spectral lines = S KA, Fe KA, Cu KA, Zn KA, As LA, Ag LA, Au MA (detailed methodology is given in appendix A).

The same standards were used as those in Kretschmar and Scott's (1976) study, consisting of Asp 57 and Asp 200, both of which are proven homogeneous arsenopyrite standards. Numerous analyses were made of a variety of sulphide minerals including arsenopyrite, pyrite, chalcopyrite, and sphalerite. However, for this study the only relevant analysis are those from the arsenopyrite; and of specific interest are the results of the atomic wt % As, the values of which are given in table 4.4. As reported in table 4.4, the average atomic wt % As determined from the samples was 31.77, which when plotted on the relevant diagram (figure 4.19) in the appropriate mineral assemblage field results in an approximate temperature of 420-430 ° C +/- 50 °. Associated with this approximate temperature are uncertainties related to aspects of equilibrium between the sulphide phases, uncertainty in the activity of sulphur, and uncertainties associated with the electron microprobe detection limits, accuracy, and precision.

In general, the results from the above two geothermometers can be used to reliably conclude that the temperature of mineralization is in the range of 425 °C. The similarities in the results from the two methods imply that the minerals chosen must have been in, or close to, equilibrium; and that the sulphur activity and related conditions within the system remained constant; thereby allowing for reliable determination of the mineralizing temperature.

4.4.4 Gold - Sulphide Relationships: LAM-ICP-MS

4.4.4.1 Introduction

Although gold has been assayed at high concentrations in both grab and channel samples from the Lodestar prospect (see section 4.4.1.1 and appendix B), the relative association and nature of the gold with respect to the sulphides could not be determined using standard analytical techniques such as ore microscopy, INAA, XRF, solution ICP-MS, SEM, and electron microprobe. The only information determined from these analytical techniques was that the gold seemed to be preferentially associated with arsenopyrite: an observation based upon the fact that a semi-massive grab sample of arsenopyrite returned an assay of 58.5 g/t gold, much higher than assay results associated with similar semi-massive samples of other sulphide phases. The fact that no visible gold was observed using techniques such as SEM and electron microprobe studies suggests that the gold is distributed as either very fine disseminations in the sulphides or within the structure of the sulphides (ie. "invisible" gold").

Recent developments for in-situ LAM-ICP-MS techniques have provided important insights into the distribution of trace elements in minerals that were not previously revealed by conventional analytical techniques (Longerich et al., 1995). Since the manner of distribution of the gold was not discernable by any of the above mentioned analytical techniques, LAM-ICP-MS analyses were undertaken to determine in which sulphide phase the gold was dominantly associated, and whether the gold was distributed homogeneously or contained in micronuggets. The analyses were conducted using a VG

PlasmaQuad 2 S+ ICP-MS instrument coupled to an in-house built 266 nm Nd-YAG laser. Using He as a carrier gas, 10 Hz laser frequency, laser energy of approximately 0.40 mJ/shot and both single spot sampling and line rastering, time-resolved analyses were collected that showed the spatial distribution of Au in the sample. Concentrations were calculated using S as an internal standard from an FeS synthesized standard containing Au. Detailed explanations regarding analytical procedures are given in appendix A.

4.4.4.2 "Invisible" Gold Background

Research into the nature of gold within sulphide phases such as arsenopyrite and pyrite is not new. The need to understand the relationship arose when it was discovered that certain gold ores were not directly amenable to the usual cyanidation process, an observation first recorded in the 1930's (Cabri et al., 1989). It is recognized that gold can occur in a number of different ways: as free particles, as inclusions within sulphide minerals (nugget effect), as chemical compounds (eg. Au-Ag tellurides), and as solid-solutions within sulphide phases such as arsenopyrite and pyrite ("invisible" gold) (Cabri et al., 1989; Genkin et al, 1998; Cook et al., 1990).

The realization that gold occurring in solid-solution in sulphide minerals can reach economic concentrations has fueled attempts to understand the mechanisms by which gold is complexed with specific sulphide minerals. The understanding of such processes is important to economic geologists and exploration companies as it may serve as a geochemically oriented exploration method in targeting economic gold deposits. The

understanding of the mineralogical characteristics of "invisible" gold is also important for processing of such ores.

It has been demonstrated that refractory sulphide-bearing gold ores can make up the majority of the gold present in some deposits. Concentrations of "invisible" gold have ranged up to 1.52 wt % (15,200 g/t) within natural arsenopyrite from the Villeranges deposit, France (Boiron,1987; Johan et al., 1989) with similar concentrations within the Congress mine, Canada (Cook and Chryssoulis, 1990), and up to 0.14 wt % (1400 g/t) within natural pyrite (Fleet et al. 1993, and Simon et al., 1999).

Controversy still exists regarding the substitution mechanisms responsible for the relationships between gold and arsenic within the structure of the sulphide minerals arsenopyrite and pyrite. Many mechanisms have been proposed for this substitution including the following: 1) Au occupying the As sites in the arsenopyrite structure (Boyle, 1979), 2) a substitution mechanism whereby 2As[Fe]↔(Au, Sb) + Fe (Johan et al., 1989), 3) a coupled substitution for arsenian pyrite involving substitution of Au for Fe and As for S (Arehart et al., 1993), and 4) Au replacing Fe in arsenopyrite and arsenian pyrite by $(Fe,Au)^{3-} = (As\text{-}S)^{3-}$ substitution (Genkin et al., 1998). Many other plausible mechanisms for substitution have also been proposed, however, for the purposes of this summary it is sufficient to say that substitution involves the replacement of As and/or Fe by Au.

4.4.4.3 Purpose and Scope of LAM-ICP-MS study

The purpose of this experiment was to determine the nature and distribution of gold within the sulphide phases of the Lodestar Prospect. The laser was utilized to ablate a series of single spot ablation pits as well as line raster ablations. All sulphide phases were ablated in order to determine gold distribution throughout the showing. For the purposes of this experiment, three thick polished sections (the same sections analyzed by the electron microprobe during geothermometry studies) containing variable amounts of mineralization and variably textured mineralization served as the ablation material. Examples of the ablation pits are shown in figure 4.21.

4.4.4.4 Results and Conclusions

The results obtained from this study serve to unambiguously illustrate a chemical affinity of the gold at the Lodestar prospect with arsenopyrite. Analysis obtained from both single spot ablation pits and line rastering indicate that gold occurs within the arsenopyrite structure preferentially compared to pyrite and chalcopyrite (Table 4.5) (figure 4.22, 4.23).

Counts per second (CPS) vs time data acquired from the LAM-ICP-MS also indicate that the gold within the arsenopyrite occurs "homogeneously" within the mineral structure, rather than distributed as micro-nuggets. This observation is based upon the typically "flat", smooth CPS data acquired from both single spot and line raster ablations (figures 4.22, 4.23), thereby indicating relatively little variation in the amount of gold distributed through the arsenopyrite. However, as illustrated in figure 4.23 a, some raster

CPS results occur as sinuous or wavy curves. Within this figure, as with the others, the gold cps increase dramatically when the laser starts ablating the arsenopyrite, thereby illustrating a direct correlation between the Au and arsenopyrite. However, unlike the other graphs illustrated, this graph varies in the cps data for Au. This data is still interpreted to illustrate a "homogeneous" gold content within the arsenopyrite (ie. no nugget effect), explained by using the data in conjunction with electron microprobe atomic weight % As analytical results obtained from the same sample. These results indicate that although there is very little variation in the atomic weight % As throughout the sample as a whole, there are some small variations observed (1.5 - 2 %) between adjacent "bright" and "dark" areas within the arsenopyrite, as viewed using the backscattered image on the microprobe. These small variations are thought to illustrate minor compositional zoning within the arsenopyrite structure leading to variable amounts of As and Fe in the structure. Assuming that the Au is actually involved in a substitution reaction with As, this variability in As and Fe thereby determines how much gold can be incorporated within the arsenopyrite structure. The smooth nature of the CPS data also argues against micronuggets of gold which would be observed as strong spikes in the signal.

Based upon the data acquired during this study, the most logical explanation as to how the gold is incorporated within the arsenopyrite structure deals with substitution of Au, along with Sb, for As and Fe in the mineral structure. However, more detailed work is needed to quantify the role of each element in the substitution process.

In conclusion, the data obtained from the LAM-ICP-MS indicates that the gold present within the Lodestar Prospect is predominantly associated with arsenopyrite (and to a lesser degree with arsenian pyrite) and it is "homogeneously" distributed throughout the arsenopyrite structure as "invisible" gold.

4.4.5 Geochronological Studies

4.4.5.1 Introduction

Due to inconsistences associated with previous age interpretations of the PHIS, and the regional exploration importance of determining the age of mineralization associated with the Lodestar prospect, U-Pb zircon dating was conducted on two phases from the intrusion. The purpose of the dating was threefold: 1) to obtain an accurate age of magmatism associated with the intrusive suite, 2) to obtain a minimum age of the host (intruded) sedimentary unit in order to determine its stratigraphic affinity, and 3) to determine the age of the breccia hosted gold-zinc-copper mineralization of the Lodestar prospect.

With these goals in mind, two samples of intrusive phases from the prospect locality were collected for U-Pb dating. The two samples consist of pre-breccia, medium-grained gabbro/diorite (collected immediately adjacent to the cross-cutting mineralized breccia), and a fine-grained felsic dyke that was initially, incorrectly, interpreted to be intruding the mineralized breccia. The dates obtained satisfied the first two unknowns; however, with additional field examinations after more stripping of the outcrop, it was determined that the felsic dyke that was previously interpreted as cutting the breccia was

itself brecciated, thereby changing its chronological position to pre-breccia or syn-breccia (plates 4.1 a,b). A sample of the post-breccia fine-grained gabbro/diorite intrusive phase that intrudes and is chilled against the breccia has since been collected and awaits geochronological analysis; the results of which will truly bracket the mineralizing event.

Geochronological analysis were conducted via TIMS at Memorial University of Newfoundland by Dr. G. R. Dunning, the results of which have been interpreted and documented by O'Brien et al., (2000). The following discussion draws upon the U-Pb geochronological interpretations within the open file report by O'Brien et al (2000), and based on the new field relationships discovered critically questions the interpretation with respect to the bracketing of the mineralizing event at the Lodestar breccia.

4.4.5.2 Geochronological Results and Interpretations/Implications

As described in O'Brien et al., (2000), the results of the two analysis were as follows: 1) the sample of the pre-breccia gabbro/diorite yielded a large amount of clear broken skeletal zircon; two fractions were concordant and near concordant (< 1 % discordant) at 603 +/- 2 Ma (figure 4.24 a). 2) the felsite sample yielded fine-grained zircon prisms (two fractions); these gave a preliminary estimate of the age as 605 +/- 5 Ma (figure 4.24 b).

These dates are useful in addressing the first two goals of the geochronological study as outlined above. The first interpretation that can be derived from the dates is that they confirm that much, if not all, of the magmatism associated with PHIS occurred at a late NeoProterozoic age. The other major implication is the minimum age of the host

sedimentary unit. Since both the gabbro and the felsic material intruded the host sedimentary unit, its minimum age is approximately 605 Ma. Therefore these strata are too old to be part of the ca. 590-570 Ma Marystown Group or the ca. 570 Ma Marystown Group. These age constraints, when interpreted in association with the lithology of the sedimentary group, imply that the intruded sedimentary rock belongs to the Connecting Point Group.

As mentioned above, additional field evidence (after more stripping of the outcrop) implies that the two dates are uninformative with respect to bracketing the age of mineralization. However, if the geochronological results of the post-breccia fine-grained gabbro indicate that it, like the other intrusive phases, is NeoProterozoic in age (as would be expected due the above arguments with respect to the fractional relationship between the pre and post-breccia gabbro/diorite units), this would imply that both the mineralization and brecciation would have formed between 600-610 Ma, during a more extensive magmatic hydrothermal event (O'Brien et al., 2000). Under these circumstances, the Lodestar Prospect would be the first example of precious metal mineralization of this age, style, and regional setting to be discovered in the western Avalon Zone. If this is the case, the Lodestar Prospect should serve to attract more exploration and prospecting within the belt of Connecting Point sediments (and the many mafic sills, dykes, plugs, and intrusions associated with it) ranging from Bonavista Bay in the north to Long Island in Placentia Bay to the south (O'Brien et al., 2000, O'Driscoll and Muggeridge, 1978).

Legend of geochemical symbols

◆ Pre-breccia medium-grained gabbro/diorite
● Post-breccia fine-grained gabbro/diorite
■ Felsic intrusive phase
△ Diabase
□ Felsic clasts from Lodestar breccia
◇ Medium-grained gabbro/diorite clasts from Lodestar breccia
✳ Mineralization

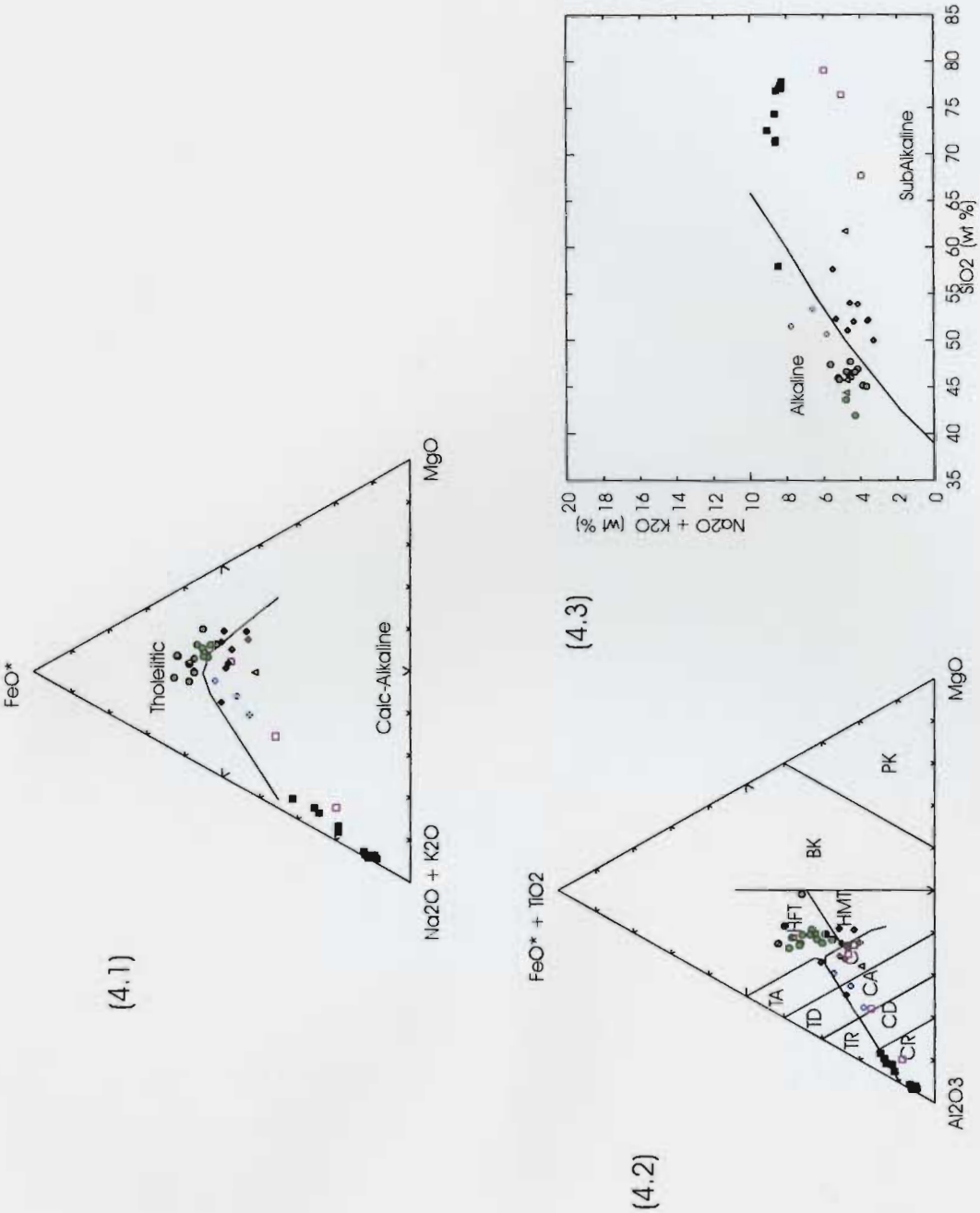

Figures 4.1 - 4.3: Irvine and Baragar's (1971) AFM plot (4.1), Jensen's (1976) cation plot (4.2), and Irvine and Baragar's (1971) TAS plot (4.3).

4.4 a)

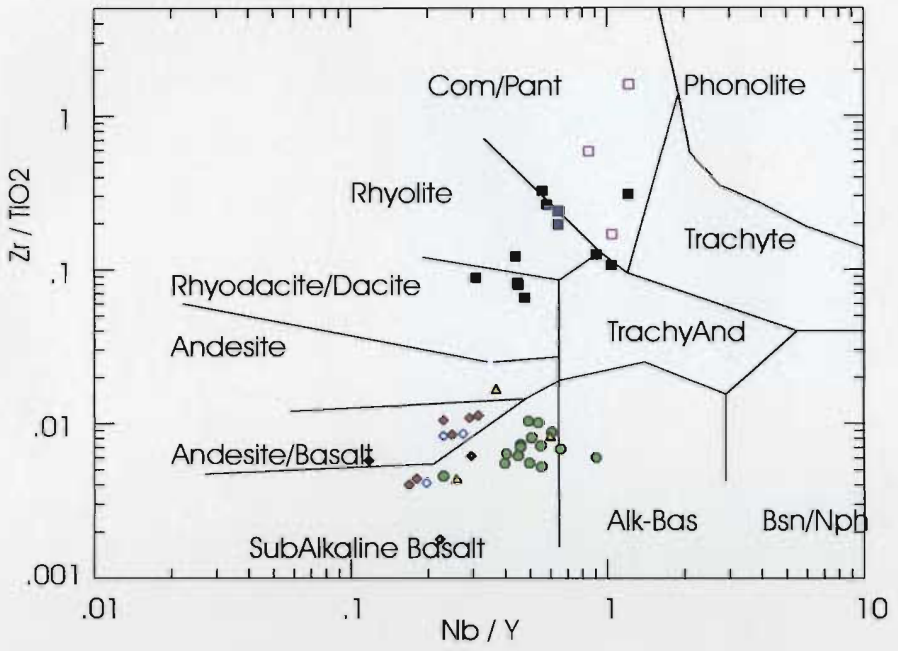

4.4 b)

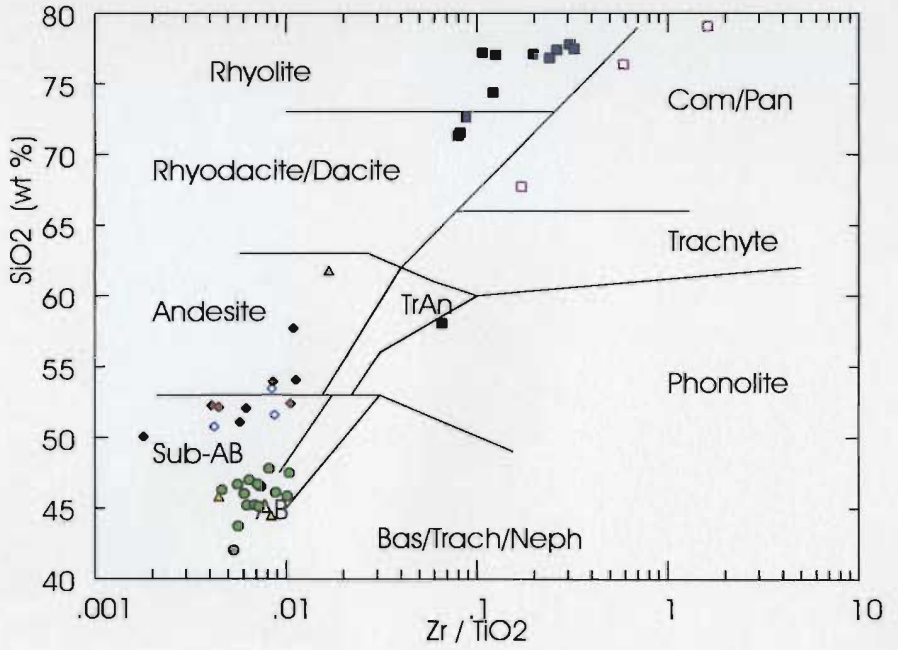

Figure 4.4 a,b: Winchester and Floyd's (1977) trace element discrimination plots for data from the PHIS.

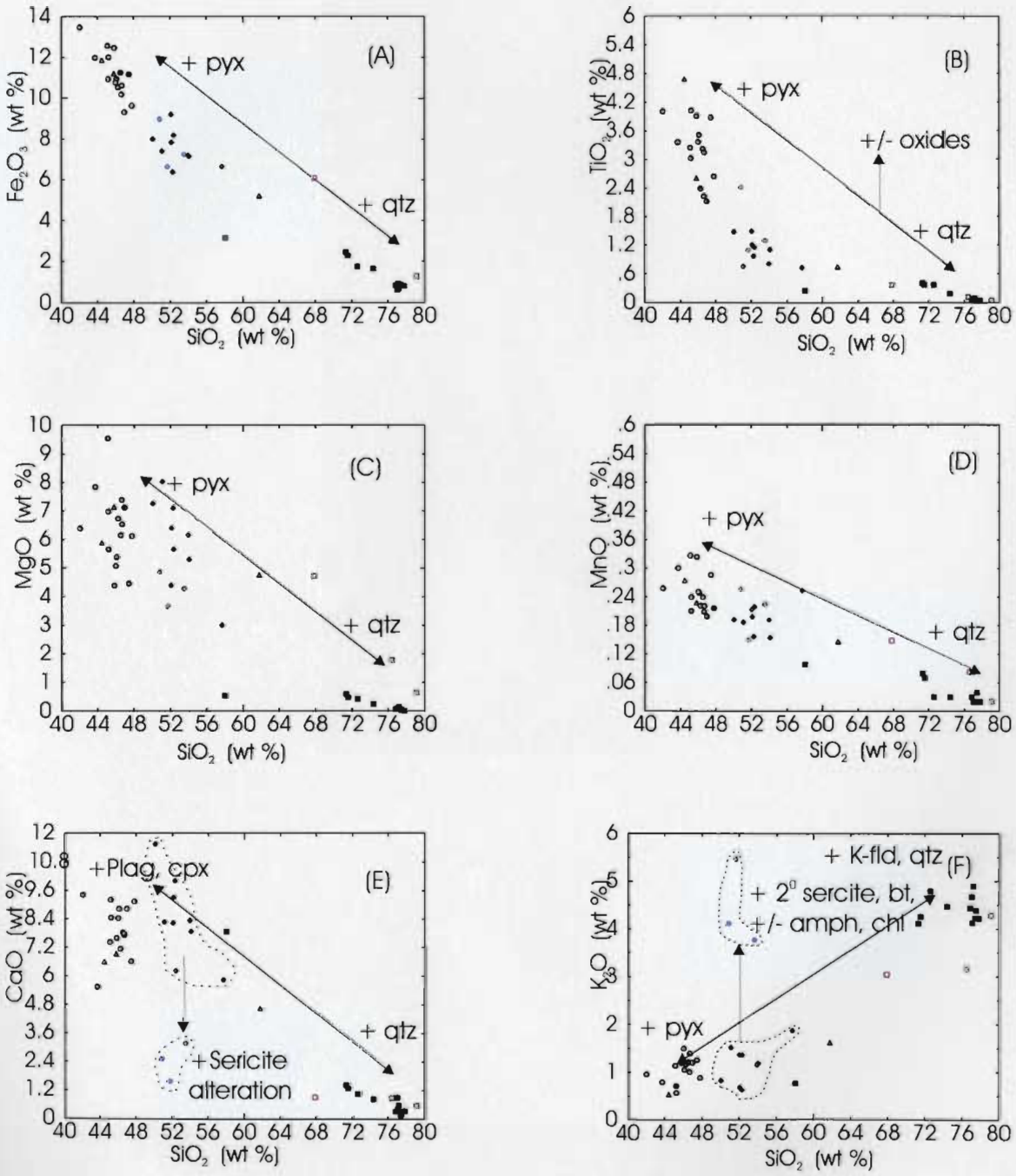

Figure 4.5: SiO_2 versus major elements including (a) Fe_2O_3, (b) TiO_2, (c) MgO, (d) MnO, (e) CaO, (f) K_2O, (g) Na_2O, (h) Al_2O_3.

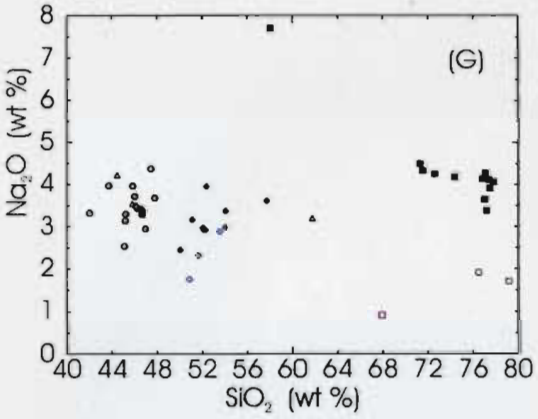

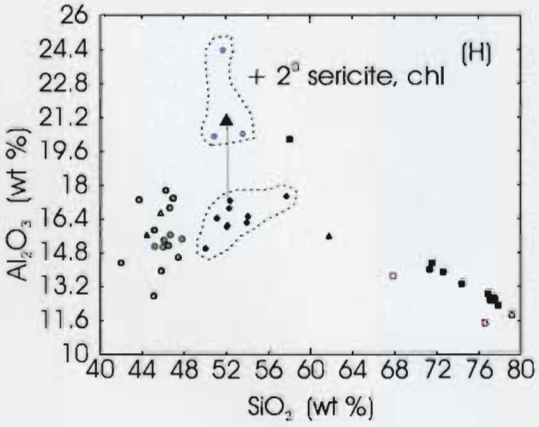

Figure 4.5 continuued

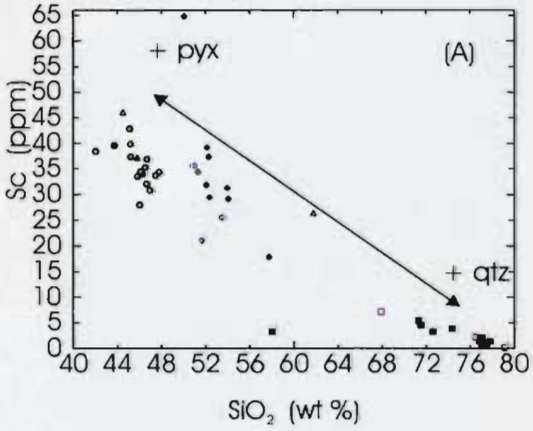

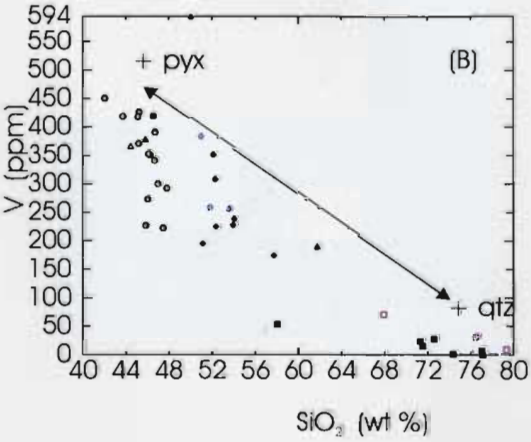

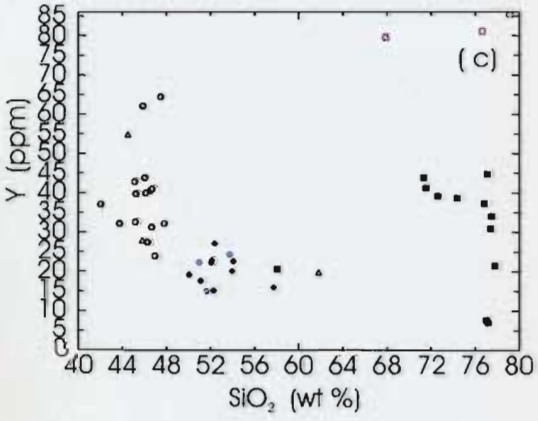

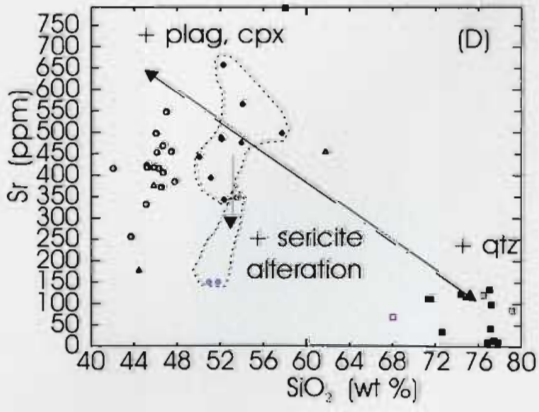

Figure 4.6: SiO_2 versus trace elements including (a) Sc, (b) V, (c) Y, (d) Sr, (e)Rb, (f) Ga, (g) Zr, (h) Ta, (i) Nb

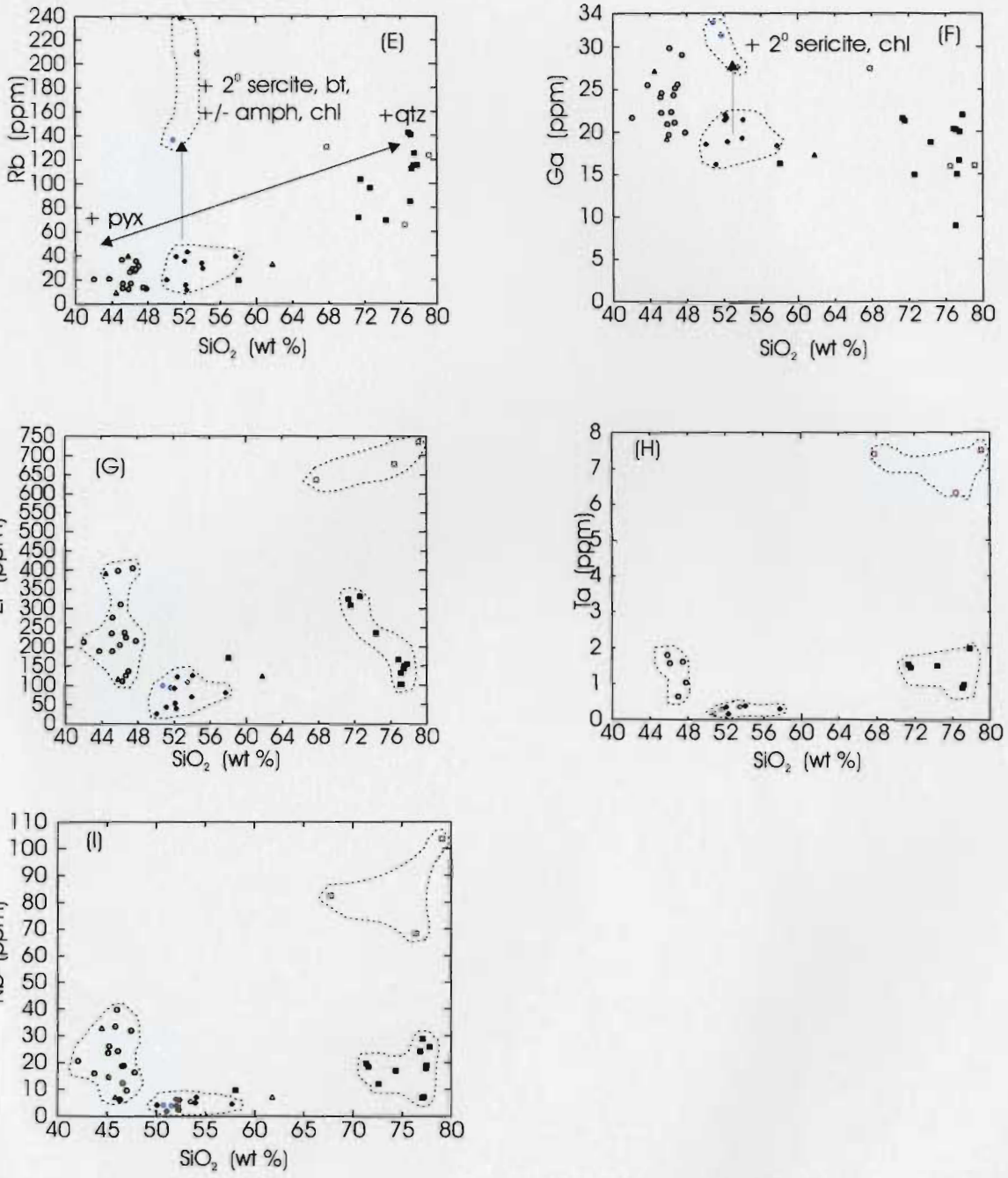

Figure 4.6 continued

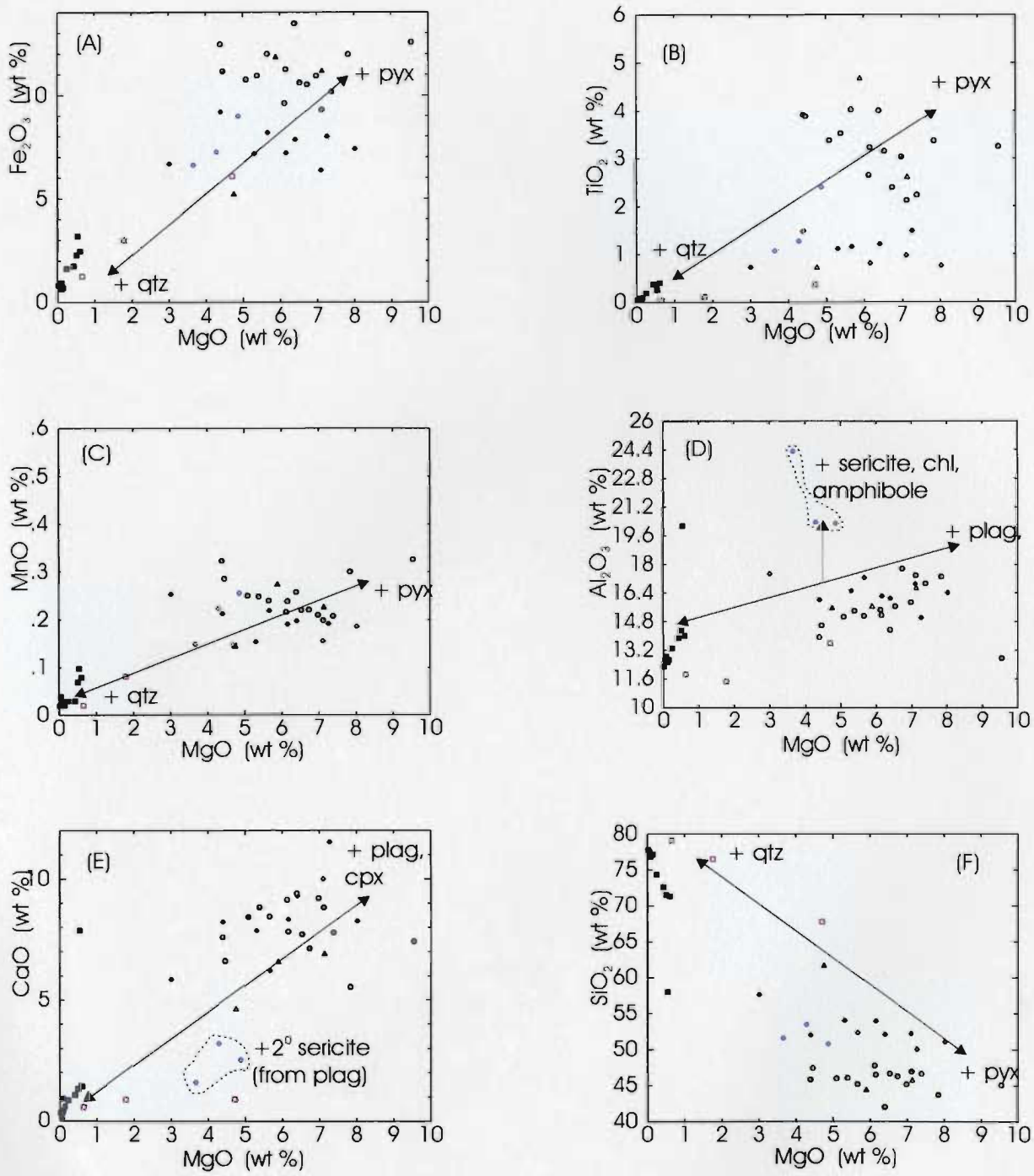

Figure 4.7: MgO versus major elementsincluding (a) Fe_2O_3, (b) TiO_2, (c) MnO, (d) Al_2O_3, (e) CaO, (f) SiO_2, (g) K_2O

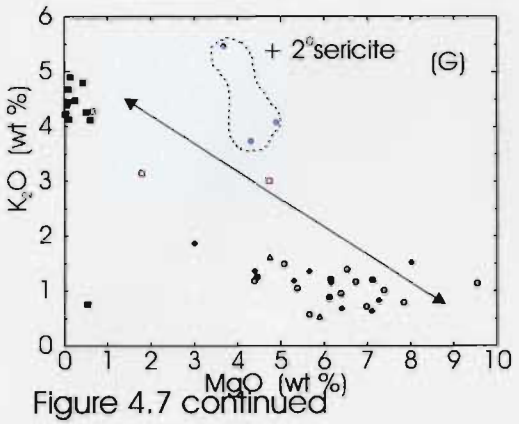

Figure 4.7 continued

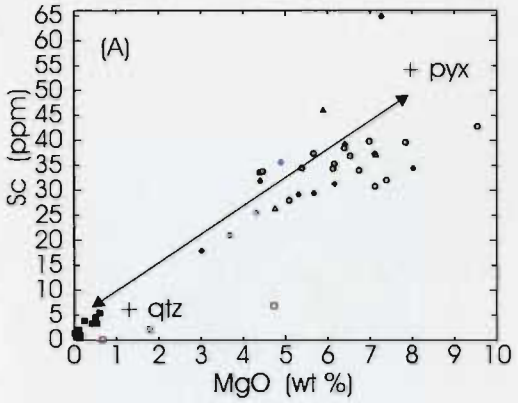

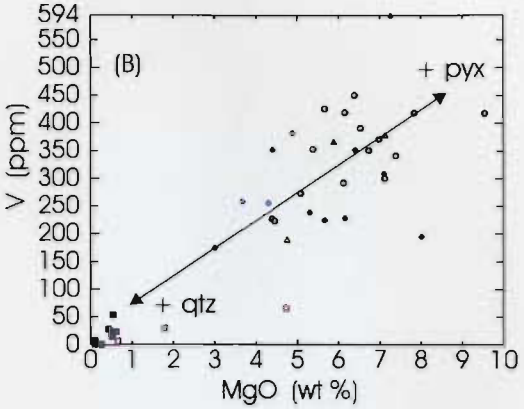

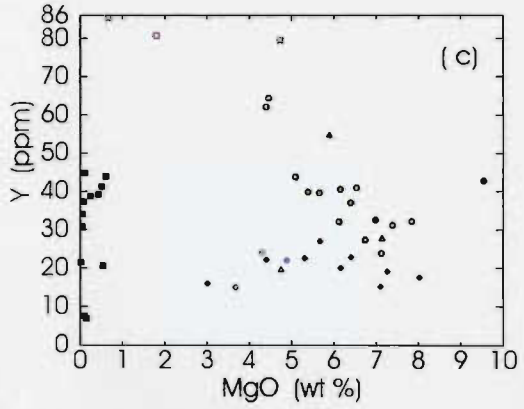

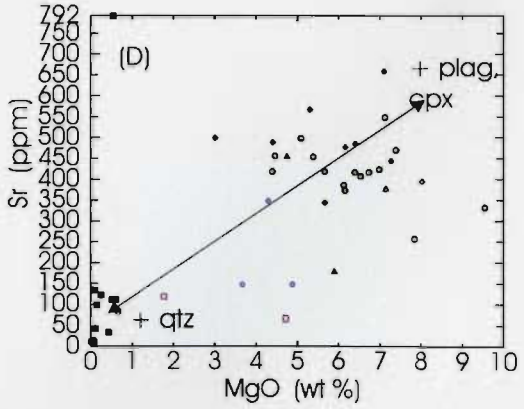

Figure 4.8: MgO versus trace elements including (a) Sc, (b) V, (c) Y, (d)Sr, (e)Rb, (f) Ga, (g) Zr, (h) Ta, (i) Nb

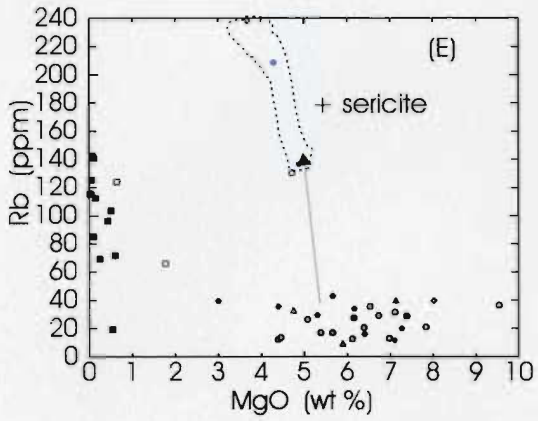

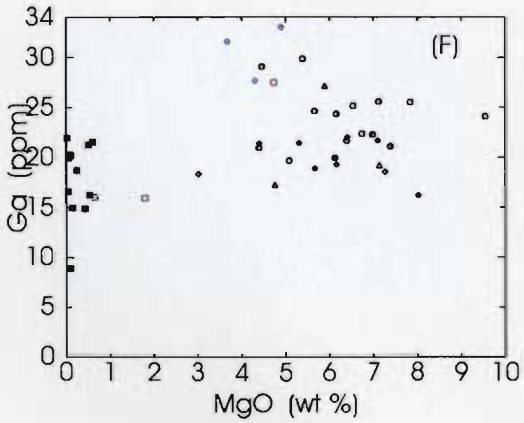

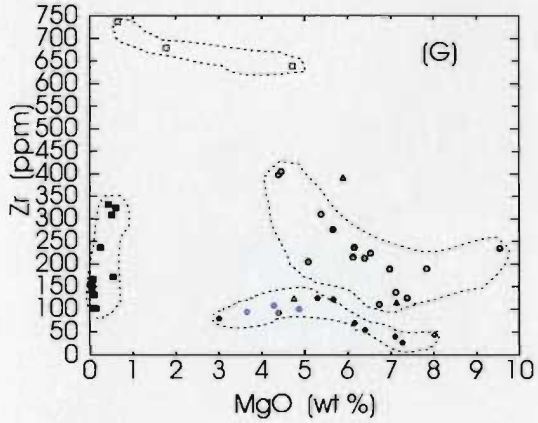

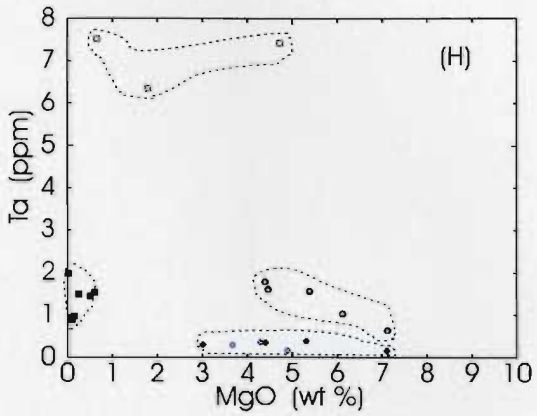

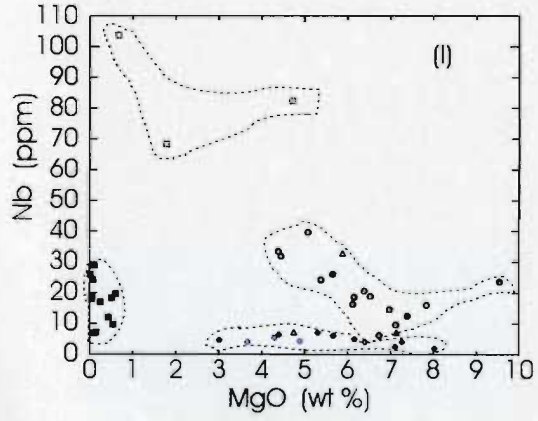

Figure 4.8 continued

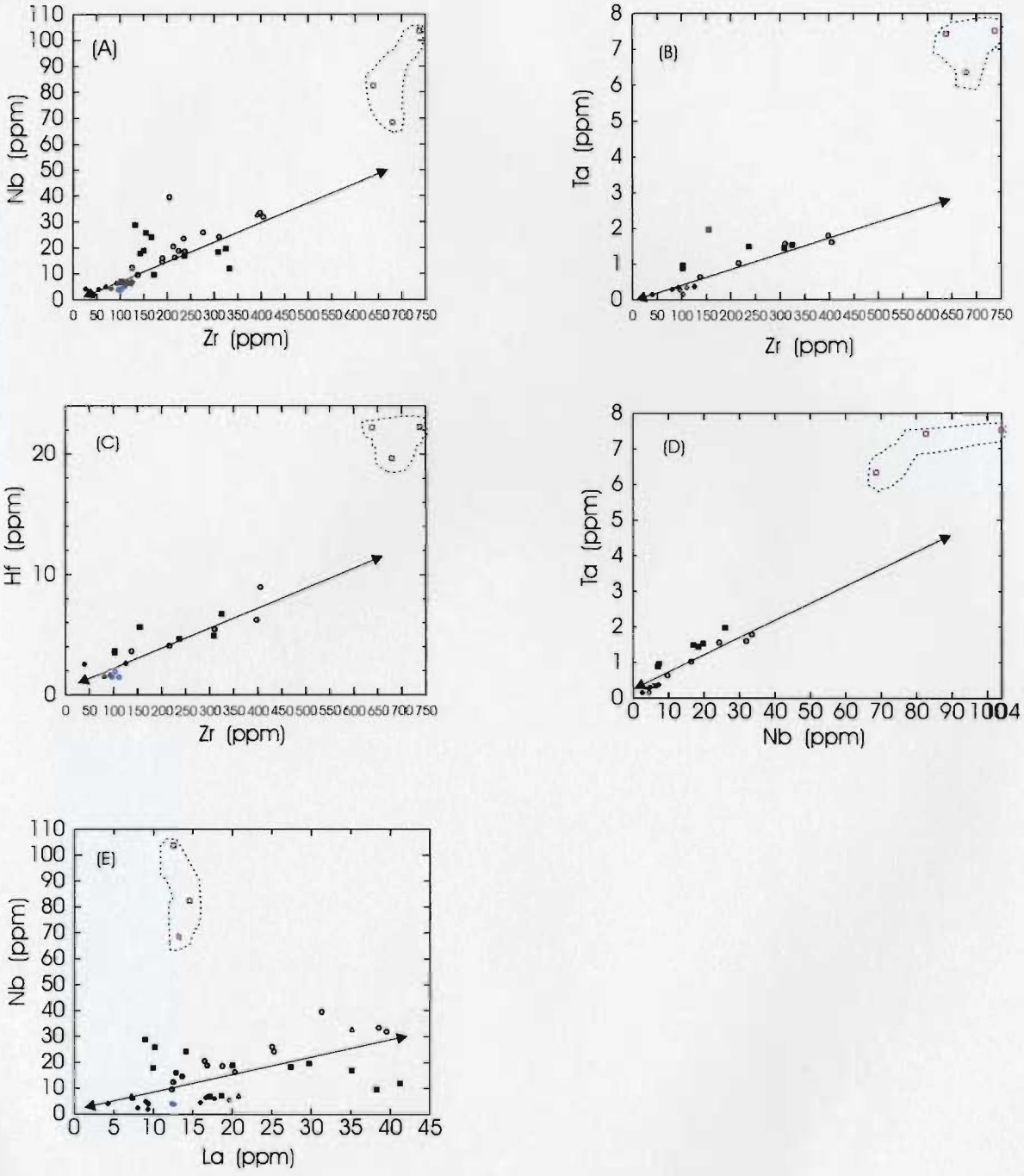

Figure 4.9: Ratio plots of immobile/incompatible elements including Zr versus Nb (a), Ta (b), Hf (c), Nb versus Ta (d), and La versus Nb (e)

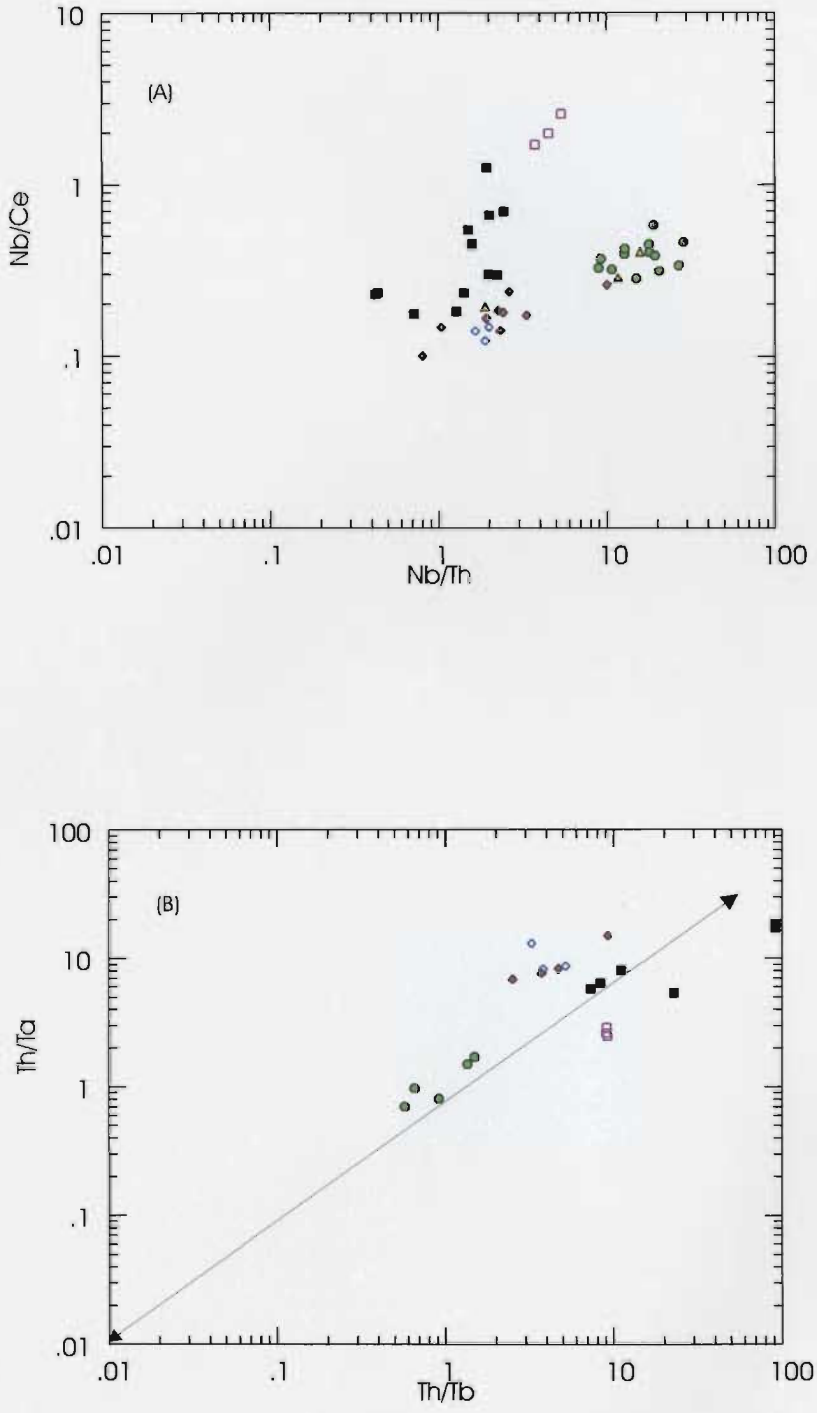

Figure 4.10: Ratio-ratio plots including Nb/Th versus Nb/Ce (a) and Th/Tb versus Th/Ta (b)

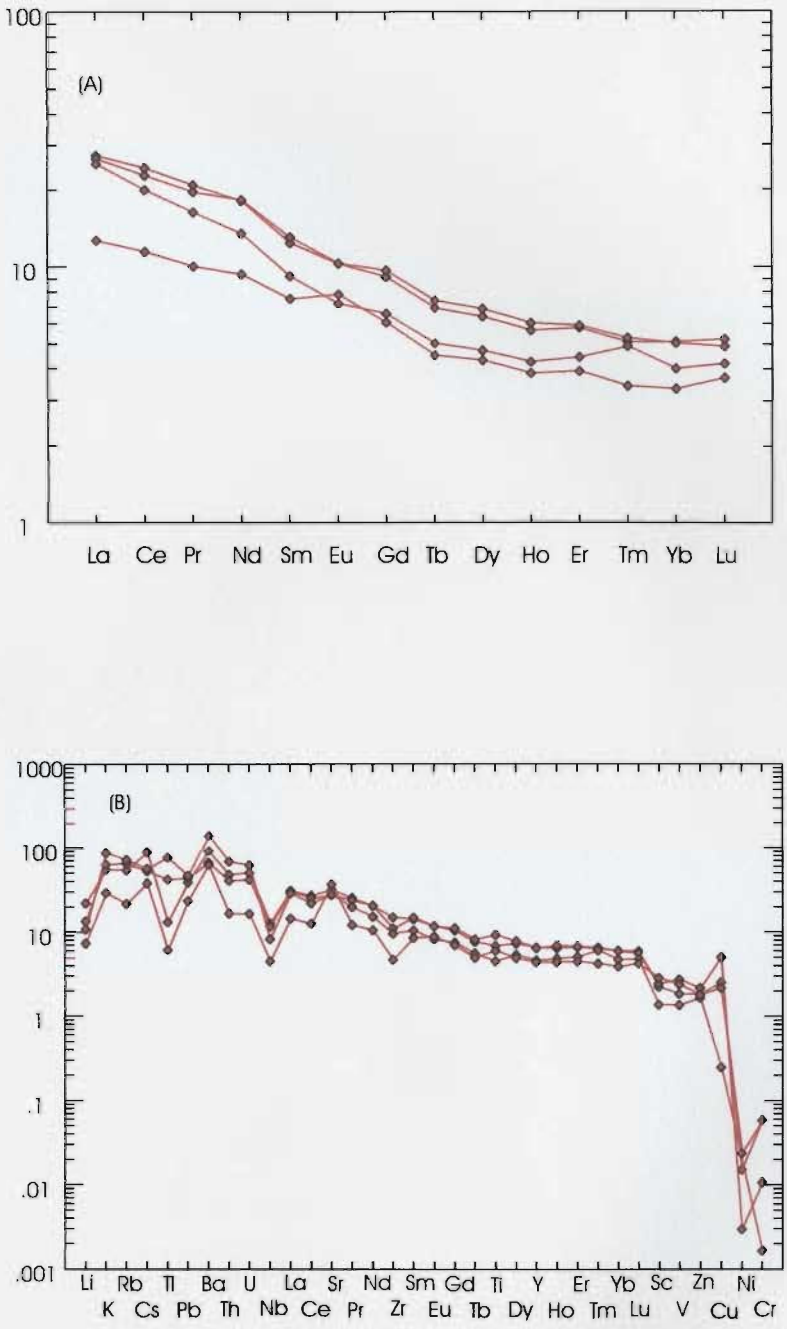

Figure 4.11: (a)Primitive mantle normalized REE plot and, (b) primitive mantle normalized extended trace element plot of the pre-breccia gabbro/diorite.

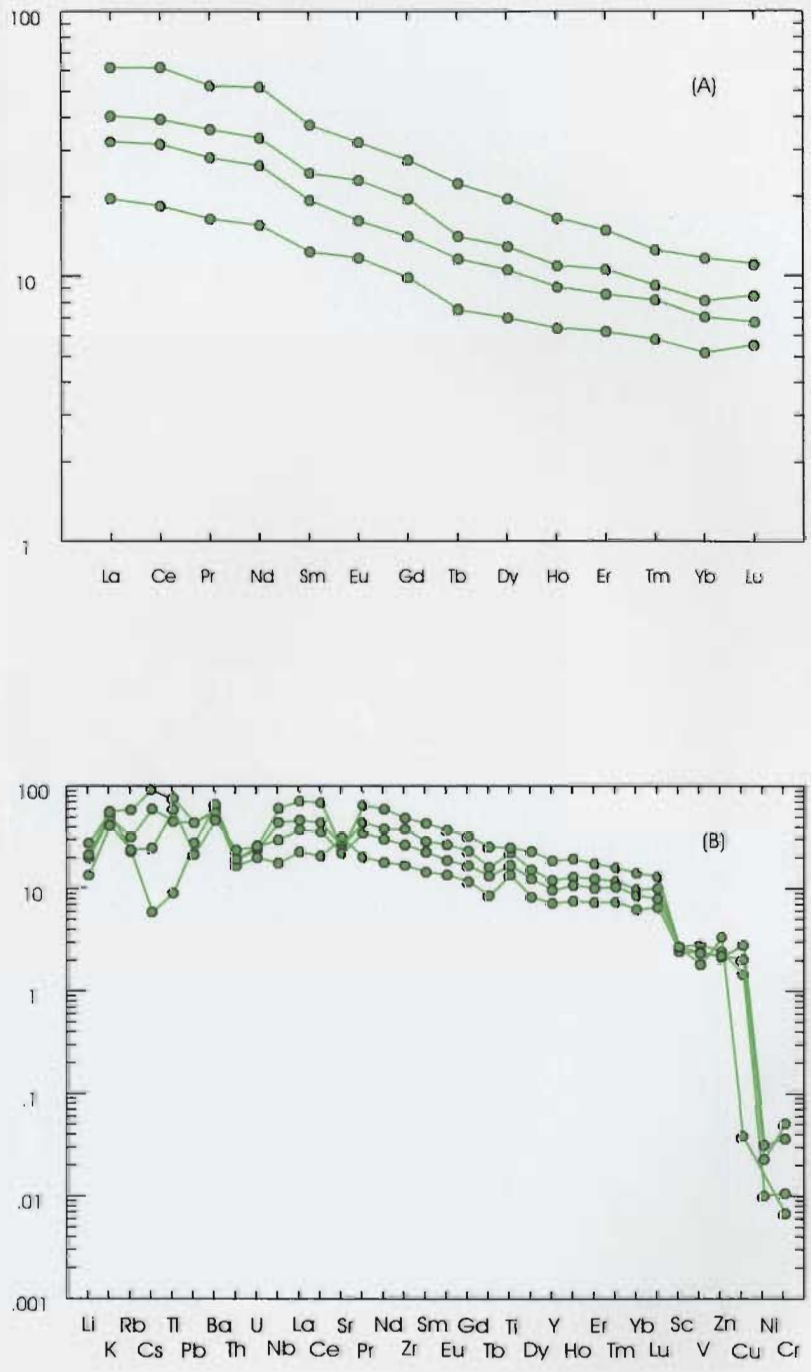

Figure 4.12: Primitive mantle normalized REE plot (a) and primitive mantle normalized extended trace element plot (b) of the post-breccia gabbro/diorite.

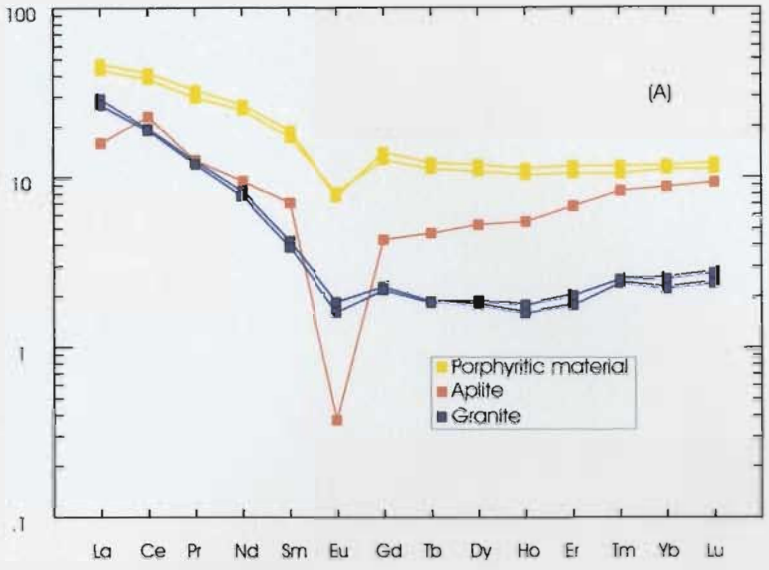

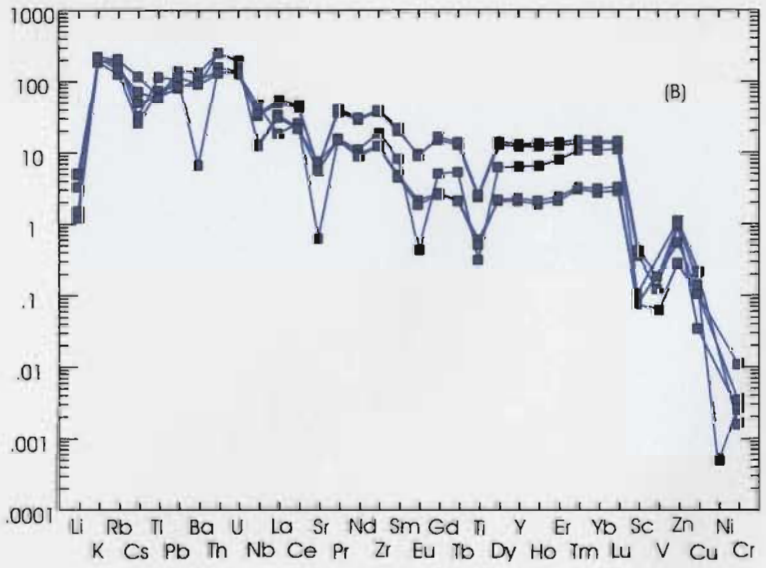

Figure 4.13: Primitive mantle normalized REE plot (a) and primitive mantle normalized extended trace element plot (b) of the felsic intrusive phase. Refer to text for explanation of different symbols for figure 4.13 a.

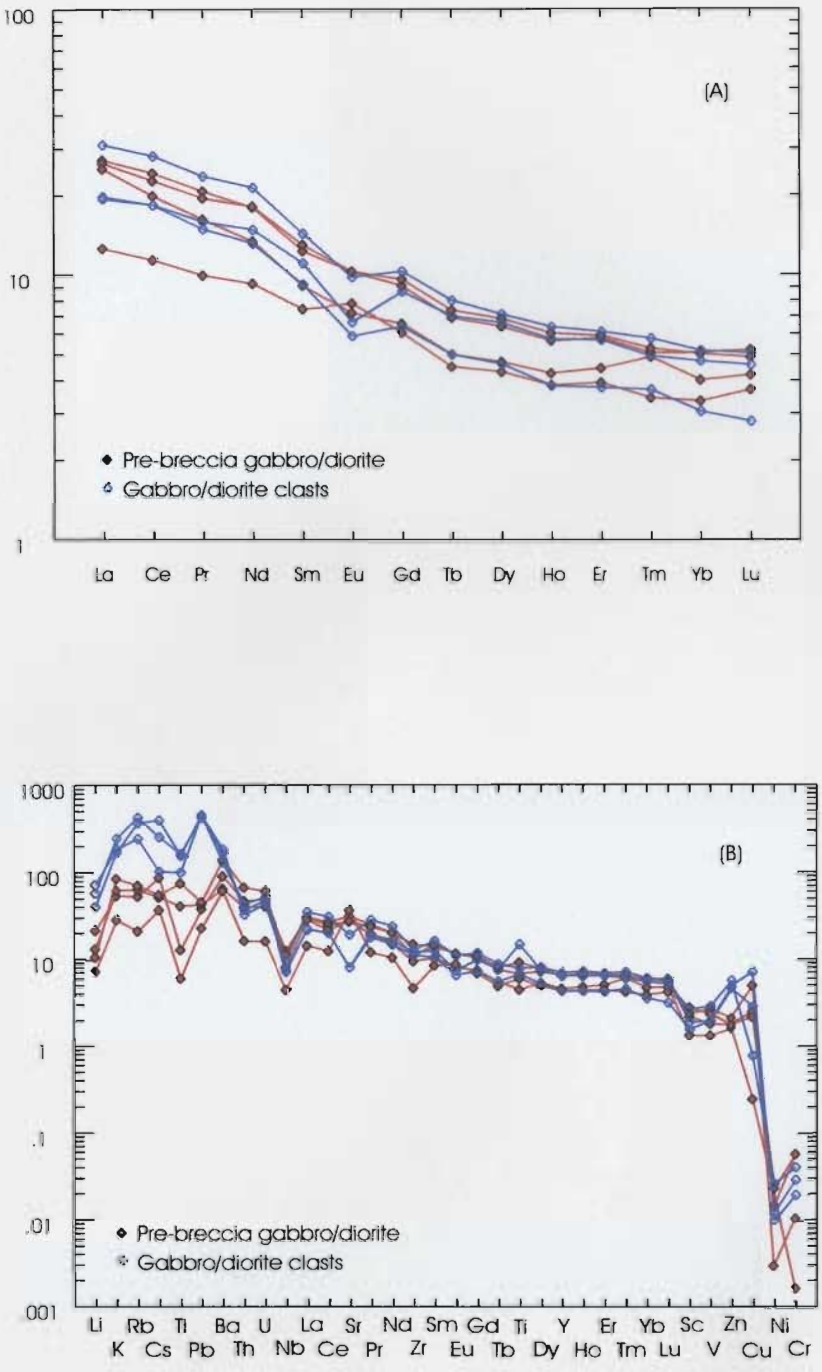

Figure 4.14: Primitive mantle normalized REE plot (a) and primitive mantle normalized extended trace element plot (b) of the pre-breccia gabbro/diorite and the gabbroic clasts.

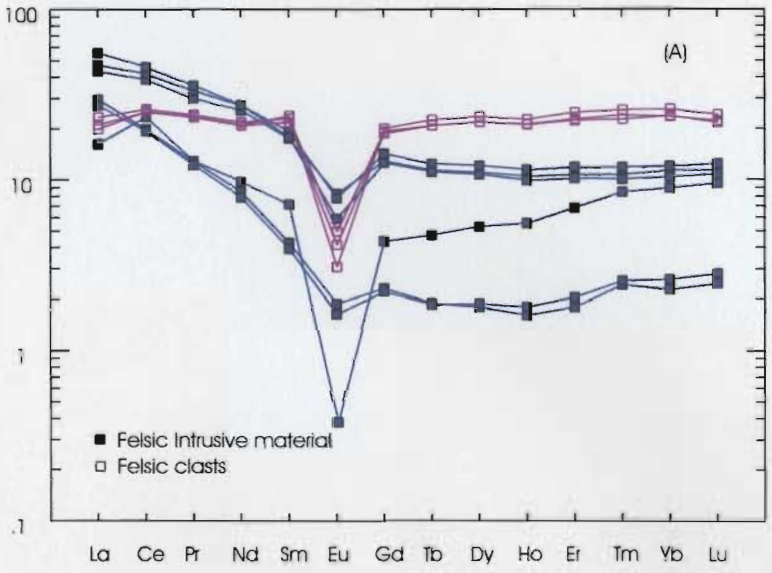

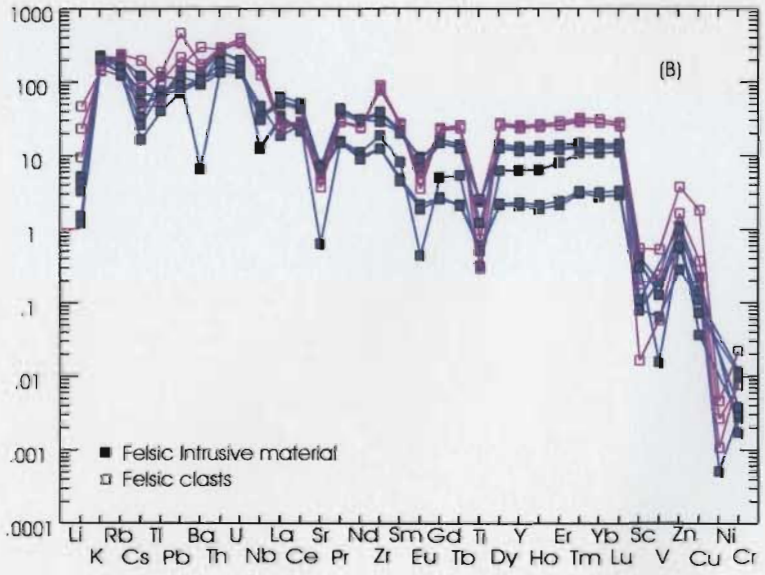

Figure 4.15: Primitive mantle normalized REE plot (a) and primitive mantle normalized extended trace element plot (b) of the felsic intrusive phase and the felsic clasts.

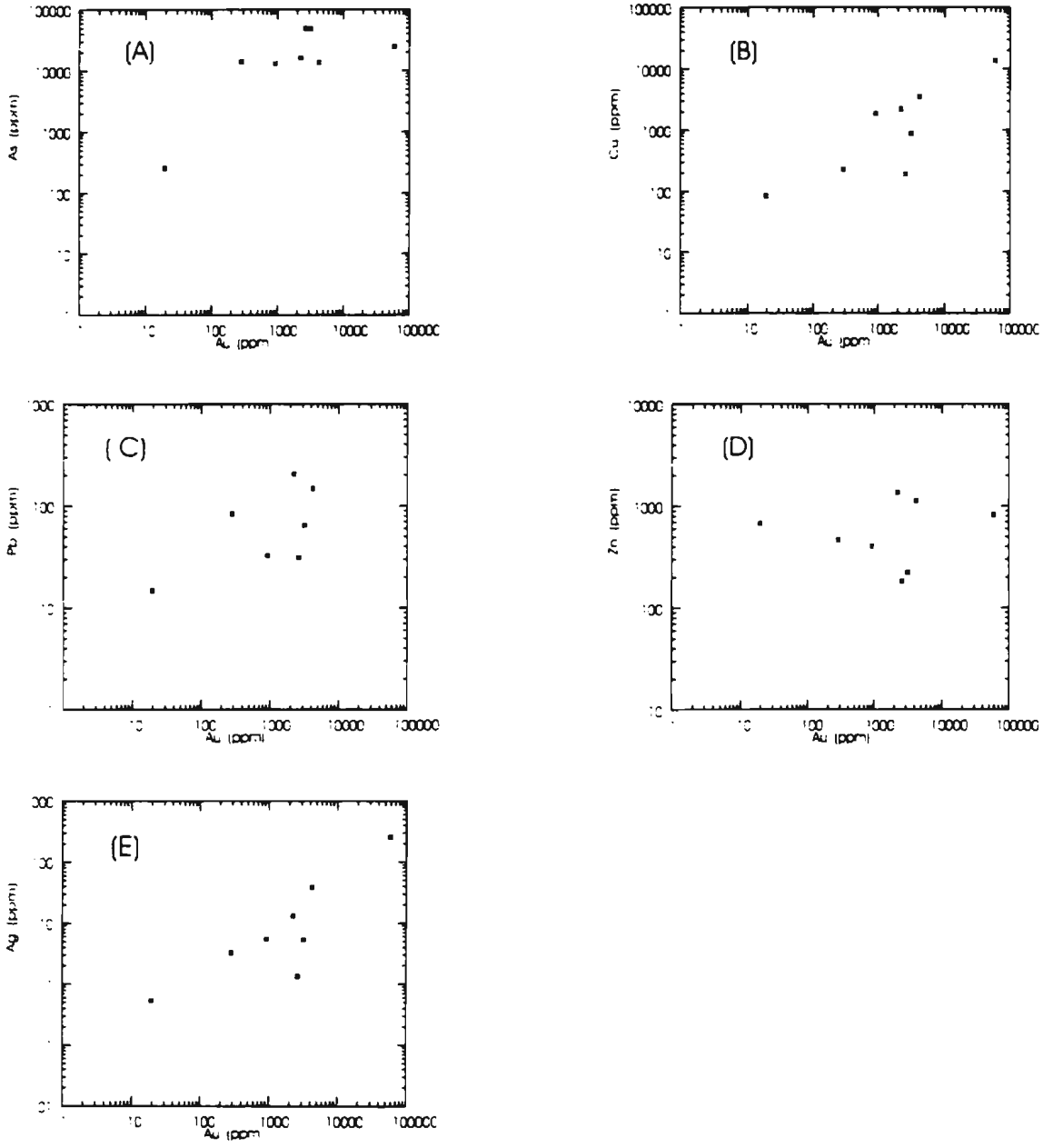

Figure 4.16: Plots of Au versus economic elements consisting of (a) As, (b) Cu, (c) Pb,(d) Zn, (e) Ag

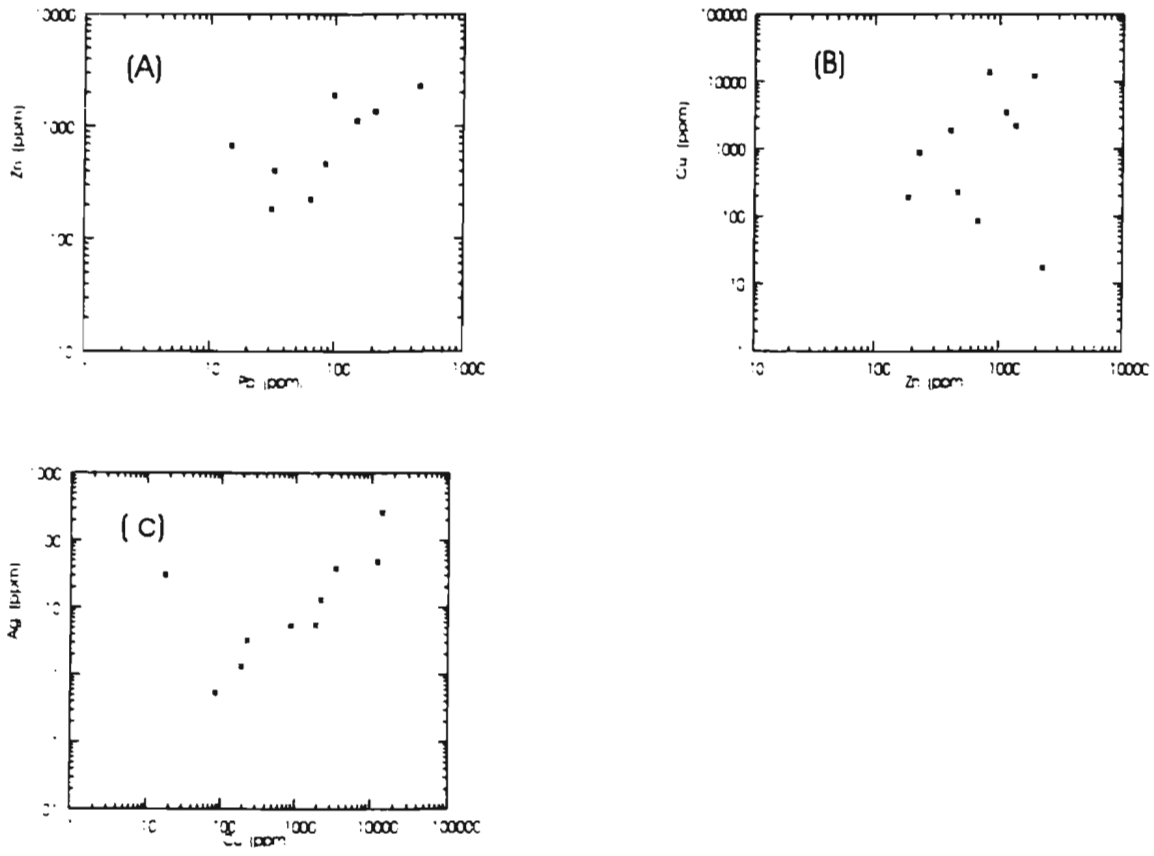

Figure 4.17: additional bivariate plots of economic elements consisting of (a) Pb vs Zn, (b) Zn vs Cu, and (c) Cu vs Ag

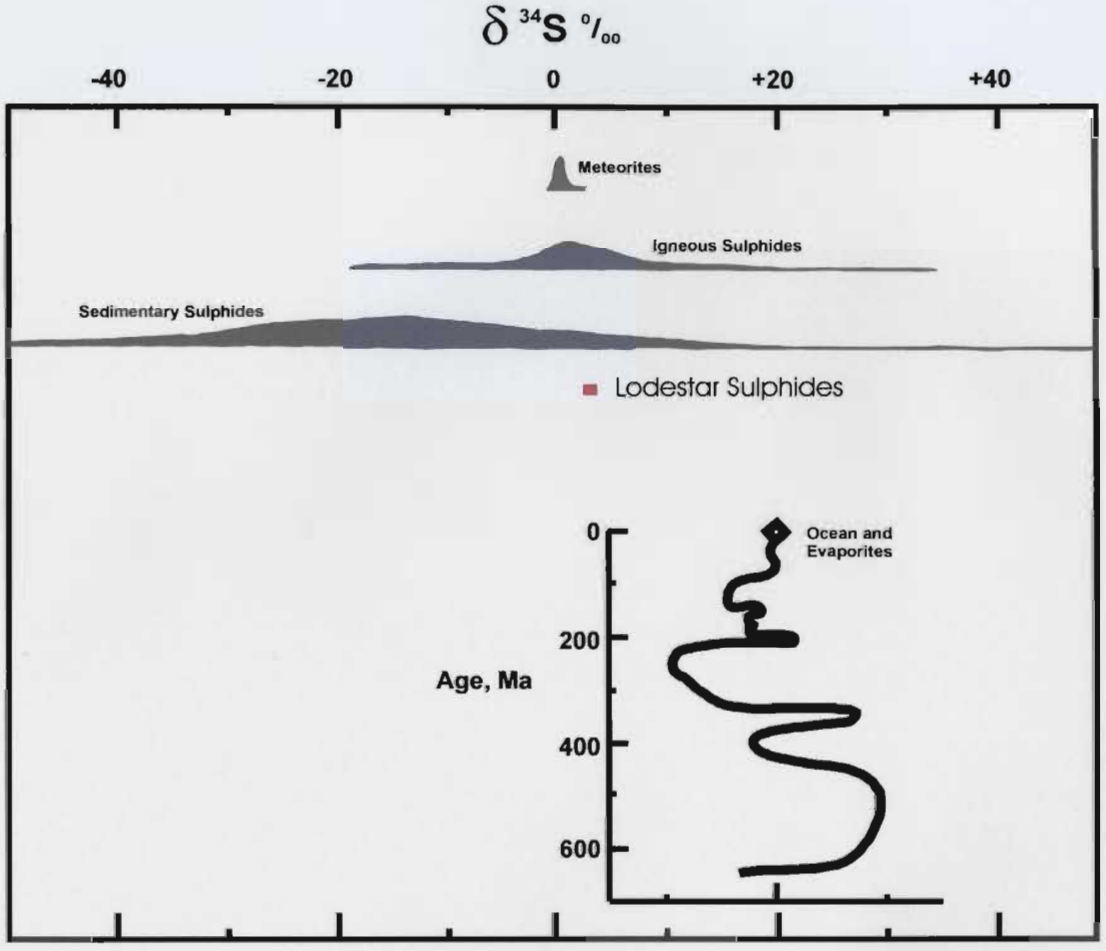

Figure 4.18: Range of $\delta\ ^{34}S$ values for igneous and sedimentary sulphur sources. (From Ohomoto and Rye, 1979). Note position of Lodestar $\delta\ ^{34}S$ ratios.

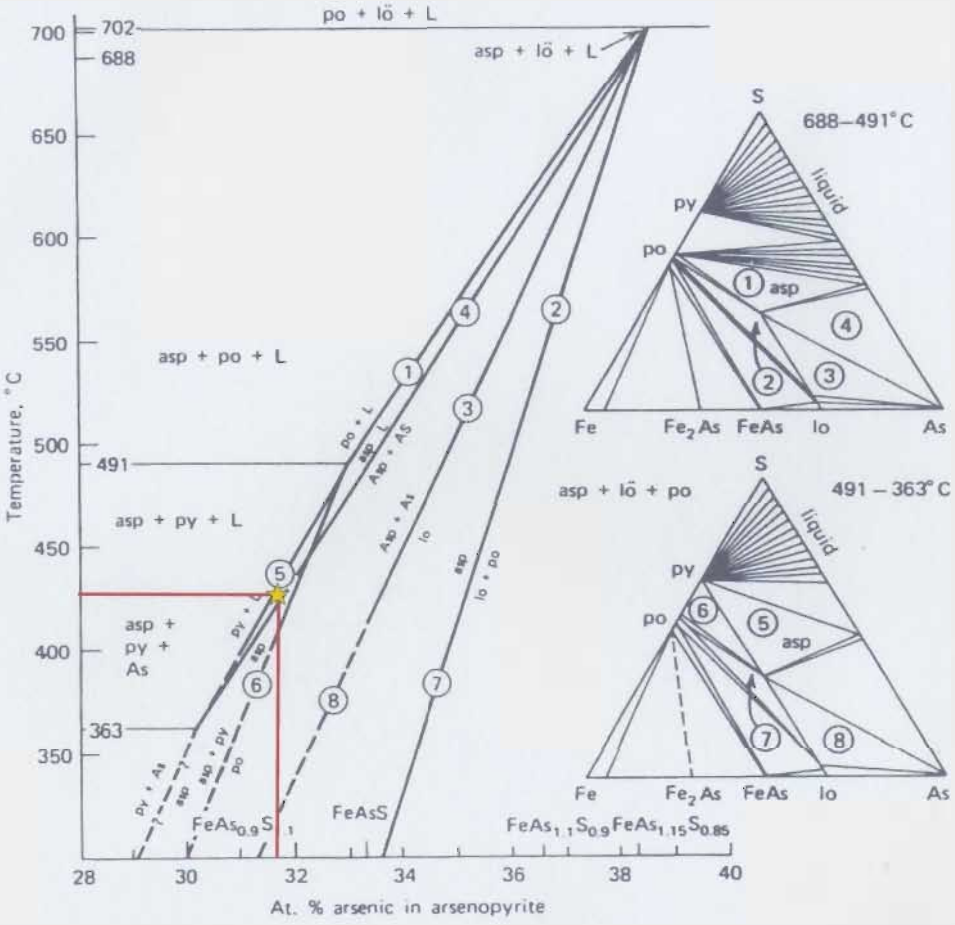

Figure 4.19: Phase relationships in the Fe-As-S system and a pseudobinary temperature-composition projection showing arsenopyrite as a function of temperature and equilibrium mineral assemblages. (From Barnes, 1977, after Kretschmer and Scott, 1976). The assemblages labelled 1-8 in the triangular diagrams correspond to the labeled curves in the composition diagram. The average At. Wt % As of arsenopyrite samples from the Lodestar Prospect is plotted on the diagram; the yellow star plots where this At. Wt % intersects with the equilibrated mineral assemblage (# 5) at the Lodestar Prospect; from which an approximate temperature of mineralization is determined (~425° C). Abbreviations are: asp=arsenopyrite; py=pyrite; po=pyrrhotite; lo=loellingite; and l=liquid.

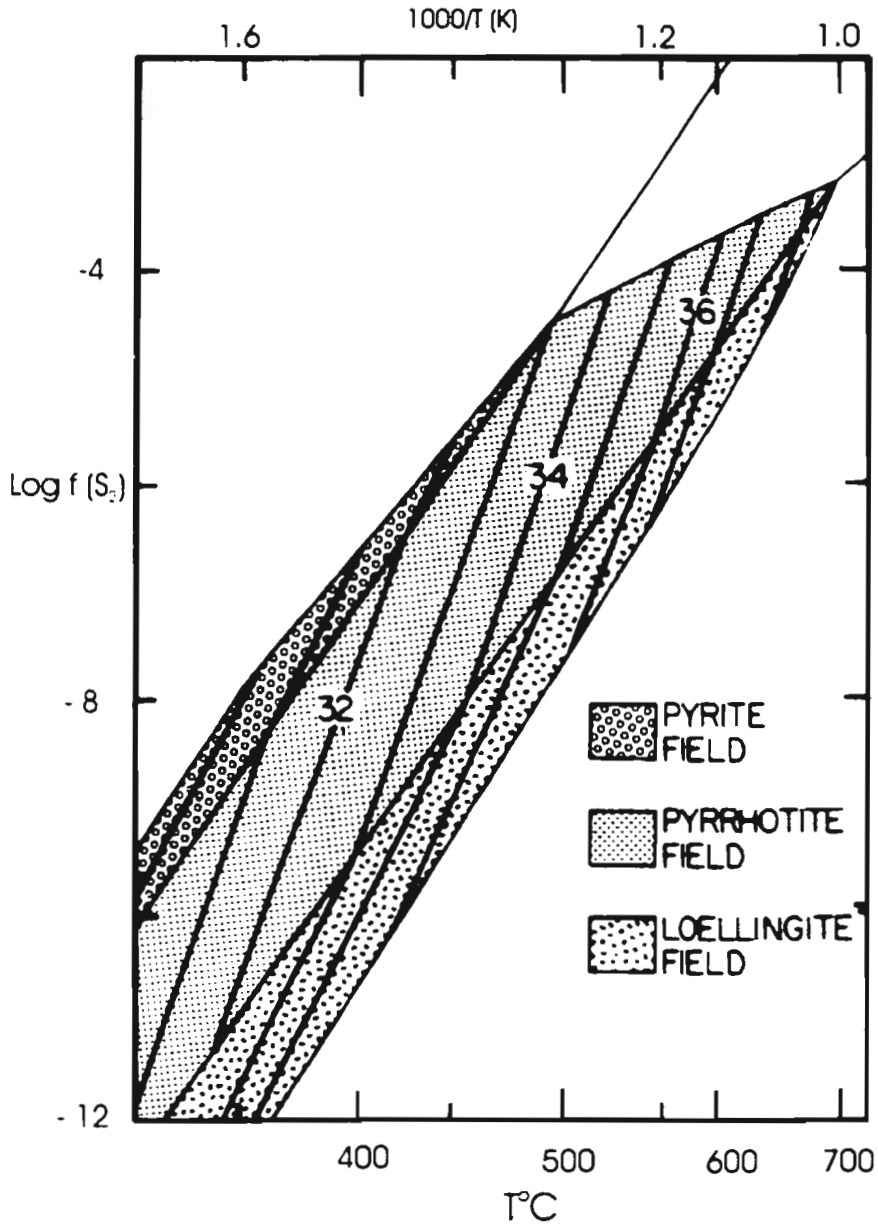

Figure 4.20: Isopleths of arsenopyrite superimposed on Barton's (1969) f (S_2)-T plot. After Kretschmar and Scott (1976).

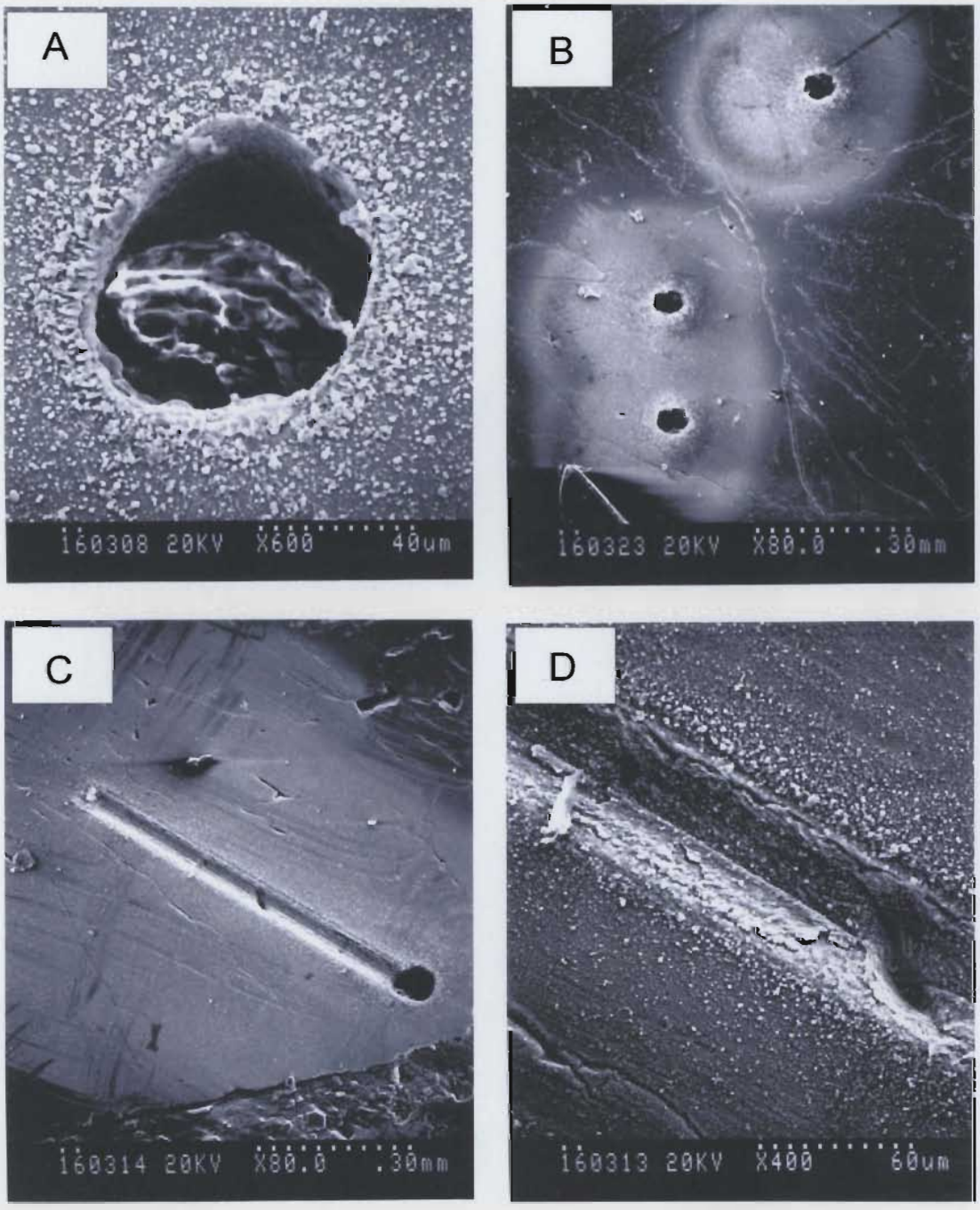

Figure 4.21: Backscatter electron images from SEM illustrating single spot ablation pits (A,B) and line raster pits (C,D) within arsenopyrite. Note the variable ablation within the line raster as illustrated in D (blowup of C).

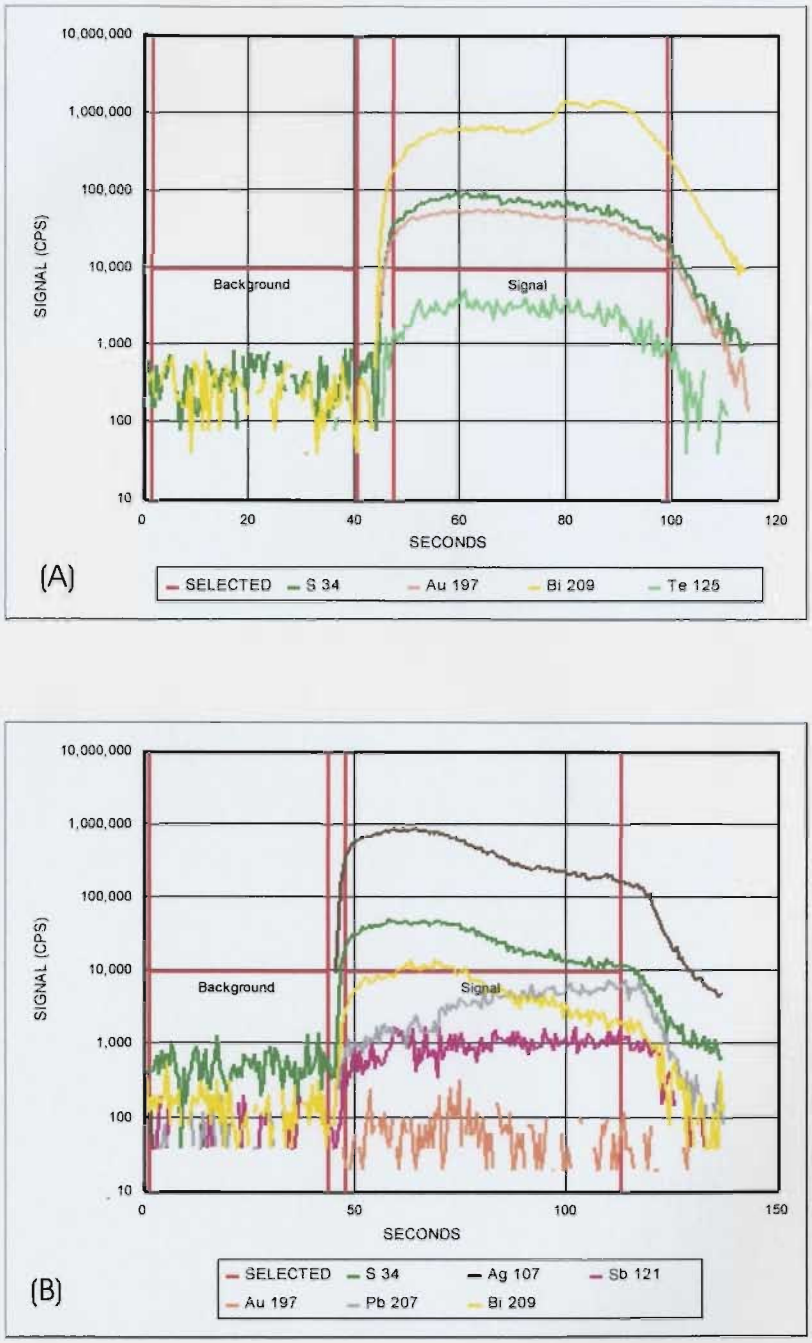

Figure 4.22: Typical results recorded as counts per second (cps) vs time obtained from single spot ablation pits in the three main sulphide phases of Arsenopyrite, Pyrite, and chalcopyrite;A,B,and C respectively. Note much higher cps acquired for the arsenopyrite, thereby suggesting a chemical association between As and Au.

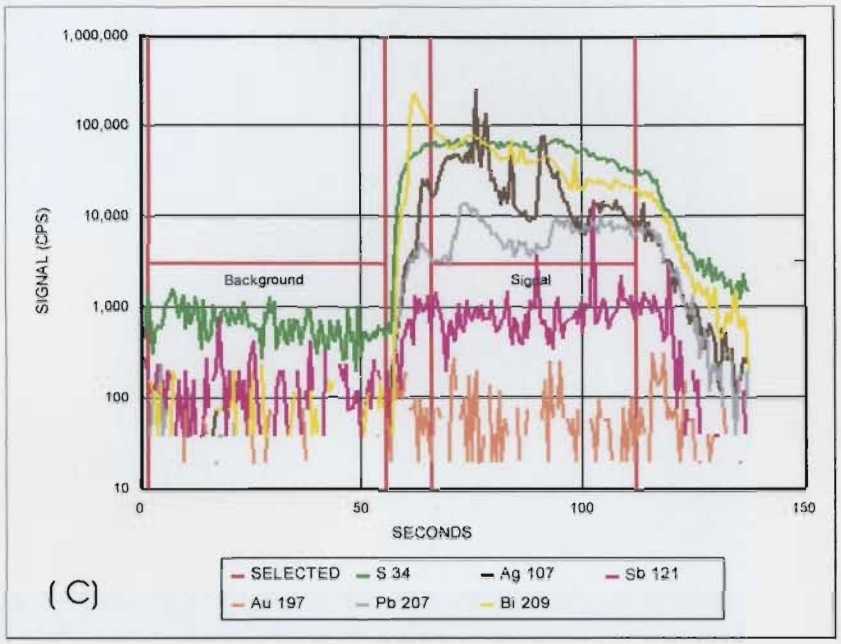

Figure 4.22 continued.

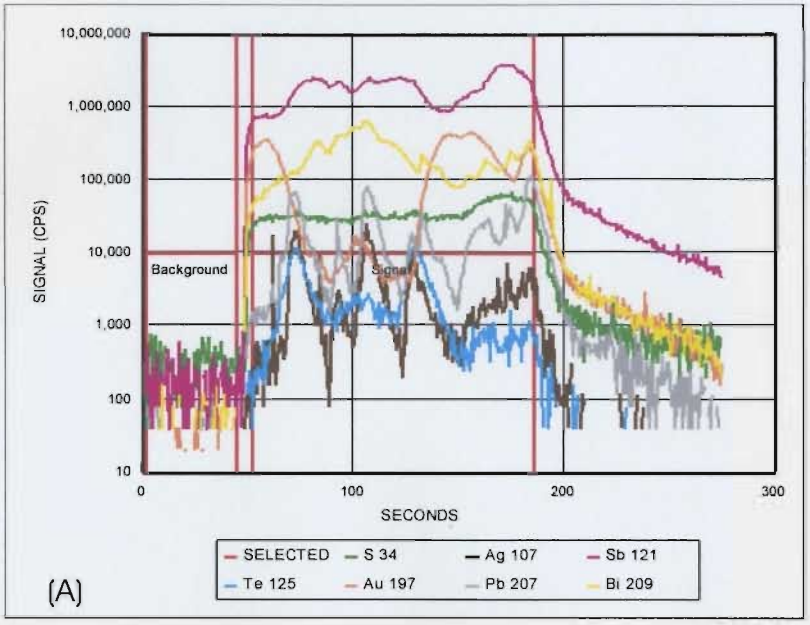

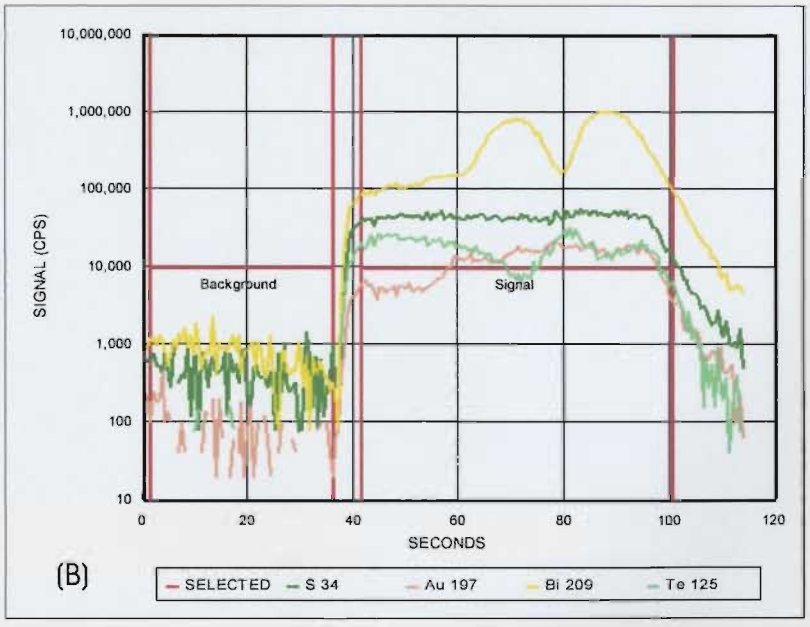

Figure 4.23 : Results obtained in counts per second vs time for two separate line rastered ablations within arsenopyrite. Note that results in A indicate that although the Au is "homogeneous" (ie.no nugget effect) within the arsenopyrite there is internal variation presumablyrelated to crystal zoning and variations in atomic weight % As and Fe. However, the raster recorded in B indicates that this variation is limited, supported by the fact that most single spot and line rasters result in flat Au signal, suggesting homogeneity.

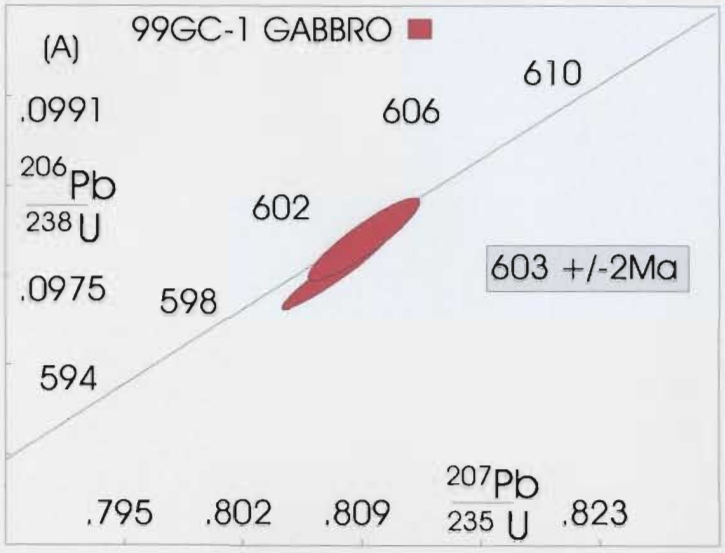

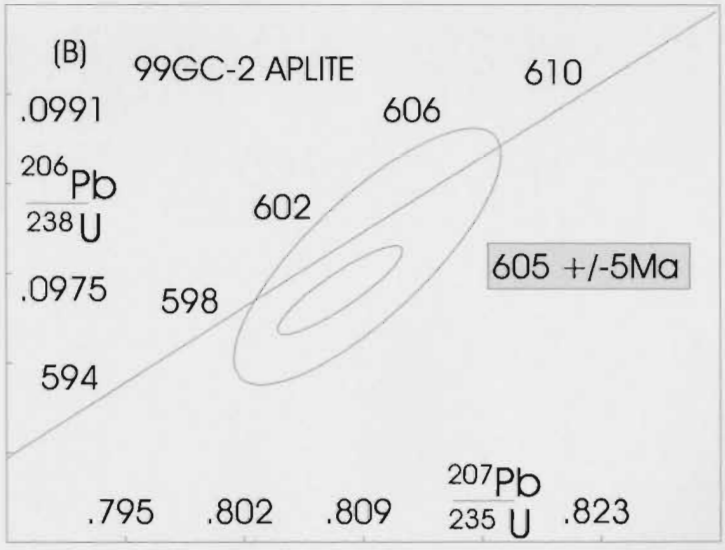

FIGURE 4.24: U-Pb concordia zircon diagrams (a) for the pre-breccia gabbro/diorite and (b) felsic intrusive phases of the PHIS.

Plate 4.1: a) Photograph illustrating the dated felsic dyke (white) being cut off by breccia; b) blow-up of same outcrop illustrating the presence of felsic clasts (white) within the breccia. These photographs serve as evidence for the reinterpretation of the dated felsic dyke (previously belied to be of post-breccia origin) as being pre-breccia. See text for discussion.

Table 4.1 a: Average composition, standard deviation, and maximum/minimum values for major elements (wt %) in each of the major rock groups.

Rock Type	Pre-Breccia Gabbro/Diorite				Post-Breccia Gabbro/diorite			
Oxide	*Mean*	*Std*	*Max*	*Min*	*Mean*	*Std*	*Max*	*Min*
SiO2	51.24	2.71	56.97	46.91	43.62	1.74	46.44	40.03
TiO2	1.05	0.26	1.47	0.72	3.05	0.58	3.89	2.03
Al2O3	15.95	0.82	17.26	14.08	14.78	1.36	16.86	11.34
Fe2O3	10.47	1.11	12.94	8.77	15.20	1.44	18.66	12.71
MnO	0.19	0.03	0.25	0.15	0.24	0.04	0.31	0.19
MgO	5.73	1.37	7.75	2.97	6.06	1.12	8.47	4.21
CaO	8.14	1.51	10.83	5.78	7.63	1.07	9.13	5.17
Na2O	3.07	0.42	3.80	2.30	3.30	0.43	4.13	2.25
K2O	1.15	0.38	1.85	0.61	1.02	0.23	1.44	0.55
P2O5	0.21	0.13	0.40	0.04	0.68	0.42	1.52	0.23

Rock Type	Felsic Intrusive Material				Diabase			
Oxide	*Mean*	*Std*	*Max*	*Min*	*Mean*	*Std*	*Max*	*Min*
SiO2	74.07	5.02	77.66	59.18	48.06	8.14	59.37	40.52
TiO2	0.17	0.14	0.41	0.05	2.50	1.45	4.27	0.71
Al2O3	13.68	2.17	20.54	12.28	15.14	0.78	16.16	14.28
Fe2O3	2.04	1.17	4.66	0.92	12.70	3.90	15.47	7.19
MnO	0.04	0.03	0.10	0.02	0.20	0.05	0.25	0.14
MgO	0.24	0.21	0.61	0.02	5.61	0.97	6.90	4.57
CaO	1.31	2.07	8.03	0.17	5.73	0.93	6.70	4.47
Na2O	4.39	1.09	7.86	3.37	3.46	0.31	3.85	3.09
K2O	4.11	1.03	4.87	0.78	1.07	0.44	1.56	0.49
P2O5	0.04	0.05	0.12	0.00	0.51	0.39	1.06	0.21

Rock Type	Felsic Clasts				Gabbroic Clasts			
Oxide	*Mean*	*Std*	*Max*	*Min*	*Mean*	*Std*	*Max*	*Min*
SiO2	70.27	7.19	76.04	60.14	48.11	1.81	50.15	45.75
TiO2	0.16	0.12	0.33	0.04	1.47	0.50	2.17	1.03
Al2O3	11.56	0.37	12.07	11.21	20.09	1.98	22.84	18.29
Fe2O3	4.56	2.46	7.75	1.76	10.09	1.10	11.58	8.94
MnO	0.08	0.04	0.13	0.02	0.19	0.04	0.23	0.14
MgO	2.18	1.49	4.18	0.62	3.95	0.39	4.39	3.44
CaO	0.75	0.14	0.88	0.56	2.26	0.62	3.00	1.49
Na2O	1.44	0.45	1.86	0.82	2.17	0.46	2.72	1.59
K2O	3.29	0.60	4.11	2.69	4.11	0.72	5.13	3.52
P2O5	0.04	0.03	0.08	0.01	0.46	0.06	0.50	0.37

Rock Type	Sediments				Mineralization			
Oxide	*Mean*	*Std*	*Max*	*Min*	*Mean*	*Std*	*Max*	*Min*
SiO2	56.29	0.65	56.93	55.64	47.21	4.08	52.83	38.61
TiO2	0.85	0.11	0.97	0.74	0.85	0.15	1.10	0.65
Al2O3	15.08	0.58	15.65	14.50	13.11	1.74	16.98	10.54
Fe2O3	8.57	0.04	8.61	8.53	13.52	3.63	22.65	10.13
MnO	0.20	0.03	0.23	0.17	0.16	0.07	0.28	0.05
MgO	4.23	0.26	4.49	3.97	5.35	1.64	7.39	2.32
CaO	3.96	0.23	4.19	3.73	1.51	0.83	3.62	0.39
Na2O	3.42	0.00	3.42	3.41	0.89	0.21	1.21	0.46
K2O	1.33	0.11	1.44	1.22	3.33	0.54	4.19	2.32
P2O5	0.18	0.03	0.20	0.15	0.20	0.04	0.30	0.15

Table 4.1 b: Average composition, standard deviation, and maximum/minimum values for trace elements (including REE's) (ppm's for all elements except Au (ppb)) in each of the major rock groups. Data for elements labeled with * are based upon subset of samples analyzed by a HF/HNO_3 ICP-MS package, as described in text.

Rock Type	Pre-Breccia Gabbro/Diorite				Post-Breccia Gabbro/diorite			
Element	Mean	Std	Max	Min	Mean	Std	Max	Min
Cr	149.22	113.11	382.00	5.00	57.00	37.06	143.00	6.00
Ni	29.11	18.00	63.00	0.00	31.60	17.55	58.00	0.00
Co	35.44	6.91	42.00	18.00	45.07	8.48	56.00	27.00
Sc	33.84	10.96	60.80	17.70	33.67	3.13	38.00	26.80
V	286.00	111.95	556.00	173.00	333.20	66.19	437.00	211.00
Cu	61.00	35.74	139.00	7.00	48.27	27.19	91.00	0.00
Pb	5.19	2.02	9.04	1.75	3.55	1.81	6.67	0.00
Zn	90.78	8.69	107.00	76.00	121.53	17.69	156.00	98.00
Cd	0.00	0.00	0.00	0.00	0.01	0.02	0.10	0.00
Sn	0.00	0.00	0.00	0.00	0.00	0.00	0.00	0.00
S	182.70	57.16	274.86	97.54	1001.18	437.51	1748.29	30.72
As	3.03	3.04	7.70	0.00	5.82	12.26	50.00	0.00
Se	0.00	0.00	0.00	0.00	0.00	0.00	0.00	0.00
Sb	0.03	0.09	0.30	0.00	0.24	0.25	0.70	0.00
Ag	0.12	0.10	0.30	0.00	0.02	0.04	0.10	0.00
Ir	0.00	0.00	0.00	0.00	0.00	0.00	0.00	0.00
Au	1.67	2.75	8.00	0.00	0.67	1.53	6.00	0.00
Hg	0.00	0.00	0.00	0.00	0.00	0.00	0.00	0.00
Rb	29.18	10.53	41.53	11.45	21.84	7.56	33.90	11.85
Ba	377.23	142.81	715.07	213.09	319.63	116.13	580.93	160.27
Sr	469.62	84.76	633.08	329.52	398.69	66.25	523.68	238.76
Ga	19.14	1.85	21.16	15.65	22.58	2.77	28.85	18.84
Li	13.04	4.73	21.40	5.95	22.70	7.69	36.83	10.73
Nb	4.58	1.52	6.95	2.46	19.87	8.51	38.42	6.38
Zr	70.81	32.72	122.12	25.03	220.39	80.14	382.42	105.54
Y	19.66	3.44	25.64	14.58	37.43	10.31	60.83	22.84
Th	2.25	1.17	4.43	0.40	1.09	0.47	2.00	0.00
La	11.61	4.62	17.03	3.72	19.73	8.87	37.29	7.21
Ce	26.43	8.25	37.62	15.41	49.31	20.91	95.13	21.40
Sm	3.53	1.00	5.12	2.20	7.48	3.15	15.20	3.70
Eu	1.18	0.22	1.53	1.00	2.81	0.92	4.92	1.67
Tb	0.52	0.32	1.00	0.00	1.27	0.42	2.24	0.70
Dy	3.32	0.66	4.47	2.62	6.73	2.67	13.50	3.76
Yb	2.25	0.53	3.30	1.43	4.03	0.89	5.30	2.18
Lu	0.34	0.08	0.51	0.24	0.61	0.13	0.77	0.35
Cl	294.38	68.58	392.74	145.58	146.30	38.57	219.10	77.68
Br	0.00	0.00	0.00	0.00	0.00	0.00	0.00	0.00
Be	0.99	0.38	1.94	0.59	1.55	0.41	2.35	0.89
Rock Type	**Pre-Breccia Gabbro/Diorite**				**Post-Breccia Gabbro/diorite**			
Bi*	0.04	0.02	0.07	0.02	0.05	0.01	0.06	0.03
Mo*	0.75	0.25	1.04	0.41	1.51	0.40	2.20	1.24
Cs*	1.08	0.39	1.73	0.68	0.79	0.58	1.59	0.10
Tl*	0.20	0.17	0.45	0.04	0.27	0.14	0.43	0.05
Ta*	0.29	0.08	0.37	0.16	1.21	0.43	1.72	0.61
Hf*	2.04	0.47	2.55	1.52	4.67	1.01	5.97	3.45
U*	0.75	0.30	1.10	0.29	0.41	0.04	0.44	0.34
Pr*	4.10	1.04	5.09	2.43	8.00	3.14	12.58	3.93
Nd*	17.49	4.40	21.70	10.90	36.85	15.29	59.98	17.93
Gd*	4.09	0.83	5.07	3.11	9.07	3.34	13.96	5.00
Ho*	0.72	0.14	0.88	0.55	1.53	0.53	2.35	0.90
Er*	2.13	0.37	2.52	1.64	4.17	1.31	6.14	2.55
Tm*	0.31	0.05	0.35	0.22	0.58	0.16	0.81	0.37

Table 4.1 b continued.

Rock Type	Felsic Intrusive Material				Diabase			
Element	Mean	Std	Max	Min	Mean	Std	Max	Min
Cr	14	10	34	0	97	73	177	0
Ni	0	1	2	0	27	16	43	5
Co	2	2	4	0	39	8	48	28
Sc	2	2	6	1	34	7	42	25
V	11	16	55	0	294	80	366	183
Cu	5	5	16	1	46	20	66	18
Pb	9	5	17	1	5	2	8	3
Zn	32	12	55	14	118	26	144	83
Cd	0	0	0	0	0	0	0	0
Sn	0	0	0	0	0	0	0	0
S	78	44	167	32	1671	1553	3795	124
As	15.43	19.26	71.00	2.80	6.53	2.71	8.50	2.70
Se	0.17	0.55	2.00	0.00	0.00	0.00	0.00	0.00
Sb	0.21	0.29	0.70	0.00	0.10	0.14	0.30	0.00
Ag	0.18	0.30	1.10	0.00	0.07	0.09	0.20	0.00
Ir	0.00	0.00	0.00	0.00	0.00	0.00	0.00	0.00
Au	0.33	1.11	4.00	0.00	0.00	0.00	0.00	0.00
Hg	0.00	0.00	0.00	0.00	0.00	0.00	0.00	0.00
Rb	100	33	141	20	26	13	39	9
Ba	288	238	688	30	267	127	418	108
Sr	126	211	807	11	323	116	439	164
Ga	18.00	3.66	21.94	8.89	19.96	3.47	24.73	16.59
Li	2.90	1.73	6.91	0.92	18.52	0.99	19.73	17.30
Nb	17.2	6.7	28.5	6.9	14.5	10.7	29.6	6.8
Zr	194	81	331	102	196	114	357	113
Y	31	13	45	7	32	13	50	19
Th	12.37	2.58	16.75	8.89	2.07	1.27	3.70	0.60
La	22.55	10.99	40.62	9.15	19.97	10.36	32.48	7.10
Ce	46.45	16.45	73.05	23.39	44.31	20.96	73.06	23.66
Sm	4.67	2.11	7.67	1.55	6.73	3.72	12.00	4.10
Eu	0.56	0.49	1.30	0.00	2.43	1.34	4.30	1.20
Tb	0.85	0.39	1.30	0.18	1.03	0.82	2.00	0.00
Dy	4.77	2.18	8.06	1.19	5.32	2.51	8.80	2.98
Yb	4.96	2.31	8.40	1.01	4.27	1.74	6.70	2.70
Lu	0.75	0.34	1.20	0.16	0.70	0.29	1.10	0.43
Cl	133	48	218	53	69	45	121	13
Br	0.00	0.00	0.00	0.00	0.00	0.00	0.00	0.00
Be	2.52	1.18	4.29	0.52	1.19	0.21	1.34	0.89
Rock Type	**Felsic Intrusive Material**				**Diabase**			
Bi*	0.23	0.21	0.53	0.03	N/A	N/A	N/A	N/A
Mo*	0.49	0.23	0.81	0.26	N/A	N/A	N/A	N/A
Cs*	0.96	0.61	2.13	0.34	N/A	N/A	N/A	N/A
Tl*	0.42	0.14	0.71	0.24	N/A	N/A	N/A	N/A
Ta*	1.39	0.37	1.98	0.89	N/A	N/A	N/A	N/A
Hf*	4.85	1.13	6.77	3.50	N/A	N/A	N/A	N/A
U*	2.83	0.47	3.54	2.33	N/A	N/A	N/A	N/A
Pr*	5.70	2.61	8.94	3.03	N/A	N/A	N/A	N/A
Nd*	21.34	10.98	33.06	9.39	N/A	N/A	N/A	N/A
Gd*	4.33	2.80	7.65	1.17	N/A	N/A	N/A	N/A
Ho*	1.01	0.61	1.72	0.24	N/A	N/A	N/A	N/A
Er*	3.15	1.77	5.17	0.78	N/A	N/A	N/A	N/A
Tm*	0.52	0.26	0.81	0.16	N/A	N/A	N/A	N/A

Table 4.1 b continued.

Rock Type	Felsic Clasts				Gabbroic Clasts			
Element	Mean	Std	Max	Min	Mean	Std	Max	Min
Cr	25	3	27	22	85	23	113	57
Ni	4	2	5	2	31	13	49	19
Co	9	5	13	4	30	6	38	23
Sc	1	1	2	0	25	5	32	20
V	19	12	30	7	276	48	344	241
Cu	8	2	10	6	95	71	190	20
Pb	36	17	53	19	51	1	52	49
Zn	57	22	79	35	240	18	264	222
Cd	0	0	0	0	0	0	0	0
Sn	0	0	0	0	0	0	0	0
S	1519	370	1889	1150	2495	1051	3784	1209
As	8500.00	3500.00	12000.00	5000.00	14266.67	9005.31	27000.00	7700.00
Se	0.00	0.00	0.00	0.00	0.00	0.00	0.00	0.00
Sb	1.55	1.55	3.10	0.00	0.00	0.00	0.00	0.00
Ag	0.25	0.05	0.30	0.20	1.93	0.90	3.00	0.80
Ir	0.00	0.00	0.00	0.00	0.00	0.00	0.00	0.00
Au	1022.00	838.00	1860.00	184.00	1292.67	1462.97	3360.00	188.00
Hg	0.00	0.00	0.00	0.00	0.00	0.00	0.00	0.00
Rb	92	27	119	65	181	42	224	124
Ba	1157	316	1474	841	770	96	860	637
Sr	99	18	117	81	200	90	327	133
Ga	15.49	0.08	15.57	15.42	28.42	1.76	29.74	25.94
Li	13.10	5.65	18.75	7.46	44.39	9.43	55.20	32.22
Nb	83.3	16.5	99.8	66.8	4.4	0.6	5.2	3.9
Zr	686	23	708	663	94	6	102	89
Y	81	2	82	79	19	4	23	14
Th	18.19	0.50	18.69	17.69	2.37	0.32	2.76	1.99
La	12.44	0.45	12.89	12.00	13.75	3.29	18.38	11.10
Ce	38.37	0.12	38.49	38.25	32.07	7.08	42.06	26.54
Sm	8.74	0.31	9.05	8.43	4.30	0.81	5.40	3.49
Eu	0.52	0.08	0.60	0.44	1.04	0.25	1.38	0.83
Tb	2.04	0.07	2.11	1.97	0.60	0.11	0.74	0.46
Dy	14.54	0.39	14.94	14.15	3.76	0.65	4.44	2.88
Yb	10.58	0.39	10.97	10.19	1.78	0.37	2.16	1.28
Lu	1.45	0.07	1.52	1.38	0.26	0.06	0.32	0.17
Cl	65	5	71	60	117	52	190	76
Br	0.00	0.00	0.00	0.00	0.00	0.00	0.00	0.00
Be	2.63	0.28	2.91	2.36	4.18	0.38	4.46	3.64
Rock Type	**Felsic Clasts**				**Gabbroic Clasts**			
Bi*	2.65	1.56	4.84	1.28	6.80	2.35	9.90	4.22
Mo*	3.23	3.02	7.47	0.73	1.30	0.30	1.73	1.04
Cs*	1.76	0.94	3.03	0.81	4.38	2.18	6.98	1.63
Tl*	0.53	0.21	0.78	0.28	0.79	0.17	0.94	0.55
Ta*	6.67	0.43	7.23	6.20	0.25	0.08	0.34	0.15
Hf*	20.11	0.94	21.40	19.21	1.53	0.15	1.74	1.41
U*	6.13	0.48	6.78	5.65	0.82	0.07	0.90	0.73
Pr*	5.55	0.15	5.67	5.33	4.25	0.94	5.58	3.54
Nd*	23.99	0.53	24.46	23.24	18.55	4.11	24.31	15.05
Gd*	9.70	0.47	10.24	9.09	4.19	0.81	5.19	3.21
Ho*	3.01	0.17	3.20	2.79	0.73	0.15	0.89	0.53
Er*	9.45	0.65	10.28	8.68	2.09	0.40	2.50	1.54
Tm*	1.53	0.10	1.66	1.43	0.30	0.05	0.37	0.24

Table 4.1 b continued.

Rock Type	Sediments				Mineralization			
Element	Mean	Std	Max	Min	Mean	Std	Max	Min
Cr	137	4	140	133	95	48	169	0
Ni	31	2	32	29	22	11	43	5
Co	26	1	27	25	39	33	111	8
Sc	24	1	25	24	16	7	26	3
V	205	2	207	203	128	56	200	38
Cu	37	7	43	30	2801	4321	13703	14
Pb	9	2	11	7	88	101	367	0
Zn	96	9	105	87	741	538	1844	163
Cd	0	0	0	0	2	5	17	0
Sn	0	0	0	0	0	0	0	0
S	209	42	251	167	23569	31939	116990	0
As	44.50	0.50	45.00	44.00	36432.00	68959.03	250000.00	12.00
Se	1.00	0.00	1.00	1.00	4.64	9.38	33.00	0.00
Sb	1.15	0.15	1.30	1.00	24.86	50.76	180.00	0.00
Ag	0.05	0.05	0.10	0.00	34.68	72.44	260.10	0.50
Ir	0.00	0.00	0.00	0.00	0.00	0.00	0.00	0.00
Au	2.50	2.50	5.00	0.00	7483.09	16460.72	58500.00	0.00
Hg	0.00	0.00	0.00	0.00	0.00	0.00	0.00	0.00
Rb	38	2	40	36	160	67	243	0
Ba	339	8	347	330	399	204	688	18
Sr	523	71	594	452	74	39	178	19
Ga	18.99	0.52	19.50	18.47	24.86	3.41	30.56	20.13
Li	23.49	3.54	27.03	19.94	26.26	9.41	36.98	6.17
Nb	6.6	0.7	7.3	5.9	18.7	18.9	73.2	0.0
Zr	130	5	135	125	230	123	566	109
Y	20	1	21	19	27	17	71	4
Th	4.00	0.10	4.10	3.90	5.87	3.97	16.22	0.90
La	15.72	0.22	15.95	15.50	12.62	5.36	22.87	0.00
Ce	32.97	0.25	33.23	32.72	31.96	8.04	50.80	21.88
Sm	3.85	0.05	3.90	3.80	4.25	1.69	8.04	1.30
Eu	1.20	0.10	1.30	1.10	0.69	0.31	1.30	0.00
Tb	0.60	0.00	0.60	0.60	0.79	0.47	1.80	0.00
Dy	3.01	0.07	3.08	2.94	4.70	3.04	12.79	0.17
Yb	2.85	0.05	2.90	2.80	3.47	2.49	9.17	0.00
Lu	0.44	0.01	0.45	0.43	0.51	0.37	1.29	0.00
Cl	104	23	127	81	112	80	305	0
Br	0.00	0.00	0.00	0.00	0.00	0.00	0.00	0.00
Be	1.30	0.02	1.31	1.28	2.46	1.04	3.92	0.45
Rock Type	Sediments				Mineralization			
Bi*	N/A	N/A	N/A	N/A	23.51	20.50	52.98	0.03
Mo*	N/A	N/A	N/A	N/A	5.42	5.07	17.04	1.40
Cs*	N/A	N/A	N/A	N/A	3.45	1.83	6.45	0.14
Tl*	N/A	N/A	N/A	N/A	0.64	0.29	1.00	0.07
Ta*	N/A	N/A	N/A	N/A	0.98	0.60	2.21	0.37
Hf*	N/A	N/A	N/A	N/A	4.23	2.43	8.47	1.16
U*	N/A	N/A	N/A	N/A	1.12	0.55	2.25	0.47
Pr*	N/A	N/A	N/A	N/A	5.30	3.49	13.50	2.68
Nd*	N/A	N/A	N/A	N/A	22.80	16.04	60.70	10.83
Gd*	N/A	N/A	N/A	N/A	5.41	4.23	15.46	1.75
Ho*	N/A	N/A	N/A	N/A	1.04	0.66	2.52	0.32
Er*	N/A	N/A	N/A	N/A	3.05	1.79	6.89	0.89
Tm*	N/A	N/A	N/A	N/A	0.46	0.22	0.86	0.14

Table 4.2: Summary of sulphur isotopic characteristics of the Lodestar Prospect mineralization.

Sample Type	Mineral Separate	Range of $\delta^{34}S$ ‰	Average $\delta^{34}S$ ‰
Mineralization from breccia matrix	Arsenopyrite (n=6)	3.6 - 4.3	3.9
Mineralization from breccia matrix	Pyrite (n=8)	3.3 - 4.4	3.7
Mineralization from breccia matrix	Chalcopyrite (n=7)	3.1 -4.6	3.6
Mineralization from breccia matrix	Bornite (n=1)	3.6	3.6
Mineralized fine-grained gabbro	Pyrite (n=1)	0.9	0.9

Table 4.3: Sulphur Isotope thermometers. (From Ohmoto and Rye, 1979).

Mineral Pair	Equation (T in Kelvin: $\Delta = \delta^{34} S_a - \delta^{34} S_b$	Uncertainties[a] 1	2
Sulphates-chalcopyrite	$T = \frac{2.85 \times 10^3}{(\Delta \pm 1)^{1.2}}$ (T>400°C)	± 25[3]	± 5[3]
	$T = \frac{2.30 \times 10^3}{(\Delta - 6 \pm 0.5)^{1.2}}$ (T<350 °C)	± 10	± 5
Sulphates-pyrite	$T = \frac{2.76 \times 10^3}{(\Delta \pm 1)^{1.2}}$ (T>400 °C)	± 25[3]	± 5[3]
	$T = \frac{2.16 \times 10^3}{(\Delta - 6 \pm 0.5)^{1.2}}$ (T<350 °C)	± 10	± 5
Pyrite-galena	$T = \frac{(1.01 \pm 0.04) \times 10^3}{\Delta^{1.2}}$	± 25	± 20
Sphalerite (pyrrhotite)- galena	$T = \frac{(0.85 \pm 0.03) \times 10^3}{\Delta^{1.2}}$	± 20	± 25
Pyrite-chalcopyrite	$T = \frac{(0.67 \pm 0.04) \times 10^3}{\Delta^{1.2}}$	± 35	± 40
Pyrite-pyrrhotite (sphalerite)	$T = \frac{(0.55 \pm 0.04) \times 10^3}{\Delta^{1.2}}$	± 40	± 55

[a] 1= uncertainty in temp. due to uncertainty in equation (at T=300 °C): 2= uncertainty in calculated temp. due to analytical uncertainty of ± .2 per mil for Δ values (at T=300 °C): 3= uncertainty in calculated temp. at 450 °C.

Table 4.4: At. Wt % As. S. Fe in arsenopyrite as determined by electron microprobe analysis.

sample	At. Wt %S	At. Wt % As	At. Wt % Fe
min1	33.73	32.45	33.82
min1	33.83	32.09	34.08
min1	34.24	31.97	33.79
min1	34.39	31.56	34.05
min1	34.64	31.66	33.7
min1	33.65	32.55	33.79
min1	34.8	31.22	33.96
min1	33.47	32.69	33.8
min1	35.57	30.54	33.87
mat	34.99	30.99	34.02
mat	34.07	32.01	33.92
mat	35.09	31.04	33.84
mat	35.41	30.66	33.9
mat	33.42	32.72	33.85
min7	34.52	32.85	32.63
min7	34.63	32.68	32.67
min7	35.07	32.26	32.62
min7	34.86	32.36	32.79
min7	34.32	32.32	33.35
min7	34.68	32.84	32.48
min2	37.57	29.52	32.91
min2	35.25	31.62	33.1
min2	37.05	30.24	32.71
Std. Dev	1.01	0.92	0.57
AVERAGE	**34.75**	**31.77**	**33.46**

Table 4.5: Ablation results (Au in ppm) and LAM-ICP-MS run detection limits for each sample analyzed. Note increased Au concentration within the arsenopyrite as compared to the pyrite and chalcopyrite.

Sample	**JH-99-MIN6**			**JH-99-MIN7**	**JH-99-MAT**		
	Asp	Pyrite	Chalco	Asp	Asp	Pyrite	Chalco
Average	72.6	2.3	.5	58.0	48.1	0.7	0.6
Standard Deviation	70.4	2.1	.4	59.5	45.6	0.65	0
Max. Value	200.7	4.4	0.9	158.1	151.9	1.3	0.6
Min. Value	1.8	0.1	0.03	0.9	1.3	0.03	0.6
Number of ablations	11	2	2	14	8	2	1
Run detection limit	**0.012 ppm**			**0.004 ppm**	**0.005 ppm**		

Chapter 5: Discussions and Conclusions

5.1 Introduction

Gold deposits and their geological classification have been widely studied and documented in the geological literature (Robert et al., 1997; Foster, 1991 (and authors therein); Bache, 1987; Sillitoe, 1985, 1991, 1995; Corbett and Leach, 1998; and many others). The work by Robert et al., (1997) provides an especially thorough, coherent and detailed classification and description of 16 globally recognized types of lode gold deposits; the reader is directed to this work and references therein for a complete review of types of gold deposits.

Previous studies have also focused on the description of the broad spectrum of gold mineralization styles associated with intrusive, epizonal environments (Sillitoe, 1985, 1991, 1995; Corbett and Leach, 1998; etc.). These studies aim to give a comprehensive review of intrusion-related gold deposit types and to draw parallels between them; as illustrated in figure 5.1.

The focus of this M.Sc. study was limited to the investigation of the various types of ore-related hydrothermal breccias in order to gain an understanding of the characteristics and qualities associated with each breccia type. These characteristics and qualities were then utilized to gain a better understanding of breccia hosted gold mineralization in the Lodestar Prospect.

The initial scope of this chapter is to examine what a breccia is and to look at the various types of ore-related hydrothermal breccias described in the literature. Each type

will be described in general terms, with more detailed descriptions for a subset of the breccia types. The mechanisms that influence and drive the brecciation process will also be examined. Once the types of breccia are examined the breccia-hosted gold associated with the Lodestar prospect will be classified according to the described classification scheme.

Most of the information used with respect to classification schemes and brecciation mechanisms was derived from works by Sillitoe (1985, 1991, 1995); Corbett and Leach (1998); and Burnham, (1985); with background from many other sources.

5.2 Mechanisms of brecciation

Sillitoe (1985) defined six major mechanisms for subsurface brecciation as follows:

1) release of magmatic-hydrothermal fluids from magma chambers during second boiling (the process of volatile exsolution due to exceeding solubility limits in magma; the process of formation of vapour bubbles as a result of crystallization (Philpotts, 1990)) and subsequent decompression which initiate and cause fragmentation and brecciation of overlying rocks.

2) the magmatic heating and related expansion of connate pore fluids which initiates increased pressures and eventual brecciation.

3) violent interaction of cool ground waters with subsurface magmas which generate explosive phreatomagmatic breccias.

4) brecciation caused by the disruption of rocks, decompression, and fragmentation and eruption of the top part of an underlying magma chamber which may occur up to the paleosurface.

5) mechanical disruption of wall rocks due to subsurface movement of magma.

6) tectonic breccias resulting from fault movement.

In the case of hydrothermal breccias, Burnham (1985) suggested that the first process involving second boiling and subsequent decompression is the most important factor in breccia formation. According to Burnham, the brecciation process is driven by the release of mechanical energy ($P\Delta V$) from hydrous magmas by the two sequential processes of second boiling and decompression. Burnham (1979) and Burnham and Ohmoto (1980) indicate that the initial process of second boiling,

H_2O-saturated melt $\rightarrow$ crystals + H_2O vapour,

releases sufficient mechanical energy to cause fracture failure of even the strongest wall rocks at depths up to 4-5 km. Following this fracture failure, additional mechanical energy is released into the system by the subsequent expansion of previously exsolved fluids, coupled with additional exsolution of fluids, by the process of decompression. According to Burnham (1985), it is this decompression that actually drives the brecciation process. However, brecciation depends upon the amount of energy released during decompression, which in turn is dependant upon a number of specific factors including: 1) bulk composition of the magma, 2) depth of emplacement of the magma body, 3) mass fraction of H_2O in the initial melt, 4) mass fraction of melt in the initial magma, 5) tensile

strength of the wall rocks, and 6) depth to the top of the second boiling induced fracture, once formed. Of these six, the most important factor for brecciation (especially in porphyry-type brecciation) is the mass fraction of H_2O in the initial melt. This factor determines both the amount of mechanical energy released by the process of second boiling and the magnitude of energy released into the fractures (if formed) by decompression forces.

5.3 Definition of a breccia and an outline of the various types of ore related hydrothermal breccias.

A hydrothermal breccia is best defined as a clastic rock comprised of fragments held together by matrix and containing cavities filled by post-brecciation hydrothermal minerals (Laznicka, 1988). The fragments within a breccia can range from locally-derived host-rock fragments to introduced exotic fragments. The matrix to a breccia is typically composed of minerals that were deposited from hydrothermal fluids, as well as locally derived and introduced rock material of a finer grain size than the fragments; with most mineralization introduced by the hydrothermal fluids. Therefore, it can be said that the process of ore formation and brecciation are intimately linked.

Before attempting to classify, or to understand documented classifications of breccias, one must realize that they are often very complex and confusing. The primary reason for this confusion is the fact that within most classification schemes, it is typically impossible to assign an actual breccia to a single definite classification; instead, in

reality, ore related hydrothermal breccias most commonly form a continuum of breccia types rather than a series of unrelated individual types.

Within most classifications, the primary distinguishing features of ore related hydrothermal breccia types are based on the role of the magma and/or aqueous fluids in the breccia formation process. However, even with these classifications, there is still significant overlap between the various breccia types.

Six ore-related breccias (figure 5.2) will be described, followed by a more detailed examination of the three most appropriate types. It should be noted that the proceeding descriptions and classifications merely summarize information from the given references, to which the reader is referred for more detailed explanations. The six main breccia types are (Corbett and Leach, 1998):

1)Magmatic-Hydrothermal breccias

2)Hydromagmatic Breccias which are subdivided into:

a) phreatomagmatic breccias

b) phreatic breccias

3) Dilational breccias

4)Magmatic-Hydrothermal injection breccias

5)Hydrothermal collapse breccias

6)Dissolution breccias

1) Magmatic-hydrothermal breccias: these breccias are produced by the release of hydrothermal fluids from magma chambers, irrespective of the original source of the fluid

involved (magmatic, meteoric, connate, or ocean waters). These breccias form at deep levels in porphyry systems and typically must be eroded in order to crop out on surface (figure 5.3). An example is at Kidston, Australia (Corbett and Leach, 1998).

2) Hydromagmatic Breccias: generated by the interaction of magma and an external source of water, ie. ground water or surface water.

2 A) Phreatomagmatic breccias: in this type, both water and magma directly contribute to breccia formation. These breccias are associated with high-level porphyry intrusions and may vent at the surface as diatremes (figure 5.4). An example is at Wau, Papua New Guinea (Corbett and Leach, 1998).

2 B) Phreatic Breccias: only magmatic heat, not actual magma, had access to the external water source in the formation of this type. These breccias are sometimes termed eruption breccias and form at surficial levels (figure 5.5). An example is at the Taupo Volcanic Zone, New Zealand (Corbett and Leach, 1998).

3) Dilational Breccias: these occur in dilational structural environments which create open spaces that can be filled by hydrothermal minerals. Typical settings include fissure or sheeted fracture systems developed during oblique convergence. Although hosts to hydrothermal mineralization, these breccias actually form by tectonic processes (Corbett and Leach, 1998).

4) Magmatic-Hydrothermal injection Breccias: these consist of host-rock fragments set in a matrix derived from magmatic-hydrothermal fluids and rock flour associated with the milling of rock fragments. Many of these breccias form in dilational structural

environments derived by movement on controlling structures; and are therefore related to the above described dilational breccias (Corbett and Leach, 1998).

5) Hydrothermal Collapse Breccias: these form during retrograde phases of porphyry development. Magmatic vapors rise above the porphyry environment, condense, and mix with ground waters; thereby allowing them to percolate downwards as low pH fluids. This process results in overprinting phyllic to argillic alteration forming clay matrix breccias in which sericite and clays grade from fractures into the host rock; leaving remnants of the original lithologies as breccia fragments (Corbett and Leach, 1998).

6) Dissolution Breccias: these form in limestone and other carbonate rocks by the removal of carbonate and subsequent collapse. They may be related to slump and karst formation (Corbett and Leach, 1998).

For the purposes of this paper, the first three types of breccia (Magmatic-hydrothermal, Phreatomagmatic, and Phreatic) will be discussed in detail. Some of the major characteristics of these breccia types are given in Table 1.

5.4 Detailed examination of three specific breccia types.

Magmatic-hydrothermal, phreatomagmatic, and phreatic breccias are the most common ore-related hydrothermal breccias, and they are the most pertinent breccia types for the Lodestar Prospect. The following descriptions are based upon the classification scheme of Sillitoe, (1985), and a review of this classification by Corbett and Leach (1998).

5.4.1 Magmatic-Hydrothermal Breccias

This breccia type has a pronounced magmatic involvement in the brecciation process, alteration, and composition of the ore fluid (e.g. Kidston, eastern Australia: Baker and Andrew, 1991: Mt.Leyshon, eastern Australia ; Paull et al., 1990). Most of the examples are hosted in subvolcanic pipes, at depths greater than 1 km, and are thought to be associated with high-level porphyry intrusions (figure 5.3).

The mechanism for this type of brecciation depends upon the violent explosion of volatiles that are rapidly exsolved from an incipiently crystalizing magma. The volatiles are interpreted to collect and become over-pressurized as the intrusion cools, contained by an impermeable or semi-impermeable carapace or cap on the system. Movement or disruption on a controlling structure, coupled with the process of second boiling, causes the carapace to become fractured, allowing the volatiles to escape violently and explosively, thereby brecciating the overlying rocks. The brecciation is generally pre-mineralization and therefore the ore distribution relates to plumbing systems and the presence of open space.

The two main types of magmatic-hydrothermal breccias are pipes related to intrusions and porphyry related breccias.

5.4.1.1. Pipes related to intrusions

Magmatic-hydrothermal breccias associated with intrusions are not related to underlying mineralized porphyry systems; instead they are related to unaltered and unmineralized intrusive rocks, typically batholiths or stocks. These breccia pipes do not

necessarily reach the surface and they typically demonstrate sharp contacts between the breccia pipes and the wall rocks, commonly marked by a series of closely spaced vertical fractures. Fragments are generally angular to sub-rounded and have a wide range of sizes. Prior to cementation by gangue and sulphides, these breccias contain approximately 5-30 % open spaces. Due to the violent, explosive release of volatiles, the matrices sometimes consist of rock flour, a silt to sand sized clastic material which is produced by the milling of fragments, accompanied by remnant rounded clasts.

These breccias are typically located at the upper parts of, or above, a pluton or stock, and typically there is limited vertical displacement of fragments resulting in "jigsaw" brecciated clasts whereby brecciated fragments can be put back together like a jigsaw puzzle. Small volumes of fine-grained porphyry intrusive rock are commonly genetically, temporally, and spatially related to these breccias; occurring as dykes and small bodies, breccia fragments, and irregular disaggregated portions of the breccia. These small felsic intrusive units have been documented at Copper Creek (Simons, 1964) and at Kidston (Placer Exploration Ltd., 1981) and they have been interpreted to indicate the presence of larger intrusive bodies at depth of the same intrusive material that drove the brecciation process.

Mineralization within this class of hydrothermal breccia ranges from copper to molybdenum, tungsten, and/or gold. Sericitization is the dominant alteration form, although some chloritization and silicification occur, as well as minor propylitic assemblages. In many cases, the mineralization associated with these breccias is not

evenly distributed throughout the breccia, leading to restricted areas or volumes of ore-grade mineralization. So and Shelton (1983) indicate that within this type of breccia, mineralizing fluids range in temperature from 310-470 °C.

The energy required is obtained from a hydrous magma through exsolution of an aqueous phase during second boiling. Water saturated melt → crystals and aqueous fluid. This is followed by the decompression of the exsolved low density aqueous fluid and the water saturated residual melt. The decompression causes expansion of previously exsolved fluid, exsolution of additional fluid, and the release of sufficient energy to induce brecciation. The decompression part of this process depends upon the rapid expulsion of a fluid from a magma which can produce or reopen faults and/or fractures. These faults/fractures can then propagate into shallower levels which gives rise to lower pressures and an increased fluid streaming from the intrusion. This in turn induces milling of fragments and the production of rock-flour matrix. If the pressure drops, possibly due to a decrease in the amounts of fluids released, caving and spalling of the wall rocks can occur; thereby allowing for a close association between rock-flour breccias and clast supported breccias.

5.4.1.2. Hydrothermal-magmatic breccias related to porphyries

Most, if not all, mineralized porphyry systems contain one or more types of associated breccia, although they are not necessarily all mineralized (Richard, 1969). These breccias share many characteristics with the intrusion related breccias discussed earlier. Fragments range from angular to rounded, and heterolithologic breccias with rock

flour matrix are much more common than in the pipe breccias; a feature related to a much higher degree of fragment displacement. This type of breccia is typically clast supported; however all gradations from 100 % clast-supported to bodies consisting of 100 % rock flour material have been documented.

Structural features, such as the contacts between intrusive rocks and host rocks provide a good location for the inward migration of breccias. Alteration within these breccias is again dominated by sericitization, but secondary biotite and K-silicate alteration is also observed. Quartz, although not always present, is a common cementing agent in addition to +/- k-feldspar, biotite, chlorite, flourite, magnetite, specularite etc. One or more of pyrite, chalcopyrite, and/or molybdenite is also typically present in the matrix. As with the intrusive related breccias, some examples have localized areas of mineralization. The origin of these breccias is the same as that given earlier for the breccias related to intrusions (second boiling and decompression processes); with the implication that the release of larger volumes of fluids from large porphyry stocks explains the higher occurrence of rock flour breccias.

5.4.2. Phreatomagmatic Breccias

As implied by the name, ("phreato" refers to water converted to steam), these breccias are related to violent eruptions which occur when a rising, depressurizing magma exsolves volatiles which come into contact with ground waters causing their rapid conversion to steam. This process forms "diatremes" which are associated with epithermal systems and high-level porphyry intrusions (figure 5.4). Many of these

breccias are very fine grained and consist predominantly of matrix (50-90 % matrix). Examples contain tuffaceous material in the matrix consisting of broken and un-broken crystals. These breccias are typically heterolithologic, containing sub-rounded to rounded fragments of all wall rock types with the fragment and matrix composition reflecting the host-rock lithology and the intrusion which drove the formation of the diatremes. Hot gasses erupted from the intrusion react with the wall rocks, resulting in alteration which is dominated by sericitization, with local chlorite and clays, etc. The phreatomagmatic diatreme eruption is pre-mineralization, and mineralization follows fractures produced by the eruption. Modern analogs of this class of breccias are present in the Taupo volcanic zone of New Zealand (Sillitoe, 1985).

The origin is related to multiple explosions associated with expansion and vaporization of ground waters, as well as fragmentation of particles from the magma; subsidence is also locally important.

5.4.3. Phreatic Breccias

These breccias have a shallow level of emplacement (<1000 m) and are associated with volcanic-hosted and hot spring related epithermal deposits (figure 5.5). They display various textures ranging from rock flour to open space breccias, but they lack any juvenile porphyry fragments characteristic of the phreatomagmatic breccias previously discussed. Many also show evidence of multiple stages of mineralization and brecciation.

Quartz occurs as a pervasive replacement of, and a cement to, fragments; and most of the mineralization (typically Au, Ag) is associated with this breccia cement. The

ore fluids in this class of breccia are assumed to be dominantly associated with meteoric waters. Modern analogies of this type of brecciation are found in active meteoric water-dominated geothermal systems in New Zealand (eg. The Taupo volcanic zone of North Island).

The origin of these phreatic breccias is dependant upon the build-up of hydrostatic pressure beneath a permeability barrier. The permeability is reduced due to the crystallization of quartz from the cooling of fluids as they move towards the surface. This permeability barrier is assumed to be fractured or broken due to the intrusion of a magma or faulting; resulting in decompression of fluids which in turn disrupts and brecciates the overlying rocks.

5.5 Classification of the hydrothermal breccia associated with the Lodestar Prospect

The next goal of this investigation is to classify the Lodestar breccia using the previously described classification scheme. Before attempting to classify the breccia, however, an important point regarding breccia classification needs to be reiterated: breccia classifications are a means of subdividing major groups of breccias based upon the driving forces and characteristics of the brecciation. In reality, individual breccias form a continuum whereby they are all related, instead of being totally unique and separate from each other. In other words it is practically impossible to pigeonhole a specific breccia into one of the above described breccia classifications without having some degree of overlap with one of the other classifications.

In order to classify the Lodestar breccia, the important characteristics of the breccia must be reiterated. The Lodestar characteristics are:

- The breccia is associated with the multi-phase Powder Horn Intrusive Suite which is dominated by a pre-breccia gabbro/dioritic phase (and minor pre-breccia felsic intrusive material) and post-breccia gabbro/dioritic and felsic intrusive phases.
- Breccia emplacement is focused along, and occurs at, the contact region between the host sedimentary unit (Connecting Point Group) and the pre-breccia gabbro/diorite intrusive phase.
- The mineralized breccia is intruded and cut off by the post-breccia gabbro/diorite.
- Both pre- and post-breccia felsic intrusive phases occur in the vicinity of the Lodestar breccia.
- The breccia contains approximately 5-15 % matrix. Mineralized matrix consists of arsenopyrite, pyrite, chalcopyrite, sphalerite, and minor hydrothermal magnetite. Unmineralized matrix consists of rock-flour (comminuted felsic QFP clasts), actinolite, tremolite, and chlorite.
- Breccia fragments range from rounded to angular and consist of host sedimentary clasts, locally derived pre-breccia gabbro/diorite clasts, and exotic felsic (QFP) clasts; of which only the exotic QFP clasts contain pre-breccia mineralization.
- The rock-flour matrix appears to be a product of comminuted exotic QFP clasts.
- Gold is dominantly associated with arsenopyrite, and to a lesser degree with the pyrite and chalcopyrite.

- Alteration associated with the breccia is dominated by sericite, with varying amounts of chlorite, epidote, and actinolite/tremolite.
- S-isotope and arsenopyrite geothermometers suggest that the temperature of mineralization was approximately 425 °C.
- Sulphur isotope ratios indicate average $\delta^{34}S$ values of + 3.3 to 4.0 ‰.

Based upon these characteristics, the Lodestar prospect would best fit classification as a magmatic-hydrothermal breccia related to a porphyry system at depth (figures 5.3, 5.6). The features that lead to this conclusion are:

- The presence of both pre- and post- felsic intrusive bodies suggest the presence of a more extensive porphyritic body at depth which may have driven the brecciation process.
- The structural control on the emplacement of the breccia body, whereby the breccia was emplaced at the intrusive contact between the pre-breccia gabbro/diorite phase of the PHIS and the host sedimentary unit is a typical characteristic of deep seated porphyry derived breccia systems.
- The presence of substantial amounts of finely comminuted pieces of rock (QFP) comprising a rock flour matrix is typically associated with the release large volumes of fluids from large porphyry stocks at depth.
- The presence of hydrothermal magnetite within the matrix of the breccia; this mineral phase is common in magmatic-hydrothermal breccias related to porphyry systems.

- Alteration minerals consisting predominantly of sericite, biotite, actinolite/tremolite, and epidote are typical of such breccias.
- The occurrence of pre-breccia mineralized, exotic QFP clasts within the breccia. These clasts are not observed as an intrusive phase in the immediate vicinity of the brecciation, and they have different geochemical signatures than the felsic intrusive phases of the PHIS, thus are therefore presumed to represent clasts from a deep seated porphyry intrusion. This is substantiated by the fact that, whereas the locally derived pre-breccia gabbro/diorite and sedimentary clasts are typically sub-angular to angular, these QFP clasts are commonly rounded and are believed to be the source of the rock flour matrix, therefore indicating that they were violently transported from depth causing comminution.
- The presence of crenulate or ptygmatically folded quartz layers (unidirectional solidification texture) (plate 3.53) within some of the QFP clasts has been related to porphyry deposits (Kirkham and Sinclair, 1988) whereby the quartz layers form in an aplitic margin (carpace) of the porphyritic intrusion at depth; later to be sampled during violent eruption or fracture of the carpace associated with the second boiling and decompression processes previously discussed.

Thus, based upon observations, it is postulated that the Lodestar breccia is of magmatic-hydrothermal origin, and was derived from the explosive fluid exsolution of a gold-bearing porphyry intrusive system at depth. Similar deposit models have been suggested for deposits such as Kidston (Baker and Andrew, 1988; Baker and Tullemans,

1990), Mount Leyshon (Paull et al., 1990), and Golden Sunlight (Porter and Ripley, 1985). In addition, based upon models proposed by Sillitoe (1991, 1995) and others (figure 5.2), it is proposed that the Lodestar prospect may actually represent a transitional environment between a deep seated porphyry system and a shallower epithermal system.

Before describing a specific multi-stage model for the Lodestar breccia, a brief examination of gold transport and deposition in a porphyry type environment is necessary. In recent years a significant amount of research has been focused on gold transport in hydrothermal systems (e.g. Richards, 1995; Foster, 1991; etc). Most researchers suggest that gold chloride and/or bisulphide complexes are the most important transport agents. Within magmatic-hydrothermal systems it is common to have both of these complexes present, resulting in a zonation of mineralization type.

Richards (1995) briefly explains this process with respect to porphyry magmatic-hydrothermal systems related to epithermal systems. Candela (1989) and Ballhaus et al., (1994) suggest that gold behaves in a manner similar to that of copper in porphyry related systems, thus Cu and Au should be concentrated in the volatile phase during magmatic devolatization, and they would be dissolved in this volatile phase as chloride complexes. Since S, present dominantly as SO_2 in the early genetic stages of such deposit types (due to the requirement of non-saturation of sulfide in the melt and relatively oxidizing conditions), the Cu, as well as Au can be carried in relatively higher proportions. With cooling of the system, however, the SO_2 becomes disproportioned to sulfate and sulphide species; resulting in the deposition of Cu-sulphides as disseminated porphyry-type

mineralization. Minor gold can also be deposited in this manner, however, most of the gold would remain in solution due to conversion to bisulphide complexes. This results in a temporal and spatial separation of copper and gold deposition within magmatic-hydrothermal systems, with the gold being deposited later, at potentially shallower levels. Therefore, in the case of magmatic-hydrothermal auriferous breccia deposits related to porphyry systems at depth, such as the case in the proposed model of the Lodestar prospect, the gold has actually been deposited beyond the depositional front of the porphyry ore. This model therefore predicts that such gold-rich systems would grade downward into zones of Cu rich mineralization, above the porphyry driving intrusion, a model originally proposed by Bonham and Giles (1983), Mutschler et al., (1984), and Werle et al. (1984).

The idea that sulphur dominantly occurs in the form of SO_2 in the early stages of porphyry related systems was also described by Gustafson (1979), who noted that the sulphur in such systems is genetically, if not economically, a more important factor than the actual metals. Hunt (1977) indicated that porphyry copper deposits are actually large sulphur anomalies with lower Cu/S ratios than ordinary crustal rocks (ie. they form by a process in which sulphur enrichment is ultimately the factor that leads to porphyry ore formation). Cu, Au and other minerals are carried in solution by the sulphur and show relatively less enrichment in the final deposit than does the sulphur.

5.5.1 Generalized model of brecciation at the Lodestar prospect.

Figure 5.7 depicts a generalized four stage model for the brecciation process at the Lodestar prospect. In the first stage of the model (figure 5.7a), pre-breccia conditions were extant whereby the pre-breccia PHIS phases (gabbroic and felsic) intruded (~605 Ma) and the porphyry source, with potential porphyry type Au-Cu mineralization is present, or is forming, at depth. As mentioned above, deposition of porphyry type mineralization at depth is associated with relatively high levels of SO2; and the mineralization would be preferentially enriched in copper with respect to gold.

The second stage in this model (figure 5.7 b) suggests that the porphyry system was crystallizing at depth with an impermeable carpace trapping exsolved volatiles; thereby causing increased pressure due to the process of second boiling. With increased crystallization and the resultant exsolution of vapors, sufficient mechanical energy was generated to induce fracturing in the overlying rock. Due to the relatively high confining pressures associated with the depth of emplacement of such a porphyry system, the fractures resulting from the process of second boiling would exploit zones of weakness; in the case of the Lodestar prospect, this zone would lie along the intrusive contact between the pre-breccia intrusive gabbroic phase and the host sedimentary unit. At this stage PHIS intrusive activity halted and the source magma of the intrusive suite underwent crustal assimilation and contamination.

This is followed by the third stage in the model which is dominated by decompression of the exsolved low density aqueous fluid and the water saturated residual

melt (figure 5.7 c). As in the general model described earlier, this decompression, through the process of expansion of previously exsolved fluid and exsolution of additional fluid, released sufficient energy to induce brecciation. This resulted in the rapid expulsion of fluids which took advantage of the previously developed faults, propagating them into shallower levels giving rise to lower pressures and increased fluid streaming, and allowing for milling of fragments and the production of rock-flour matrix. As described above, the gold in this type of system is preferentially deposited in this stage at relatively shallow depth under relatively cooler conditions than those at the porphyry level.

The final stage illustrates events which occurred after the brecciation (figure 5.7 d). In this stage, the remaining phases of the PHIS, including post-breccia gabbro/diorite and felsic intrusions are emplaced, and in the case of the gabbroic phase cuts the breccia. The pre-breccia gabbro/diorite phase is slightly more alkalic than the pre-breccia gabbroic phase; presumably related to crustal assimilation and contamination.

5.6. Conclusions

The PHIS and the associated Lodestar Prospect provide an excellent area for the study of intrusion related, magmatic-hydrothermal breccia systems. This study has provided a description and interpretation of the nature of a magmatic-hydrothermal breccia system in an area relatively unexplored for this type of deposit. The major conclusions that can be drawn from this study are as follows:

1) The PHIS consists of a multi-phase intrusion, dominated by gabbro/diorite, and lesser

amounts of felsic and diabase material. Two dates returned from the intrusive suite indicate an age of approximately 603-605 Ma (Neoproterozoic); thereby suggesting that the intruded sedimentary unit belongs to the Connecting Point Group.

2) Based upon field, petrographic, and geochemical studies it is suggested that the three main phases of the PHIS are related by fractionational processes. The PHIS is interpreted to represent an "open" magmatic system with variable physicochemical conditions. As such, some of the geochemical data appear to argue against fraction processes as discussed in chapter four. The major irregularities consist of lower Y, Zr, and Nb with increasing SiO_2 and decreasing MgO, and the presence of a negative Nb anomaly in the pre-breccia gabbro/diorite which is not present in the post-breccia gabbro/diorite. These discrepancies have been explained and interpreted to result from increased proportions of accessory minerals within the more mafic (ie. lower SiO_2) post-breccia gabbro/diorite, thereby allowing it to contain increased proportions of incompatible elements and reverse the expected trends on diagrams such as SiO_2 versus Y, Zr, and Nb. The negative Nb anomaly associated with the pre-breccia gabbro/diorite is an expected result since it would have assimilated much more crustal material while preparing the plumbing for the rest of the intrusive phases which would be effectively "shielded" from crustal contamination by the pre-breccia gabbro/diorite.

3) The magmatic-hydrothermal breccia comprising the Lodestar Prospect is interpreted to be the product of fluid exsolution from an auriferous porphyry intrusive system at depth. The main process driving the brecciation was the violent exsolution of magmatic-

hydrothermal fluids from the cooling porphyry stock at depth (second boiling and decompression). These fluids took advantage of a contact zone between the pre-breccia gabbroic intrusive phase and the host sedimentary unit to intrude along this zone of weakness.

4) Breccia clasts are dominantly comprised of locally derived sedimentary and gabbroic material, as well as "exotic" quartz-feldspar porphyry clasts. Some of the "exotic" QFP clasts contain pre-breccia mineralization; suggestive of a mineralized system at depth. REE and trace element chemistry indicate that the QFP clasts were derived from a different parental magma than the phases of the PHIS.

5) Gold is dominantly associated with arsenopyrite mineralization within the matrix of the breccia. The association is on the lattice scale whereby Au is assumed to substitute for Fe/As; thereby making the auriferous mineralization refractory (invisible gold).

6) Sulphur isotope ratios from mineralization of the Lodestar Prospect indicate that the mineralizing fluids were most probably of magmatic origin, however, the ratios do indicate some contamination, potentially associated with the milling of, and/or assimilation of, sedimentary clasts.

7) Geothermometers indicate that the approximate temperature of the mineralizing fluids was ~ 425 °C +/- 50 °.

8) High level felsic intrusions which intrude both the pre- and post-breccia gabbroic phases are interpreted to represent late stage intrusions from the deep parental magma which fed the pre and post gabbro/diorite.

9) The Lodestar prospect may represent a transitional environment between a deep seated porphyry system and a shallower epithermal system. This is important in that it opens the possibility of discovering similar mineralization types elsewhere on the Burin and Bonavista Peninsulas.

5.6.1. Directions for further study.

In addition to the work presented in this thesis, there are many other areas of future study that could be addressed. Firstly, additional detailed geochronological studies should be carried out; the purposes of which would be two-fold. The first which is currently underway, involves dating the post-breccia gabbro/diorite which cuts the breccia showing; the results in conjunction with the dates determined for the pre-breccia intrusive phases, would definitively bracket the age of brecciation and mineralization. The second is a study of the felsic clasts from the breccia; the results of which would temporally compare the suspected "blind" porphyry body at depth to the PHIS phases. Both of these geochronological studies would have profound impact on the importance of the Lodestar Prospect on a regional scale whereby the resultant dates would aid in pinpointing other areas of potential interest for future exploration.

Another study which could be conducted from a magmatic evolution perspective would involve radiogenic isotope studies (eg.Sm/Nd, Rb/Sr, Pb/Pb) on the felsic clasts within the breccia and the felsic intrusive phase. By conducting such studies, additional information could be gathered regarding the comparisons/contrasts between the parental magma bodies of both units; the results of which would serve to aid in the argument for,

or against, the presence of a possible mineralized porphyry system (unique from the PHIS in its magmatic source) at depth.

From an exploration point of view, a number of additional techniques could be undertaken, both at the Lodestar Prospect proper and in the Burin and Bonavista Peninsula area.

Firstly, in terms of the Lodestar Prospect, additional geophysical surveys should be conducted in the area. Original studies (NDT Ventures Ltd. and Noveder Inc.) consisting of magnetic, VLF-EM, and Induced Polarization/Resistivity (IP), were conducted along a grid now thought to be parallel or sub-parallel to the main mineralized breccia zone. This has made interpretation difficult and relatively uninformative with respect to the breccia showing; hence the data were not discussed in the scope of this thesis. However, one interesting result obtained from these surveys was definition of a prominent magnetic low directly adjacent to, and east of the main showing. Within the scope of the proposed models associated with this thesis, this magnetic low could be inferred to represent a fault zone along which the breccia intruded (associated with the contact between the pre-breccia gabbroic phase and the host sedimentary unit), or alternatively it could represent a porphyritic intrusive body (source of the breccia) and associated alteration halo at depth. Additional IP and VLF-EM geophysical surveys are recommended in the area of the breccia in order to determine the strike and extent of the zone, and to determine if the magnetic low has associated VLF-EM and/or IP anomalies, the results of which would aid in detecting additional structural controls and

mineralization. Following these studies, it is recommended to test the mineralized breccia by drilling with the goal of determining the vertical extent and nature of the breccia zone. The possibility of additional mineralized occurrences along the contact of the sedimentary unit and the pre-breccia gabbro/diorite phase in the PHIS area should also be examined with detailed prospecting along the contact areas as illustrated in figure 1.2.

On a regional scale, the age and style of the Lodestar Breccia Prospect symbolizes the metallogenic potential of the Avalon Zone, specifically the Burin and Bonavista Peninsulas, with respect to magmatic-hydrothermal breccia systems and associated mineralized porphyry systems at depth. A good place to explore for these types of deposits would be in the known high-sulphidation epithermal systems that occur along the length of the Burin and Bonavista Peninsulas (figure 2.6), and in areas of known mafic intrusions into the 620-600 Ma volcanic belt along the length of the two peninsulas (figure 2.6). Exploration should be carried out in conjunction with geophysical studies (ie. magnetic studies) and regional lake sediment databases.

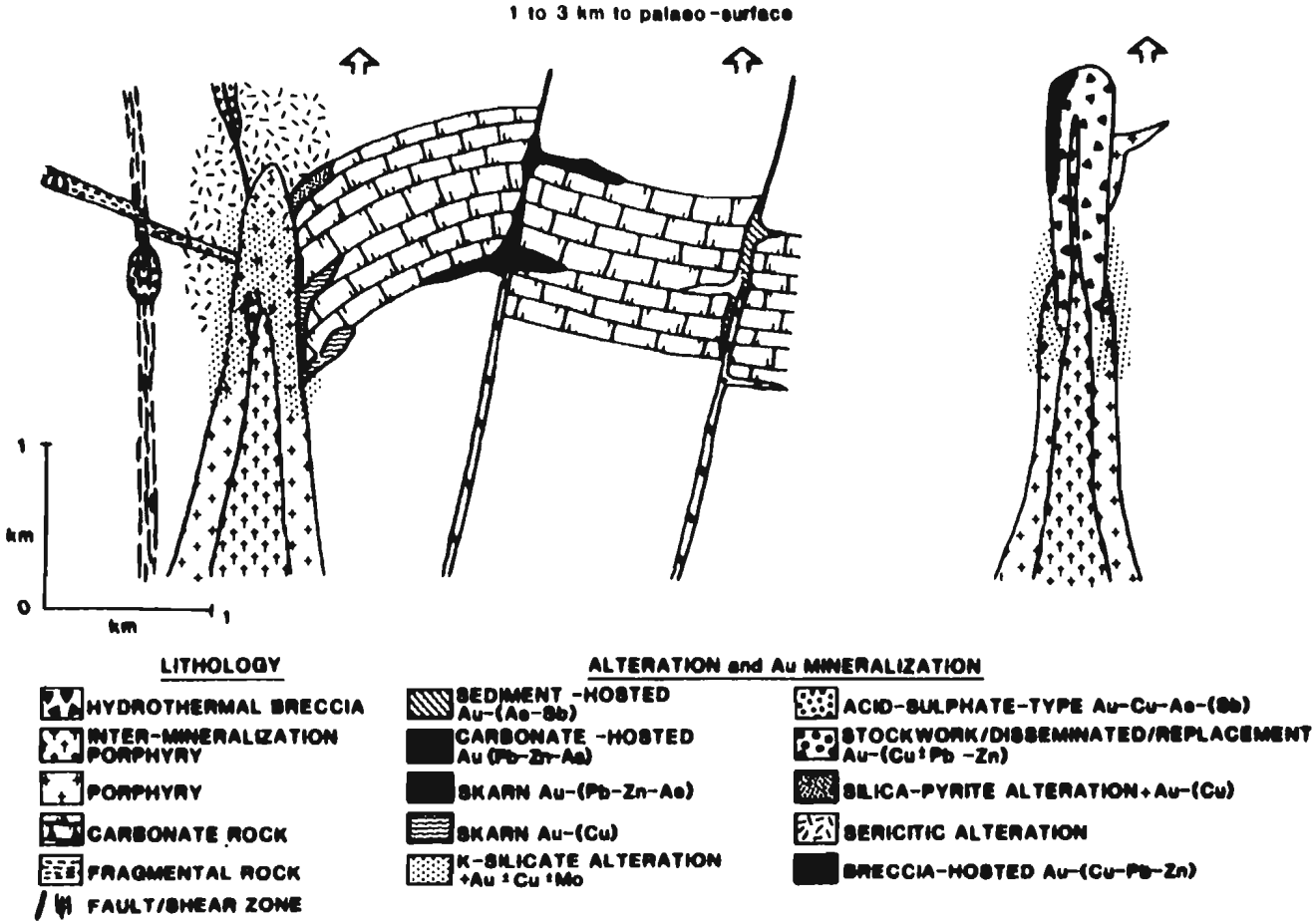

Figure 5.1: Schematic illustrating interrelationships between "porphyry" intrusions at depth and some of the major hydrothermal gold deposit types. The environments depicted grade up into the epithermal environment. Note that the presence of all styles of mineralization in a single district is not implied. (From Sillitoe, 1991).

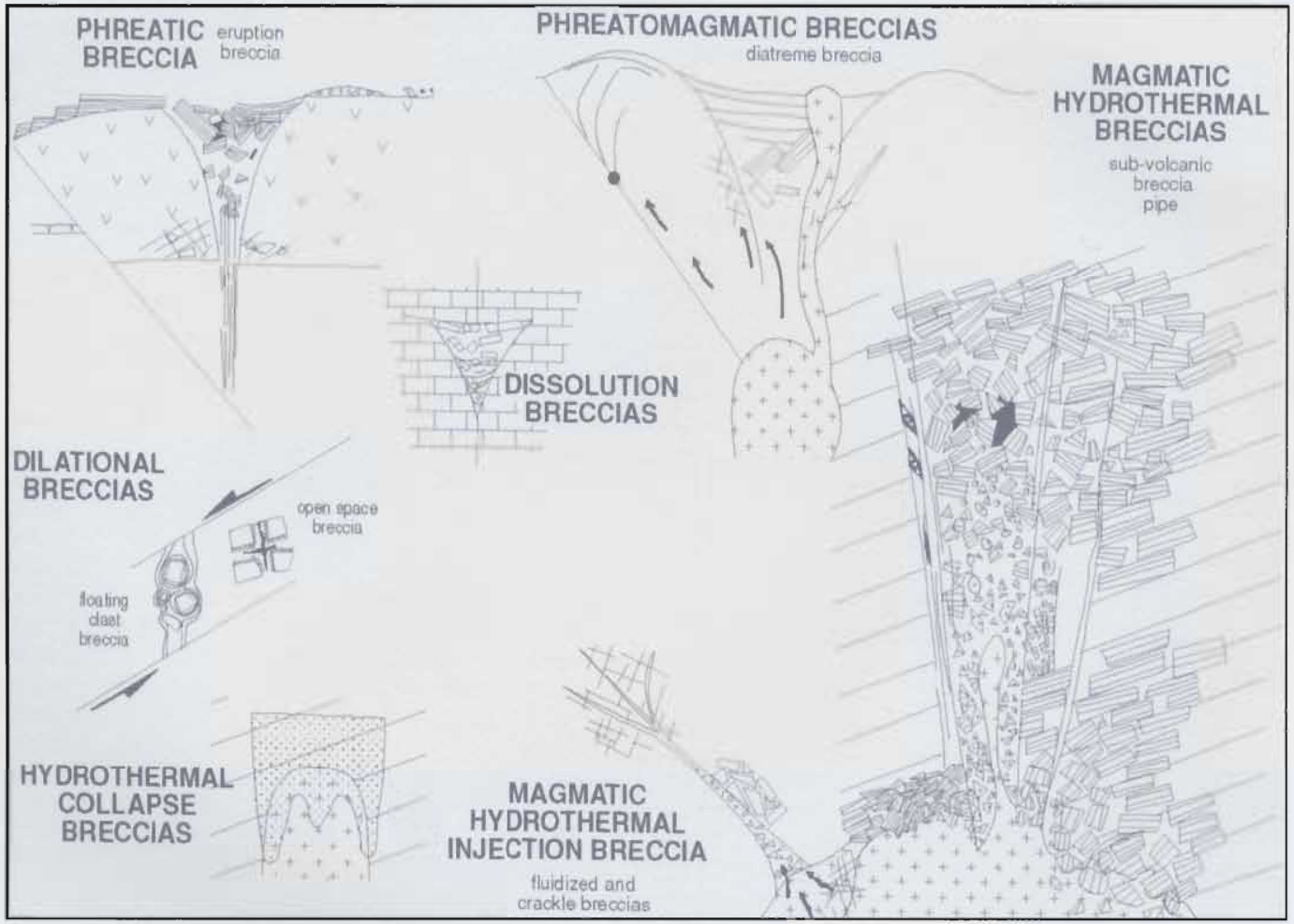

Figure 5.2: Environments of breccia formation. (From Corbett and Leach, 1998).

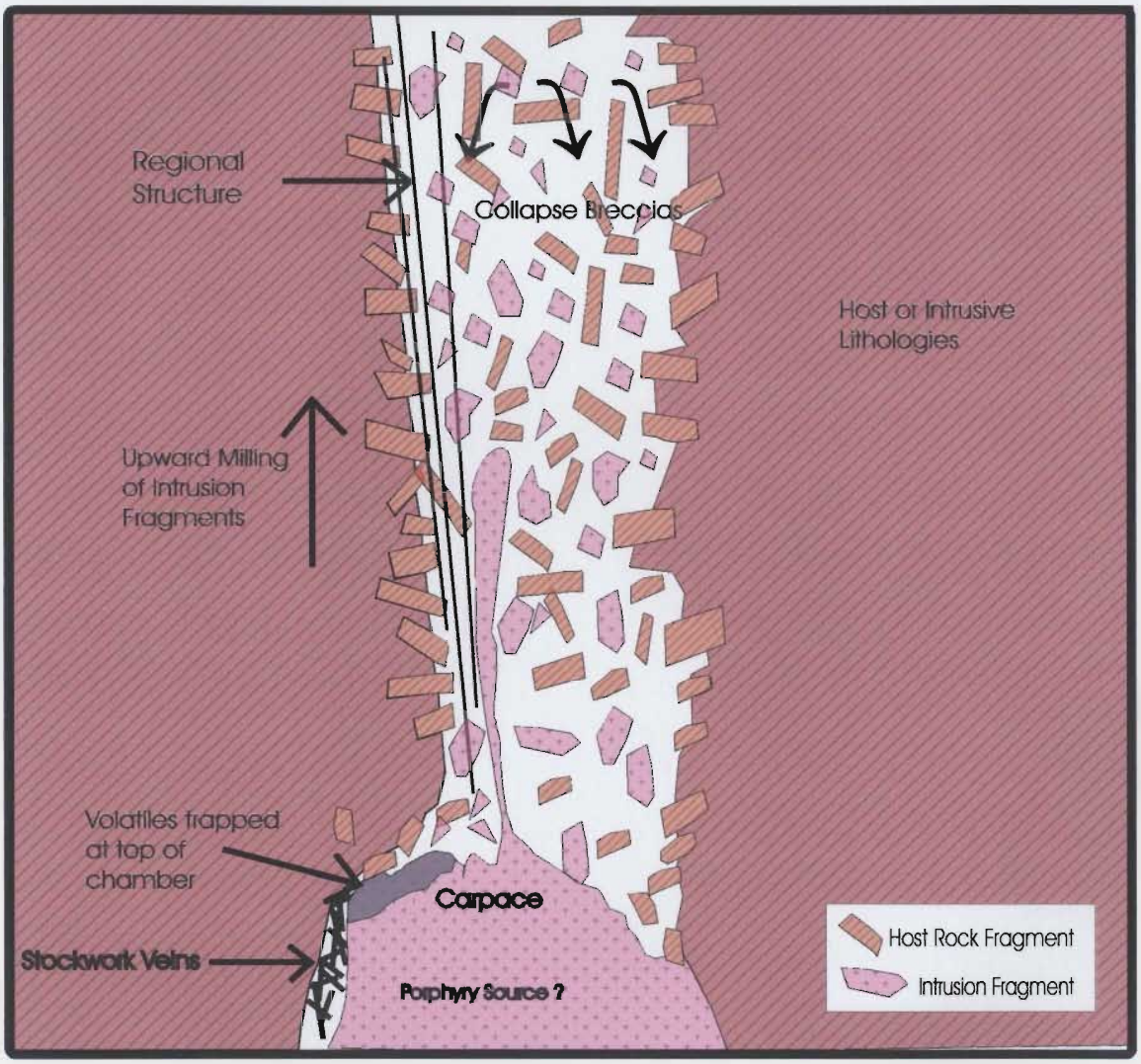

Figure 5.3: Model of a magmatic-hydrothermal breccia - subvolcanic breccia pipe.(After Corbett and Leach, 1998).

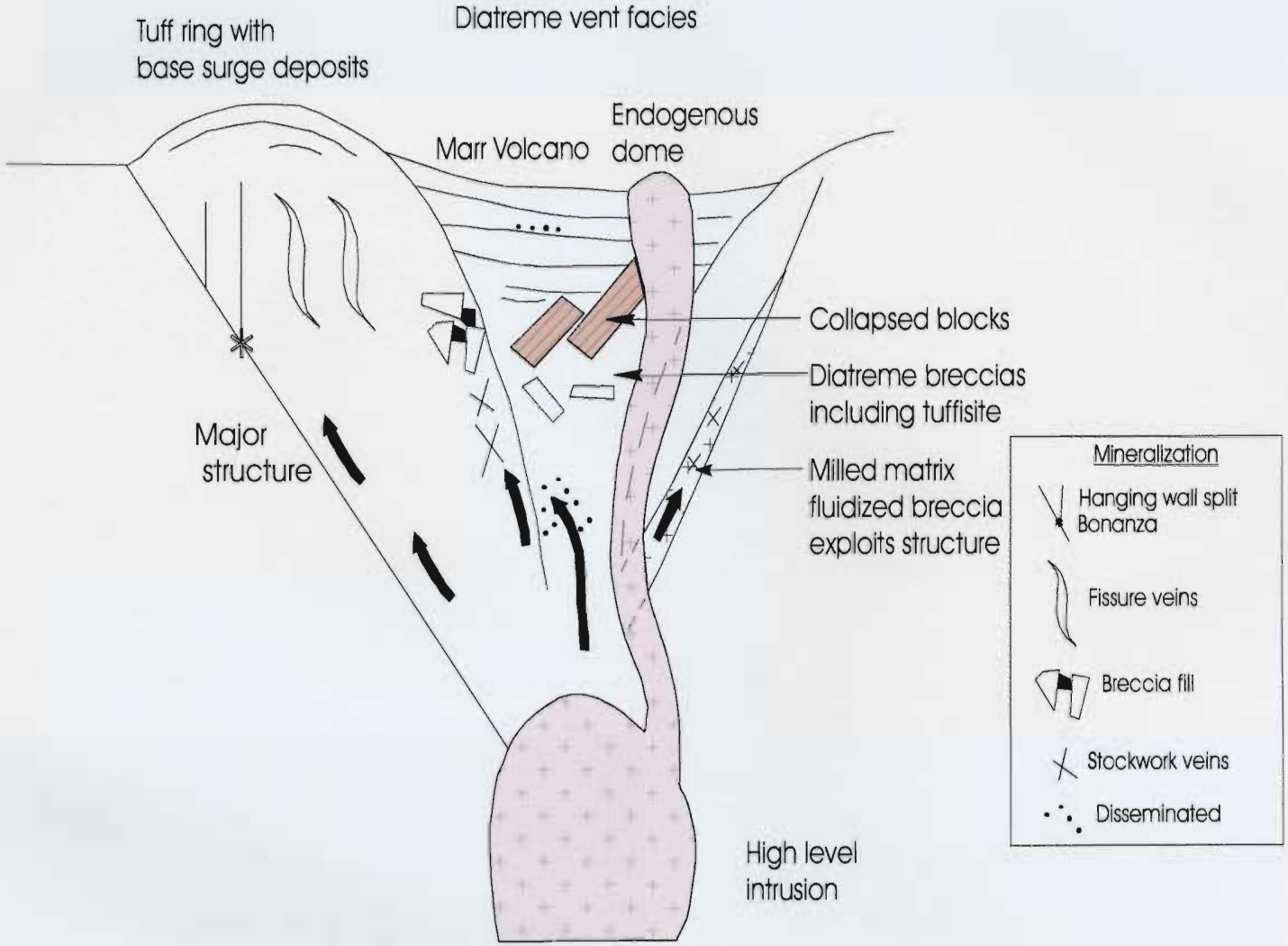

Figure 5.4: Model of a phreatomagmatic breccia. (After Corbett and Leach, 1998).

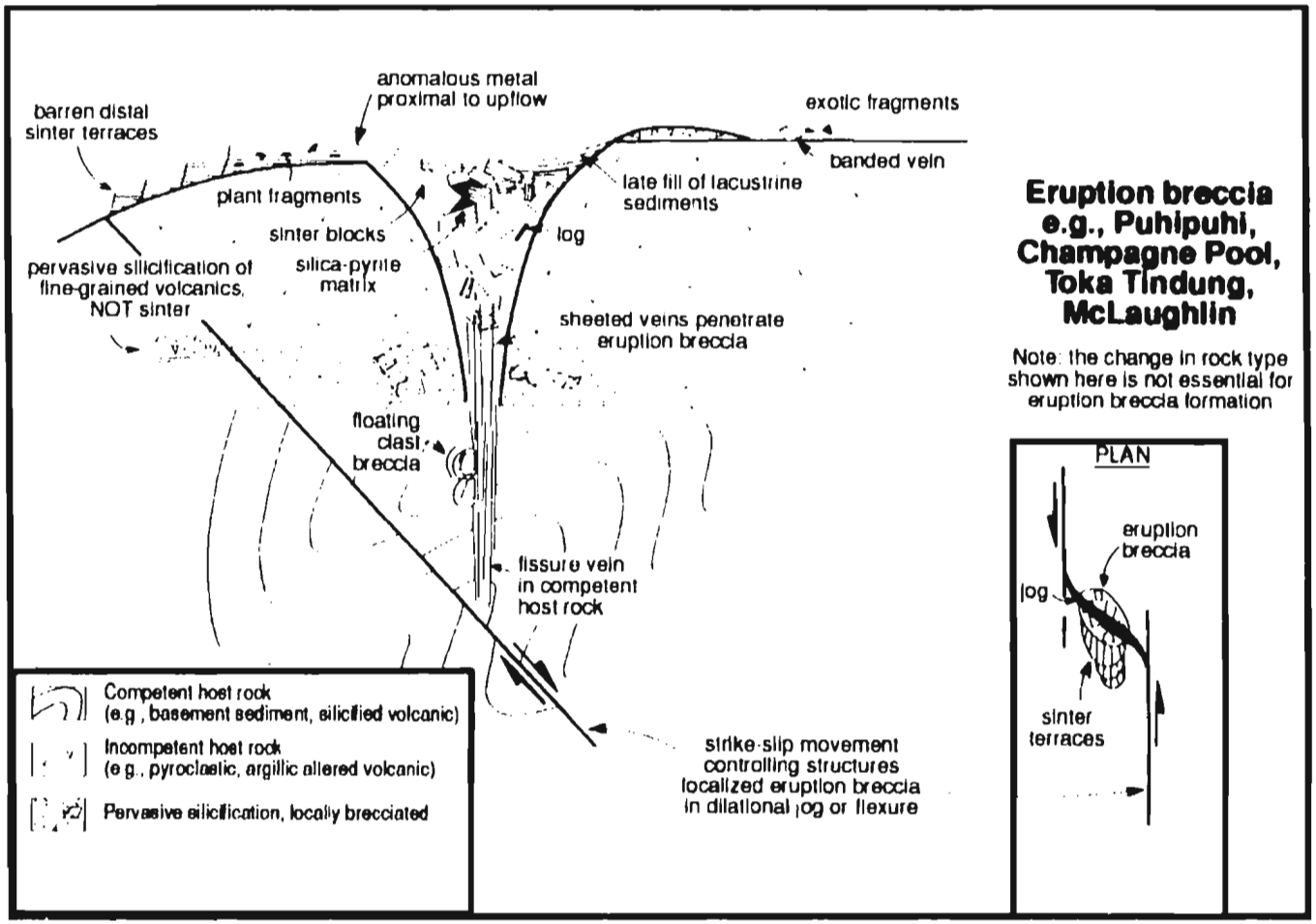

Figure 5.5: Model of a phreatic breccia. (From Corbett and Leach, 1998)

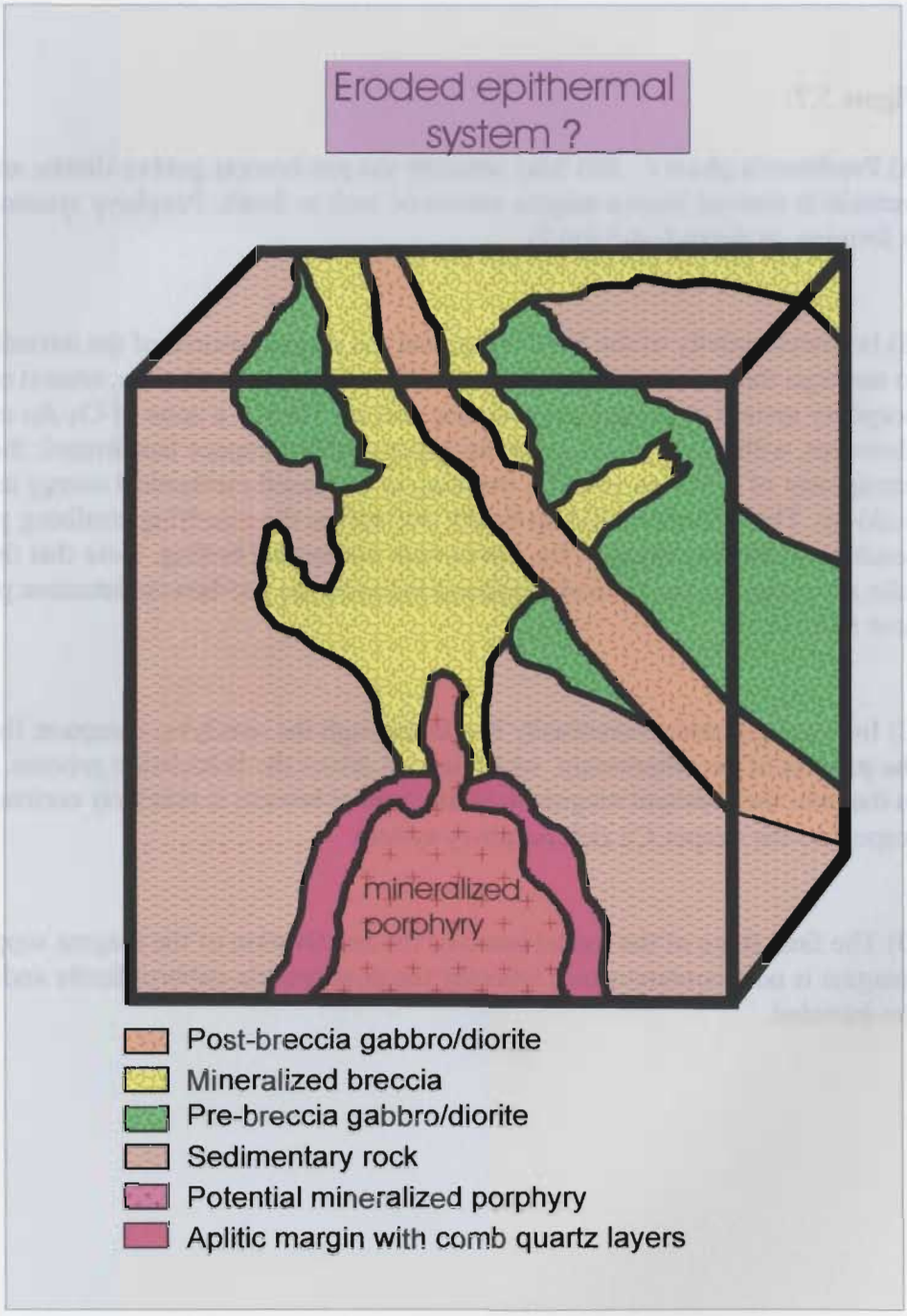

Figure 5.6: Schematic model for the Lodestar Prospect.

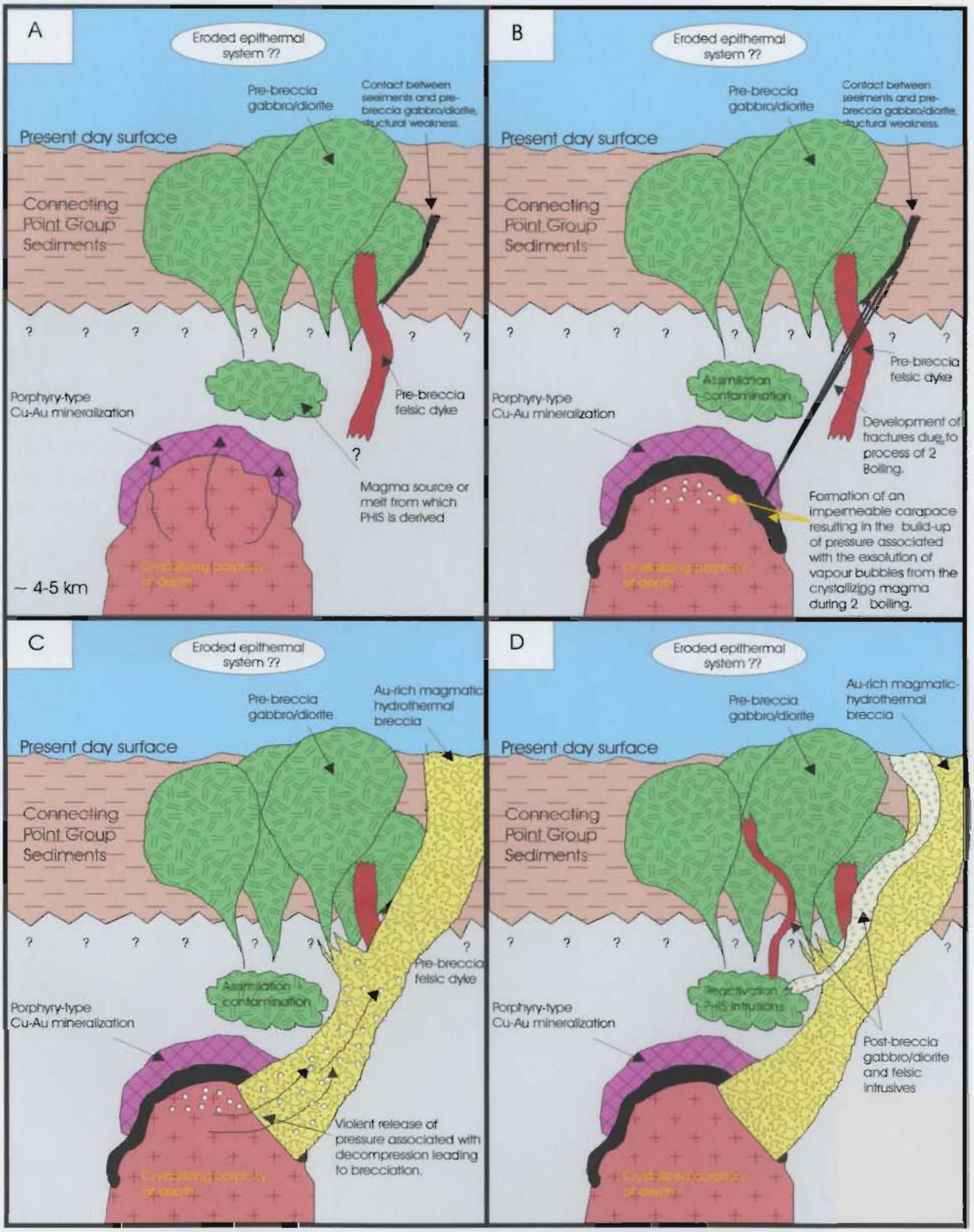

Figure 5.7: multi-stage diagram illustrating the formation of the PHIS and the Lodestar Breccia. Discussion on opposing page.

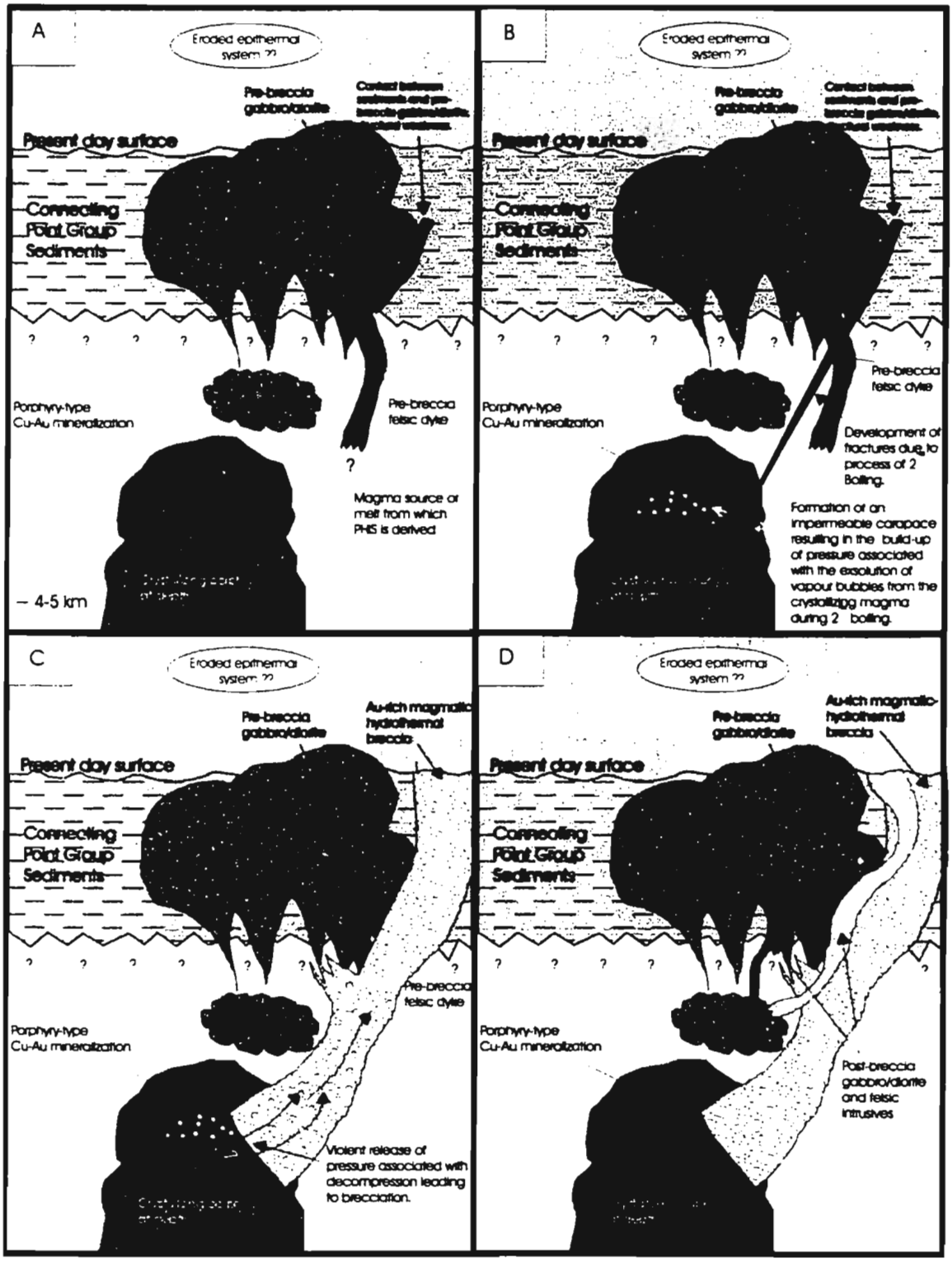

Figure 5.7: multi-stage diagram illustrating the formation of the PHIS and the Lodestar Breccia. Discussion on opposing page.

Table 5.1: Comparison of the major characteristics of the three types of magmatic-hydrothermal breccia investigated in detail for this study. (From Corbett and Leach, 1998).

	MAGMATIC	PHREATOMAGMATIC	PHREATIC
Common Name	• sub-volcanic breccia pipes • magmatic hydrothermal breccia pipes	• diatreme breccia • milled matrix fluidized breccia	• eruption breccia
Origin	• violent exsolution of volatiles from intrusion	• venting of volatiles and rapid heating of ground waters	• depressurisation of geothermal waters
Level	• deep at porphyry level • need not vent	• intermediate diatreme vents • milled matrix fluidized breccia exploits structure	• surficial • form sinter outflows
Intrusive activity	• porphyry-derived, dikes	• endogenous domes	• none exposed
Style of mineralization	• quartz-sulphide-gold ± copper, grading to carbonate-base metal-gold	• carbonate-base metal-gold • high sulphidation gold-copper	• adularia-sericite epithermal gold silver
Alteration	• sericite-quartz • biotite, K-feldspar • actinolite, epidote	• sericite to smectite • disseminated fine crystalline pyrite	• silica-fine pyrite/marcasite
Form	• intrusion styles dominated by introduced intrusive fragments • collapse styles dominated by local fragments	• vent facies within diatreme • tuff ring facies thrown out of diatreme	• cone-shaped pipes • vent and tuff ring facies
Fragments	• magmatic and local • tabular shingle breccias in collapse styles • milled fragments in injection styles	• juvenile intrusion fragments characteristic • local accretionary lapilli • tuffisites are well milled	• locally derived, commonly angular
Matrix	• rock flour, open space	• milled and fluidized clay-pyrite altered	• silica-pyrite
Examples	• Kidston, San Cristobal, Golden Sunlight, Mt. Leyshon	• Wau, Kelian, Acupan, Kerimenge, Lepanto, Tolukuma	• Champagne Pool, Puhipuhi, Toka Tindung, McLaughlin

References

Anderson, F.D.
1965: Belleoram, Newfoundland. Geological Survey of Canada, Map 8-1965.

Arehart G.B., Chryssoulis S.L., Kesler S.E.
1993: Gold and Arsenic in iron sulphides from sediment-hosted gold deposits: implications for depositional processes. Econ Geol 88: 171-185.

Bach, J.J.
1987: World Gold Deposits - A Quantitative Classification: Elsevier Science Publishing Company, 178 p.

Baker, E.M., and Andrew, A.S.
1988: Processes associated with gold mineralization within the Kidston breccia pipe, north Queensland, in Bicentennial Gold '88, extended abstracts oral programme (eds. A.D.T. Goode and L.I. Bosma), Geol. Soc. Aust. Abst., 22: 102-109.

1991: Geologic, fluid inclusion, and stable isotope studies of the gold-bearing breccia pipe at Kidston, Queensland, Australia: Economic Geology., vol. 86, pages 810-830.

Baker, E.M., and Tullemans, F.J.
1990: Kidston gold deposit. In Huges, F.E., Ed., Geology of the Mineral Deposits of Australia and Papa New Guinea, v. 2: Australian Institute of Mining and Metallurgy, Monograph 14, 1461-1465.

Ballhaus, C., Ryan, C.G., Mernagh, T.P., and Green, D.H.
1994: The partitioning of Fe, Ni, Cu, Pt, and Au between sulphide, metal, and fluid phases: A pilot study. Geochim. Cosmochim. Acta, vol. 58. Pages 811-826.

Barton, P.B.
1969: Thermochemical study of the system Fe-As-S: Geochimica et Cosmochimica Acta, vol., 278, pages 1412-1427.

Blackwood, R.F.
1978: Northeastern Gander Zone, Newfoundland; in Report of Activities for 1977, (ed.) R.V. Gibbons; Newfoundland Department of Mines and Energy, Mineral Development Division, Report 78-1, p. 72-79.

1982: Geology of the Gander Lake (2D/15) and Gander River (2E/2) area: Newfoundland Department of Mines and Energy, Mineral Development Division, Report 82-4, 56 p.

Blackwood, R.F. and Kennedy, M.J.
1975: The Dover Fault: western boundary of the Avalon Zone in northeastern Newfoundland; Canadian Journal of Earth Sciences, v.12, p. 320-325.

Blackwood, R.F. and O'Driscoll, C.F.
1976: The Gander Avalon Zone boundary in southeastern Newfoundland: Canadian Journal of Earth Sciences, v.13, p. 1155-1159.

Bonham, H.F. and Giles, D.L.
1983: Epithermal gold/silver deposits: the geothermal connection. Geothermal Resources Council, Special Report, vol. 13, pages 257 - 262.

Boiron, M.C.
1987: Mineralisations a Au, As, Sb, alterations hydrothermales et fluides associes dans le bassin de Villeranges (Combrailles, Massif Central Francais): Nancy University, Geologie, Geochimie et Uranium Memoire 15, 310 p.

Boyle, R.W.
1979: The geochemistry of gold and its deposits: Geological Survey of Canada Bulletin 280, p.584.

Burnham, C.W.
1979: Magmas and hydrothermal fluids, in Barnes, H.L., ed., Geochemistry of hydrothermal ore deposits: New York, Wiley, p. 71-136.

1985: Energy Release in Subvolcanic Environments: Implications for Breccia Formation. Economic Geology, Vol. 80, pp. 1515-1522.

Burnham, C.W., and Ohmoto, H.
1980: Late stage processes of felsic magmatism, in Ishihara, S., and Takenouchi, S., eds., Granitic magmatism and related mineralization: Soc. Mining Geologists Japan, Spec. Issue 8, p. 7727-7738.

Cabri, L.J., Chryssoulis, S.L, De Villiers, J.P.R., Laflamme, J.H., Buseck, P.R.
1989: The Nature of "Invisible" Gold in Arsenopyrite; The Canadian Mineralogist, vol., 27, pages 353-362.

Candela, P.A.
1989: Felsic magmas, volatiles, and metallogenesis. Reviews Econ. Geol. Vol 4, pages 223-233.

Carpenter, P.A.
1972: Gold resources of North Carolina. North Carolina Department of Natural and Economic Resources. Information Circular 21, 56 pages.

Cook, N.J., and Chryssoulis, S.L.
1990, Concentrations of "invisible" gold in the common sulphides: Canadian Mineralogist, v. 28, p. 1-16.

Corbett,G. and Leach, T.
1998: Southwest Pacific Rim gold-copper systems: structure, alteration and mineralization. Society of Economic Geologists, Special Publication Number 6, 237 pages.

Cox, K.G., Bell, J.D., and Pankhurst, R.J.
1979: The interpretation of igneous rocks. George, Allen and Unwin, London.

Dahl, O.M.
1934: Third report on the iron deposits at Hickey's Pond, Placentia Bay, Newfoundland. Davenport and Company, Aldwych, W.C. 2, London, England. Unpublished report, 9 pages. [1M/16/2]

Dallmeyer, R.D., Blackwood, R.F., and Odom, A.L.
1981: Age and origin of the Dover Fault: tectonic boundary between the Gander and Avalon zones of the northeastern Newfoundland Appalachians: Canadian Journal of Earth Sciences, v. 18, p. 1431-1442.

Dec, T., O'Brien, S. J. and Knight, I.
1992: Late Precambrian volcaniclastic deposits of the Avalonian Eastport Basin (Newfoundland Appalachians): Petrofacies, detrital clinopyroxene geochemistry and paleotectonic implications. Precambrian Research, Volume 59, pages 243-262.

Dimmell, P. and MacGillivray, G.
1989: First year assessment report on the Project 7427 Hickey's Pond Property, Burin Peninsula area, Newfoundland. Unpublished report, Corona Corporation, 9 pages plus maps and appendices.

Dubé, B., Dunning, G. and Lauzière, K.
1998: Geology of the Hope Brook Mine, Newfoundland, Canada: a preserved late Proterozoic high-sulphidation epithermal gold deposit and its implications for exploration. Economic Geology, Volume 98, pages 895-913.

Faure, G.
1986: Sulphur. In Principles of Isotope Geochemistry. Pages 523-553

Faure, G., Hoels, J., and Mensing, T.M.
1984: Effect of oxygen fugacity on sulphur isotope compositions and magmatic concentrations in the Kirkpatrick basalt, Mount Falla, Queen Alexandra Range, Antarctica. Isotope Geoscience, vol 2, pages 301-311.

Fleet, M.E., Chryssoulis, S.L., MacLean, P.J., Davidson, R., and Weisener, G.
1993: Arsenian pyrite from gold deposits: Au and As distribution investigated by SIMS and EP, and color staining and surface oxidation by XPS and LIMS: Canadian Mineralogist, v. 31, p. 1-17.

Foster, R.P. (Editor)
1991: Gold Metallogeny and Exploration. London, Blackie and Son Ltd.

Friedman, I., and O'Neil, J.R.
1977: Compilation of stable isotope fractionation factors of geochemical interest. In M. Fleischer, ed., Data of Geochemistry, sixth ed., chapter KK. U.S. Geol. Surv. Prof. Paper 440-KK, 12 pages and 49 figures.

Gardner, S., and Hiscott, R.N.
1988: Deep-water facies and depositional setting of the lower Conception Group (Hadrynian), southern Avalon Peninsula, Newfoundland: Canadian Journal of Earth Sciences, v. 25, p. 1579-1594.

Genkin, A.D., Bortnikov, N.S., Safonov, Y.G., Cabri, L.J., McMahon, G., Stanley, C.G., Wagner, F.E., Friedl, J., Kurzin, A.L., and Gamyanin, G.N.
1998: A multidisciplinary study of invisible gold in arsenopyrite from four mesothermal gold deposits in Siberia, Russian Federation. Economic Geology, vol. 93, pages 463-487.

Gustafson, L.B.
1979: Porphyry copper deposits and calc-alkaline volcanism. In: The Earth: Its origin, Structure, and Evolution (McElhinney, M.W. ed.). Academic Press, London. 427–468.

Hall, J., Marille, F., and Dehler, S.
1998: Geophysical studies of the structure of the appalachian orogen in the Atlantic borderlands of Canada. Canadian Journal of Earth Sciences, v.35: pages 1205-1221.

Hayes, A.O.
1948: Geology of the area between Bonavista and Trinity Bays, eastern Newfoundland. Geological Survey of Newfoundland, Bulletin 32, part 1, 36 pages.

Hayes, J.P.,
1997: Geological setting and genesis of the eastern avalon high-alumina belt. Unpublished MSc thesis, Memorial University of Newfoundland, St. John's, Newfoundland, Canada, 172 pages.

Hayes, J.P. and O'Driscoll, C.F.
1990: Regional setting and alteration within the eastern Avalon high-Alumina belt, Avalon Peninsula, Newfoundland. *In* Current Research. Newfoundland Department of Mines and Energy, Geological Survey Branch, Report 90-1, pages 145-155.

1994: Regional geological setting and hydrothermal alteration within the eastern Avalon high-alumina belt: Canadian Institute of Mining, Metallurgy and Petroleum, Field Trip Guide, 25 p.

Hibbard, J.P.
1983: Geology of the Baie Verte Peninsula, Newfoundland; Newfoundland Department of Mines and Energy, Mineral Development Division, Memoir 2, 279 p.

Hinchey, J.G., O'Driscoll, C.F., Wilton, D.H.C.
2000: Breccia-Hosted Gold on the Northern Burin Peninsula, Newfoundland. In Current Research (2000), Newfoundland Department of Mines and Energy, Geological Survey, Report 2000-1, pages 299-309.

Hofmann, A.W.
1988: Chemical differentiation of the Earth: the relationship between mantle, continental crust and oceanic crust. Earth and Planetary Science Letters, volume 90, pages 297-314.

Huard, A.
1990: Epithermal alteration and gold mineralization in Late Precambrian volcanic rocks on the northern Burin Peninsula, southeastern Newfoundland, Canada. Unpublished M.Sc. thesis, Memorial University of Newfoundland, St. John's, Newfoundland, 273 pages.

Huard, A. and O'Driscoll, C.F.
1984: Auriferous specularite-alunite-pyrophyllite deposits of the Hickey's Pond area, Newfoundland. In Report of Activities for 1984. Newfoundland Department of Mines and Energy, Mineral Development Division, pages 71-73.

1986: Epithermal gold mineralization in Late Precambrian volcanic rocks on the Burin Peninsula. In Current Research. Newfoundland Department of Mines and Energy, Mineral Development Division, Report 86-1, pages 65-78.

Hughes, C.J. and Bruckner, W.D.,
1971: Late Precambrian rocks of eastern Avalon Peninsula, Newfoundland - a volcanic island complex. Canadian Journal of Earth Sciences, Volume 8, pages 899-915.

Hunt, J.P.
1977: Porphyry Copper Deposits. In: Volcanic processes in ore genesis (abs.). Inst. Mining Metallurg. London, UK.

Hussey, E.M.
1978: Geology of the Sound Island map area, (west half), Newfoundland. *In* Report of Activities. Newfoundland Department of Mines and Energy, Mineral Development Division, Report 78-1, pages 110-115.

Irvine, T.N. and Baragar, W.R.A
1971: A guide to the chemical classification of the common volcanic rocks. Canadian Journal of Earth Science., Vol.8, pages 523-548.

Jenness, S.E.
1958: Geology of the lower Gander River ultrabasic belt, Newfoundland; Geological Survey of Newfoundland; Report 11, 58p.

1963: Terra Nova and Bonavista map areas, Newfoundland. Geological Survey of Canada, Memoir 327, 184 pages.

Jenner, G.A., Longerich, H.P., Jackson, S.E. and Fryer, B.J.
1990: ICP-MS - A powerful tool for high precision trace element analysis in the earth sciences: Evidence from analysis of selected USGS reference samples. Chemical Geology, 83. Pages 133-148.

Jenson, L.S.
1976: A new plot for classifying subalkalic volcanic rocks. Ontario Division of Mines, MP 66, 22 pages.

Johan Z, Marcoux E, Bonnemaison, M.
1989: Arsenopyrite aurifere: mode de substitution de Au dans la structure de FeAsS. C R Acad Sci (Paris) 308: 185-191.

Kerr, L.C., Craw, D., and Youngson, J.H.
1999: Arsenopyrite compositional variation over variable temperatures of mineralization, Otago Schist, New Zealand. Economic Geology, Vol. 94, pages 123-128.

King, A.F.
1990: Geology of the St. John's area. Newfoundland Department of Mines and Energy, Geological Survey Branch, Report 90-2, 88 pages.

1988: (compiler), Late Precambrian sedimentation and related orogenesis of the Avalon Peninsula, Eastern Avalon Zone, in Geological Association of Canada-Mineralogical Association of Canada-Canadian Society of Petroleum Geologists, Annual Meeting, Field Trip A-4, Guidebook: St.John's, Newfoundland, 84 p.

King, A.F., Bruckner, W.D., Anderson, W.D., and Fletcher, T.P.
1974: Late Precambrian and Cambrian sedimentary sequences of eastern Newfoundland: Geological Association of Canada, Annual Meeting 1974, Field trip manual B-6: St. John's, Newfoundland, 59 p.

Kirkham, R.V., and Sinclair, W.D.
1988: Comb quartz layers in felsic intrusions and their relationship to porphyry deposits, in Recent Advances in the Geology of Granite-Related Mineral Deposits, Special Volume 39: The Canadian Institute of Mining and Metallurgy, Taylor, R.P., and Strong (D.F.) (Editors), 1988, Pages 50-71.

Knight, I. and O'Brien, S.J.
1988: Stratigraphy and sedimentology of the Connecting Point Group, Eastport (2C/12) and St. Brendan's (2C/13) areas. *In* Current Research, Newfoundland Department of Mines, Mineral Development Division, Report 88-1, pages 207-228.

Kretschmar, U., and Scott, S.D.
1976: Phase relations involving arsenopyrite in the system Fe-As-S and their application: Can. Mineral., vol. 14, pages 364-386.

Krogh, T.E., Strong, D.F., O'Brien, S.J. and Papezik, V.S.
1988: Precise U–Pb zircon dates from the Avalon Terrane in Newfoundland. Canadian Journal of Earth Sciences, Volume 25, pages 442-453.

Laznicka, P.
1988: Breccias and coarse fragmentites. Petrology, environments, associations, ores. Developments in Economic Geology, 25. Elsevier Science Publishing Company Inc.

Leblanc, M.
1981: The late Proterozoic ophiolites at Bou Azzer, Morocco: evidence for Pan-African plate tectonics. In Precambrian Plate Tectonics, ed. Kroner, A. Elsevier, Amsterdam, pages. 435-441.

Longerich, H.P.
1995: Analysis of pressed pellets of geological samples using wavelength-dispersive X-Ray Fluorescence Spectrometry. X-Ray Spectrometry, 24: 123-136.

McCartney, W.D.
1958: Geology of the Sunnyside map area, Newfoundland. Geological Survey of Canada, Paper 58-8.

1967: Whitbourne map area, Newfoundland. Geological Survey of Canada, Memoir 327, 184 pages.

McKenzie, C.M.
1983: Hickey's Pond 1M/16 diamond drilling report. Claim Block 3317. License 2268. Unpublished report. Selco Inc. [1M/16/209]

1986: Geology and mineralization of the Chetwynd deposit, southwestern Newfoundland, Canada. In Proceedings of Gold '86, An International Symposium on the Geology of Gold. Edited by A.J. Macdonald. Gold '86. Toronto. pages 137-148.

Mills, J., O'Brien, S.J., Dubé, B., Mason, R., and O'Driscoll,C.F.
1999. The Steep Nap Prospect: a low-sulfidation, gold-bearing epithermal vein system of Late Neoproterozoic age, Avalon Zone, Newfoundland Appalachians: *in* Current Research: Newfoundland Department of Mines and Energy, Report 99-1, pages 255-274.

Mutschler, F.E., Griffin, M.E., Stevens, D.S., and Shannon, S.S.
1984: Precious metal deposits related to alkaline rocks in the North American Cordillera. Geol. Soc. Am. Abstr. Programs, vol. 16, page 606.

Nielson, H.
1979: Sulphur isotopes. In E. Jager and J. C. Hunziker, eds.: Lectures in Isotope Geology, 283-312. Springer-Verlag, Berlin.

O'Brien, S.J., Wardle, R.J. and King, A.F.
1983: The Avalon Zone: A Pan-African terrane in the Appalachian Orogen of Canada. Geological Journal, Volume 18, pages 195-222.

O'Brien, S.J. and Knight, I.
1988: Avalonian geology of southwest Bonavista Bay: Parts of the St. Brendans's (2C/13) and Eastport (2C/13) map areas. *In* Current Research. Newfoundland Department of Mines, Mineral Development Division, Report 88-1, pages 193-205.

O'Brien, S.J., Dunning, G.R., Knight, I., and Dec, T.
1989: Late Precambrian geology of the north shore of Bonavista Bay (Clode Sound to Lockers Bay). In report of activities, Newfoundland Department of Mines and Energy, Geological Survey Branch, p. 49 - 50.

O'Brien, S.J., Strong, D.F. and King, A.F.
1990: The Avalon Zone type area: southeastern Newfoundland Appalachians. *In*

Avalonian and Cadomian Geology of the North Atlantic. *Edited by* R.A. Strachan and G.K. Taylor. Glasgow, Blackies and Son, pages 166-193.

O'Brien, S.J., O'Driscoll, C.F. and Tucker, R.D.
1992: A reinterpretation of the geology of parts of the Hermitage Peninsula, southwestern Avalon zone, Newfoundland. *In*: Current Research, Newfoundland Department of Mines and Energy, Geological Survey Branch, Report 92-1, pages 185-194

O'Brien, S.J., Tucker, R.D. and O'Driscoll, C.F.
1994: Neoproterozoic basement-cover relationships and the tectonomagmatic record of the Avalon Zone on the Hermitage Peninsula and environs, Newfoundland. *In*: New Perspectives in the Appalachian - Caledonian orogen, Geological Association of Canada, Williams NUNA Conference, Program and Abstracts, pages 21-22.

O'Brien, S.J., O'Driscoll, C.F., Greene, B.A. and Tucker, R.D.
1995: Pre-Carboniferous geology of the Connaigre Peninsula and the adjacent coast of Fortune Bay, southern Newfoundland. *In* Current Research, Newfound-land Department of Natural Resources, Geological Survey Branch, Report 95-1, pages 267-297.

O'Brien, S.J. and O'Driscoll, C.F.,
1996a: Preliminary investigation of Neoproterozoic (Avalonian) rocks, northeastern Holyrood (NTS 1N/6) map area: notes on geology, mineralization and mineral exploration potential. *In* Current Research, Newfoundland Department of Mines and Energy, Geological Survey, pages 311-327.

1996b: Geochemical data listing: 1996 field season (parts of 1N/3,6,7,10, and 11). Newfoundland Department of Mines and Energy, Geological Survey, Open File 001N/0579

O'Brien, S.J., King, A.F. and O'Driscoll, C.F.
1997: Late Neoproterozoic geology of the central Avalon Peninsula, Newfoundland, with an overview of mineralization and hydrothermal alteration. *In* Current Research, Newfoundland Department of Mines and Energy, Geological Survey, Report 97-1, pages 257-282.

O'Brien, S.J., O'Brien, B.H., Dunning, G.R. and Tucker, R.D.
1996: Late Neoproterozoic evolution of Avalonian and associated peri-Gondwanan rocks of the Newfoundland Appalachians. *In*: Avalonian and Related

Terranes of the Circum-North Atlantic. *Edited by* M.D. Thompson and R.D. Nance. Geological Society of America, Special Paper 304, pages 9-28

O'Brien, S.J., Dubé, B. and O'Driscoll, C.F.
1996: The regional setting and style of gold mineralization in Neoproterozoic Avalonian rocks of the Newfoundland Appalachians. *In* Report of Activities. Newfoundland Department of Mines and Energy, Geological Survey, pages 19-23.

1999: High sulphidation, epithermal-style hydrothermal systems in late Neoproterozoic Avalonian rocks on the Burin Peninsula, Newfoundland: Implications for gold exploration. *In* Current Research. Newfoundland Department of Mines and Energy, Geological Survey, Report 99-1, pages 275-296.

O'Brien, S.J., Dubé, B., O'Driscoll, C.F. and Mills, J.
1998: Geological setting of gold mineralization and related hydrothermal alteration in late Neoproterozoic (post-640 Ma) Avalonian rocks of Newfoundland, with a review of coeval gold deposits elsewhere in the Appalachian Avalonian belt. In Current Research. Newfoundland Department of Mines and Energy, Geological Survey, Report 98-1, pages 93-124.

O'Brien, S.J., Dubé, B., Dunning, G., O'Driscoll, C.J., Hinchey, J., and Cochrane, G.,
2000: Contrasting styles and ages of precious-metal mineralization in Neoproterozoic Avalonian rocks: implications for exploration. Government of Newfoundland and Labrador, Department of Mines and Energy, Geological Survey, Open File NFLD 2700.

O'Driscoll, C.F.
1977: Geology of the Sound Island map area (east half). *In* Report of Activities for 1976. Newfoundland Department of Mines and Energy, Mineral Development Division, Report 77-1, pages 43-47.

1984: The Hickey's Pond Belt: auriferous specularite–alunite–pyrophyllite–sericite mineralization near Placentia Bay, Newfoundland. Newfoundland Department of Mines and Energy, Mineral Development Division, Open File Report 1M/16 (221), 12 pages.

O'Driscoll, C.F. and Hussey, E.M.
1976/77: Sound Island (1M/16). Newfoundland Department of Mines and Energy, Mineral Development Division, Map 7863.

O'Driscoll, C.F., and Muggeridge, W.W.
1978: Geology of the Merasheen (1M/8) and Harbour Buffet (1M/9 east half), Newfoundland. In Report of Activities for 1978. Government of Newfoundland and Labrador, Mineral Development Division, Report 79-1, pages 82-89.

O'Driscoll, C.F. and Strong, D.F.
1979: Geology and geochemistry of the Late Precambrian volcanic and intrusive rocks of the southwestern Avalon Zone in Newfoundland. Precambrian Research, Volume 8, pages 19-48.

O'Driscoll, C.F., Collins, C.J. and Tuach, J.
1988: Volcanic-hosted, high-alumina, epithermal environments and the St. Lawrence fluorite deposit in the Avalon Zone, eastern Newfoundland. Field Trip Guidebook A5. GAC-MAC Annual Meeting, St. John's, Newfoundland, 76 pages.

O'Driscoll, C.F., Dean, M. T., Wilton, D.H.C, and Hinchey, J.G.
2001: The Burin Group: A Late Neoproterozoic Ophiolite Containing Shear-Zone Hosted Mesothermal-Style Gold Mineralization in the Avalon Zone, Burin Peninsula, Newfoundland, in Current Research: Newfoundland Department of Mines and Energy, Geological Survey, Report 2000-1, pages 229-246.

O'Neill, P.P and Blackwood, F.
1989: A proposal for revised stratigraphic nomenclature of the Gander and Davidsville groups and the Gander River Ultrabasic Belt of northeast Newfoundland; in Current Research; Newfoundland Department of Mines, Mineral Development Division, Report 89-1, p. 165-176.

Ohmoto, H.
1972: Systematics of sulphur and carbon isotopes in hydrothermal ore deposits: Economic Geology, Vol. 67, pages 551-579.

Ohomoto, H. and Rye, R.O.
1979: Isotopes of Sulphur and Carbon. In Geochemistry of Hydrothermal Ore Deposits, 2nd edition. Ed., H.L. Barnes. 509-567. John Wiley, NewYork, 798 p.509-567.

Ohomoto, H., and Goldhaber, M.B.
1997: Sulphur and carbon Isotopes. In Geochemistry of Hydrothermal Ore Deposits, Barnes, 1997, Wiley and Sons. Pages 517-613.

Paull, P.L., Hodkinson, I.P., Morrison, G.W., and Teale, G.S.
1990: Mount Leyshon Gold Deposit. Geology of the Mineral Deposits of Australia and Papua New Guinea. Ed. F.E. Hughes, pp. 1471-1481.

Philpotts, A.R.
1990: Principles of igneous and metamorphic petrology, Prentice Hall, New Jersey.

Placer Exploration Ltd.
1981: The Kidston gold deposit, in Gold in Eastern Australia [abs.]: New South Wales Dept. Mineral Resources and Sydney Mineral Explor. Disc. Group, Seminar, Sydney 1981, Abstracts, p. 17.

Porter, E.W., and Ripley, E.
1985: Petrologic and stable isotope study of the gold-bearing breccia pipe at the Golden Sunlight deposit, Montana: Econ. Geol., v. 80, p. 1689-1706.

Quinlan, G.G, Beamont, C., and Hall, J.
1993: Tectonic model for crustal seismic reflectivity patterns in compressional orogens. Geology, v. 21, pages 663-666.

Richard, K.
1969: Process of formation of mineralized breccia pipes [abs.]: Econ. Geol., vol. 64, p. 832.

Richards, J.P.
1995: Alkalic-Type Epithermal Gold Deposits - A Review. In Magmas, Fluids, and Ore Deposits. J.F.H. Thompson (editor). Pages 367- 400.

Robert, F., Poulsen, K.H., and Dube, B.
1997: Gold deposits and their geological characteristics, Exploration Geochemistry, paper 29. In "Proceedings of exploration 97: Fourth Decennial International Conference on Mineral Exploration", edited by A.G. Gubins, 1997, p. 209-220.

Rollinson, H.
1993: Using Geochemical Data: Evaluation, Presentation, Interpretation. Longman Scientific and Technical, New York.

Rose, E.R.

1948: Geology of the area between Bonavista, Trinity and Placentia bays, eastern Newfoundland. Geological Survey of Newfoundland, Bulletin 32, Part 2, pages 39-52.

1952: Torbay Map area, Newfoundland. Geological Survey of Canada Memoir 265, 64 pages.

Rye, R.O., and Ohmoto, H.

1974: Sulphur and carbon isotopes and ore genesis: A review. Economic Geology. Vol. 60, pages 826-842

Sakai, H.

1968: Isotopic properties of sulphur compounds in hydrothermal processes. Geochemical Journal., vol. 2, pages 29-49.

Saunders, P.

1986: Geological and rock geochemical surveys on the Foxtrap claims, Newfoundland, licence 2551, 2557, October 1985 to January 1986. Apex Geological Consultants Ltd, unpublished report [001N/07/468]

1991: Summary report on 1991 exploration on the Dog Pond Property (Licence 4112, NTS 1N/7) Avalon Peninsula, Newfoundland. [001N/07/0521]

Scott, S.D.

1983: Chemical behaviour of sphalerite and arsenopyrite in hydrothermal and metamorphic environments. Mineral. Mag., vol. 47., pages 427-435.

Sears, W.A.

1990: A geochemical, petrographic and metallogenic analysis of volcanogenic sulphide deposition within the Connaigre Bay Group, Hermitage Peninsula, southern Newfoundland. Unpublished M.Sc. thesis, Memorial University of Newfoundland, St. John's, Newfoundland. 282 pages.

Sharp, Z.D., Essene, E.J., and Kelly, W.C.

1985: A re-examination of the arsenopyrite geothermometer: Pressure considerations and applications to natural assemblages: Canadian Mineralogist. Vol., 23, pages 517-534.

Sillitoe, R.H.

1985: Ore-related breccias in volcanoplutonic arcs. Economic Geology, Volume 80, pages 1467-1514.

1991: Intrusion related gold deposits. *In* Gold Metallogeny and Exploration. Edited by R.P. Foster. London, Blackies, pages 165-209.

1995: Exploration and discovery of base- and precious-metal deposits in the Circum-Pacific region during the last 25 years. Resource Geology Special Issue No. 19, 1995. Published by the society of Resource Geology, editors: Metal Mining Agency of Japan.

Simon G, Kesler SE, Chryssoulis S.

1999: Geochemistry and textures of gold-bearing arsenian pyrite, Twin Creeks, Nevada: implications for deposition of gold in Carlin-type deposits. Econ Geol 94: 405-421.

Simons, F.S.

1964: Geology of the Klondike quadrangle, Graham and Pinal Counties, Arizona: U.S. Geol. Survey Prof. Paper 461, 173 p.

So, C.S., and Shelton, K.L.

1983: A sulphur isotopic and fluid inclusion study of the Cu-W-bearing tourmaline breccia pipe, Ilkwang mine, Republic of Korea: Econ. Geol., vol. 78, p. 326-332.

Strong, D.F.

1979: Proterozoic tectonics of Northwestern Gondwanaland: New evidence from eastern Newfoundland. Tectonophysics, v. 54., pages 81-101.

Strong, D.F., O'Brien, S.J., Strong, P.G., Taylor, S.W. and Wilton, D.H.C.

1978: Aborted Proterozoic rifting in Newfoundland. Canadian Journal of Earth Sciences, Volume 15, pages 117-131.

Taylor, S.R. and McLennan, S.M.

1985: The continental crust: its composition and evolution. Blackwell, Oxford.

Taylor, S.W.

1976: Geology of the Marystown map sheet (E/2), Burin Peninsula, Newfoundland. Unpublished M.Sc. thesis, Memorial University of Newfoundland, St.John's, Newfoundland, Canada.

Taylor, S.W., O'Brien, S.J. and Swinden, H.S.
1979: Geology and mineral potential of the Avalon Zone and granitoid rocks of eastern Newfoundland. Newfoundland Department of Mines and Energy, Mineral Development Division Report 79-3, 50 pages.

Walcott, C.D.
1900: Random-Precambrian Upper Algonkian terrane. Geological Survey of America, Bulletin 11, pages 3-5.

Werle, J.L., Ikramuddin, M., and Mutschler, F.E.
1984: Allard Stock, La Plata Mountains, Colorado - an alkaline rock hosted porphyry copper-precious metal deposit. Can. J. Earth Sci., vol. 21, pages 630-641.

Widmer, K.
1950: The geology of the Hermitage Bay area, Newfoundland [Ph.D. thesis]: Princeton, New Jersey, Princeton University, 439 p.

Williams, H.
1971: Geology of the Belleoram map area, Newfoundland. Geological Survey of Canada, Paper 70-65, 39 pages.

1978: Tectonic-lithofacies map of the Appalachian orogen (1:1 000 000): Department of Earth Sciences, Memorial University of Newfoundland, St.John's, Newfoundland, Map 1.

1979: Appalachian Orogen in Canada: Canadian Journal of Earth Sciences, Volume 16, pages 792-807.

1999: Tectonics of Atlantic Canada: Geoscience Canada, Volume 26, Number 2, pages 51-70.

Williams, Harold, ed.
1995: Geology of the Appalachian-Caledonian Orogen in Canada and Greenland: Geological Survey of Canada, Geology of Canada, no. 6, pages 226-237 (also Geological Society of America, The Geology of North America, Volume F-1).

Williams, H. and St-Julien, P.
1982: The Baie Verte-Bromrton Line: Early-Paleozoic Continent-Ocean interface in the Canadian Appalachians: in Major Structural Zones and Faults of the Northern Appalachians, (ed.) P. St-Julien and J. Beland; Geological Association of Canada, Special Paper 24, p. 177-207.

Winchester, J.A., and Floyd, P.A.
1977: Geochemical discrimination diagrams on different magma series and their differentiation products using immobile elements. Chemical Geology, vol. 20, pages 325-343.

Wilson, M.
1989: Igneous petrogenesis. Unwin Hymam, London.

Appendix A: Analytical Methods

A.1 Sample collection and Preparation

Samples were collected from surface units of the PHIS and the Lodestar Breccia showing during the 1999 summer mapping season. The sample collection process and goals varied for the intrusive suite and the mineralized breccia showing. For the intrusive suite, samples were collected as to obtain maximum geographical, as well as compositional/alteration, variation within each of the phases. Sampling of the mineralized breccia zone was conducted with the goal of obtaining sufficient variation in samples as to adequately describe the variable characteristics such as amount/type of mineralization and/or matrix, and to sufficiently describe the clast types and characteristics associated with the breccia. All samples from the intrusive phases were trimmed of all weathered to ensure a fresh sample. Minimal "high-grading" sampling was conducted for breccia samples in order to aid in the study of the nature of the auriferous mineralization.

Sufficient material was sampled to allow for lithogeochemical and petrologic analysis. Samples were cut with a diamond tipped saw in order to obtain material for chemistry, with small blocks kept for thin sections and hand samples. Individual phases of the PHIS were crushed individually, followed by mineralized samples in order to reduce contamination between samples. The jaw crusher was extensively cleaned between each sample, and silica sand was periodically powered in the bowl-puck mill in addition to the normal cleaning between samples to account for any potential cross contamination between samples.

All samples were crushed in a steel jaw crusher to reduce the samples to ~ 1 cm size rock chips, and these were then placed in an alumina ceramic bowl-puck mill and ground for ~ 2-3 minutes to reduce the sample to a very fine powder (200 mesh/74 μ). These powders were used in all of the whole rock geochemical techniques (eg. INAA, ICP-ES, XRF, and ICP-MS (REE)). All processing occurred at the Department of Mines and Energy Laboratories, St. John's, Newfoundland.

Thick thin sections from the Lodestar mineralization were used for LAM-ICP-MS, electron microprobe, whereas mineralized chip samples were used for sulphur isotope studies. Polished thin sections were produced at the Department of Earth Sciences, Memorial University.

A.2 Major and Trace element Analysis.

The following is a description of the analytical techniques used to analyze major and trace elements with whole rock geochemistry in this thesis.

A.2.1 X-Ray Fluorescence (XRF) analysis.

Selected major and trace element analysis were carried out at Memorial University of Newfoundland, Department of Earth Science, X-Ray Fluorescence laboratory using a Fisons/ARL model 8420 + sequential wavelength-dispersive X-Ray spectrometer. Analysis were from pressed pellets which were prepared following the method of Longerich (1995) as follows:

1) 5.00 grams of rock powder and 0.70 grams of BRP-5933 bakelite phenolic powder resin were placed in a glass jar with two stainless steel ball bearings and homogenized for

~10 minutes, or till well mixed.

2) the mixture was then placed in a pellet press and pressed for 5 seconds at a pressure of 20 tonnes.

3) these pressed pellets were then placed in an oven and baked for 15 minutes at 200°C.

Data collection was carried out via an automated computer system attached to the XRF. In addition to the pressed pellets obtained from the samples being analyzed for the purpose of this thesis, four quality control reference materials (AGV-1, DNC-1, JG-1, and BCR-1) as well as five internal standards were analyzed (DTS-1, United States Geological Survey (USGS) reference material; BHVO-1, USGS reference; SY-2 and SY-3, syenite from the Canadian Certified Reference Materials Project and PACS-1, National Research Council of Canada reference material). Published values for the reference materials used are published in Potts et. al., (1992), Jenner at al., (1990), and Longerich et al., (1990).

Analysis for 30 elements were conducted via this method consisting of: quantitative elements (P, S, Cl, K, Ca, Sc, Ti, V, Cr, Mn, Fe, Ni, Cu, Zn, Ga, As, Rb, Sr, Y, Zr, Nb, Ba, Ce, Pb, Th, and U) and semi-quantitative (Na, Mg, Al, Si).

The limits of detection vary depending upon the elemental group being considered; details of calibration, matrix corrections, precision and accuracy are all described in detail in Longerich et al., (1997). As quoted by Longerich et al., (1997), limits of detection range from 120 ppm for Na_2O and MgO to less than 20 ppm for MnO, K_2O, and CaO; with detection limits for trace elements, in brackets, as: Sc (6), V (6), Cr

(7), Ni (5), Cu (4), Zn (3), Rb (0.7), Sr (1.2), Y(0.7), Zr (1.2), Nb (0.7), Ba (23), and Pb (4).

A.2.1.1 Precision and accuracy

Precision and accuracy associated with the XRF analysis are based upon five replicate analysis on standard DNC-1 during the collection of the data associated with this thesis. Precision is typically good for all of the major oxides (RSD 3-8%); as well as trace element data with the exceptions of Pb, Ba, Ga, Rb, Sc, V, and Nb (table A-1). Many of these elements with higher RSD's have very low concentrations in this standard; thereby explaining the lower precision. Longerich (1995) typically lists lower long term RSD's for these elements than presented in the scope of this thesis.

Accuracy is typically considered good (table A-1)(RD's from 0-8 %) with the exception of P_2O_5, Sc, V, Zn, Nb, and Pb. Again, low concentrations of these elements explain the poor statistical results.

Although the elements of Na, Al, Mg, and Si are typically considered to be semi-quantitative (Longerich, (1995)), they were found to have good accuracy and precision in this study; thereby making them reliable.

A.2.2 ICP-ES

A.2.2.1 Major Elements

Samples were also ran for major element analysis via the Inductively Coupled Plasma-Emission Spectrometer Method, conducted at the Department of Mines and Energy Laboratory in St. John's. Sample preparation was the same as that for the XRF for

the purposes of crushing and powdering the sample. The following procedure is based upon that given in Finch. (1998). Once powdered, typically 0.1 g of <180 micro material is weighed into a graphite crucible with 0.5 g of lithium metaborate, these are mixed and placed in a 1000 °C furnace and fused. After one hour, the samples are removed from the furnace, tipped into a mixture of 4 % HCl and HF contained in a polycarbonate digestion bottle. The caps are sealed and the samples are placed in a water bath at 90 °C. After 1 ½ hours the samples are removed and 50 ml of 50 g/l boric acid solution is added, after which the samples are returned to the bath. After a further 1 ½ hours the samples are removed, cooled, transferred to flasks, made to volume and analyzed by ICP-ES (Lichte et al. 1987).

All oxides have detection limits of 0.01 % with the exception of P_2O_5 with 0.001%. For analysis of samples within this thesis, two standards (Ga-1 and SDC-1) were ran in conjunction with a number of duplicate samples. As illustrated in figure A.1, both the duplicate samples and the reference standards were both reproduced within accepted values.

A.2.2.2 Trace elements via ICP-ES

As with the major elements, the following sample preparation technique is based upon that given in Finch. (1998). For digestion associated with trace element analysis, 1 g of sample is weighed into a 125 ml teflon beaker with 5 ml of HCL, 15 ml of HF, and 5 ml of 1:1 perchloric acid. Samples are then placed on a hot plate at 200 °C, evaporated to dryness, after which an additional amount of HCl (half-fill the beaker) is added to the

beaker which is returned to the hot-plate. After the residue is dissolved, 1 ml of 50 g/l bornic acid is added, the samples are brought to volume and analyzed.

Finch (1998) quotes detection limits in the range of 1 ppm for most elements analyzed, with a few at 0.1 ppm (ie. Be, Dy, Li, Sc). As with the major elements, the reference standards and the duplicate samples were reproduced with acceptable values.

A.2.3 ICP-MS

A subset of the samples analysed by XRF and ICP-ES were subsequently analyzed via ICP-MS to determine REE's and selective trace elements. For the purposes of this thesis, due to the presence of substantial arsenic within the mineralized samples and due to the larger number of elements analyzed, analysis were conducted via the HF/HNO_3 method. Elemental masses analyzed via this method consist of ^{7}Li, ^{85}Rb, ^{86}Sr, ^{89}Y, ^{90}Zr, ^{93}Nb, ^{95}Mo, ^{133}Cs, ^{137}Ba, ^{139}La, ^{140}Ce, ^{141}Pr, ^{145}Nd, ^{147}Sm, ^{151}Eu, ^{157}Gd, ^{159}Tb, ^{160}Gd, ^{163}Dy, ^{165}Ho, ^{167}Er, ^{169}Tm, ^{173}Yb, ^{175}Lu, ^{177}Hf, ^{181}Ta, ^{205}Tl, ^{206}Pb, ^{207}Pb, ^{208}Pb, ^{209}Bi, ^{232}Th, ^{238}U and $^{254}(UO)$. Sample preparation, described by Jenner et al., (1990), initially involved the dissolution of previously described rock powder (0.1 g) using HF and HNO_3. The Hf-HNO_3 mixture is then left to evaporate after which the sample is taken up in 2-3 ml of 8 N HNO_3, transferred to a 125 ml bottle, and diluted to 90 g with water.

The instrumentation in use at the Memorial Laboratory consists of a SCIEX ELAN model 250 ICP-MS; changes to which are documented by Longerich et al., (1986), Longerich, (1989 a, b, c). Data acquisition is via manufacturer software whereas data

reduction and concentration calculations are carried out using spreadsheets.

The exploration package has the ability to run up to 27 samples at once: including samples, standards, blanks, and duplicates. Addition of spikes to samples serve as the method of internal standardization, and external standards are used to calibrate most elements. The sample analysis as well as the standard analysis must be background corrected and corrected for a number of variables such as matrix factors, drift factors etc. Full details pertaining to the relevant procedures associated with these technique are given in Jenner et al., (1990), and others.

Average detection limits observed during this study for the analysed elements consisted of: 0.1 - 0.3 ppm for Rb, Sr, Zr, Ba, and Ta; 0.094, 0.071 and 0.052 ppm for Pb, Li, and Cs respectively; from 0.03 - 0.05 ppm for Mo, Sm, Nd and Eu; from 0.1 - 0.3 for Y, La, , Ce, Pr, Gd, Dy, Er, Tm, Yb, Lu, Hf, Bi, and U; and below 0.01 ppm for Nb, Tb, Ho, Ta, and Th. However, with the Hf-HNO_3 method, some elements, such as Zr, pose dissolution problems. To investigate this problem, four samples were analysed via the alternative sinter method (Longerich et al., (1990)). The resultant comparison of values, illustrated in figure A.2, indicates that some elements, especially Zr and Hf were not dissolved via the Hf package; this point has to be kept in mind when dealing with REE's since zircon has the ability to harbour these elements. This dissolution problem was also determined through the use of linear correlation diagrams between XRF and ICP-MS data, which illustrated scatter associated with some elements such as Zr due to probable

dissolution, solution instability, and memory problems (Jenner et al., 1990). Therefore alternative analytical methods were utilized for some elements (ie. XRF for Zr).

The precision and accuracy of analysis via this analytical method were determined through the use of standard MRG-1, which was ran four times during the collection of the data associated with this thesis. The data is presented in table 4.2. Precision for all elements, excluding Li, Nb, Mo, Cs, Er, Tm, Lu, Tl, Pb, Bi, and U was observed as mostly excellent (0-3 % RSD) (table 4.2); whereas the accuracy of all elements excluding Rb, Nb, Mo, Eu, Tm, Lu, Hf, Tl, Bi, and U ranged from excellent to good (table 4.2). Better precision and accuracy are quoted for longer periods of time with more standard runs.

A.2.4 Instrumental Neutron Activation Analysis (INAA)

This analytical technique was performed by Activation laboratories, of Ontario, under contract by the Newfoundland Department of Mines and Energy for the multi-element analysis. Elements analyzed by this method include Au, Ag, As, Ba, Br, Ca, Co, Cr, Cs, Fe, Hf, Hg, Ir, Mo, Na, Ni, Rb, Sb, Sc, Se, Sn, Sr, Ta, Th, U, W, Zn, La, Ce, Nd, Sm, Eu, Tb, Yb, Lu, and Zr.

In this procedure a 30 gram aliquot of sample is encapsulated, irradiated, and measured in a multi-element mode by INAA for Au + 34 elements. Samples are left in the nuclear reactor for sufficient time so as to irradiate the entire sample. The irradiated sample is then removed from the reactor, placed in a lead containment to cool; during

which the gamma radiation given off is measured and quantified using scintillometers, and reduced by computers to determine elements and concentrations present.

For the purposes of this thesis, this analytical technique was dominantly used as a method for the assay of mineralized samples of the Lodestar breccia; with Au being the most useful and valuable element analyzed; however other elements such as As etc were deemed useful. During the analysis associated with the collection of data for this thesis, three reference standards were ran once each consisting of WMG-1, MRG-1, and WPR-1. According to information given by Govindaraju,(1994) regarding these standards, the WMG-1 and WPR-1 have recommended values for Au, whereas MRG-1 doesn't. Due to the purpose of the data set, only the two standards with recommended Au values will be investigated to determine the accuracy of the gold analysis (both Au and Ir will be investigated for accuracy). As demonstrated in table A.3, Au and Ir data have excellent to fairly good accuracy as defined by Jenner et al., (1990). Activation Laboratories quote better accuracy and good precision over longer periods of time.

A.2.5 Laser Ablation Inductively Coupled Plasma Mass Spectrometry (LAM-ICP-MS)

The LAM at Memorial University of Newfoundland was designed to carry out high-resolution sampling of minerals within petrographic thin-sections. This recent development has allowed for the accurate determination of trace elements both vertically and horizontally in samples. The Mun LAM consists of a frequency doubled and quadrupled Q-switched Nd-YAG laser which gives choice of three different wavelengths,

and lasering repetitions up to 20 Hz (Fryer et al. 1995). This system allows for sampling pits in the range of 10-100 um to be produced by laser ablation, after which the ablated material is carried by a flow of argon into the ICP torch where it is broken down into atoms and ionized before emplacement in the mass spectrometer (Fryer et al., 1995). The analytical technique of LAM-ICP-MS is very flexible in terms of sample requirements and preparation procedures. Most materials can be ablated effectively and the actual sample preparation is limited to the preparation that the analyst must carry out in order to isolate the required sampling sites (Longerich et. al., 1997). The major pre-requisite for the sample preparation is that the sample must be compatible with the ablation cell of the instrument.

The laser ablation technique serves as the sample introduction procedure used in the analytical technique of LAM-ICP-MS. The laser ablation microprobe is basically made up of a laser and some attached optical devices. The most commonly used source for laser ablation consists of a Nd:YAG laser which has a fundamental wavelength of 1064 nm, thereby operating in the infrared. However, the incorporation of a harmonic generator by Longerich et al., (1991) allowed for shorter wavelength (532 nm and 266 nm) laser radiation to be generated. The lower radiations in the ultraviolet (ie 255 nm) are more desirable since most minerals and glasses absorb them more readily, thereby allowing for more controlled ablation sampling and better resolution. The Nd:YAG laser consists of a Nd doped Yttrium Aluminum Garnet rod a few mm in diameter. The actual sampling behavior of the laser beam is dependant upon many factors, the most important

of which are the lasers focus, laser-pulse power, sampling rate, and the samples absorptivity at certain wavelengths.

The laser ablation apparatus is typically ran using Q-switched lasers whereby an optical switch is used to concentrate the lasers output energy into large pulses. In order to carry out high-resolution, laser-ablation sampling, it is very important to be able to control the laser pulse energy. It is necessary to control this energy in order to obtain well formed small ablation pits, produced by controlled ablation, thereby resulting in high-resolution and favorable results. The LAM-ICP-MS instrument at Memorial University uses the lasers own natural linear polarization in conjunction with polarizing optics to produce a variable optical attenuator consisting of a rotatable quartz half wave plate and a calcite polarizer combination. Rotation of the crystal quartz half wave plate in affect rotates the plane of polarization of the laser entering the polarizer. This in turn changes the proportions of the laser that reach the sample in relation to the proportion of the laser energy that is discarded. Once the energy of the laser is controlled, the next step is to direct and focus the laser beam onto the sample. This is carried out with the use of mirrors and prisms. In order to focus the beam on a very small section of the sample to allow for micro-analysis, a focusing objective is used.

Results are obtained in counts per second (cps), which through the use of the internal S standard with LAM-Trace computer software are reduced to concentrations. Reduction via this software involves background, matrix/drift, and internal standard corrections; after which the concentrations are calculated from the internal standard.

LAM-ICP-MS is capable of limits of detection (LOD) for trace elements from a few ppb to a few ppm (Jackson et al., 1992). The actual LOD, as well as the precision, are based upon a number of operating variables. The major factors effecting the precision and LOD as outlined by Longerich et al., (1997) are:

- ablation pit volume
- analysis time
- number of analytes
- transfer efficiency
- analyzer elemental sensitivity
- analyzer elemental background
- elemental isotope abundance
- elemental ionization potential

The major variables are the pit volume and the analysis time. The size of the ablation pit is dependant upon ablation time, laser intensity, and the mineral analyzed. The pit size determines the amount of material that is presented to the ICP for analysis. The analysis time or count time is dependant upon the number of elements analyzed. Since the quadrupole is a sequential analyzer, the more elements analyzed, the less proportional counting time per element. Therefore the more elements analyzed, the poorer the counting statistics, resulting in degradation of the LOD and precision. Typically a larger pit results in higher count-rates and improved detection-limits (Jackson et al. 1992). The accuracy of the analysis depends upon the mass of material ablated and the counting time per element used. The LAM-ICP-MS at Memorial University is capable of a relative standard deviation of < 10 % for the REE (Jackson et al. 1992) and an accuracy of +/- 5% for the lithophile suite Sr, Y, Zr, Nb, Ba, REE, Hf, Ta and U.

For the purposes of this experiment, LAM-ICP-MS analyses were undertaken to determine whether Au was distributed homogeneously or contained in micronuggets within the sulphide mineralization phases. We utilized the above described VG PlasmaQuad 2 S+ ICP-MS instrument coupled to an in-house built 266 nm Nd-YAG laser. Using He as a carrier gas, 10 Hz laser frequency, laser energy of approximately 0.40 mJ/shot and both single spot sampling and line rastering, we were able to collect time-resolved analyses that showed the spatial distribution of Au in the sample. Concentrations were calculated using S as an internal standard an FeS synthesized standard containing Au. All concentrations, as well as standard deviations, accuracy measurements, and precision were conducted via the "LAM-TRACE" software at Memorial University Department of Earth Science.

The standard used in this experiment was the Balhaus Au standard, which was ran 16 times during data collection. Accuracy and Precision (as determined by LAM-Trace software) were relatively good, considering the "sticky" nature of gold, ranging from approximately 5 - 13 % RSD and RD.

A.2.6 Sulphur Isotopes

Sulphur isotope analysis were conducted on crystal separate samples of pyrite, arsenopyrite, chalcopyrite, and bornite. Crystals of these sulphide phases were separated from non-sulphide phases in breccia samples (with one host rock sample analyzed). The degree of difficulty of this step is dependant upon the state of the sulphides within the

rock, ie. disseminated versus massive. This step in the process was carried out using a small hammer and clean chisel in order to chip off small pieces of the rock which contain sulphides in some form. This material was then pulverized or broken up using a small hand pulverizer. This step serves to separate the actual sulphides from the host silicate lithology. The next step involves examining this crushed product with the aid of a stereoscope, during which individual sulphide mineral grains are separated and removed using a small set of clean tweezers. This step requires great care as it is necessary to separate sulphides cleanly with no other forms of sulphides or silicate material attached. Once the individual sulphides are cleanly separated, the next step involves the powdering of the samples in a small mortar and pestle. Again, as with all steps in the sample preparation, the equipment used in this step must be thoroughly cleaned with ethanol. Once powdered, the samples may be stored in small sample vials before the next step is carried out. The next step in the sample preparation involves the use of a microbalance in order to weigh out sample specific quantities of sulphide material , as well as V2O5, into small, high purity tin capsules.

Once the samples are weighed out into the small tin capsules, the remaining steps involve the introduction of the sample into the machinery for analysis. A generalized overview of the flow of the sample (taken from Fisons Instruments technical note) through the machinery is explained herein. After the samples are prepared and weighed into the high purity tin capsules, they are then loaded onto a elemental analyzer carousel. The sample details such as title, weight etc. are entered into a auto run file in the machine.

The machines auto-run is then started which sequentially drops each sample into a combustion region of the elemental analyzer (The elemental analyzer used in the stable isotope laboratory at Memorial University consists of a Carlo Erba Automatic Gas Chromatographic Elemental Analyzer). Gas or effluent from the elemental analyzer is then sampled by the mass spectrometer which determines the isotopic signature of the sample. A pulse of reference gas is introduced to the mass spectrometer prior to the arrival of the sample peak, to which the sample is then isotopically compared. The laboratory at Memorial University of Newfoundland conducts sulphur isotope ratios by continuous flow isotopic ratio mass spectrometry with the use of a Finnigan MAT 252 Ion Ratio Mass Spectrometer. Sulphur dioxide gas samples are run on the mass spectrometer against internal standards, (ie. Mun-Py). Full detailed regarding analytical procedures associated with this process are given in Giesemann et al., (1994). Calibration standards (NBS-123, NBS-127, and NZ1) were ran during the course of the analysis and resulting in calibration standard deviations in the range of ± 0.3 ‰, thereby giving a measure of analytical accuracy.

A.2.7 Electron Microprobe

Sulphide mineral analysis were carried out on a Cameca SX50 electron microprobe analyser at the Department of Earth Sciences, Memorial University. The Beam current was set at 40.20 nA with a 20.00 kV acceleration voltage. Analysis for S and Fe were done by energy-dispersive (ED) mode whereas Cu, Zn, As, Ag, and Au were done by wavelength-dispersive (WD) mode. Count times were 100 seconds. The most

important element analyzed consisted of As, as At. Wt. % As was used in geothermometer calculations (Table 4.4). Two standards consisting of Asp 57 and Asp 200 were ran in conjunction with the analysis; resulting in calibration standard deviations of ~ 0.15 wt % giving a measure of analytical accuracy.

A)

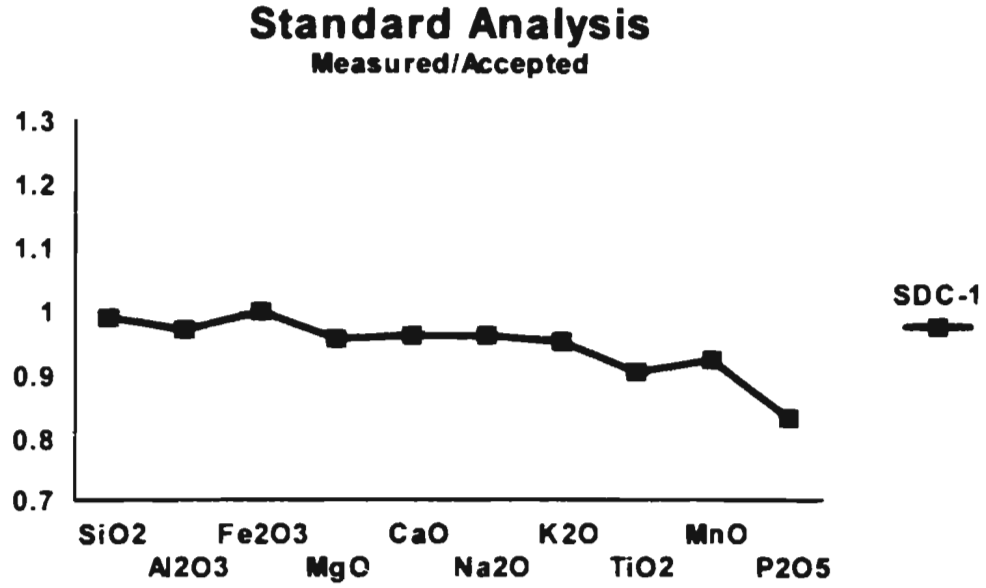

B)

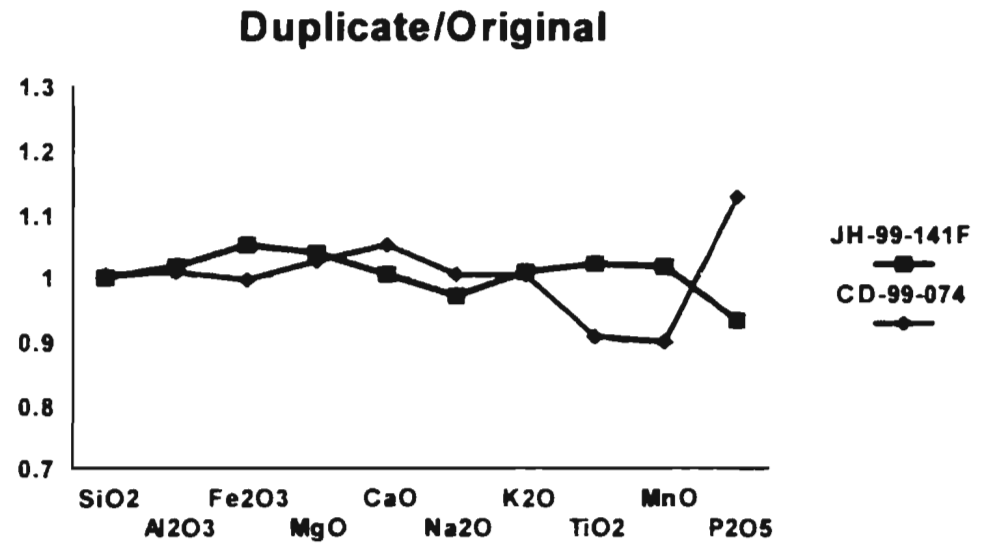

Figure A.1: A) Standard and B) duplicate analysis from the ICP-ES method.

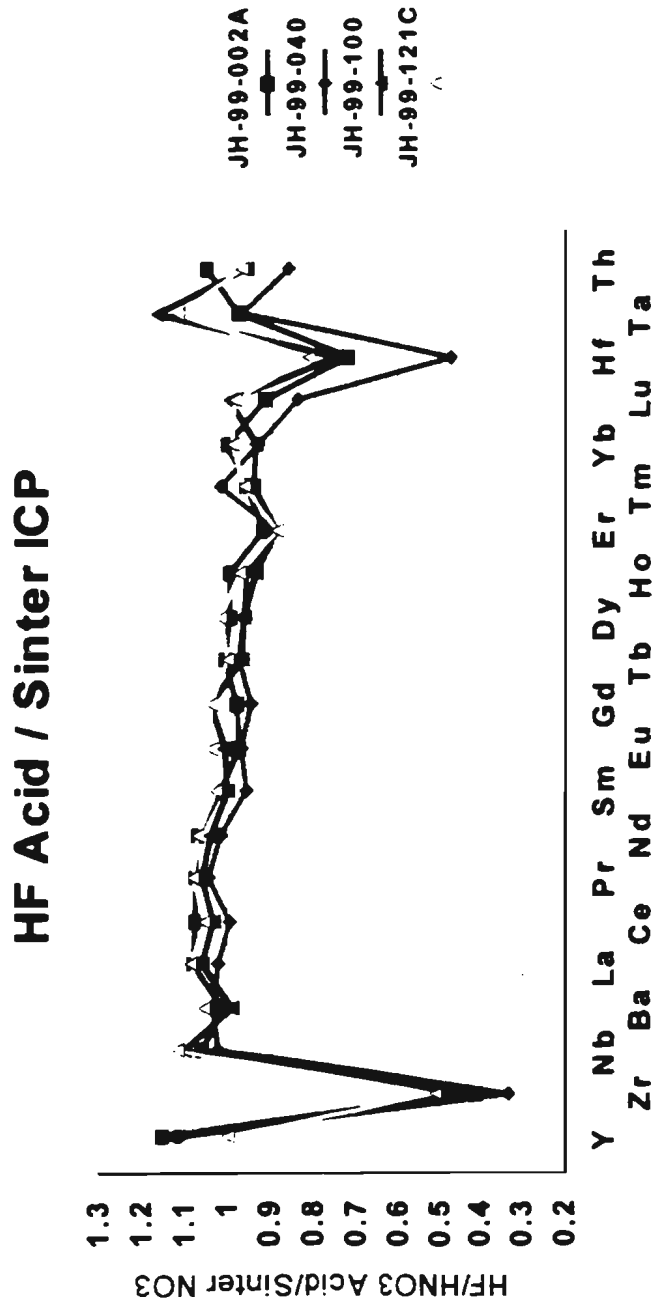

Figure A.2: Comparison of ICP-MS HF nitric and Sinter values.

Table A.1. - Precision and accuracy for XRF analysis of standard DNC-1. Data represent five analyses conducted during the duration of this thesis.

Element[a]	Minimum	Maximum	Std. Deviation	Mean (n=5)	Quoted MUN Values[a,b]	RSD (%)[c]	RD (%)[d]
SiO_2	38.16	44.48	2.71	41.71	43.56	6.49	-4.24
TiO_2	0.37	0.45	0.03	0.42	0.45	7.88	-6.72
Al_2O_3	16.32	18.94	1.20	17.58	17.67	6.83	-0.52
$Fe_2O_{3\ Total}$	8.95	9.85	0.41	9.43	10.12	4.32	-6.80
MnO	0.13	0.14	0.01	0.14	0.15	3.70	-8.18
MgO	8.58	10.34	0.72	9.51	9.9	7.56	-3.90
CaO	9.32	11.06	0.75	10.30	11.02	7.25	-6.51
Na_2O	1.78	2.04	0.12	1.91	1.94	6.10	-1.63
K_2O	0.22	0.27	0.02	0.25	0.26	6.15	-5.68
P_2O_5	0.09	0.10	0.01	0.09	0.89	5.58	-89.67
S	1083	1101	7	1094	1032	0.64	6.04
Cl	816	904	43	850	871	5.05	-2.36
Sc	16.3	39.9	10.3	27.3	31.0	37.67	-11.78
V	109.2	147.7	14.3	130.2	148.0	11.02	-12.02
Cr	255.3	296.4	18.7	281.5	307.0	6.66	-8.30
Ni	235.6	244.0	4.0	239.6	252.0	1.65	-4.91
Cu	80.4	87.8	2.9	84.9	87.0	3.38	-2.42
Zn	48.9	55.6	2.8	52.6	60.0	5.24	-12.31
Ga	12.3	16.5	1.7	14.2	14.0	11.98	1.39
As	1.2	9.4	3.31	4.2	<LD (13)[e]	-	-
Rb	2.5	4.7	0.9	3.5	3.4	26.34	4.00
Sr	141	144	1	143	142	0.79	0.65
Y	15.2	16.9	0.8	16.0	15.9	4.82	0.40
Zr	34.8	36.2	0.7	35.5	36.0	1.86	-1.27
Nb	0.8	1.9	0.5	1.5	1.9	31.07	-19.11
Ba	92	113	8	106	115	7.70	-8.25
Ce	-65.0	40.6	39.20	-15.3	<LD (39)[e]	-	-
Pb	-0.4	11.6	4.8	4.1	7.3	115.60	-43.56
Th	-1.7	1.1	1.13	0.2	<LD (2.8)[e]	-	-
U	-3.2	1.2	1.69	-1.6	<LD (3.4)[e]	-	-

[a]Major element oxides reported as wt. % and trace elements as ppm.
[b]Data represent extended durations means of Longerich (1995).
[c]RSD is the relative standard deviation (standard deviation/mean).
[d]RD is the relative difference to the standard value [(mean-quoted value)/quoted values] * 100
[e]Values in the standard are below the limit of detection (LD) values quoted in parantheses.

Table A.2. - Precision and accuracy for analysis of standard MRG-1via ICP-MS. Data represent four analyses conducted during the duration of this thesis. Good precision and accuracy is defined as 3-7%, excellent as 0-3% (Jenner et al., 1990)

Element[a]	Minimum	Maximum	Std. Deviation	Mean (n=4)	Quoted MUN Values[a]	RSD (%)[b]	RD (%)[c]
Li	2.72	3.90	0.53	3.45	3.71	15.49	-7.61
Rb	6.78	7.28	0.21	7.01	7.65	2.94	-9.17
Sr	270.53	281.18	4.35	275.99	274.00	1.58	0.72
Y	11.55	11.94	0.16	11.75	11.60	1.37	1.26
Zr	95.39	99.06	1.51	97.16	93.70	1.55	3.56
Nb	22.05	27.62	2.37	24.58	22.30	9.64	9.28
Mo	1.17	1.64	0.20	1.38	1.26	14.58	8.70
Cs	0.57	0.70	0.06	0.62	0.60	9.29	2.83
Ba	44.02	46.87	1.34	45.68	47.50	2.93	-3.99
La	8.41	8.97	0.23	8.72	9.07	2.68	-4.04
Ce	23.56	25.11	0.70	24.43	26.20	2.86	-7.25
Pr	3.57	3.82	0.11	3.72	3.79	3.00	-1.81
Nd	17.04	17.92	0.41	17.58	18.30	2.32	-4.10
Sm	4.21	4.59	0.16	4.42	4.51	3.54	-2.15
Eu	1.28	1.38	0.04	1.34	1.46	3.17	-8.96
Gd	3.75	4.00	0.11	3.91	4.11	2.91	-5.18
Tb	0.50	0.55	0.02	0.53	0.55	4.20	-4.27
Dy	2.75	2.99	0.11	2.88	3.01	3.76	-4 60
Ho	0.46	0.51	0.02	0.49	0.51	4.41	-4.08
Er	1.10	1.33	0.10	1.21	1.21	8.03	-0.41
Tm	0.15	0.28	0.06	0.20	0.15	28.33	25.93
Yb	0.76	0.82	0.03	0.80	0.81	3.77	-1.89
Lu	0.06	0.10	0.02	0.09	0.11	21.63	-25.71
Hf	4.20	4.80	0.30	4.54	3.76	6.55	17.09
Ta	0.83	0.95	0.05	0.90	0.83	5.67	7.78
Tl	0.04	2.16	1.00	0.68	0.05	146.39	92.65
Pb	4.41	6.33	0.84	5.39	5.20	15.66	3.44
Bi	0.12	0.28	0.07	0.22	0.13	33.43	39.53
Th	0.70	0.84	0.06	0.75	0.78	8.29	-4.00
U	0.22	0.37	0.06	0.29	0.25	21.26	13.79

[a]Trace element values are reported as ppm.

[b] RSD is the relative standard deviation (standard deviation/mean).

[c] RD is the relative difference to the standard value [(mean-quoted value)/quoted values] * 100

Table A.3. - Precision and accuracy for Au analysis via INAA, based upon one run of each of the standards WMG-1 and WPR-1.

Standard	Element[a]	Detected[b]	Quoted Values[c]	RD (%)[d]
WMG-1	Au	115	110	4.55
WMG-1	Ir	41	46	-10.87
WPR-1	Au	46	42	9.52
WPR-1	Ir	14	13.5	3.70

[a] data reported in ppb.

[b] based upon one sample

[c] stamdard values from Govindaraju, (1995)

[d] RD = relative difference relative to the standard value: [(mean determined-standard)/standard)] *100

References Sited in Appendix A

Finch, C.J.
1998: Inductively Coupled Plasma-Emission Spectrometry (ICP-ES) at the Geochemical Laboratory. In Current Research (1998) Newfoundland Department of Mines and Energy, Geological Survey, Report 98-1, pages 179-193.

Fryer, B.J., Jackson, S.E. and Longerich, H.P.
1995. The design, operation and role of the laser-ablation microprobe coupled with an inductively coupled plasma-mass spectrometer (LAM-ICP-MS) in the earth sciences. The Canadian Mineralogist. 33: 303-312.

Giesemann,A., Jäger, H.-J., Norman, A.L.,Krouse, H.R. and Brand, W.A
1994: On-line sulfur-isotope determination using an elemental analyser coupled to a mass spectrometer. Anal. Chem. 66, pgs. 2816-2819.

Govindaraju, K.
1994: Compilation of working values and samples description for 383 geostandards. Geostandards Newsletter, Vol. 18, Special Issue, July 1994.

Jackson, S.E., Longerich, H.P., Dunning, G.R., and Fryer, B.J.
1992. The application of laser ablation microprobe-inductively coupled plasma-mass spectrometry (LAM-ICP-MS) to in situ trace element determinations in minerals. The Canadian Mineralogist. 30: 1049-1064.

Jenner, G.A., Longerich, H.P., Jackson, S.E., Fryer, B.J.
1990: ICP-MS- A powerful tool for high-precision trace-element analysis in Earth Sciences: Evidence from analysis of selected U.S.G.S. reference samples. Chemical Geology, vol. 83, pages 133-148.

Licthe, F.E., Golightly, D.W., and Lamothe, P.J.
1987: Inductively Coupled Plasma-Atomic Emission Spectrometry. In Methods for Geochemical Analysis. U.S. Geological Survey Bulletin 1770, pages B1-B10.

Longerich, H.P., Strong, D.F. and Kantipuly, C.J.
1986. Progress in evaluation of instrumental and other parameters affecting chemical and isotopic analysis by inductively coupled plasma-mass spectrometry (ICP-MS). Canadian Journal of Spectroscopy. 31(5): 111-121.

Longerich, H.P.

1989a. Mass spectrometric determinations of the temperature of an argon inductively coupled plasma from the formation of the singly charged monoxide rare earths and their dissociation energies. Journal of analytical atomic spectrometry, 4: 491-497.

1989b. The effects of nitric acid, acetic acid and ethanol on inductively coupled plasma-mass spectrometric ion signals as a function of nebulizer gas flow, with implications on matrix suppression and enhancements. Journal of analytical atomic spectrometry, 4: 665-677.

1989c. Automatic shutoff circuit for use on a Sciex-Perkin Elmer ELAN ICP-MS. ICP Information Newsletter, 15: 157-160.

Longerich, H.P., Jenner, G.A., Fryer, B.J., and Jackson, S.E.

1990: Inductively Coupled Plasma-Mass Spectrometric analysis of geological samples: A critical evaluation based on case studies. Chemical Geology, vol. 83, pages 105-118.

Longerich, H.P., Jackson, S.E., Fryer, B.J., and D.F. Strong.

1991:The Laser Ablation Microprobe-Inductively Coupled Plasma-Mass Spectrometer, Geoscience Canada, 20 (1) (1991),p. 21.

Longerich, H.P.

1995: Analysis of pressed pellets of geological samples using wavelength-dispersive X-ray fluorescence. X-Ray Spectrometry, vol. 24, pages 123-136.

Longerich, H.P., Jackson, S.E. and Günther, D., 1997.

Inductively coupled plasma mass spectrometry: sample introduction methodology and mixed gas plasmas ablation techniques. In ICP-MS, edited by Diane Beauchemin, in press.

Potts, P.J., Tindle, A.G., and Webb, P.J.

1992: Geochemical Reference Material Compositions. CRC Press Inc., Boca Raton, 313 pages.

Appendix B: Data Tables

Table B.1: Pressed Powder X-ray flourescence (XRF) data for PHIS and Lodestrar Breccia samples.

Sample Name	JH-99-002A Pre-Breccia	JH-99-002B Pre-Breccia	JH-99-009 Pre-Breccia	JH-99-019A Pre-Breccia	JH-99-034 Pre-Breccia	JH-99-040 Pre-Breccia
Rock Type	gabbro	gabbro	gabbro	gabbro	gabbro	gabbro
SiO_2	48.73%	46.52%	45.74%	46.36%	44.37%	51.90%
TiO_2	1.19%	1.22%	0.98%	1.68%	1.18%	0.93%
Al_2O_3	12.78%	13.73%	12.02%	12.48%	13.92%	13.45%
$Fe_2O_{3\ Total}$	9.97%	11.22%	10.23%	12.94%	10.76%	9.41%
MnO	0.15%	0.21%	0.19%	0.21%	0.19%	0.25%
MgO	7.21%	7.98%	8.00%	5.57%	6.81%	4.44%
CaO	7.67%	5.97%	8.29%	8.11%	8.94%	5.78%
Na_2O	2.38%	2.72%	2.07%	2.24%	2.32%	2.66%
K_2O	0.91%	1.12%	0.91%	1.17%	0.69%	1.62%
P_2O_5	0.43%	0.36%	0.16%	0.50%	0.18%	0.21%
Total	91.43%	91.05%	88.58%	91.26%	89.36%	90.66%
S	189.97	274.86	200.19	152.02	126.48	245.19
Cl	361.93	266.28	315.68	392.74	302.29	145.58
Sc	24.02	36.11	27.80	40.58	44.41	26.57
V	267.88	270.26	253.19	405.36	309.57	210.76
Cr	172.81	175.07	257.71	32.02	100.27	5.42
Ni	26.67	30.70	40.84	<LD	12.70	<LD
Cu	66.97	69.83	30.52	140.04	54.18	13.63
Zn	47.18	48.79	44.73	60.46	39.28	39.53
Ga	20.85	18.05	19.14	21.05	21.16	18.13
As	12.59	<LD	2.72	11.76	0.12	<LD
Rb	29.38	41.53	33.81	41.59	15.51	43.69
Sr	571.75	353.28	523.01	561.07	549.65	554.23
Y	23.07	24.87	17.07	26.44	20.93	18.19
Zr	122.12	117.67	69.42	91.15	52.10	79.25
Nb	5.14	5.98	4.74	5.03	1.33	5.91
Ba	439.93	429.45	331.49	425.21	391.00	896.19
Ce	19.59	54.17	50.55	78.46	41.89	<LD
Pb	1.58	1.75	6.99	4.04	9.04	14.45
Th	<LD	3.99	2.04	0.08	0.95	5.48
U	0.66	2.75	2.76	<LD	<LD	2.00

Table B.1continued: Pressed Powder X-ray flourescence (XRF) data for PHIS and Lodestrar Breccia samples.

Sample Name	JH-99-041	JH-99-049B	JH-99-175	JH-99-003	JH-99-008	JH-99-019C
Pre-Breccia gabbro	Pre-Breccia gabbro	Pre-Breccia gabbro	Pre-Breccia gabbro	Post-breccia gabbro	Post-breccia gabbro	Post-breccia gabbro
SiO_2	46.87%	44.11%	42.58%	38.29%	40.64%	41.40%
TiO_2	0.87%	0.85%	1.44%	2.06%	2.74%	3.51%
Al_2O_3	16.08%	11.79%	12.09%	13.09%	12.75%	12.59%
$Fe_2O_{3\ Total}$	8.77%	10.24%	10.72%	14.27%	14.86%	16.42%
MnO	0.15%	0.18%	0.18%	0.21%	0.20%	0.23%
MgO	6.24%	10.61%	6.85%	8.35%	8.21%	6.19%
CaO	9.63%	8.00%	10.83%	6.78%	8.77%	8.10%
Na_2O	2.61%	2.04%	1.91%	2.24%	2.44%	2.62%
K_2O	0.72%	1.08%	0.73%	0.94%	0.57%	0.51%
P_2O_5	0.15%	0.22%	0.07%	0.28%	0.50%	0.91%
Total	92.09%	89.12%	87.40%	86.51%	91.68%	92.48%
S	97.54	230.35	127.70	819.21	1109.44	1393.61
Cl	268.04	342.71	254.19	153.11	114.82	135.40
Sc	17.69	38.95	61.88	28.78	38.31	26.09
V	239.23	225.97	562.20	377.89	354.60	404.06
Cr	171.36	382.28	46.51	120.58	64.59	14.69
Ni	46.66	73.92	13.16	54.69	41.21	20.04
Cu	64.96	67.22	41.58	51.69	68.12	55.31
Zn	26.82	35.74	30.42	55.40	45.15	86.00
Ga	20.82	15.65	17.39	21.21	21.19	23.56
As	0.91	1.79	15.88	4.69	3.14	44.57
Rb	10.46	38.25	18.84	27.84	12.57	16.41
Sr	640.31	406.38	534.83	422.08	452.82	476.90
Y	12.57	15.70	17.51	25.05	31.90	38.84
Zr	38.30	42.28	25.03	105.54	180.40	264.95
Nb	3.97	2.17	0.73	5.52	11.98	21.90
Ba	362.20	252.59	250.82	217.52	218.35	283.07
Ce	21.13	<LD	<LD	29.40	15.87	7.70
Pb	6.46	5.65	5.32	0.40	<LD	4.07
Th	0.41	0.47	<LD	<LD	1.19	<LD
U	<LD	0.50	<LD	<LD	0.82	<LD

Table B.1continued: Pressed Powder X-ray flourescence (XRF) data for PHIS and Lodestrar Breccia samples.

Sample Name	JH-99-023	JH-99-033	JH-99-047B	JH-99-170B	JH-99-161	JH-99-146
Rock Type	Post-breccia gabbro	Post-breccia gabbro	Post-breccia gabbro	Post-breccia gabbro	Post-breccia gabbro	Post-breccia gabbro
SiO_2	42.46%	43.36%	40.30%	32.51%	43.49%	42.82%
TiO_2	3.02%	3.11%	2.76%	2.23%	1.89%	2.72%
Al_2O_3	12.55%	12.87%	12.26%	11.64%	13.25%	11.48%
$Fe_2O_{3\ Total}$	15.45%	15.11%	14.73%	15.95%	12.71%	17.07%
MnO	0.23%	0.24%	0.24%	0.28%	0.19%	0.31%
MgO	7.32%	6.55%	4.76%	9.89%	9.47%	5.15%
CaO	7.53%	8.54%	8.08%	5.17%	8.44%	7.29%
Na_2O	2.73%	2.75%	3.09%	1.90%	2.20%	3.23%
K_2O	1.01%	1.01%	1.32%	0.47%	0.96%	1.03%
P_2O_5	0.61%	0.84%	1.53%	0.41%	0.27%	1.53%
Total	92.92%	94.39%	89.07%	80.45%	92.87%	92.63%
S	1484.43	1748.29	1108.96	270.31	1050.65	951.70
Cl	141.12	219.10	186.09	77.68	142.63	143.86
Sc	58.37	29.40	28.02	44.45	28.89	27.96
V	423.69	368.76	245.49	372.21	306.76	224.53
Cr	54.67	29.97	35.87	61.61	100.31	18.79
Ni	30.33	14.14	3.06	49.20	64.58	<LD
Cu	70.41	43.73	27.98	43.76	65.60	9.53
Zn	84.66	59.36	67.23	64.17	55.20	102.95
Ga	23.37	28.85	18.84	23.78	24.45	20.07
As	7.29	0.41	8.90	<LD	10.98	<LD
Rb	26.61	19.11	25.49	19.76	30.96	12.81
Sr	412.83	496.59	548.39	257.45	526.75	385.26
Y	41.13	46.33	42.14	31.72	23.74	65.70
Zr	227.91	300.18	196.31	176.77	131.13	381.44
Nb	16.20	24.91	38.55	11.12	8.03	33.91
Ba	558.55	384.59	526.28	192.63	318.96	360.51
Ce	29.25	35.38	87.85	<LD	109.48	86.46
Pb	6.67	4.38	4.67	4.24	5.85	7.37
Th	<LD	2.42	1.62	<LD	2.38	2.99
U	0.39	<LD	1.75	<LD	<LD	1.28

Table B.1continued: Pressed Powder X-ray flourescence (XRF) data for PHIS and Lodestrar Breccia samples.

Sample Name	JH-99-158	JH-99-218B	JH-99-274	CD-99-045	JH-99-258	JH-99-021
	Post-breccia	Post-breccia	Post-breccia	Post-breccia	Post-breccia	
Rock Type	gabbro	gabbro	gabbro	gabbro	gabbro	Felsic material
SiO_2	46.87%	45.94%	39.03%	44.97%	40.03%	83.11%
TiO_2	2.60%	2.49%	3.22%	1.95%	2.88%	0.08%
Al_2O_3	13.31%	14.39%	12.54%	15.17%	11.34%	16.32%
$Fe_2O_{3\ Total}$	13.37%	14.43%	18.66%	13.97%	15.94%	1.18%
MnO	0.21%	0.21%	0.25%	0.20%	0.29%	0.02%
MgO	7.76%	8.85%	7.52%	9.84%	8.47%	0.06%
CaO	8.89%	7.35%	9.13%	7.48%	6.59%	0.35%
Na_2O	3.06%	2.94%	2.59%	2.71%	2.25%	5.35%
K_2O	0.75%	1.24%	0.82%	0.85%	1.01%	4.90%
P_2O_5	0.76%	0.56%	0.67%	0.37%	0.40%	0.00%
Total	97.60%	98.40%	94.44%	97.51%	89.19%	111.39%
S	729.67	1054.71	1527.21	877.85	30.72	32.27
Cl	217.54	133.71	122.85	182.84	116.07	180.66
Sc	51.51	37.13	32.75	29.19	45.12	0.09
V	304.76	378.80	444.62	332.52	409.88	0.93
Cr	142.97	47.83	50.70	55.32	49.39	4.91
Ni	45.32	40.13	30.70	65.48	33.46	<LD
Cu	51.44	75.11	49.84	86.31	28.12	4.20
Zn	45.37	48.17	45.19	42.04	80.34	22.22
Ga	19.36	23.92	21.01	20.25	21.38	21.94
As	<LD	<LD	<LD	<LD	6.41	<LD
Rb	16.39	33.90	20.21	27.77	32.62	130.67
Sr	470.76	449.04	478.75	532.28	321.89	12.63
Y	38.35	37.63	36.25	27.77	36.76	21.26
Zr	209.75	213.57	206.71	120.38	208.32	154.50
Nb	16.28	15.10	16.42	10.50	21.82	29.20
Ba	298.83	689.66	464.70	336.86	537.41	36.39
Ce	51.08	2.13	45.41	39.23	20.15	26.36
Pb	1.46	3.23	1.99	3.12	6.14	11.69
Th	1.87	3.22	0.91	<LD	2.22	12.77
U	2.15	<LD	<LD	0.51	<LD	3.57

Table B.1continued: Pressed Powder X-ray flourescence (XRF) data for PHIS and Lodestrar Breccia samples.

Sample Name	JH-99-030C	JH-99-061	JH-99-100	JH-99-184	JH-99-225	JH-99-245
Rock Type	Felsic material	Felsic material	Felsic material	Felsic material	Felsic material	Felsic material
SiO_2	75.20%	54.85%	68.39%	72.14%	65.64%	71.02%
TiO_2	0.52%	0.44%	0.39%	0.09%	0.37%	0.09%
Al_2O_3	16.29%	19.69%	14.19%	12.68%	13.45%	13.19%
$Fe_2O_{3\ Total}$	2.50%	4.66%	3.26%	1.29%	3.54%	1.35%
MnO	0.03%	0.10%	0.07%	0.04%	0.08%	0.02%
MgO	1.09%	1.38%	0.87%	0.11%	1.16%	0.26%
CaO	1.06%	8.03%	1.32%	0.17%	1.45%	0.44%
Na_2O	4.68%	6.41%	4.22%	3.94%	4.06%	4.36%
K_2O	5.21%	1.19%	3.95%	3.82%	3.48%	3.74%
P_2O_5	0.10%	0.15%	0.11%	0.00%	0.13%	0.01%
Total	106.68%	96.92%	96.77%	94.29%	93.36%	94.49%
S	56.64	112.81	53.54	44.93	84.13	43.74
Cl	114.82	63.48	171.27	135.86	218.32	153.21
Sc	3.06	<LD	7.64	5.96	5.87	2.13
V	63.93	85.99	32.87	1.09	29.98	10.12
Cr	3.81	25.31	7.95	9.88	8.55	15.76
Ni	<LD	<LD	<LD	<LD	-6.55	<LD
Cu	13.82	12.36	<LD	V	4.74	6.98
Zn	3.26	1.64	18.27	3.56	18.17	2.45
Ga	14.85	16.58	21.30	16.69	21.69	20.28
As	2.42	16.08	1.54	2.11	<LD	<LD
Rb	95.85	19.95	110.53	115.64	83.52	141.29
Sr	36.07	840.67	118.52	15.16	120.58	45.96
Y	47.36	18.13	43.19	38.24	48.26	45.13
Zr	330.65	175.15	308.91	143.03	326.82	132.76
Nb	19.33	10.55	18.43	26.81	21.02	36.83
Ba	408.87	124.28	614.65	52.33	547.02	67.49
Ce	72.98	63.41	68.97	71.55	100.08	5.34
Pb	3.53	1.49	4.23	7.20	4.50	1.49
Th	11.50	10.17	8.02	13.89	9.31	14.71
U	0.84	2.79	1.10	2.74	2.68	5.07

Table B.1continued: Pressed Powder X-ray flourescence (XRF) data for PHIS and Lodestrar Breccia samples.

Sample Name	JH-99-173	JH-99-092A	JH-99-092B	JH-99-126A	JH-99-121C	JH-99-004C
Rock Type	Felsic material	Felsic material	Felsic material	Felsic material	Felsic material	diabase
SiO_2	73.61%	70.47%	71.97%	73.27%	58.17%	38.97%
TiO_2	0.07%	0.09%	0.09%	0.08%	0.19%	2.28%
Al_2O_3	13.25%	14.35%	13.88%	14.05%	10.96%	12.69%
$Fe_2O_{3\ Total}$	1.23%	1.00%	0.92%	1.21%	2.36%	15.47%
MnO	0.02%	0.02%	0.02%	0.03%	0.03%	0.22%
MgO	0.14%	0.32%	0.22%	0.11%	0.41%	8.30%
CaO	0.21%	0.59%	0.91%	0.33%	0.85%	6.70%
Na_2O	3.85%	3.67%	3.98%	4.28%	3.29%	2.31%
K_2O	4.02%	4.79%	4.72%	4.27%	3.51%	0.93%
P_2O_5	0.01%	0.01%	0.01%	0.01%	0.05%	0.30%
Total	96.40%	95.32%	96.71%	97.63%	79.81%	88.18%
S	47.56	141.36	118.52	37.58	167.09	1092.44
Cl	52.55	144.58	158.31	128.31	72.07	121.43
Sc	6.77	<LD	<LD	<LD	9.88	23.87
V	0.09	4.57	10.54	3.12	5.69	402.46
Cr	<LD	34.24	11.05	16.98	30.57	113.19
Ni	<LD	-9.31	<LD	<LD	<LD	50.70
Cu	<LD	6.76	5.09	2.21	3.24	57.27
Zn	8.33	6.11	<LD	4.79	4.32	84.29
Ga	19.96	14.92	8.89	20.16	18.77	18.56
As	<LD	80.83	11.03	2.26	13.33	<LD
Rb	125.21	128.93	95.46	141.22	73.95	38.76
Sr	13.05	111.04	147.64	12.20	124.14	408.18
Y	48.86	7.81	7.14	36.50	39.31	26.02
Zr	150.40	101.53	101.75	165.08	237.08	112.77
Nb	26.51	8.39	7.78	30.69	18.30	4.38
Ba	73.85	770.44	502.14	6.12	541.11	238.52
Ce	56.08	50.56	85.64	74.84	137.08	70.26
Pb	9.85	13.01	7.85	9.55	4.71	3.14
Th	12.41	19.27	18.55	14.23	15.99	2.17
U	2.51	3.82	5.59	5.94	2.12	<LD

Table B.1continued: Pressed Powder X-ray flourescence (XRF) data for PHIS and Lodestrar Breccia samples.

Sample Name	JH-99-002C	JH-99-031	JH-99-141A	JH-99-141B	JH-99-286	JH-99-141D
Rock Type	diabase	diabase	QFP clast	QFP clast	QFP clast	gabbro clast
SiO_2	30.56%	47.74%	56.75%	59.62%	60.14%	37.18%
TiO_2	3.31%	0.64%	0.12%	0.05%	0.33%	0.89%
Al_2O_3	8.63%	11.45%	8.56%	9.74%	12.07%	17.75%
$Fe_2O_{3\ Total}$	15.45%	7.19%	4.17%	1.76%	7.75%	8.94%
MnO	0.25%	0.14%	0.08%	0.02%	0.13%	0.14%
MgO	4.90%	6.03%	2.81%	1.20%	4.18%	4.21%
CaO	6.02%	4.47%	0.88%	0.56%	0.80%	1.49%
Na_2O	2.17%	2.21%	1.20%	1.12%	0.82%	1.07%
K_2O	0.44%	1.37%	2.15%	3.15%	2.69%	4.02%
P_2O_5	1.00%	0.15%	0.03%	0.01%	0.08%	0.30%
Total	72.73%	81.39%	76.76%	77.22%	88.99%	76.00%
S	3795.05	124.30	1149.67	1889.14	2543.18	1208.94
Cl	72.72	12.50	70.65	60.16	83.83	83.97
Sc	52.65	23.20	<LD	<LD	3.97	17.83
V	344.11	172.93	34.41	11.70	70.89	244.94
Cr	<LD	177.45	22.38	27.32	59.35	57.03
Ni	0.59	33.90	4.82	<LD	<LD	5.98
Cu	28.11	43.88	6.72	3.48	35.71	137.75
Zn	91.79	45.82	45.04	10.70	117.50	152.65
Ga	24.73	16.59	15.57	15.42	24.37	29.60
As	2.87	<LD	4423.66	9424.96	12327.27	6828.01
Rb	8.74	31.89	74.82	136.40	125.94	248.62
Sr	179.83	468.27	136.50	91.26	61.67	146.29
Y	57.29	18.64	101.98	102.19	96.84	10.09
Zr	357.07	119.30	663.05	708.15	566.14	89.35
Nb	30.35	6.79	85.66	111.35	78.59	3.99
Ba	78.53	444.54	1654.80	1895.75	834.81	979.93
Ce	115.62	78.66	567.45	1155.21	1403.83	774.31
Pb	8.35	3.58	13.59	44.06	16.32	48.06
Th	0.94	4.22	22.82	20.78	17.32	10.31
U	3.13	<LD	10.87	9.97	4.78	3.61

Table B.1continued: Pressed Powder X-ray flourescence (XRF) data for PHIS and Lodestrar Breccia samples.

Sample Name	JH-99-141E	JH-99-141F	CD-99-074	JH-99-092C	JH-99-092D	JH-99-146
Rock Type	gabbro clast	gabbro clast	mineralization	seds	seds	min.gabbro
SiO_2	32.76%	38.99%	31.99%	42.90%	39.90%	37.17%
TiO_2	1.40%	1.18%	0.66%	0.80%	0.68%	2.26%
Al_2O_3	11.71%	13.47%	9.19%	9.98%	10.74%	9.72%
$Fe_2O_{3\ Total}$	11.58%	9.76%	15.93%	8.53%	8.61%	15.06%
MnO	0.23%	0.21%	0.12%	0.17%	0.23%	0.27%
MgO	6.24%	5.83%	3.77%	4.87%	5.24%	4.41%
CaO	2.28%	3.00%	1.10%	4.19%	3.73%	6.25%
Na_2O	0.66%	1.52%	0.60%	2.35%	2.07%	2.80%
K_2O	2.28%	2.91%	2.13%	1.04%	0.86%	0.91%
P_2O_5	0.36%	0.38%	0.19%	0.12%	0.11%	1.30%
Total	69.51%	77.27%	65.68%	74.96%	72.18%	80.13%
S	3783.78	2493.61	40412.03	250.63	167.09	860.93
Cl	76.25	189.72	84.31	126.61	81.01	107.71
Sc	32.81	16.18	10.77	19.33	22.93	21.39
V	330.75	248.89	154.11	163.27	176.41	178.94
Cr	112.73	85.48	61.27	140.49	132.72	6.42
Ni	42.60	18.39	<LD	25.93	22.56	<LD
Cu	30.67	72.37	8914.16	31.38	28.23	10.13
Zn	226.98	168.76	1936.86	61.31	46.40	97.51
Ga	29.74	25.94	25.01	18.47	19.50	27.45
As	27954.36	7914.92	36546.04	27.68	20.45	13.47
Rb	145.36	202.76	161.42	40.17	36.13	13.38
Sr	150.42	346.39	69.97	459.62	616.14	397.94
Y	21.01	16.71	24.40	18.86	18.84	66.72
Zr	91.38	102.19	157.37	135.10	125.16	382.42
Nb	7.93	4.63	17.40	8.87	8.87	33.87
Ba	948.20	606.22	527.88	333.36	371.16	357.02
Ce	2081.72	895.01	2439.85	92.58	97.90	89.55
Pb	51.70	53.69	340.88	11.04	6.51	6.20
Th	7.53	5.29	25.94	7.40	6.75	0.87
U	5.21	2.05	1.81	1.31	3.50	0.15

Table B.1 continued: Pressed Powder X-ray flourescence (XRF) data for PHIS and Lodestrar Breccia samples.

Sample Name	JH-99-281	JH-99-282	JH-99-283	JH-99-284	JH-99-285	JH-99-287
Rock Type	mineralization	mineralization	mineralization	mineralization	mineralization	mineralization
SiO_2	47.45%	46.20%	38.61%	46.73%	52.83%	49.15%
TiO_2	0.82%	0.70%	0.65%	1.10%	0.75%	0.79%
Al_2O_3	14.13%	11.09%	10.54%	16.98%	13.25%	12.49%
$Fe_2O_{3\ Total}$	10.13%	11.57%	22.65%	12.34%	10.99%	14.31%
MnO	0.11%	0.20%	0.05%	0.14%	0.25%	0.18%
MgO	5.64%	5.45%	2.32%	5.21%	6.57%	5.57%
CaO	1.59%	1.21%	0.39%	1.69%	1.55%	1.08%
Na_2O	1.11%	0.71%	0.46%	0.90%	0.90%	0.84%
K_2O	2.87%	3.25%	2.32%	3.52%	4.19%	3.65%
P_2O_5	0.22%	0.19%	0.16%	0.15%	0.19%	0.17%
Total	84.07%	80.59%	78.15%	88.75%	91.48%	88.25%
S	13511.09	17214.58	116989.89	24118.73	4273.67	28448.72
Cl	70.33	112.28	76.14	51.15	213.74	86.01
Sc	24.57	24.83	24.81	33.81	13.60	18.94
V	226.30	152.86	135.43	200.36	169.31	166.25
Cr	66.73	72.00	90.62	168.68	98.15	142.45
Ni	2.09	10.36	12.66	32.17	10.78	11.33
Cu	751.94	1605.84	11767.60	1465.25	179.32	2753.87
Zn	175.85	1118.82	1891.84	312.68	342.77	933.35
Ga	30.56	25.39	22.06	26.85	24.03	20.13
As	43363.58	12541.56	4093.04	10486.48	12162.83	11523.59
Rb	202.34	220.54	110.22	190.58	243.25	201.17
Sr	103.81	77.29	23.47	93.49	93.26	70.64
Y	20.06	38.04	8.74	20.89	40.69	35.17
Zr	148.93	239.77	109.34	271.30	249.29	232.04
Nb	14.08	31.69	9.38	14.00	30.50	26.76
Ba	484.81	594.31	234.96	537.14	631.35	478.66
Ce	3235.01	1209.82	156.61	1032.11	1397.26	897.72
Pb	55.25	148.18	119.92	34.13	76.85	130.53
Th	9.71	22.44	29.47	9.67	15.65	25.61
U	2.15	<LD	1.96	<LD	8.11	<LD

Table B.1 continued: Pressed Powder X-ray flourescence (XRF) data for PHIS and Lodestrar Breccia samples.

Sample Name	JH-99-288	JH-99-289
Rock Type	mineralization	mineralization
SiO_2	51.15%	49.70%
TiO_2	0.99%	1.02%
Al_2O_3	12.88%	13.51%
$Fe_2O_{3\ Total}$	11.34%	12.44%
MnO	0.15%	0.28%
MgO	7.09%	7.39%
CaO	1.40%	3.62%
Na_2O	0.87%	1.01%
K_2O	3.29%	3.93%
P_2O_5	0.21%	0.20%
Total	89.37%	93.11%
S	10775.52	966.56
Cl	147.41	304.76
Sc	25.11	28.38
V	195.74	253.47
Cr	139.90	151.47
Ni	7.95	22.35
Cu	184.16	68.70
Zn	153.65	498.76
Ga	30.00	20.19
As	46170.68	221.95
Rb	234.86	226.33
Sr	78.47	187.53
Y	22.13	27.34
Zr	171.37	151.77
Nb	17.74	16.69
Ba	408.18	587.70
Ce	3900.64	20.23
Pb	33.16	13.70
Th	7.86	4.90
U	1.44	<LD

Table B.2: Major element ICP-ES results for PHIS and surrounding rocks

Sample	JH-99-002A	JH-99-002B	JH-99-009	JH-99-019A	JH-99-034
Rock type	pre-breccia gabbro	pre-breccia gabbro	pre-breccia gabbro	pre-breccia gabbro	pre-breccia gabbro
SiO2	52.59	50.20	53.60	51.25	50.06
Al2O3	16.08	16.56	16.14	15.79	15.47
Fe2O3	9.44	9.50	9.20	12.46	11.81
MgO	5.16	5.43	6.12	4.33	6.15
CaO	7.75	5.67	8.63	8.28	9.70
Na2O	3.29	3.80	2.97	2.94	2.82
K2O	1.16	1.31	1.15	1.35	0.66
TiO2	1.08	1.11	0.81	1.47	1.17
MnO	0.15	0.19	0.17	0.20	0.20
P2O5	0.40	0.36	0.12	0.40	0.12

Sample	JH-99-040	JH-99-041	JH-99-049B	JH-99-175	JH-99-003
Rock type	pre-breccia gabbro	pre-breccia gabbro	pre-breccia gabbro	pre-breccia gabbro	post-breccia gabbro
SiO2	56.97	50.24	49.38	46.91	43.92
Al2O3	17.26	16.26	15.88	14.08	16.86
Fe2O3	8.50	10.44	9.01	12.79	12.79
MgO	2.97	6.83	7.75	6.81	6.39
CaO	6.13	10.28	8.40	11.95	8.22
Na2O	3.58	2.82	3.07	2.30	3.26
K2O	1.85	0.61	1.47	0.78	1.11
TiO2	0.72	0.94	0.73	1.39	2.27
MnO	0.21	0.17	0.15	0.20	0.19
P2O5	0.18	0.11	0.19	0.04	0.23

Sample	JH-99-008	JH-99-019C	JH-99-023	JH-99-033	JH-99-047B
Rock type	post-breccia gabbro	post-breccia gabbro	post-breccia gabbro	post-breccia gabbro	post-breccia gabbro
SiO2	42.99	43.31	44.71	44.55	44.06
Al2O3	15.12	14.49	14.57	14.89	14.45
Fe2O3	14.52	16.95	15.69	15.95	13.71
MgO	6.64	5.42	5.91	5.20	4.87
CaO	9.69	8.61	8.09	8.59	8.89
Na2O	2.99	3.16	3.29	3.37	3.56
K2O	0.68	0.55	1.17	1.02	1.44
TiO2	2.88	3.85	3.10	3.39	3.23
MnO	0.22	0.26	0.25	0.27	0.24
P2O5	0.43	0.73	0.56	0.74	1.52

Table B.2 continued: Major element ICP-ES results for PHIS and surrounding rocks

Sample	JH-99-170B	JH-99-161	JH-99-146	JH-99-158	JH-99-218B
Rock type	post-breccia gabbro	post-breccia gabbro	post-breccia gabbro	post-breccia gabbro	post-breccia gabbro
SiO2	40.72	44.87	43.94	46.44	44.41
Al2O3	16.14	16.62	13.37	15.03	14.90
Fe2O3	15.43	12.42	16.02	13.12	15.19
MgO	7.30	6.80	4.21	5.95	6.21
CaO	5.66	8.65	8.08	8.63	7.67
Na2O	3.70	2.82	3.80	3.58	3.21
K2O	0.74	1.15	1.14	0.86	1.33
TiO2	3.13	2.03	3.75	2.57	2.99
MnO	0.31	0.19	0.31	0.22	0.24
P2O5	0.45	0.25	1.45	0.65	0.48

Sample	JH-99-274	CD-99-045	JH-99-021	JH-99-030C	JH-99-061
Rock type	post-breccia gabbro	post-breccia gabbro	Felsic material	Felsic material	Felsic material
SiO2	40.76	44.79	77.66	72.24	59.18
Al2O3	13.91	16.27	12.28	13.82	20.54
Fe2O3	16.73	13.57	1.06	1.74	3.18
MgO	6.20	7.09	0.02	0.43	0.55
CaO	8.46	7.96	0.23	0.57	5.65
Na2O	3.22	3.16	4.06	4.24	7.86
K2O	0.93	0.97	4.21	4.77	0.78
TiO2	3.89	2.15	0.05	0.37	0.27
MnO	0.26	0.22	0.01	0.01	0.06
P2O5	0.57	0.32	<LD	0.09	0.12

Sample	JH-99-100	JH-99-184	JH-99-225	JH-99-245	JH-99-173
Rock type	Felsic material	Felsic material	Felsic material	Felsic material	Felsic material
SiO2	71.58	77.65	71.76	77.35	77.40
Al2O3	14.32	12.70	14.09	12.58	12.62
Fe2O3	2.77	0.97	2.90	1.25	1.01
MgO	0.51	0.05	0.61	0.11	0.06
CaO	1.19	0.13	1.30	0.40	0.18
Na2O	4.34	4.13	4.53	4.29	3.91
K2O	4.26	4.24	4.14	4.14	4.38
TiO2	0.38	0.05	0.41	0.07	0.05
MnO	0.05	0.02	0.05	0.00	0.01
P2O5	0.10	<LD	0.10	<LD	0.03

Table B.2 continued: Major element ICP-ES results for PHIS and surrounding rocks

Sample	JH-99-092A	JH-99-092B	JH-99-126A	JH-99-121C	JH-99-004C
Rock type	Felsic material	Felsic material	Felsic material	Felsic material	diabase
SiO2	76.81	76.61	76.15	74.50	44.29
Al2O3	12.60	12.54	12.74	13.34	16.16
Fe2O3	0.91	0.80	1.26	2.11	13.54
MgO	0.15	0.10	0.08	0.25	6.90
CaO	0.56	0.86	0.30	0.85	7.83
Na2O	3.37	3.63	4.10	4.19	3.43
K2O	4.87	4.65	4.40	4.48	1.17
TiO2	0.09	0.08	0.07	0.19	2.53
MnO	0.02	0.01	0.02	0.02	0.22
P2O5	<LD	<LD	<LD	0.04	0.25

Sample	JH-99-002C	JH-99-031	JH-99-141A	JH-99-141B	JH-99-141D
Rock type	diabase	diabase	QFP clast	QFP clast	Gabbro clast
SiO2	40.52	59.37	74.64	76.04	48.43
Al2O3	14.28	14.99	11.21	11.41	22.84
Fe2O3	17.63	8.52	4.03	2.49	8.87
MgO	5.37	4.57	1.74	0.62	3.44
CaO	7.35	5.44	1.34	0.79	2.12
Na2O	3.85	3.09	1.86	1.63	2.19
K2O	0.49	1.56	3.08	4.11	5.13
TiO2	4.27	0.71	0.11	0.04	1.03
MnO	0.31	0.14	0.07	0.01	0.16
P2O5	1.06	0.21	0.03	0.01	0.50

Sample	JH-99-141E	JH-99-141F	JH-99-092C	JH-99-092D
Rock type	Gabbro clast	Gabbro clast	Seds	Seds
SiO2	45.75	50.15	55.64	56.93
Al2O3	18.29	19.14	14.50	15.65
Fe2O3	11.90	9.42	9.34	9.21
MgO	4.39	4.02	4.49	3.97
CaO	3.32	3.79	5.84	4.96
Na2O	1.59	2.72	3.42	3.41
K2O	3.69	3.52	1.44	1.22
TiO2	2.17	1.22	0.97	0.74
MnO	0.27	0.21	0.18	0.23
P2O5	0.50	0.37	0.20	0.15

Table B.3: Trace element ICP-ES results for PHIS and Lodestar sample analysis.(HF,HCL, HCLO4 DIGESTION)
Measurements in ppm.

Sample	JH-99-002A	JH-99-002B	JH-99-009	JH-99-019A	JH-99-034
Rock Type	pre-breccia gabbro	pre-breccia gabbro	pre-breccia gabbro	pre-breccia gabbro	pre-breccia gabbro
Mo	1.25	<LD	<LD	<LD	<LD
Cr	108.19	109.99	167.43	19.41	62.92
Zn	90.41	95.47	90.66	107.48	100.06
Pb	<LD	<LD	<LD	<LD	<LD
Co	33.34	34.12	35.28	36.40	42.03
Ni	29.56	29.84	37.37	5.56	26.24
Cd	<LD	<LD	<LD	<LD	<LD
Ti	6558.27	6870.08	5517.77	9530.80	7449.80
V	232.34	215.54	227.49	345.65	337.59
Be	1.12	1.94	0.92	1.06	0.80
Nb	5.59	5.75	4.86	7.01	3.82
Cu	69.16	85.93	34.32	139.25	49.31
Dy	3.79	4.00	2.98	4.00	3.15
Sc	28.44	28.35	31.06	31.39	37.71
Y	24.56	25.64	20.02	26.96	22.41
Mn	1217.48	1487.13	1387.84	1597.92	1627.18
Sr	516.47	329.52	474.28	503.54	466.17
La	16.21	17.03	9.07	16.64	9.18
Ce	35.62	36.16	20.85	36.54	23.06
Ba	470.90	467.67	345.56	378.59	313.97
Li	17.35	21.40	12.73	12.62	11.55
As	6.32	5.23	4.23	6.17	3.19

Table B.3 continued: Trace element ICP-ES results for PHIS and Lodestar sample analysis.(HF,HCL, HCLO4 DIGESTION) Measurements in ppm.

Sample	JH-99-040	JH-99-041	JH-99-049B	JH-99-175	JH-99-003
Rock Type	pre-breccia gabbro	pre-breccia gabbro	pre-breccia gabbro	pre-breccia gabbro	post-breccia gabbro
Mo	<LD	<LD	<LD	<LD	<LD
Cr	3.12	160.34	296.50	25.71	84.24
Zn	81.60	86.70	75.80	88.91	97.61
Pb	<LD	<LD	<LD	<LD	<LD
Co	17.85	41.21	41.35	39.23	45.87
Ni	<LD	46.38	62.72	23.75	44.82
Cd	<LD	<LD	<LD	<LD	<LD
Ti	4786.77	5786.85	4859.52	9448.81	13303.63
V	172.93	296.51	189.17	555.82	332.84
Be	1.11	0.59	0.74	0.63	0.89
Nb	4.34	3.24	2.46	3.82	6.38
Cu	7.48	59.24	72.97	33.23	58.27
Dy	3.02	2.61	2.62	2.67	3.76
Sc	17.72	35.87	33.27	60.82	32.26
Y	19.75	15.94	16.95	17.59	25.64
Mn	1654.35	1364.85	1228.98	1585.37	1494.45
Sr	516.80	542.99	381.02	415.76	395.16
La	17.17	6.01	8.95	3.72	7.21
Ce	30.25	17.26	20.09	15.41	21.40
Ba	786.76	296.51	250.24	213.09	233.34
Li	9.78	6.07	18.01	9.77	26.30
As	3.29	5.28	<LD	4.28	2.79

Table B.3 continued: Trace element ICP-ES results for PHIS and Lodestar sample analysis.(HF,HCL, HCLO4 DIGESTION) Measurements in ppm.

Sample	JH-99-008	JH-99-019C	JH-99-023	JH-99-033	JH-99-047B
Rock Type	post-breccia gabbro	post-breccia gabbro	post-breccia gabbro	post-breccia gabbro	post-breccia gabbro
Mo	<LD	1.29	1.10	1.31	1.35
Cr	73.70	21.81	46.68	33.32	33.33
Zn	106.34	146.52	137.38	115.43	114.49
Pb	<LD	<LD	<LD	<LD	<LD
Co	52.57	47.28	47.61	42.96	34.61
Ni	37.20	23.84	33.92	18.99	11.39
Cd	<LD	<LD	<LD	<LD	<LD
Ti	17322.43	23223.61	18296.35	20413.28	19366.44
V	352.83	407.59	402.61	341.31	261.63
Be	1.24	1.90	1.65	1.97	1.40
Nb	14.06	25.04	17.69	26.75	38.42
Cu	68.97	46.95	78.79	38.28	23.41
Dy	4.75	5.98	6.14	7.22	6.87
Sc	37.93	35.81	33.86	33.33	26.75
Y	31.16	37.68	39.38	43.59	41.54
Mn	1693.02	1987.76	1885.90	1981.23	1794.67
Sr	403.27	400.53	358.14	429.05	477.41
La	13.31	24.34	18.31	24.79	30.27
Ce	34.64	55.32	43.98	57.90	65.02
Ba	160.27	208.76	478.79	311.44	439.19
Li	14.91	14.52	27.23	15.96	20.35
As	<LD	46.07	5.70	2.95	2.80

Table B.3 continued: Trace element ICP-ES results for PHIS and Lodestar sample analysis.(HF,HCL, HCLO4 DIGESTION) Measurements in ppm.

Sample	JH-99-170B	JH-99-161	JH-99-146	JH-99-158	JH-99-218B
Rock Type	post-breccia gabbro	post-breccia gabbro	post-breccia gabbro	post-breccia gabbro	post-breccia gabbro
Mo	<LD	<LD	<LD	<LD	<LD
Cr	89.75	83.30	1.66	117.12	60.07
Zn	112.60	99.20	156.10	104.36	121.18
Pb	<LD	<LD	<LD	<LD	<LD
Co	55.61	49.82	28.31	42.21	48.57
Ni	47.64	58.12	<LD	43.29	35.79
Cd	<LD	0.09	<LD	<LD	<LD
Ti	17610.09	11487.27	22890.79	15388.47	16539.99
V	389.97	286.58	217.59	284.09	371.91
Be	1.70	1.01	2.35	1.57	1.41
Nb	14.80	9.07	36.46	18.38	17.80
Cu	37.26	73.02	1.13	53.84	79.76
Dy	5.00	3.76	10.93	5.98	5.84
Sc	36.93	29.48	32.17	33.42	35.10
Y	29.97	24.92	62.95	37.81	38.87
Mn	2322.55	1416.44	2277.45	1621.45	1762.90
Sr	238.76	468.37	346.59	393.97	387.44
La	12.22	10.67	36.65	20.38	16.14
Ce	35.43	27.39	83.76	48.56	42.10
Ba	194.99	280.00	328.11	259.42	580.93
Li	36.83	20.95	17.08	13.06	29.68
As	3.80	4.75	<LD	4.70	6.75

Table B.3 continued: Trace element ICP-ES results for PHIS and Lodestar sample analysis.(HF,HCL, HCLO4 DIGESTION) Measurements in ppm.

Sample	JH-99-274	CD-99-045	JH-99-258b	JH-99-021	JH-99-030C
Rock Type	post-breccia gabbro	post-breccia gabbro	post-breccia gabbro	Felsic material	Felsic material
Mo	<LD	<LD	<LD	1.02	<LD
Cr	43.45	50.80	54.17	<LD	3.21
Zn	123.69	113.75	125.92	55.11	25.75
Pb	<LD	<LD	<LD	3.34	<LD
Co	48.85	54.35	49.05	<LD	4.21
Ni	28.93	57.48	33.36	<LD	1.76
Cd	<LD	<LD	<LD	0.09	<LD
Ti	22716.31	11840.86	18856.58	445.95	2155.32
V	437.38	327.78	371.46	<LD	28.19
Be	1.39	1.13	1.40	2.69	1.23
Nb	20.22	11.73	21.08	22.15	11.91
Cu	51.77	91.27	22.42	5.95	15.66
Dy	6.00	4.98	6.35	2.99	5.64
Sc	37.26	30.85	38.03	1.41	3.34
Y	36.06	30.30	37.86	24.16	39.07
Mn	1826.45	1662.45	2110.83	169.31	178.74
Sr	404.21	450.83	295.26	12.16	34.33
La	15.66	11.98	16.23	9.79	40.62
Ce	43.19	32.41	40.58	29.25	65.72
Ba	357.98	273.63	453.29	38.14	370.39
Li	26.12	27.33	35.86	0.86	6.91
As	7.10	3.10	17.44	<LD	2.05

Table B.3 continued: Trace element ICP-ES results for PHIS and Lodestar sample analysis.(HF,HCL, HCLO4 DIGESTION) Measurements in ppm.

Sample	JH-99-061	JH-99-100	JH-99-184	JH-99-225	JH-99-245	JH-99-173	JH-99-092A
Rock Type	Felsic material	Felsic material	Felsic material	Felsic material	Felsic material	Felsic material	Felsic material
Mo	<LD	1.35	1.24	1.28	<LD	<LD	<LD
Cr	3.08	2.17	2.99	3.78	1.65	<LD	1.07
Zn	26.08	46.88	26.58	50.47	24.19	29.90	26.82
Pb	<LD	<LD	5.72	<LD	<LD	5.93	7.41
Co	2.72	4.37	<LD	4.19	1.56	<LD	<LD
Ni	<LD	<LD	<LD	1.44	<LD	<LD	<LD
Cd	<LD	<LD	<LD	<LD	<LD	<LD	0.27
Ti	1881.98	2561.26	386.31	2933.14	560.60	360.05	628.84
V	55.48	16.30	<LD	24.37	1.19	<LD	<LD
Be	0.94	2.90	3.51	3.02	3.66	4.29	1.49
Nb	10.06	15.31	17.88	18.24	28.54	18.58	4.49
Cu	13.31	1.08	1.43	4.24	7.15	3.35	3.25
Dy	2.67	6.29	4.18	7.19	5.96	5.00	1.10
Sc	3.45	4.64	0.92	5.45	2.06	0.95	1.02
Y	20.55	44.85	30.79	51.61	45.26	34.13	8.33
Mn	588.34	502.03	225.99	561.11	144.69	172.62	197.13
Sr	807.01	116.22	14.96	113.81	43.49	12.97	111.53
La	38.81	28.84	9.80	36.50	9.15	20.01	20.53
Ce	57.36	56.07	33.32	69.20	23.39	41.82	28.57
Ba	94.91	603.53	57.54	562.03	66.14	84.91	749.59
Li	4.45	4.85	1.99	4.47	1.53	2.15	3.17
As	20.45	2.90	3.06	3.96	<LD	2.36	64.54

Table B.3 continued: Trace element ICP-ES results for PHIS and Lodestar sample analysis.(HF,HCL, HCLO4 DIGESTION) Measurements in ppm.

Sample	JH-99-092B	JH-99-126A	JH-99-121C	JH-99-004C	JH-99-002C	JH-99-031	JH-99-141A
Rock Type	Felsic material	Felsic material	Felsic material	diabase	diabase	diabase	QFP clast
Mo	1.16	<LD	<LD	<LD	1.78	<LD	1.95
Cr	1.34	<LD	1.87	84.06	1.86	155.97	7.59
Zn	14.09	27.37	28.57	126.23	143.55	83.45	79.11
Pb	4.34	5.24	<LD	<LD	<LD	<LD	13.94
Co	<LD	<LD	1.95	47.98	39.76	28.02	12.79
Ni	<LD	<LD	<LD	43.44	4.95	32.96	5.39
Cd	0.15	<LD	<LD	<LD	<LD	<LD	<LD
Ti	628.96	487.05	1529.99	14885.47	24924.77	4767.51	897.06
V	7.64	<LD	2.39	366.16	333.94	182.73	30.02
Be	0.52	3.77	2.22	0.89	1.34	1.32	2.36
Nb	4.44	23.77	12.29	7.10	29.56	6.82	70.98
Cu	2.66	2.42	2.15	65.89	18.13	53.62	9.95
Dy	0.80	5.27	6.20	4.18	8.80	2.98	13.76
Sc	0.99	1.52	3.93	36.01	42.01	25.43	2.22
Y	9.31	36.96	42.33	26.91	49.73	19.14	98.22
Mn	138.17	220.51	311.19	1545.18	2157.51	1141.79	665.17
Sr	150.01	10.65	127.06	366.44	164.25	439.38	135.77
La	19.34	14.01	38.87	7.10	32.48	20.32	16.06
Ce	28.71	36.12	68.13	23.66	73.06	36.23	40.30
Ba	551.29	29.61	543.72	273.88	108.10	417.73	1289.15
Li	1.37	0.92	3.55	19.73	17.30	18.54	20.42
As	7.62	2.16	22.18	4.06	9.61	3.51	4946.00

Table B.3 continued: Trace element ICP-ES results for PHIS and Lodestar sample analysis.(HF,HCL, HCLO4 DIGESTION) Measurements in ppm.

Sample	JH-99-141B	JH-99-286	JH-99-141D	JH-99-141E	JH-99-141F	CD-99-074	JH-99-092C	JH-99-092D
Rock Type	QFP clast	QFP clast	Gabbro clast	Gabbro clast	Gabbro clast	min.	seds.	seds.
Mo	<LD	8.14	1.01	1.44	1.06	3.47	1.57	1.55
Cr	2.21	24.93	45.18	86.23	64.73	59.25	126.71	127.22
Zn	35.15	164.64	233.69	264.25	222.38	1843.60	105.41	86.64
Pb	43.13	17.22	35.76	41.59	37.79	350.75	<LD	<LD
Co	4.22	11.44	23.44	38.32	29.13	32.66	27.44	25.10
Ni	1.55	7.67	19.22	49.05	23.52	17.67	31.90	28.78
Cd	<LD	<LD	<LD	<LD	<LD	<LD	<LD	<LD
Ti	376.94	2022.84	6653.93	10080.21	8002.13	4158.49	6588.75	5114.74
V	6.88	60.31	243.23	344.00	241.48	164.12	207.08	202.77
Be	2.91	2.42	4.46	4.43	3.64	2.68	1.28	1.31
Nb	94.32	67.97	2.67	5.42	3.65	8.23	7.29	5.94
Cu	6.16	44.16	189.54	20.05	76.24	9570.00	42.88	29.78
Dy	13.01	11.42	2.35	3.44	3.73	3.23	3.08	2.94
Sc	0.17	6.34	19.83	32.15	24.03	17.40	25.05	23.65
Y	91.55	79.37	16.00	21.69	22.38	23.31	20.71	18.88
Mn	144.69	1009.74	1305.22	1976.89	1769.76	1172.21	1449.76	1760.44
Sr	84.52	61.05	138.82	144.05	318.19	61.47	451.96	594.17
La	13.02	13.64	11.79	11.22	16.65	7.67	15.50	15.95
Ce	34.63	35.87	26.76	27.76	34.68	28.26	33.23	32.72
Ba	232.82	725.86	826.27	848.29	632.17	45.89	330.24	347.20
Li	7.20	33.94	38.00	49.71	31.96	19.37	19.94	27.03
As	10559.00	13468.00	7585.00	27315.00	7321.00	31603.00	62.16	18.79

Table B.3 continued: Trace element ICP-ES results for PHIS and Lodestar sample analysis.(HF,HCL, HCLO4 DIGESTION) Measurements in ppm.

Sample	JH-99-146	JH-99-280	JH-99-281	JH-99-282	JH-99-283	JH-99-284	JH-99-285	JH-99-287
Rock Type	min. gabbro	min.	min.	min.	min.	min.	min.	min.
Mo	<LD	<LD	6.45	23.04	<LD	1.15	8.46	10.83
Cr	1.68	10.10	44.01	69.76	50.86	126.83	78.98	121.18
Zn	148.84	822.64	187.80	1092.44	1475.57	357.24	423.62	989.83
Pb	<LD	2127.00	46.23	138.78	96.26	24.43	66.22	129.24
Co	27.20	101.89	27.37	26.14	111.16	37.38	18.15	33.88
Ni	<LD	10.58	17.76	21.50	35.53	43.00	22.52	25.75
Cd	<LD	<LD	<LD	<LD	17.36	<LD	<LD	<LD
Ti	22133.54	747.15	4023.22	3950.35	2199.55	5722.08	4267.73	3973.60
V	210.80	38.04	197.30	139.36	82.86	173.72	149.82	153.16
Be	2.25	1.19	3.55	2.70	1.21	3.92	2.85	2.37
Nb	30.98	<LD	5.84	22.53	<LD	8.64	23.04	18.80
Cu	<LD	13703.00	734.34	1772.47	9386.57	1649.20	206.09	3049.00
Dy	10.70	0.17	3.12	5.13	1.23	3.59	5.46	4.39
Sc	31.86	3.30	21.25	17.44	9.78	25.05	17.59	19.77
Y	61.44	3.69	20.20	35.62	7.50	22.08	38.11	28.75
Mn	2221.30	339.77	835.84	1700.80	434.13	1027.77	1951.43	1404.03
Sr	366.35	35.40	89.29	70.82	17.21	86.62	88.87	63.20
La	37.43	<LD	10.81	11.58	2.59	21.90	14.87	12.80
Ce	83.22	24.43	28.34	31.50	27.61	46.47	32.79	33.87
Ba	309.64	17.51	270.10	66.01	49.37	183.80	600.13	107.72
Li	16.71	6.17	26.47	29.93	11.43	34.65	36.98	26.56
As	16.10	285800.00	40663.00	13932.00	2618.00	11435.00	13249.00	11181.00

Table B.3 continued: Trace element ICP-ES results for PHIS and Lodestar sample analysis.(HF,HCL, HCLO4 DIGESTION) Measurements in ppm.

Sample	JH-99-288	JH-99-289
Rock Type	min.	min.
Mo	3.15	37.70
Cr	97.22	107.19
Zn	162.88	625.77
Pb	24.86	5.13
Co	32.97	23.21
Ni	26.18	29.64
Cd	<LD	5.24
Ti	4592.08	5564.25
V	160.50	199.97
Be	2.98	3.41
Nb	7.92	11.56
Cu	169.83	78.20
Dy	3.75	5.13
Sc	20.75	25.78
Y	23.11	32.45
Mn	1111.46	2008.26
Sr	71.06	178.39
La	10.25	17.97
Ce	25.03	39.67
Ba	268.72	523.05
Li	27.36	34.54
As	46245.00	243.21

Table B.4: ICP-MS REE and trace element data analysis from PHIS and Lodestar Breccia samples.

Sample	JH-99-002A	JH-99-019A	JH-99-040	JH-99-041	JH-99-033	JH-99-161	JH-99-146	JH-99-158
rock type	pre-breccia gabbro	pre-breccia gabbro	pre-breccia gabbro	pre-breccia gabbro	post-breccia gabbro	post-breccia gabbro	post-breccia gabbro	post-breccia gabbro
Li	17.86	11.12	8.92	5.95	15.68	21.60	16.62	10.73
Rb	28.93	35.22	39.07	11.45	16.54	30.41	11.85	12.46
Sr	552.31	481.55	492.87	633.08	438.68	523.68	401.46	375.01
Y	22.03	21.90	15.79	14.58	38.57	22.84	59.48	31.25
Zr	49.29	33.98	34.67	53.24	167.94	116.36	207.70	139.40
Nb	6.95	6.45	4.61	2.47	23.49	9.27	32.12	15.91
Mo	1.04	0.93	0.41	0.64	2.20	1.31	1.24	1.29
Cs	1.73	0.89	1.02	0.68	1.05	1.59	0.10	0.41
Ba	453.60	330.02	715.07	305.84	285.99	269.07	319.02	227.30
La	16.69	16.40	15.74	7.71	24.43	11.80	36.95	19.75
Ce	37.62	35.65	31.43	17.56	59.99	27.90	93.42	48.73
Pr	5.09	4.84	4.05	2.43	8.68	3.93	12.58	6.83
Nd	21.27	21.70	16.11	10.90	38.82	17.93	59.98	30.69
Sm	4.82	5.12	3.63	2.89	9.43	4.68	14.20	7.46
Eu	1.51	1.53	1.07	1.13	3.32	1.67	4.58	2.35
Gd	4.73	5.07	3.45	3.11	10.03	5.00	13.96	7.28
Tb	0.65	0.71	0.48	0.42	1.32	0.70	2.08	1.10
Dy	4.12	4.47	3.08	2.75	8.24	4.41	12.38	6.78
Ho	0.82	0.88	0.62	0.55	1.57	0.90	2.35	1.31
Er	2.45	2.52	1.91	1.64	4.41	2.55	6.14	3.58
Tm	0.34	0.35	0.33	0.22	0.60	0.37	0.81	0.53
Yb	2.21	2.21	1.77	1.43	3.45	2.18	4.93	3.02
Lu	0.34	0.32	0.28	0.24	0.54	0.35	0.70	0.43
Hf	2.55	1.62	1.52	2.46	5.27	3.45	5.97	3.96
Ta	0.37	0.35	0.30	0.16	1.51	0.61	1.72	1.00
Tl	0.08	0.25	0.45	0.04	0.26	0.43	0.05	0.34
Pb	4.53	5.14	5.54	2.70	4.99	4.94	3.12	2.47
Bi	0.02	0.05	0.07	0.03	0.05	0.06	0.03	0.06
Th	3.06	2.64	4.43	1.06	1.21	1.04	1.20	1.48
U	0.89	0.74	1.10	0.29	0.41	0.34	0.44	0.44

Table B.4 continued: ICP-MS REE and trace element data analysis from PHIS and Lodestar Breccia samples.

Sample	JH-99-021	JH-99-100	JH-99-225	JH-99-092A	JH-99-092B	JH-99-121C	JH-99-141A	JH-99-141B	JH-99-141D
rock type	felsic material	felsic material	felsic material	felsic material	felsic material	felsic material	QFP clast	QFP clast	gabbro clast
Li	1.00	4.28	4.13	2.72	1.25	3.50	18.75	7.46	45.75
Rb	115.33	103.58	72.31	111.90	84.64	69.54	64.67	119.20	223.89
Sr	11.16	111.67	111.71	98.12	132.68	122.68	116.93	80.76	138.82
Y	21.42	41.26	44.19	7.01	7.66	38.83	79.05	82.26	14.17
Zr	116.47	117.14	180.80	86.67	84.34	99.54	465.76	571.00	39.35
Nb	25.91	18.41	19.86	7.27	6.93	17.07	66.84	99.78	3.89
Mo	0.39	0.80	0.81	0.25	0.31	0.39	1.47	0.73	1.14
Cs	0.59	0.98	0.46	2.13	1.28	0.34	0.81	1.42	4.53
Ba	33.75	559.42	469.29	688.33	474.22	528.29	1473.57	840.78	812.47
La	10.19	27.40	29.90	18.52	17.03	35.16	12.89	12.00	11.76
Ce	36.90	61.41	66.72	31.24	30.37	73.05	38.49	38.25	27.60
Pr	3.20	7.52	8.37	3.16	3.03	8.94	5.67	5.64	3.54
Nd	11.68	30.72	33.05	10.14	9.39	33.06	24.46	24.26	15.05
Sm	2.83	6.95	7.67	1.68	1.55	7.06	8.43	9.05	3.49
Eu	0.06	1.23	1.17	0.28	0.24	0.88	0.60	0.44	0.83
Gd	2.32	6.88	7.65	1.22	1.17	6.74	9.76	10.24	3.21
Tb	0.46	1.11	1.22	0.18	0.18	1.09	1.97	2.11	0.46
Dy	3.54	7.32	8.06	1.19	1.24	7.15	14.15	14.94	2.88
Ho	0.83	1.56	1.72	0.24	0.27	1.48	3.04	3.20	0.53
Er	2.98	4.66	5.17	0.78	0.88	4.43	9.38	10.28	1.54
Tm	0.57	0.72	0.81	0.16	0.17	0.68	1.49	1.66	0.24
Yb	3.96	5.02	5.35	1.01	1.15	4.61	10.19	10.97	1.28
Lu	0.63	0.75	0.82	0.16	0.19	0.71	1.38	1.52	0.17
Hf	5.63	4.92	6.77	3.62	3.50	4.67	19.21	21.40	1.44
Ta	1.98	1.45	1.54	0.97	0.89	1.50	6.20	7.23	0.27
Tl	0.71	0.38	0.46	0.37	0.35	0.24	0.28	0.78	0.94
Pb	13.05	9.79	10.53	16.98	14.23	8.61	19.36	52.89	49.26
Bi	0.17	0.51	0.07	0.53	0.10	0.03	1.28	1.85	6.27
Th	10.59	9.26	8.89	16.75	16.48	12.05	17.69	18.69	2.35
U	2.44	2.33	2.44	3.34	3.54	2.87	5.96	6.78	0.83

Table B.4 continued: ICP-MS REE and trace element data analysis from PHIS and Lodestar Breccia samples.

Sample	JH-99-141E	JH-99-141F	CD-99-074	JH-99-146	JH-99-281	JH-99-282	JH-99-283	JH-99-284
rock type	gabbro clast	gabbro clast	mineralization	min. gabbro	mineralization	mineralization	mineralization	mineralization
Li	55.20	32.22	19.33	16.69	25.65	28.83	13.30	36.14
Rb	123.62	195.88	142.68	13.10	173.71	199.88	85.47	163.63
Sr	133.09	326.97	63.41	430.46	88.32	71.38	19.15	83.92
Y	20.01	22.72	21.19	60.83	16.94	31.43	8.13	18.99
Zr	38.99	28.05	74.88	234.53	75.59	163.64	48.54	25.93
Nb	3.95	5.22	11.39	30.15	9.22	29.09	5.61	10.87
Mo	1.73	1.04	4.42	1.40	7.26	17.04	3.26	1.81
Cs	1.63	6.98	3.81	0.14	3.80	6.45	2.31	2.86
Ba	860.40	636.72	520.00	311.92	376.01	588.67	216.19	422.85
La	11.10	18.38	10.87	37.29	11.94	14.13	9.78	22.87
Ce	26.54	42.06	25.30	95.13	28.36	33.51	21.88	50.80
Pr	3.62	5.58	3.43	13.50	3.63	4.56	2.68	6.01
Nd	16.28	24.31	15.03	60.70	15.18	19.06	10.83	25.09
Sm	4.02	5.40	3.65	15.20	3.78	5.25	2.21	5.40
Eu	0.90	1.38	0.71	4.92	0.61	0.78	0.33	0.88
Gd	4.18	5.19	3.72	15.46	3.50	5.27	1.75	4.58
Tb	0.62	0.74	0.59	2.24	0.59	0.91	0.26	0.67
Dy	3.96	4.44	3.84	13.50	3.59	6.43	1.70	4.12
Ho	0.77	0.89	0.80	2.52	0.75	1.29	0.32	0.79
Er	2.23	2.50	2.35	6.89	2.23	4.10	0.89	2.32
Tm	0.30	0.37	0.39	0.86	0.32	0.68	0.14	0.40
Yb	1.90	2.16	2.33	5.15	2.04	3.83	0.88	1.91
Lu	0.27	0.32	0.33	0.74	0.29	0.53	0.12	0.26
Hf	1.74	1.41	3.17	8.47	3.01	7.01	2.35	1.16
Ta	0.15	0.34	0.62	1.52	0.68	2.21	0.37	0.64
Tl	0.55	0.89	0.83	0.07	0.65	1.00	0.44	0.68
Pb	50.46	52.42	366.91	3.16	54.02	165.29	76.36	28.95
Bi	9.90	4.22	52.98	0.03	12.54	38.73	47.60	6.17
Th	1.99	2.76	3.69	1.47	3.73	7.37	2.63	4.98
U	0.73	0.90	1.23	0.47	1.12	2.25	0.63	0.81

Table B.4 continued: ICP-MS REE and trace element data analysis from PHIS and Lodestar Breccia samples.

Sample	JH-99-286	JH-99-288
rock type	mineralization	mineralization
Li	34.34	26.97
Rb	116.12	203.16
Sr	58.08	68.62
Y	70.67	21.47
Zr	457.96	104.54
Nb	73.24	11.88
Mo	7.47	2.79
Cs	3.03	4.77
Ba	688.10	329.34
La	12.92	10.71
Ce	36.34	24.58
Pr	5.33	3.28
Nd	23.24	13.70
Sm	8.04	3.42
Eu	0.66	0.66
Gd	9.09	3.57
Tb	1.80	0.58
Dy	12.79	4.07
Ho	2.79	0.85
Er	8.68	2.58
Tm	1.43	0.42
Yb	9.17	2.61
Lu	1.29	0.39
Hf	19.71	4.46
Ta	6.59	0.86
Tl	0.53	0.83
Pb	22.79	27.82
Bi	4.83	6.49
Th	16.22	4.34
U	5.65	1.35

Table B.5: INAA results from PHIS and Lodestar breccia samples (ppm except Au, Ir in ppb, and Ca, Fe, Na, Sn, Sr, and Zr in wt %)

Sample	JH-99-002A	JH-99-002B	JH-99-009	JH-99-019A	JH-99-034	JH-99-040	JH-99-041	JH-99-049B	JH-99-175	JH-99-003
rock type	pre-breccia gabbro	pre-breccia gabbro	pre-breccia gabbro	pre-breccia gabbro	pre-breccia gabbro	pre-breccia gabbro	pre-breccia gabbro	pre-breccia gabbro	pre-breccia gabbro	post-breccia gabbro
Au	<LD	<LD	5	2	8	<LD	<LD	<LD	<LD	<LD
Ag	<LD	<LD	<LD	<LD	<LD	<LD	<LD	<LD	<LD	<LD
As	7.7	5.6	2.1	5.9	<LD	<LD	6	<LD	<LD	<LD
Ba	520	520	310	410	230	760	260	300	280	270
Br	<LD	<LD	<LD	<LD	<LD	<LD	<LD	<LD	<LD	<LD
CaO	6	4	8	6	8	4	8	7	9	6
Co	29	29	29	30	36	16	34	34	34	40
Cr	130	120	190	17	77	<LD	170	320	27	98
Cs	2	<LD	1	1	1	1	<LD	<LD	<LD	<LD
Fe2O3	6.69	6.8	6.51	8.38	8.45	6.13	7.24	6.27	9.15	8.9
Hf	4	4	2	3	2	3	2	2	1	3
Hg	<LD	<LD	<LD	<LD	<LD	<LD	<LD	<LD	<LD	<LD
Ir	<LD	<LD	<LD	<LD	<LD	<LD	<LD	<LD	<LD	<LD
Mo	<LD	<LD	3	<LD	<LD	3	<LD	<LD	<LD	<LD
Na	2.54	2.94	2.2	2.12	2.1	2.77	2.02	2.33	1.77	2.37
Ni	<LD	<LD	<LD	<LD	<LD	<LD	<LD	<LD	<LD	<LD
Rb	45	24	35	36	21	40	<LD	30	<LD	38
Sb	<LD	<LD	<LD	0.3	<LD	<LD	<LD	<LD	<LD	<LD
Sc	28	29	30	29	37	18	33	33	59	32
Se	<LD	<LD	<LD	<LD	<LD	<LD	<LD	<LD	<LD	<LD
Sn	<LD	<LD	<LD	<LD	<LD	<LD	<LD	<LD	<LD	<LD
Sr	0.08	<LD	0.07	0.06	<LD	0.07	0.07	<LD	0.07	0.08
Ta	0.5	<LD	<LD	0.4	<LD	0.5	<LD	<LD	<LD	0.4
Th	2.6	3.1	1.9	2.5	1.2	5.4	0.8	2.5	0.4	0.4
U	<LD	<LD	0.5	<LD	0.5	1.1	<LD	0.5	<LD	<LD
W	<LD	<LD	<LD	<LD	<LD	<LD	<LD	<LD	<LD	<LD
Zn	139	136	132	119	116	103	107	118	121	134
La	18	19	10	17	11	20	7.7	11	5.5	8.4
Ce	43	46	26	40	27	41	19	26	15	24
Nd	19	19	11	19	13	16	7	13	9	15
Sm	4.2	4.6	2.8	4.5	3	3.4	2.3	2.7	2.2	3.7
Eu	1.6	1.4	1	1.5	1	1.3	1	1	1	1.7
Tb	0.5	0.8	1	0.7	0.6	0.6	<LD	<LD	<LD	0.8
Yb	2.9	3.3	2.5	2.8	2.8	2.6	1.7	2.1	1.9	3.2
Lu	0.44	0.51	0.38	0.42	0.43	0.4	0.26	0.31	0.29	0.47
Zr	<LD	<LD	0.02	<LD	<LD	<LD	<LD	<LD	<LD	<LD

Table B.5 continued: INAA results from PHIS and Lodestar breccia samples (ppm except Au, Ir in ppb, and Ca, Fe, Na, Sn, Sr, and Zr in wt %)

Sample	JH-99-008	JH-99-019C	JH-99-023	JH-99-033	JH-99-047B	JH-99-170B	JH-99-161	JH-99-146	JH-99-158	JH-99-218B
	post-breccia	post-breccia	post-breccia	post-breccia	post-breccia	post-breccia	post-breccia	post-breccia	post-breccia	post-breccia
rock type	gabbro	gabbro	gabbro	gabbro	gabbro	gabbro	gabbro	gabbro	gabbro	gabbro
Au	<LD	6	<LD	<LD	<LD	<LD	<LD	1	2	1
Ag	<LD	<LD	<LD	<LD	<LD	<LD	<LD	<LD	<LD	<LD
As	<LD	50	<LD	2.2	2	<LD	4 3	<LD	<LD	4 9
Ba	320	300	470	400	430	340	300	360	430	760
Br	<LD	<LD	<LD	<LD	<LD	<LD	<LD	<LD	<LD	<LD
CaO	8	7	6	6	6	3	6	7	7	6
Co	48	45	44	37	31	56	44	25	40	47
Cr	82	24	49	34	34	110	91	<LD	140	74
Cs	<LD	<LD	2	1	<LD	2	2	<LD	<LD	2
Fe2O3	10.7	12.5	11.4	10 8	9 73	12 9	9 12	10.6	10.1	11.6
Hf	5	7	6	7	5	6	4	9	6	7
Hg	<LD	<LD	<LD	<LD	<LD	<LD	<LD	<LD	<LD	<LD
Ir	<LD	<LD	<LD	<LD	<LD	<LD	<LD	<LD	<LD	<LD
Mo	<LD	<LD	<LD	<LD	<LD	<LD	<LD	<LD	<LD	<LD
Na	2.24	2.31	2.41	2.36	2 58	3.28	2 24	2.58	2.66	2.6
Ni	<LD	<LD	82	<LD	<LD	<LD	<LD	<LD	<LD	<LD
Rb	32	27	34	<LD	25	36	<LD	<LD	29	33
Sb	<LD	0.6	0.4	0.7	0.3	<LD	0.3	<LD	<LD	0.3
Sc	39	36	35	33	26	43	31	30	34	38
Se	<LD	<LD	<LD	<LD	<LD	<LD	<LD	<LD	<LD	<LD
Sn	<LD	<LD	<LD	<LD	<LD	<LD	<LD	<LD	<LD	<LD
Sr	0.09	0.07	0.1	0.08	0 08	<LD	0 09	<LD	<LD	0.08
Ta	1	1.4	0.8	1.4	2 5	1.1	0 6	2.1	1.1	1.2
Th	1.1	1.4	1	1.1	2	<LD	1.1	1.2	1 9	1.4
U	<LD	<LD	<LD	<LD	0 9	<LD	<LD	0.6	0.7	-0.2
W	<LD	<LD	<LD	<LD	3	<LD	<LD	<LD	<LD	<LD
Zn	134	211	173	141	120	159	136	192	135	175
La	16	28	21	27	33	17	13	36	24	20
Ce	36	57	46	58	66	42	29	79	55	48
Nd	21	31	31	29	38	21	17	43	32	23
Sm	5.4	7.4	6.7	8.1	8.2	6 2	4.1	11	6.8	6.8
Eu	2.3	3	2.8	3.1	3 6	2.4	1.6	4.3	2.5	2.7
Tb	0.9	1.3	1.3	1.4	1.4	1.4	0.9	2.2	1.3	1.4
Yb	4	4.8	5.1	5 3	4.3	4 3	3.2	7	4.9	5.3
Lu	0.8	0.76	0 76	0.8	0.68	0.63	0.49	1.12	0.72	0.77
Zr	<LD	0.02	0 02	0 02	0.01	<LD	<LD	<LD	0.02	<LD

Table B 5 continued. INAA results from PHIS and Lodestar breccia samples (ppm except Au, Ir in ppb, and Ca, Fe, Na, Sn, Sr, and Zr in wt %)

Sample	JH-99-274	CD-99-045	JH-99-258b	JH-99-021	JH-99-030C	JH-99-061	JH-99-100	JH-99-184	JH-99-225	JH-99-245
	post-breccia	post-breccia	post-breccia							
rock type	gabbro	gabbro	gabbro	felsic material	felsic material	felsic material	felsic material	felsic material	felsic material	felsic material
Au	<LD	<LD	<LD	<LD	<LD	<LD	<LD	<LD	<LD	<LD
Ag	<LD	<LD	<LD	<LD	<LD	<LD	<LD	<LD	<LD	<LD
As	<LD	4 3	10	2 8	4 1	24	3 8	3 6	6 1	5.5
Ba	530	540	430	79	400	120	670	140	600	120
Br	<LD	<LD	<LD	<LD	<LD	<LD	<LD	<LD	<LD	<LD
CaO	7	7	5	<LD	<LD	4	<LD	<LD	<LD	<LD
Co	50	53	39	<LD	4	3	4	<LD	4	2
Cr	51	59	54	<LD	<LD	<LD	<LD	<LD	<LD	<LD
Cs	2	3	3	<LD	<LD	<LD	<LD	<LD	<LD	1
Fe2O3	11.4	11.3	9.66	0 93	1 37	2 78	2 26	0 81	2.34	1.13
Hf	6	5	5	8	10	5	11	6	11	8
Hg	<LD	<LD	<LD	<LD	<LD	<LD	<LD	<LD	<LD	<LD
Ir	<LD	<LD	<LD	<LD	<LD	<LD	<LD	<LD	<LD	<LD
Mo	<LD	<LD	<LD	4	<LD	2	3	<LD	<LD	<LD
Na	2.45	2.5	2.35	3 3	3 11	6 04	3 63	3.13	3.55	3.41
Ni	<LD	<LD	<LD	<LD	<LD	<LD	<LD	<LD	<LD	<LD
Rb	19	30	43	130	86	27	110	110	90	150
Sb	<LD	<LD	0 4	<LD	<LD	0 7	<LD	<LD	<LD	0 2
Sc	37	34	36	1 8	3 9	3 8	5 1	1 3	5 8	2 5
Se	<LD	<LD	<LD	<LD	<LD	<LD	<LD	<LD	<LD	<LD
Sn	<LD	<LD	<LD	<LD	<LD	<LD	<LD	<LD	<LD	<LD
Sr	0.06	<LD	<LD	<LD	<LD	0 1	<LD	<LD	<LD	<LD
Ta	1 3	0 4	0 8	2 2	1 2	1	1 4	2 1	1 4	2 9
Th	0 7	1 3	0 7	12	9 4	14	10	12	10	15
U	-0 2	-0 2	-0 2	1 8	2 2	1 5	1 7	2 2	1 8	2 7
W	<LD	<LD	<LD	<LD	<LD	3	<LD	<LD	<LD	<LD
Zn	157	140	127	56	<LD	<LD	61	<LD	71	<LD
La	18	15	19	11	40	39	31	10	38	10
Ce	34	28	33	32	64	55	59	33	69	27
Nd	25	20	22	12	33	20	30	12	36	11
Sm	6	5.1	5 8	2 6	7	3 7	6 7	2 8	7 3	4 8
Eu	2.5	2	2 3	0 2	1 3	1	1 5	-0 2	1 5	-0 2
Tb	1	0 8	1 3	0 6	1 3	0 6	1 1	0 8	1 5	1 2
Yb	3 4	3 3	4 1	5 2	6 4	2 6	6 6	6 3	8	7 4
Lu	0.53	0 5	0 67	0 8	0 96	0 4	0 98	0 96	1 18	1 12
Zr	<LD	0 01	<LD	<LD	<LD	<LD	<LD	<LD	0 02	<LD

Table B.5 continued: INAA results from PHIS and Lodestar breccia samples (ppm except Au, Ir in ppb, and Ca, Fe, Na, Sn, Sr, and Zr in wt %)

Sample	JH-99-173	JH-99-092A	JH-99-092B	JH-99-126A	JH-99-121C	JH-99-004C	JH-99-002C	JH-99-031	JH-99-141A	JH-99-141B
rock type	felsic material	felsic material	felsic material	felsic material	felsic material	diabase	diabase	diabase	QFP clast	QFP clast
Au	<LD	<LD	<LD	<LD	4	<LD	<LD	<LD	184	1860
Ag	<LD	<LD	<LD	<LD	<LD	<LD	<LD	<LD	<LD	<LD
As	8.4	71	12	7.9	36	2.7	8.5	8.4	5000	12000
Ba	150	740	500	68	550	390	330	410	2000	2600
Br	<LD	<LD	<LD	<LD	<LD	<LD	<LD	<LD	<LD	<LD
CaO	<LD	<LD	<LD	<LD	<LD	6	6	4	<LD	<LD
Co	<LD	<LD	1	<LD	2	45	40	23	12	4
Cr	<LD	<LD	<LD	<LD	<LD	100	<LD	170	7	<LD
Cs	<LD	2	1	1	<LD	<LD	<LD	2	1	2
Fe2O3	0.9	0.72	0.7	0.94	1.62	10.3	12.5	6.07	3.2	1.76
Hf	7	4	4	8	8	3	8	4	24	30
Hg	<LD	<LD	<LD	<LD	<LD	<LD	<LD	<LD	<LD	<LD
Ir	<LD	<LD	<LD	<LD	<LD	<LD	<LD	<LD	<LD	<LD
Mo	<LD	<LD	3	<LD	3	<LD	<LD	<LD	<LD	<LD
Na	3.09	2.52	2.78	3.14	3.02	2.45	2.87	2.27	1.35	1.31
Ni	<LD	<LD	<LD	<LD	<LD	<LD	<LD	<LD	<LD	<LD
Rb	120	140	93	140	79	48	<LD	40	91	190
Sb	<LD	0.7	0.7	<LD	0.2	<LD	<LD	0.3	3.1	<LD
Sc	1.3	1.2	1.2	1.9	3.9	38	43	23	2.9	1
Se	<LD	<LD	<LD	<LD	2	<LD	<LD	<LD	<LD	<LD
Sn	<LD	<LD	<LD	<LD	<LD	<LD	<LD	<LD	<LD	<LD
Sr	<LD	<LD	<LD	<LD	<LD	<LD	<LD	<LD	<LD	<LD
Ta	2.3	1.1	0.8	2.4	1.2	<LD	1.7	0.6	8.1	8.9
Th	12	16	16	12	12	0.6	1.9	3.7	22	23
U	2.6	2.9	3.1	2.6	2.9	0.3	<LD	0.4	6.1	6
W	<LD	<LD	<LD	<LD	<LD	<LD	<LD	<LD	<LD	<LD
Zn	<LD	<LD	<LD	<LD	62	177	181	117	97	<LD
La	22	18	18	13	37	9	36	19	18	17
Ce	45	29	32	43	82	26	85	36	52	46
Nd	23	9	10	16	32	12	42	15	19	24
Sm	5.8	1.4	1.5	4.2	6	4.1	12	4.1	9.3	8.9
Eu	0.3	0.3	0.3	0.3	1	1.8	4.3	1.2	1	1
Tb	1.2	<LD	<LD	0.9	1	1.1	2	<LD	2.9	3
Yb	7.3	1.6	1.7	8.4	6.7	3.4	6.7	2.7	15.3	16.3
Lu	1.15	0.24	0.26	1.2	1.02	0.56	1.1	0.43	2.42	2.5
Zr	<LD	<LD	<LD	0.01	0.02	<LD	<LD	<LD	0.04	0.05

Table B.5 continued. INAA results from PHIS and Lodestar breccia samples (ppm except Au, Ir in ppb, and Ca, Fe, Na, Sn, Sr, and Zr in wt %)

Sample	JH-99-286	JH-99-141D	JH-99-141E	JH-99-141F	CD-99-074	JH-99-092C	JH-99-092D	JH-99-146	JH-99-280
rock type	QFP clast	gabbro clast	gabbro clast	gabbro clast	mineralization	seds	seds	min gabbro	mineralization
Au	237	188	3360	330	12600	5	<LD	<LD	58500
Ag	<LD	<LD	<LD	<LD	39	<LD	<LD	<LD	250
As	13000	8100	27000	7700	30000	44	45	9.6	250000
Ba	880	1000	880	700	540	330	360	530	<LD
Br	<LD	<LD	<LD	<LD	<LD	<LD	<LD	<LD	<LD
CaO	<LD	1	2	3	2	4	3	6	<LD
Co	10	21	34	27	28	22	21	29	87
Cr	24	49	100	70	65	130	130	<LD	15
Cs	3	5	2	7	3	<LD	<LD	<LD	<LD
Fe2O3	5.23	6.24	8.17	6.85	14.4	6.44	6.57	11.3	30.1
Hf	20	2	2	3	5	4	4	11	<LD
Hg	<LD	<LD	<LD	<LD	<LD	<LD	<LD	<LD	<LD
Ir	<LD	<LD	<LD	<LD	<LD	<LD	<LD	<LD	<LD
Mo	<LD	<LD	<LD	<LD	<LD	<LD	<LD	<LD	<LD
Na	1.02	1.64	1.06	2.29	0.92	2.51	2.51	2.86	0.78
Ni	<LD	<LD	<LD	<LD	<LD	<LD	<LD	<LD	<LD
Rb	121	240	140	190	160	37	40	28	60
Sb	0.5	<LD	<LD	<LD	<LD	1.3	1	0.6	180
Sc	7.1	20	32	24	18	24	23	38	4.7
Se	<LD	<LD	<LD	<LD	6	1	1	<LD	33
Sn	<LD	<LD	<LD	<LD	<LD	<LD	<LD	<LD	<LD
Sr	<LD	<LD	<LD	<LD	<LD	<LD	<LD	<LD	<LD
Ta	6.6	<LD	<LD	<LD	<LD	0.4	0.3	2	<LD
Th	19	2.2	2	3	4.2	3.9	4.1	1.8	0.9
U	<LD	<LD	<LD	<LD	<LD	<LD	<LD	0.9	<LD
W	<LD	22	62	14	<LD	<LD	<LD	<LD	<LD
Zn	172	320	331	272	2150	130	111	208	1010
La	18	14	14	18	12	16	16	36	16
Ce	47	27	29	37	28	37	39	98	25
Nd	25	8	22	10	10	18	19	56	<LD
Sm	7.8	2.8	3.9	4	3.4	3.9	3.6	13	1.3
Eu	0.9	0.8	0.7	1.4	0.6	1.3	1.1	5.5	<LD
Tb	2.8	0.5	<LD	0.7	<LD	0.6	0.6	2.3	<LD
Yb	13.2	1.7	3.6	2.8	3.3	2.9	2.8	6.6	<LD
Lu	2.03	0.27	0.56	0.42	0.48	0.45	0.43	1.33	<LD
Zr	0.02	0.04	<LD	<LD	0.02	0.02	0.02	<LD	<LD

Table B.5 continued: INAA results from PHIS and Lodestar breccia samples (ppm except Au, Ir in ppb, and Ca, Fe, Na, Sn, Sr, and Zr in wt. %)

Sample	JH-99-281	JH-99-282	JH-99-283	JH-99-284	JH-99-285	JH-99-287	JH-99-288	JH-99-289
rock type	mineralization	mineralization	mineralization	mineralization	mineralization	mineralization	mineralization	mineralization
Au	2660	1790	12000	819	260	3710	2320	18
Ag	9	13	38	6	<LD	22	6	<LD
As	41000	13000	3000	11600	12900	12000	44000	240
Ba	360	690	320	550	710	660	460	480
Br	<LD	<LD	<LD	<LD	<LD	<LD	-2.8	<LD
CaO	2	<LD	<LD	<LD	<LD	<LD	<LD	2
Co	26	23	110	33	16	32	30	18
Cr	47	65	63	130	80	130	99	110
Cs	5	7	3	3	8	7	6	8
Fe2O3	9.14	8.73	28.2	9.97	6.98	11	8.51	6.84
Hf	5	8	3	6	8	8	5	6
Hg	<LD	<LD	<LD	<LD	<LD	<LD	<LD	<LD
Ir	<LD	<LD	<LD	<LD	<LD	<LD	<LD	<LD
Mo	<LD	15	<LD	<LD	<LD	<LD	<LD	35
Na	1.27	0.79	0.53	1.14	1.1	1.11	0.98	1.23
Ni	<LD	55	<LD	<LD	<LD	<LD	<LD	<LD
Rb	193	210	88	180	220	210	230	190
Sb	35.6	<LD	3.8	8.5	0.2	0.2	36.7	2.6
Sc	22	18	11	24	18	21	20	25
Se	6	<LD	8	<LD	<LD	4	<LD	<LD
Sn	<LD	<LD	<LD	<LD	<LD	<LD	<LD	<LD
Sr	<LD	<LD	<LD	<LD	<LD	<LD	<LD	<LD
Ta	0.7	2.4	<LD	0.6	2	2.4	1	1.4
Th	4.8	7.7	2.8	6.1	8.3	8.5	5.1	3.9
U	<LD	<LD	<LD	<LD	<LD	<LD	<LD	-0.2
W	44	<LD	18	18	21	26	<LD	19
Zn	207	1320	1850	427	486	1250	195	652
La	15	17	12	25	18	18	14	22
Ce	27	26	24	46	33	41	28	37
Nd	9	19	10	19	15	16	13	20
Sm	3.8	4	2.1	4.3	4.4	4.3	2.4	5
Eu	0.5	0.7	0.3	0.9	0.8	0.9	0.6	1.3
Tb	<LD	1.1	0.5	0.9	1.2	1.2	0.8	0.9
Yb	3.4	5.6	1.5	2.8	5.6	5.8	3.6	4
Lu	0.53	0.84	0.24	0.44	0.88	0.88	0.56	0.68
Zr	<LD	<LD	<LD	<LD	0.02	<LD	<LD	<LD